Jagiellonian University

Faculty of Physics, Astronomy and Applied Computer Science

DOCTORAL THESIS

Evaluation of the NEMA characteristics for the Modular J-PET scanner

---

Author:

Faranak Tayefi Ardebili

Supervisor:

Prof. Dr hab. Paweł Moskal

Auxiliary Supervisor:

Dr. Szymon Niedźwiecki

Kraków

2023

Wydział Fizyki, Astronomii i Informatyki Stosowanej,

Uniwersytet Jagielloński

Oświadczenie

Ja nizej podpisana Faranak Tayefi Ardebili (nr indeksu: 1169581) doktorantka Wydziału Fizyki, Astronomii i Informatyki Stosowanej Uniwersytetu Jagiellońskiego oświadczam, że przedłożona przeze mnie rozprawa doktorska pt. 'Evaluation of the NEMA characteristics for the Modular J-PET scanner' jest oryginalna i przedstawia wyniki badań wykonanych przeze mnie osobiście, pod kierunkiem prof. dr hab. Pawła Moskala. Pracę napisałam samodzielnie.

Oświadczam, że moja rozprawa doktorska została opracowana zgodnie z Ustawą o prawie autorskim i prawach pokrewnych z dnia 4 lutego 1994 r. (Dziennik Ustaw 1994 nr 24 poz. 83 wraz z późniejszymi zmianami).

Jestem świadom, że niezgodność niniejszego oświadczenia z prawdą ujawniona w dowolnym czasie, niezaleznie od skutków prawnych wynikających z ww. ustawy, może spowodować unieważnienie stopnia nabytego na podstawie tej rozprawy.

Author: Faranak Tayefi Ardebili

Signed:

ACKNOWLEDGEMENTS

TABLE OF CONTENTS

Abstract

This study aim is to evaluate the performance characteristics of the Modular Jagiellonian Positron Emission Tomograph (Modular J-PET) in accordance with the recognized standards established by the National Electrical Manufacturers Association (NEMA) for Positron Emission Tomography (PET) scanners. The Modular J-PET represents the latest prototype within the Jagiellonian-PET group, distinguished by its utilization of plastic scintillator strips optimized for the precise detection of back-to-back gamma quanta arising from electron-positron annihilations. The Modular J-PET comprises 24 individual modules arranged in a symmetrical 24-sided polygon circumscribing a circular configuration with a diameter of 73.9 cm. Each module is constructed from 13 scintillator strips, aligned adjacently, each measuring 50 cm in length and possessing a cross-sectional dimension of 6 mm × 24 mm. Dual-ended scintillation light readout is accomplished through analog Silicon Photomultipliers (SiPMs).

Data collected during the experimentation phase were subjected to analysis employing software known as the J-PET Framework. The average system sensitivity of the Modular J-PET was determined to be 0.768 ± 0.003 cps/kBq in the center with the peak sensitivity of 2.1 cps/kBq. The system sensitivity has improved by sixfold compared to the first generation of the J-PET prototype with 192 strips.

Radial spatial resolution for TOF image reconstruction methods was found to be 4.92 ± 0.56 mm, 7.38 ± 0.49 mm, and 6.94 ± 0.38 mm at positions 1 cm, 10 cm, and 20 cm from the detector center, respectively. Tangential spatial resolution for TOF image reconstruction methods was determined as 7.38 ± 0.51 mm, 7.37 ± 0.10 mm, and 14.67 ± 0.31 mm at the same positions, while axial spatial resolution was calculated as 30.73 ± 0.52 mm, 30.73 ± 0.64 mm, and 31.96 ± 0.29 mm. It is worth noting that the tangential and radial spatial resolution values of the Modular J-PET detector align closely with those of commercial PET devices. Future enhancements are anticipated in axial spatial resolution through an extended axial field of view scanner and the application of wavelength shifting (WLS) techniques. The determination of the scattered fraction based on single-scatter randoms background (SSRB) algorithms yielded a value of 41.68 ± 0.19 [%], which is consistent with that observed in commercial PET devices. To validate the experimental findings, GATE simulations were conducted.

The simulations included spatial resolution assessments using a sodium source, as well as evaluations of sensitivity and scatter fraction involving a phantom conforming to NEMA standards. The simulations indicated that the Modular J-PET achieves a

system sensitivity of 1.324 $\pm$ 0.032 cps/kBq at the center of the detector's field of view and 1.313 $\pm$ 0.001 cps/kBq at a 10 cm offset from the tomograph center. The peak sensitivity at the center of the detector's filed of view to be 2.9 cps/kBq across various multiplicity cuts. Furthermore, the scatter fraction, computed utilizing SSRB algorithms, was established at (40.25$\pm$2.3)%. Radial spatial resolution for TOF image reconstruction methods was found to be 4.80 $\pm$ 0.59 mm, 7.26 $\pm$ 0.55 mm, and 6.67 $\pm$ 0.42 mm at positions 1 cm, 10 cm, and 20 cm from the detector center, respectively. Tangential spatial resolution for TOF image reconstruction methods was determined as 7.27 $\pm$ 0.47 mm, 7.27 $\pm$ 0.59 mm, and 15.1 $\pm$ 0.4 mm at the same positions, while axial spatial resolution was calculated as 29.97 $\pm$ 0.49 mm, 30.53 $\pm$ 0.74 mm, and 31.78 $\pm$ 0.11 mm.

The Modular J-PET, characterized by its single-layer configuration with 50 cm scintillator strips, exhibits the potential for extension to an extended axial field-of-view through multi-layer arrangements. Consequently, the presented Modular J-PET prototype holds promise for the cost-effective development of a total-body J-PET system constructed from plastic scintillators.

Streszczenie

Celem tej pracy jest ocena charakterystyk wydajnościowych Modularnego Jagiellońskiego Tomografu Emisji Pozytonowej (Modular J-PET) zgodnie z uznanymi standardami ustanowionymi przez Narodowe Stowarzyszenie Producentów Sprzętu Elektrycznego (NEMA) dla skanerów tomografii emisji pozytonowej (PET). Modularny J-PET stanowi najnowszy prototyp w grupie Jagielloński PET, wyróżniający się wykorzystaniem pasków scyntylacyjnych z plastiku zoptymalizowanych do precyzyjnej detekcji kwantów gamma poruszających się w przeciwnych kierunkach, pochodzących z anihilacji elektronu i pozytonu. Modularny J-PET składa się z 24 indywidualnych modułów ułożonych w symetryczny wielobok o 24 bokach, opartych na okręgu o średnicy 73.9 cm. Każdy moduł składa się z 13 sąsiadujących pasków scyntylacyjnych, z których każdy ma długość 50 cm i przekrój o wymiarach 6 mm x 24 mm. Odczyt światła scyntylacyjnego z obu końców jest realizowany za pomocą analogowych fotopowielaczy krzemowych (SiPMs).

Dane zebrane podczas fazy eksperymentalnej zostały poddane analizie przy użyciu oprogramowania znanego jako J-PET Framework. Średnia czułość Modularnego J-PET wyniosła 0.768 ± 0.003 cps/kBq w centrum, z maksymalną czułością wynoszącą 2.1 cps/kBq. Czułość systemu uległa poprawie sześciokrotnie w porównaniu z pierwszą generacją prototypu J-PET z 192 paskami.

Rozdzielczość przestrzenna promieniowa dla metody rekonstrukcji obrazów w trybie TOF wyniosła odpowiednio 4.92 ± 0.56 mm, 7.37 ± 0.49 mm i 6.94 ± 0.38 mm w odległościach 1 cm, 10 cm i 20 cm od środka detektora. Rozdzielczość przestrzenna styczna dla metody rekonstrukcji obrazów w trybie TOF została ustalona odpowiednio jako 7.38 ± 0.51 mm, 7.37 ± 0.10 mm i 14.67 ± 0.31 mm w tych samych pozycjach, podczas gdy rozdzielczość przestrzenna osiowa została obliczona jako 30.73 ± 0.52 mm, 30.73 ± 0.64 mm i 31.96 ± 0.29 mm. Warto zaznaczyć, że wartości rozdzielczości przestrzennej stycznej i promieniowej detektora Modularnego J-PET są zbliżone do tych obserwowanych w komercyjnych urządzeniach PET. Przewiduje się przyszłe ulepszenia w rozdzielczości przestrzennej osiowej poprzez rozszerzenie pola widzenia osiowego skanera oraz zastosowanie technik wykorzystujących przesuwacze długości fali (WLS). Określenie frakcji rozproszenia na podstawie algorytmu SSRB dało wynik 41.68 ± 0.19 [%], co jest zgodne z wartościami obserwowanymi w komercyjnych urządzeniach PET. Aby potwierdzić wyniki eksperymentalne, przeprowadzono symulacje przy użyciu programu GATE.

Symulacje obejmowały ocenę rozdzielczości przestrzennej przy użyciu źródła sodu oraz ocenę czułości i frakcji rozproszeniowej z udziałem fantomów zgodnych ze

standardami NEMA. Symulacje wykazały, że Modularny J-PET osiąga czułość wynoszącą 1.324 ± 0.032 cps/kBq w centrum pola widzenia detektora oraz 1.313 ± 0.001 cps/kBq przy przesunięciu 10 cm od środka tomografu. Maksymalna czułość w centrum pola widzenia detektora wynosi 2,9 cps/kBq przy różnych cięciach wielokrotności. Ponadto frakcja rozproszeniowa, obliczona przy użyciu algorytmu SSRB, wyniosła $(40.25 \pm 2.3)\%$. Rozdzielczość przestrzenna promieniowa dla metody rekonstrukcji obrazów w trybie TOF wyniosła odpowiednio 4.80 ± 0.59 mm, 7.26 ± 0.55 mm i 6.67 ± 0.42 mm w odległościach 1 cm, 10 cm i 20 cm od środka detektora. Rozdzielczość przestrzenna styczna dla metody rekonstrukcji obrazów w trybie TOF została ustalona odpowiednio jako 7.27 ± 0.47 mm, 7.27 ± 0.59 mm i 15.1 ± 0.4 mm w tych samych pozycjach, podczas gdy rozdzielczość przestrzenna osiowa została obliczona jako 29.97 ± 0.49 mm, 30.53 ± 0.74 mm i 31.78 ± 0.11 mm.

Modularny J-PET, charakteryzujący się jednowarstwową konfiguracją z paskami scyntylacyjnymi o długości 50 cm, wykazuje potencjał do rozszerzenia pola widzenia osiowego poprzez układy wielowarstwowe. W związku z tym prezentowany prototyp Modularnego J-PET obiecuje efektywny kosztowo rozwój systemu J-PET na całe ciało, wykonanego ze scyntylatorów plastikowych.

ROZDZIAŁ 1

INTRODUCTION

This thesis aims to comprehensively investigate the performance characteristics of the Positron Emission Tomography scanner utilizing plastic scintillators [1, 2, 3, 4, 5], in alignment with the standards prescribed by the National Electrical Manufacturers Association (NEMA) [6].

Cancer, a complex and pervasive disease characterized by uncontrolled cell growth, remains a formidable challenge to public health worldwide. The number of the deaths due to cancer is increasing year by year [7, 8] and this is the reason why significant advancements have been made in understanding its underlying mechanisms, leading to the development of diverse treatment strategies.

The imperative of cancer prevention and the enhancement of accessibility to diagnostics and treatment have ascended to the forefront of contemporary healthcare concerns. Presently, Positron Emission Tomography (PET) has emerged as a superior diagnostic modality compared to traditional methods like Computed Tomography (CT) and Magnetic Resonance Imaging (MRI) [9, 10, 11] . While CT and MRI excel in anatomical visualization (present images of body's internal organs and tissues) , PET offers the unique advantage of not only capturing anatomical structures but also illuminating functional and molecular activities within tissues [12]. This capability facilitates early disease detection and precise treatment planning [13, 14]. At present, the realm of nuclear imaging predominantly comprises hybrid systems, amalgamating a minimum of two techniques: PET integrated with CT (PET/CT) or PET integrated with MRI (PET/MRI) [15, 16]. It is noteworthy that the comprehensive assessment of a patient's bodily state necessitates the amalgamation of structural (CT or MRI) and functional (PET) scans, thereby offering a holistic depiction as shown in Figure 1.1 [17].
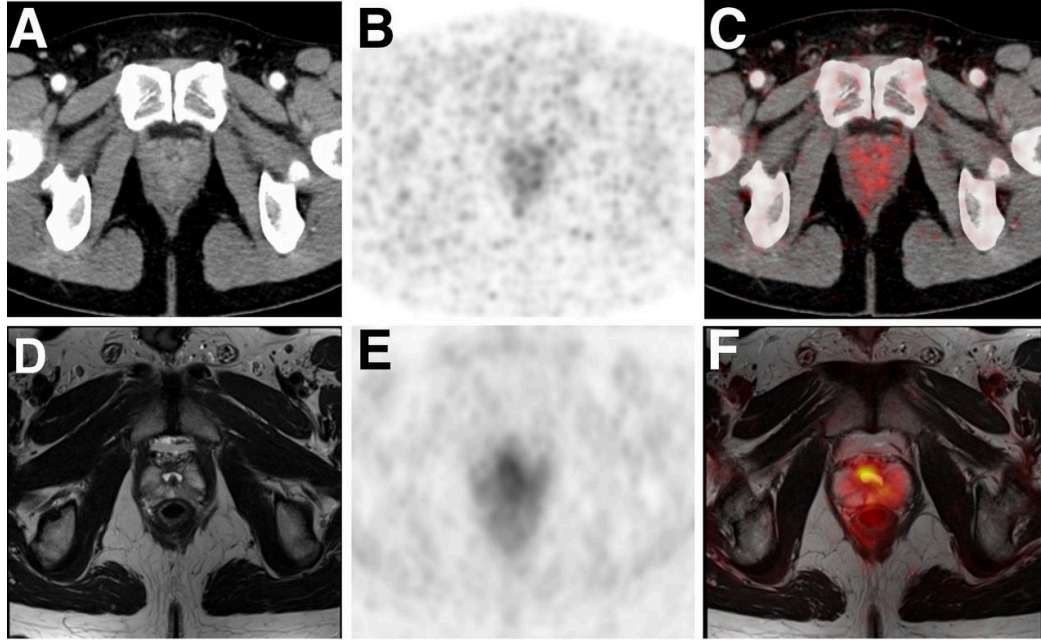
Rysunek 1.1: Comparison of the CT, MRI and PET images and combinations of these images of a 51-y-old man with prostate cancer. Contrast-enhanced CT (A), PET (B), and fused 68Ga-PSMA PET/CT (C) images are displayed in comparison to T2-weighted MRI (D), PET (E), and fused 68Ga-PSMA PET/MR (F). Full information may be obtained only from combined images such as restricted diffusion of soft-tissue mass is indicative of malignancy. Figure adapted from [17].

PET, a non-invasive imaging technique, expedites the identification of cancerous tumors while affording real-time elucidation into the metabolic and biochemical operations within organs and tissues [14, 18]. Primarily employed for the detection and monitoring of cancer, PET scans assume a paramount role in medical diagnostics. In addition, PET scans serve as a diagnostic avenue for evaluating the functional integrity of the heart and brain [19].

During PET measurements, the detection of gamma radiation emanating from the annihilation of electrons and positrons takes place. These positrons stem from a radionuclide tracer with positron-emitting properties, typically comprising biologically active molecules, and are introduced into the patient's body. Following the measurement process, advanced computer-aided techniques are employed to reconstruct an image depicting the concentration of the tracer within the body [20]. While Fluorodeoxyglucose (FDG) remains a prominent subject of imaging in the majority of PET

scans, the realm of PET encompasses a diverse array of radioactive tracers. These tracers play a pivotal role in visualizing the concentration of various distinct types of molecules within tissue [21].

Commercial PET scanners, often coupled with CT or MRI modalities, typically possess an axial coverage of 15–30 cm. Consequently, there are trade-offs among detected positron annihilation coincidence events, scanning duration, and administered dosage within clinical PET applications [22]. The Signal-to-Noise Ratio (SNR) within reconstructed images is intrinsically linked to the tally of detected events, thereby influencing image quality. Presently, PET scanners yield images produce by noise and are ill-suited for high-resolution dynamic imaging studies that incorporate tracer kinetic modeling [23]. This predicament can be remedied by extending the axial coverage of the scanner to an extent that encompasses the entirety of the human body. Employing a total-body-length PET scanner range would significantly enhance sensitivity and facilitate comprehensive total-body dynamic imaging for capturing dynamic data from all patient tissues [22, 24, 25]. However, the implementation of Total Body PET remains a formidable challenge due to factors such as cost and technical complexities [26]. Despite these substantial challenges, the potential clinical dividends engendered by Total Body PET underscore the imperative of persistent research and technological innovations within this domain [27].

The Jagiellonian PET (J-PET) collabration is diligently pursuing the development of an economically viable total body PET apparatus [1, 2, 3, 4, 5]. Its innovation arises from applying plastic scintillators instead of inorganic rystals used in classical PET scanners [28, 29]. The excellent time properties of plastic scintillators allow effective application of the time-of-flight (TOF) technique. This technique plays a pivotal role in enhancing the contrast of reconstructed images, thereby contributing to improved diagnostic accuracy [30, 31]. The intrinsic cost-effectiveness of plastic scintillators renders them an attractive and practical choice, positioning them as a credible alternative to crystal scintillators [18] . Furthermore, the utilization of plastic PET with axially arranged scintillator strips decreases significantly costs of readout electronics and Silicon Photomultipliers (SiPMs) for the PET scanner, which are expected to be

about five times less than the current crystal-based PET tomograph [4].

The history of the whole-body J-PET detector traces its origins back to 2009 [32, 33], and culminated in the realization of a cylindrical chamber structure, formed through the arrangement of three concentric layers of plastic scintillator strips in 2016 [34, 35, 36]. Subsequently, in 2021, the latest iteration of J-PET scanners, known as the Modular J-PET, emerged in the form of a regular 24-sided polygonal configuration, circumscribing a scanner affording a total axial field of view (AFOV) of 50 cm [37] an advancement at least twice the magnitude of contemporary commercial PET instruments, as depicted in Figure 1.2 .
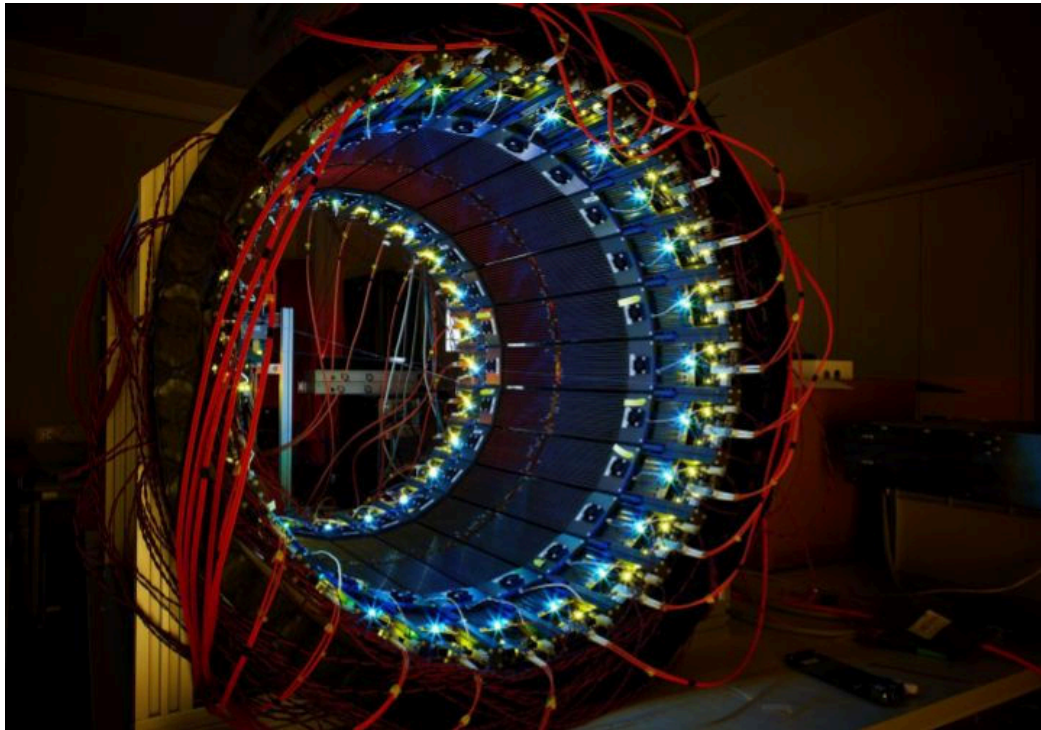
Rysunek 1.2: Modular J-PET detector, built out of 24 modules which each module is composed of 13 scintillator strips, read out by a silicon photomultiplier (SiPM) array from both sides.

To assess performance and compare modular J-PET characteristics with the other available scanners, methods and standards recommended by National Electrical Manufacturers Association (NEMA) have been used [6]. NEMA standards is an authoritative entity that establishes normative standards for electrical equipment, including

medical diagnostic imaging apparatus. It defines the characteristics of PET scanners such as the spatial resolution, scatter fraction, noise equivalent count rate (NECR), count losses, sensitivity [38]. The aim of this work is to estimate the performance characteristics of the Modular J-PET detector with a large AFOV and the dependence of these characteristics on the geometry, subsequently contrasted against simulation outcomes.

The exploration of the defined objectives is expounded upon in the ensuing sections, organized as follows. Chapter 2 constitutes an appraisal of the fundamental principles underlying Positron Emission Tomography (PET), encompassing topics such as the interaction of gamma radiation with matter and the operational principles governing PET tomography. Chapter 3 is dedicated to an exposition of the J-PET detector, and principle of operation of the J-PET scanner. Subsequently, Chapter 4 explains characteristics of NEMA standards.

Chapter 5 resides with the simulation of the J-PET detector through the utilization of the GATE software. Furthermore, this chapter presents the criteria for the event selection. Chapter 6 describes on evaluation performance characteristics of the Modular J-PET based on simulation. This entails a meticulous evaluation of sensitivity, spatial resolution, and scatter fraction through simulation.

Chapter 7 contains data collection for all measurements, explanation of energy calibration procedures, and preselection conditions applied to data collected during experimental measurements. In chapter 8 performance of characteristics of the Modular J-PET based on experimental measurements according to the NEMA standard is evaluated. Chapter 9 includes a detailed discussion of obtained results in comparison with state of the art PET scanner. The conclusion of the evaluation performance characteristics of the Modular J-PET and perspectives of development of the J-PET detector into total body PET scanner are described in Chapter 10.

Author Contribution:

The author has demonstrated active involvement in multiple facets of this study, rendering valuable contributions across several domains, notably, taking an active role in the assembly of the Modular J-PET apparatus within the laboratory environment.

The author's pivotal role commenced with the inception of geometric simulations, progressively extending to an in depth exploration of the scanner's performance characteristics, alongside a analysis of pre-selected data in congruence with the NEMA standards. In the realm of software utilization, the author displayed adeptness in autonomously employing the pre-existing QETIR software for the purpose of image reconstruction derived from GATE simulation results. Notably, the author facilitated the formulation of algorithms pertaining to Single Slice Rebinning, serving as a foundational mechanism for the calculation of scatter fraction and NECR. The author also undertook the development of sensitivity calculation algorithm, integral to the evaluation of the Modular J-PET scanner's performance.

In the context of empirical endeavors, the author was integral to the formulation and execution of the experimental setup, encompassing the PET Scatter Phantom, PET Sensitivity Phantom, and point-like sources measurements. Furthermore, the author actively participated in data monitoring and acquisition throughout the experimental phase, thereby playing a critical role in data acquisition.

Moreover, the author's role spanned the comprehensive spectrum of data handling, extending to the formulation of pre-selection protocols and Time-Over-Threshold (TOT) calibration within J-PET Framework analysis modules. Furthering the contributions, the author assumed responsibility for the development of pre-selection procedures and preparation of post-processing algorithms including the adaptation of Single Slice Rebinning algorithms to experimental data.

Subsequent to the intricate analysis of data, the author harnessed the capabilities of the QETIR software to meticulously scrutinize the output stemming from both GATE simulations and experimental data.

It is relevant to describe in this thesis articles with the main contribution of the author of the thesis which the authors have contributed on preparation of the simulations, image reconstructions, and processing.

1. M. Dadgar, F. Tayefi Ardebili, et al., "Simulation based investigation of the DOI capable Total-Body J-PET in the framework of the parallax issue," submitted to in IEEE Transactions on Radiation and Plasma Medical Sciences, 2022.

2. M. Dadgar, S. Parzych and F. Tayefi Ardebili, "Introduction of the DOI capable Total-Body J-PET, a simulation study," Journal of Nuclear Medicine, 63 (supplement 2) 3316, June 2022.

3. M. Dadgar, S. Parzych and F. Tayefi Ardebili, et al., "Investigation of novel preclinical Total Body PET designed with J-PET technology: A simulation study," in IEEE Transactions on Radiation and Plasma Medical Sciences, 2022.

4. M. Dadgar, S. Parzych and F. Tayefi Ardebili, "A Simulation Study to Estimate Optimum LOR Angular Acceptance for the Image Reconstruction with the Total-Body J-PET" Lecture Notes in Computer Science 12722 (2021) 189-200.

ROZDZIAŁ 2

BASICS OF POSITRON EMISSION TOMOGRAPHY

2.1   Interaction of gamma radiation with matter

The interaction of gamma radiation with matter constitutes a fundamental pheno-
menon in the realm of radiation physics. Comprising high-energy photons, gamma
radiation possesses distinct characteristics that govern its interaction mechanisms
with diverse forms of matter. Profound comprehension of these interactions holds pi-
votal importance across a spectrum of applications, encompassing radiation therapy,
nuclear energy, and radiation detection [39, 40, 41].

2.1.1   Compton scattering

One of the primary interactions of gamma radiation with matter is Compton scatte-
ring, when a gamma interacts with a loosely bound electron in the outer shell of an
atom, thereby initiating a scattering process. During this Compton scattering pheno-
menon the gamma quantum transfers a portion of its energy and momentum to the
electron, resulting in a change in its direction and a decrease in photon energy. The
scattered photon can exit the medium without further interaction, or it can undergo
other processes like photoelectric absorption or another Compton scattering event (as
depicted in Figure 2.1). The relationship between the energy of the incoming photon
(E_γ) and the energy of the scattered gamma (E'_γ) based on the scattering angle (θ)
is described with the formula:

$$E'_\gamma = \frac{m_e c^2}{\frac{m_e c^2}{E_\gamma} + 1 - cos\theta} \tag{2.1}$$

where m_e stand for electron mass and c stand for speed of light. Maximum amount of
energy is transferred to electron when θ is equal to 180 ^{o} [39, 40, 41]. This phenomenon
is significant in understanding the behavior of gamma rays in materials and is utilized

8

in various imaging techniques, such as Compton imaging [42].
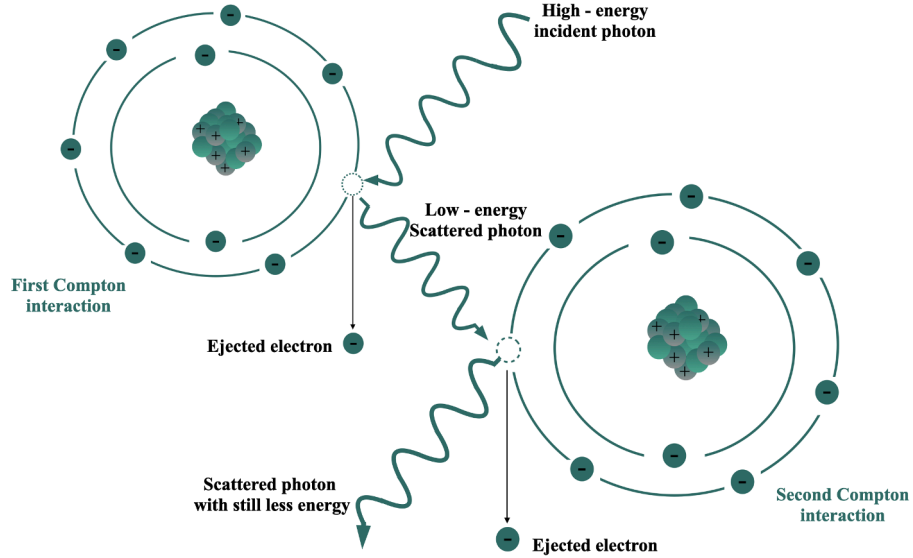
Rysunek 2.1: The Compton scattering process in which a gamma ray transfers only a portion of its energy to an electron in a shell, resulting in its own scattering with reduced energy. Figure adapted from [39].

2.1.2 Photoelectric effect

The photoelectric effect is another important interaction mechanism between gamma radiation and matter. In this process, a gamma photon interacts with an atom, and if its energy exceeds the binding energy of an inner shell electron, the electron is ejected from the atom (as depicted in Figure 2.2). Kinetic energy of the ejected electron is equal to $E_\gamma - E_B$, where $E_\gamma = h\nu$ is the energy of incident photon and E_B is the electron binding energy in the shell [39, 40, 41]. In human tissues for 511 keV gamma, it has much lower probability than Compton scattering. This interaction is responsible for the absorption of gamma radiation in materials and plays a crucial role in radiation shielding design and gamma spectroscopy.
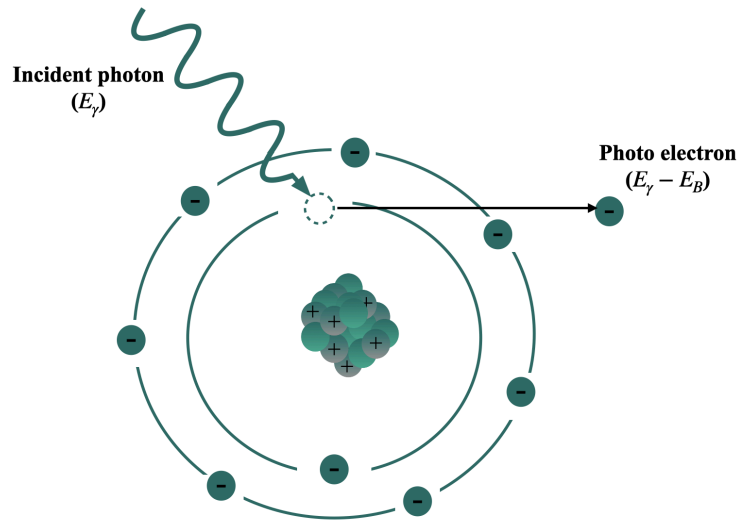
Rysunek 2.2: An illustration of photoelectric effect, where a g gamma photon transfers all its energy E_γ to a L-shell electron, and the electron is ejected with $E_\gamma - E_B$, where E_B is the binding energy of the electron in the L-shell. Figure adapted from [39].

2.1.3 Electron-positron pair production

Electron-positron pair production is a fundamental process in particle physics that occurs when high-energy photons, such as gamma rays, interact with matter.
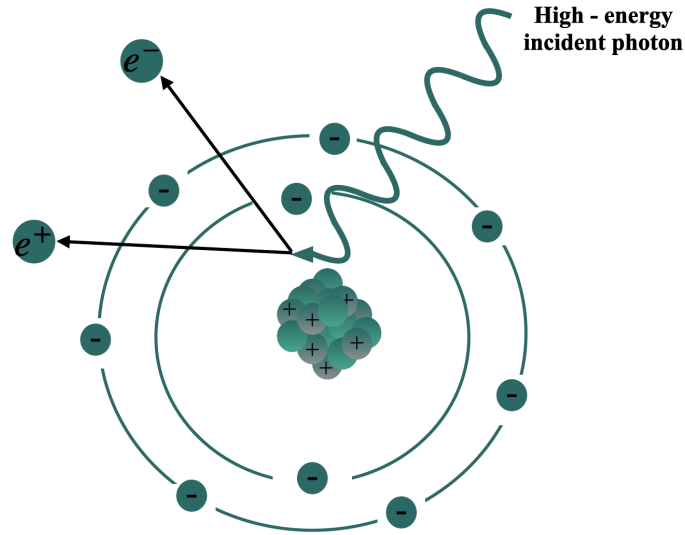
Rysunek 2.3: An illustration of electron-positron pair production, When the gamma photon energy is higher than 1.022 MeV, the photon interacts with the nucleus of an absorber atom during its passage through it and produces a positron and an electron. Figure adapted from [41].

This process involves a high-energy photon (exceeding 1.022 MeV) approaching a nucleus or atomic electron, thereby spontaneously transmuting into an electron-positron pair, as depicted in Figure 2.3. The photon's energy is converted into the rest mass energy of the electron and positron (According to Einstein's equation, $E = mc^2$, energy can be converted into matter). Upon positron thermalization, its annihilation with an electron engenders the creation of two 511 keV annihilation photons, as previously expounded [39, 40, 41].

2.1.4 Coherent scattering

Coherent scattering, also known as Rayleigh scattering, occurs when a gamma photon interacts with an entire atom or molecule without any energy transfer. The photon changes direction of scattered photon, but its energy remains unchanged as depicted in Figure 2.4. Although coherent scattering is relatively rare compared to other interaction processes, it plays a role in scattering gamma radiation at low energies and

contributes to background noise in imaging systems.
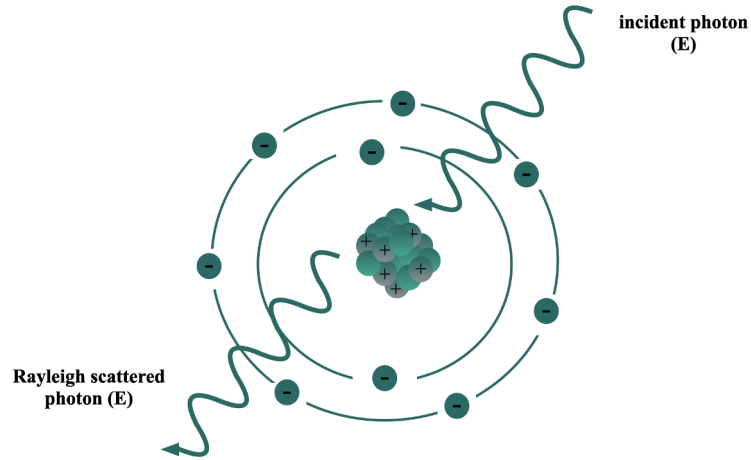
Rysunek 2.4: An illustration of Rayleigh scattering, when the gamma quantum interacts with an entire atom. Direction of scattered photon changes but its energy remains unchanged. Figure adapted from [43].

2.2 Detector design for 511 keV Gamma Photon Detection

2.2.1 Scintillators

Scintillators are a key component in radiation detection and measurement systems. These materials possess the unique property of emitting light when exposed to ionizing radiation, such as gamma rays, X-rays, or charged particles. Scintillators can consist of a scintillating crystal or a liquid solution embedded with fluorescent molecules [39, 40, 41]. When radiation interacts with the scintillator material, it transfers energy to the atoms or molecules within the material, causing them to enter an excited state. As the excited state decays, the scintillator emits light photons, which can be detected and measured using photodetectors, such as photomultiplier tubes or silicon photomultipliers [44, 45]. The emitted light intensity is proportional to the energy deposited by the incident radiation, allowing scintillators to provide valuable information about the type and intensity of the radiation. Due to their excellent energy resolution, fast response time, and versatility, scintillators find applications in various fields such as medical imaging [45, 46, 47].

In general, there are two type of the scintillators: organic and inorganic scintillator.

Inorganic scintillation crystals

Inorganic scintillation crystals, such as sodium iodide (NaI), cesium iodide (CsI), lutetium oxyorthosilicate (LSO) and bismuth germanate (BGO), are widely utilized in radiation detection and imaging due to their excellent energy resolution and high light output [48, 49, 50]. These crystals have a well-defined crystalline structure, allowing for efficient conversion of ionizing radiation into scintillation light, which can be easily detected and measured. Inorganic scintillation crystals offer desirable properties such as good stopping power, high density, and temperature stability, making them suitable for a nuclear medicine, and high-energy physics experiments [51, 52].

Organic scintillators

Organic scintillators are composed of carbon-based compounds and offer unique advantages in radiation detection applications. These scintillators exhibit fast response times, good radiation hardness, and high sensitivity to various types of radiation, including neutrons and gamma rays [49, 51, 52]. Organic scintillators are often favored for their flexibility, portability, and versatility, finding applications in areas such as particle physics experiments, nuclear power plants, and environmental monitoring [51, 53].

2.2.2 Photomultipliers

A photomultiplier tube (PMT) is a highly sensitive device used to detect and amplify light pulses [54]. It consists of a photocathode, a series of electron multiplier stages called dynodes, and an anode. When a photon strikes the photocathode, it releases an electron through the photoelectric effect. The released electron is then accelerated towards the first dynode, where it triggers the emission of multiple secondary electrons. These secondary electrons are successively multiplied as they cascade through the dynodes, resulting in a significantly amplified electron signal. Finally, the amplified

signal is collected at the anode for further processing as displayed in Figure 2.5 [54, 55].
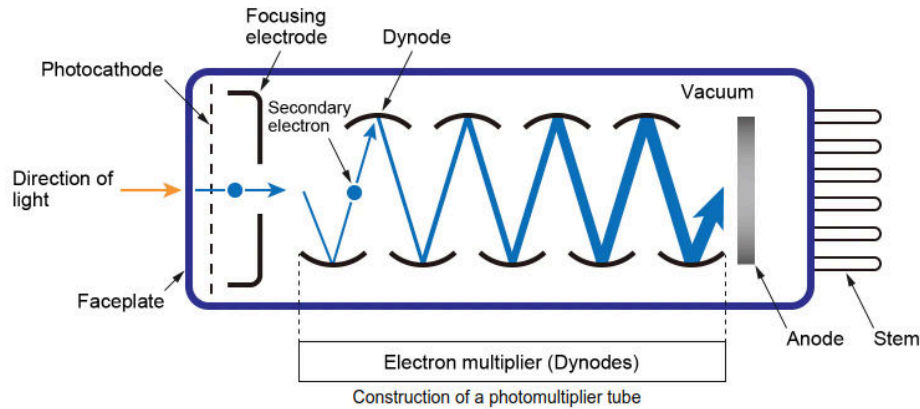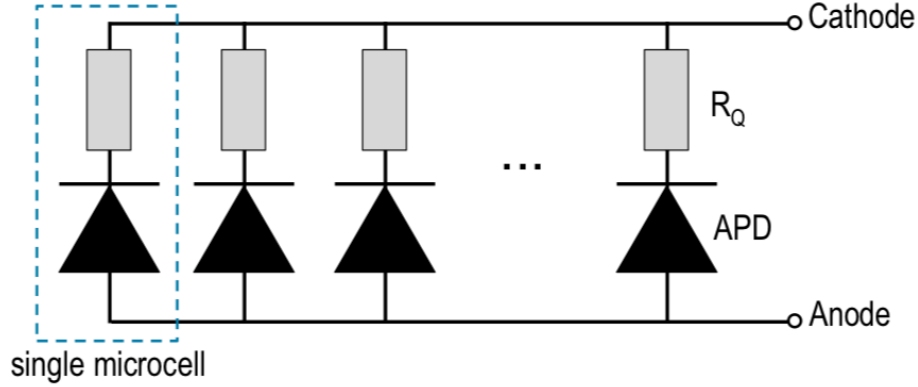

Rysunek 2.5: Schematic view of photomultiplier tube. Figure adapted from [55].

Silicon photomultiplier

Silicon photomultiplier (SiPM), also known as silicon PMT, is a relatively new type of photodetector that has gained popularity in recent years. It is based on a matrix of closely packed avalanche photodiodes (APDs) operated in Geiger mode (as illustrated in Figure 2.6) [56, 57, 58]. Each APD operates as a single-photon detector, and when photons strike the SiPM, they generate electron-hole pairs within the APDs. The resulting charge is then multiplied through an avalanche effect, providing an amplified output signal [58].

Silicon PMTs offer several advantages compared to traditional photomultiplier tubes. They have a compact and solid-state design, making them more robust and less prone to damage from external factors. SiPMs are insensitive to magnetic fields, making them suitable for applications where magnetic interference may be present. Additionally, SiPMs exhibit low operating voltages, which simplifies their integration into systems [59, 60]. One of the notable advantages of SiPMs is their excellent photon counting capability and high photon detection efficiency. They can detect single photons, enabling sensitive and precise measurements in low-light conditions. SiPMs

Rysunek 2.6: Schematic view of Silicon photomultiplier(SiPM) structure which All of the microcells are connected in parallel [59].

also exhibit excellent timing resolution, making them suitable for time-of-flight measurements and other applications requiring precise temporal information [61]. The versatility of SiPMs allows them to be employed in various fields, including medical imaging, particle physics, LiDAR (Light Detection and Ranging), and high-energy physics experiments. Ongoing research and development efforts continue to improve SiPM performance, enhancing their photon detection efficiency, timing characteristics, and temperature stability, further expanding their range of applications [62].

2.3   Principle of operation of the PET tomograph

PET is a nuclear medicine imaging technique employed to evaluate physiological function by assessing parameters such as blood flow, metabolism, neurotransmitters, and the behavior of radiolabelled drugs. It provides quantitative analysis, enabling the monitoring of relative changes over time in response to stimuli or disease progression. The methodology relies on the detection of emitted radioactivity subsequent to the administration of a small dose of a radioactive tracer through a peripheral vein [63, 64]. One common application of PET is the measurement of glucose consumption rates in different body regions. By utilizing the radiolabelled glucose analogue 18-fluorodeoxyglucose (FDG), the rate of glucose consumption can be determined. This approach finds clinical utility in distinguishing between benign and malignant tumors, as malignant tumors exhibit a higher glucose metabolic rate [65]. The PET imaging
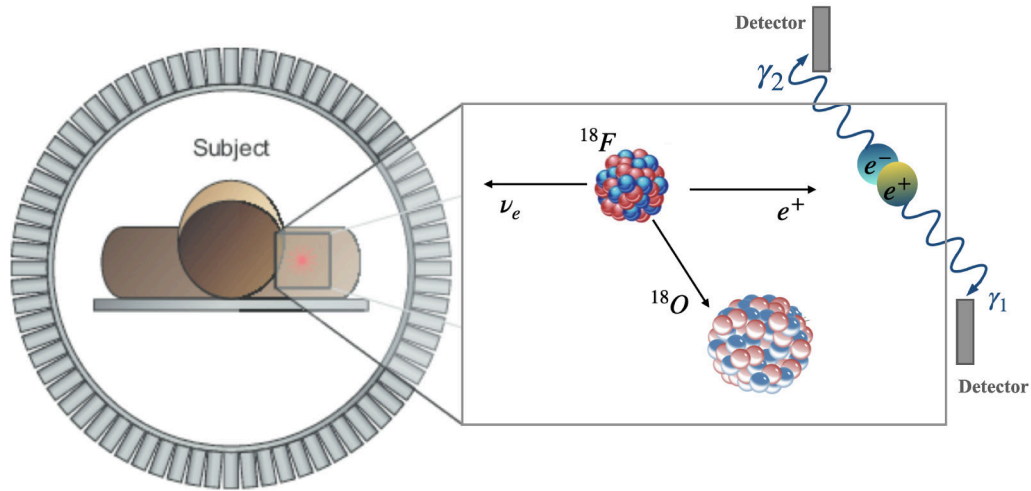
15

process encompasses a series of well-defined steps, visually depicted in Figure 2.7. The process begins with the administration of a suitable radiotracer—a molecular compound bearing a positron-emitting radionuclide— into the patient's body (Radiotracer Injection). The choice of radiotracer depends on the physiological process or specific target that is being investigated. The radiotracer behaves like a biological molecule and is taken up by the tissues or organs of interest. Commonly used molecules, based on ^{18}F, like 18F-Fludeoxyglucose (18F-FDG) allows to identify tumor cells with higher glucose consumption [66, 67].
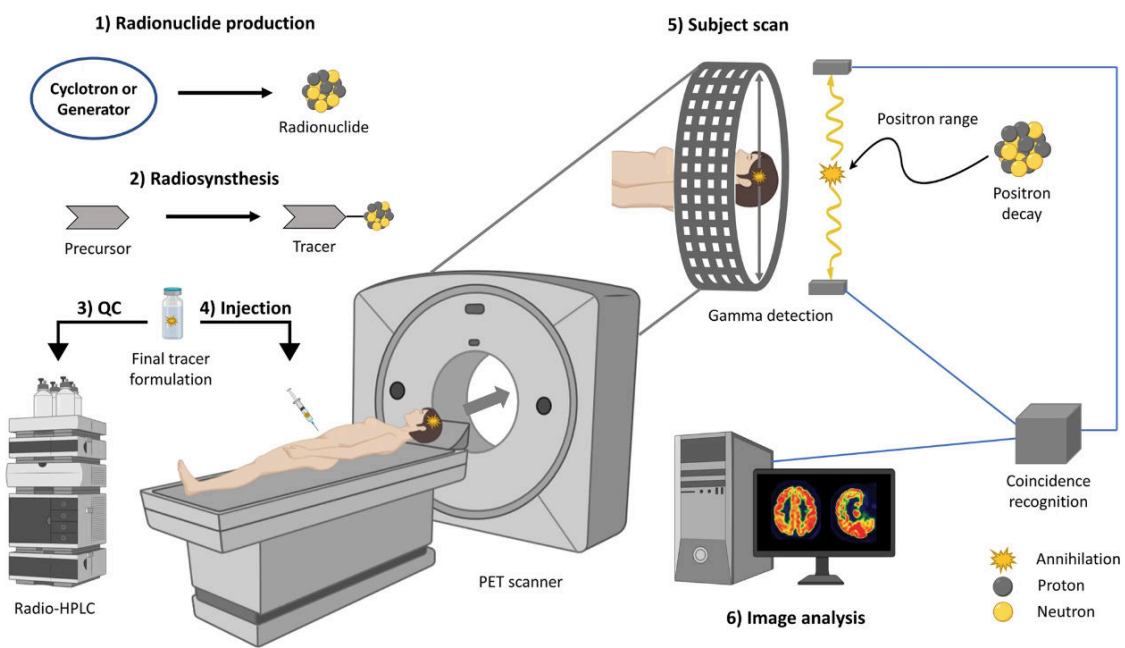
Rysunek 2.7: A schematic view depicting the various distinct steps of the PET imaging process. Figure adapted from [65].

Post-administration, the radiotracer undergoes radioactive decay. During this decay, the nucleus of the radioactive isotope becomes unstable and releases a positively charged particle called a positron. This positron emission finds origin in the transformation of a nucleus-bound proton into a neutron, concurrent with the emission of a positron and a neutrino—a phenomenon visually represented in Figure 2.8. Notably, the emitted positrons from ^{18}F attain peak energies of 0.63 MeV, thereby traversing a distance of approximately 2-3 millimeters within soft tissue [66, 67]. Positron

annihilates with electron predominantly into two gamma quanta. Remarkably, each gamma quantum bears an energy quantum of 511 keV, equating to sum up the rest mass energy of the positron-electron pair. The annihilation event is characterized by the complete conversion of the mass of the particles into energy. These process is illustrated in Figure 2.8.

Rysunek 2.8: Schematic representation of the ^{18}F decay process involving the emission of a positron particle (e^+). The emitted positron interacts with an electron through the process of pair annihilation, resulting in the emission of two gamma quantum each with an energy of 511 keV. 511 keV photon is detected and a signal is sent to computer for image reconstruction. Figure adapted from [68].

The detection of these 511 keV gamma rays forms the core of the imaging process in a PET scan. Sensitive detectors arranged in a ring around the patient record the simultaneous arrival of the gamma rays, and through a process known as coincidence detection, the originating location of the annihilation event can be determined. The ensuing electrical signals, harnessed by photomultiplier tubes (PMTs), are channeled to a computational domain for the purposes of data acquisition and processing. Herein, the temporal attributes, spatial coordinates, and intensity of the recorded gamma quanta are registered. Subsequently, these data coalesce to craft a raw projection image. The raw projection image is subjected to mathematical algorithms to reconstruct a three-dimensional image of the radiotracer distribution within the body (image reconstruction), as elaborated in Figure 2.7. This image offers valuable

insights into physiological processes and metabolic activity, making PET an essential tool in oncology, cardiology, and neurology, among other medical disciplines [63, 64, 65, 66, 69, 67]. Example of few most commonly used radionuclides emitting positrons are listed in Tab. 2.1 [69].

Tabela 2.1: List of the most commonly used radionuclides for PET imaging. Last column refers to the percentage of decay that occurs by positron emission from the radionuclide isotope. Table adapted from [69].

Radionuclide	Half-life time	Decay Mode
^{11}C	20.3 min	$\beta^+(99.75\%)$
^{13}N	10.0 min	$\beta^+(99.82\%)$
^{15}O	2.07 min	$\beta^+(99.89\%)$
^{18}F	110 min	$\beta^+(96.86\%)$
^{22}Na	2.603 year	$\beta^+(90.2\%)$
^{44}Sc	3.97 h	$e^+(98.2\%)$
^{68}Ga	67.7 min	$\beta^+(87.94\%)$

2.4 Type of coincidence events in PET

In PET, the detection of 511 keV back-to-back gamma rays relies on recognizing coincident events, where two gamma rays are detected simultaneously with predefined time window. When two photons are registered within each other's coincidental timeframe, it is inferred that they originate from the same annihilation event. Consequently, an event is ascribed to the Line Of Response (LOR) that interconnects the two points of detection within the sensitively monitored imaging volume, as depicted in Figure 2.9. These coincidence events can be categorized into four main types: true coincidence event, random coincidence event, detector scatters coincidence event, and phantom scatters coincidence event. Understanding these categories is essential for accurate imaging and for minimizing the various artifacts that can distort the final image [70]. By recognizing and correcting for these various coincidence events, medical professionals can achieve clearer, more precise images, enhancing the diagnostic value of the PET technology.
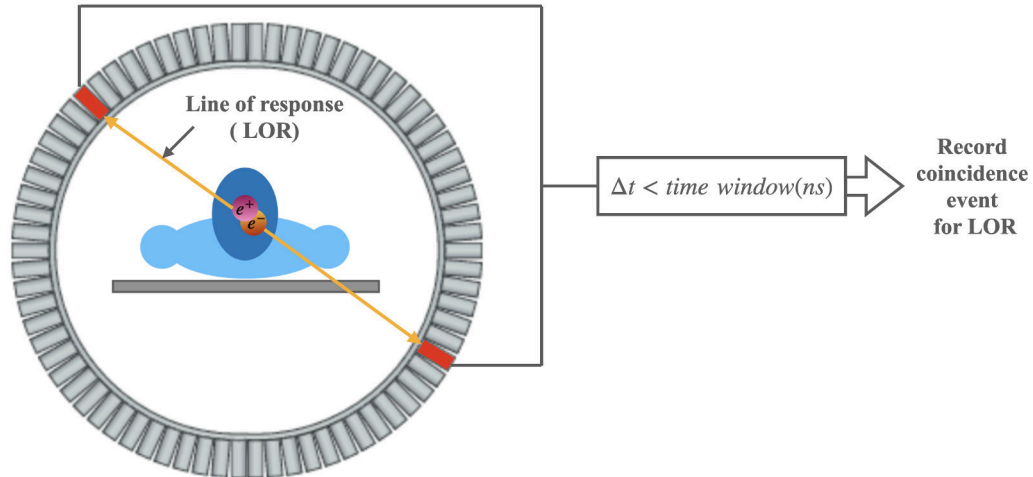
Rysunek 2.9: Coincidence event processing in PET data acquisition. Figure adapted from [70].
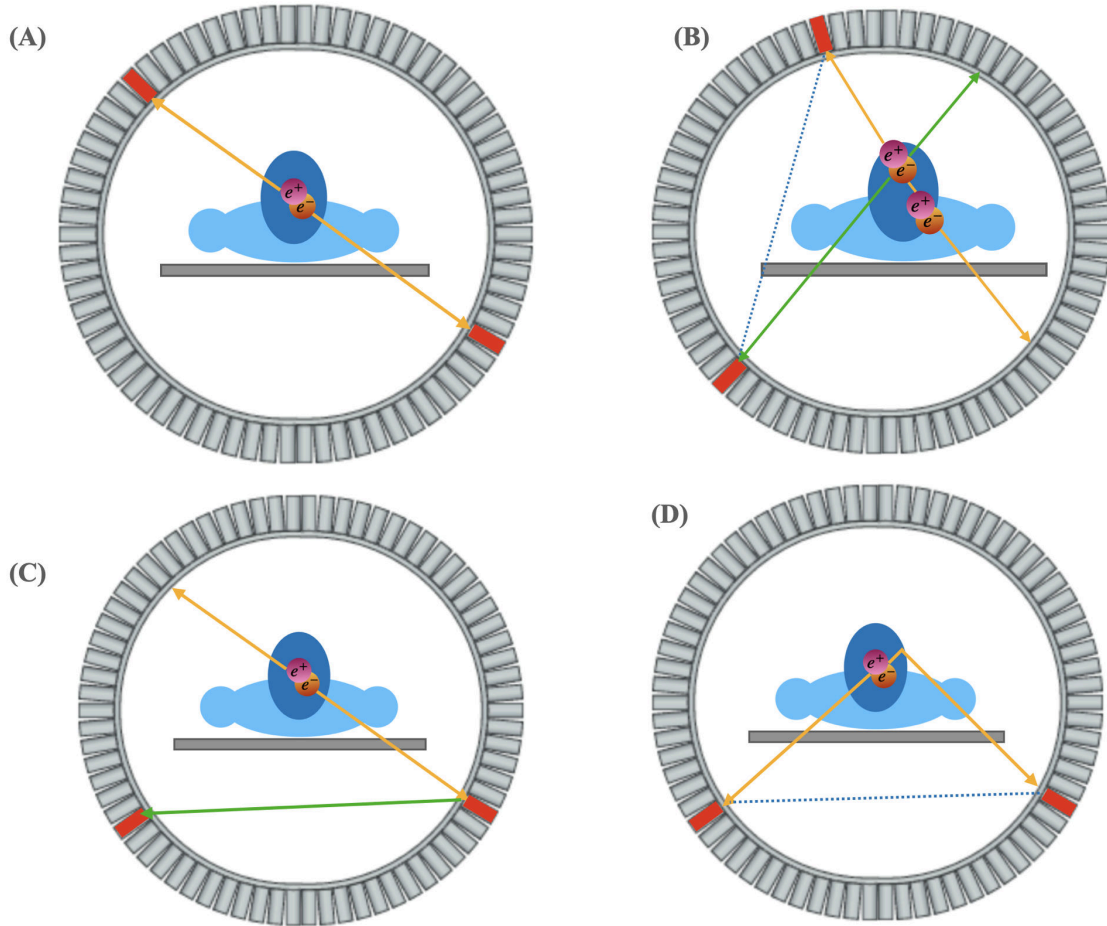
2.4.1 True Coincidences

True coincidences represent the ideal detection in PET scanning. They occur when both 511 keV gamma rays, resulting from the annihilation of a positron and an electron, are detected by the PET scanner without any interference, as elaborated in Figure 2.10(A). This type of coincidence provides an accurate representation of the tracer distribution and is the basis for creating the final image.

2.4.2 Random Coincidences

Random coincidences occur when gamma rays from different annihilation events are detected simultaneously but are unrelated to one another. These coincidences can introduce noise into the image since they do not correspond to a specific location of tracer concentration, as one can see in the figure 2.10(B). Various techniques, such as delayed-window subtraction, can be used to correct for random coincidences.

2.4.3 Detector Scatters Coincidences

Detector scatters happen when one or both of the gamma rays undergo scattering within the detector material itself, causing a deviation from their original paths, as

Rysunek 2.10: Schematic definitions of different types of coincidences: (a) true coincidence, (b) random coincidence, (c) detector-scattered coincidence, and (d) phantom-scattered coincidence. The circle in the center of the detector demonstrates the patient, and red detector indicate interactions of gamma quanta with specific detector. In the background coincidences event (scatter and random coincidences), the annihilation event (marked with a e^+, e^-) does not lie on the apparent line of response between the two-photon detections.

elaborated in Figure 2.10(C). This scattering can lead to mispositioning of the detected event in the reconstructed image. Correction techniques are often implemented to compensate for these distortions, usually involving modeling of the scatter process or utilizing additional hardware.

2.4.4 Phantom Scatters Coincidences

Phantom scatters, or object scatters, occur when gamma rays are scattered within the patient's body or surrounding objects before reaching the detectors, as elaborated in Figure 2.10(D). This can create errors in the positioning of the detected event, similar to detector scatters. Correction for phantom scatters typically involves sophisticated modeling techniques that consider the scattering properties of the tissues and other objects in the imaging field.

2.5 Sinogram

Within the scanner, the detection of coincidences occurs along Lines of Response (LORs), connecting pairs of detector elements. To systematically handle this raw data as it is acquired, a specific organization is employed. LORs are structured in such a manner that all LORs traversing a single point within the patient's body trace sinusoidal curves in the raw data histogram. Consequently, this data format is termed a "sinogram" [70]. The horizontal axis of a sinogram signifies the angular position of either the radiation source or the detector in relation to the imaged object. This axis effectively records the various projection angles during the data acquisition process (refer to Figure 2.11). Conversely, the vertical axis represents the radial position, measuring the distance of the detected radiation signal from the center of rotation. It encodes vital spatial information within the object. Each cell within the sinogram grid contains a numerical value that quantifies the intensity of the radiation signal at a specific angular and radial position [71, 72]. Sinogram formation stands as an indispensable intermediary step in the process of PET data acquisition. It often involves the application of necessary corrections to enhance data accuracy. Sinograms, in turn, serve as the cornerstone for image reconstruction, particularly in PET, where they are pivotal in reconstructing the radiotracer distribution. Notable example of sinograms is presented in Figure 2.12 [72]. This organization and utilization of sinograms play an instrumental role in PET imaging. They are paramount in ensuring precise image reconstruction, contributing significantly to the accuracy and clinical interpretability
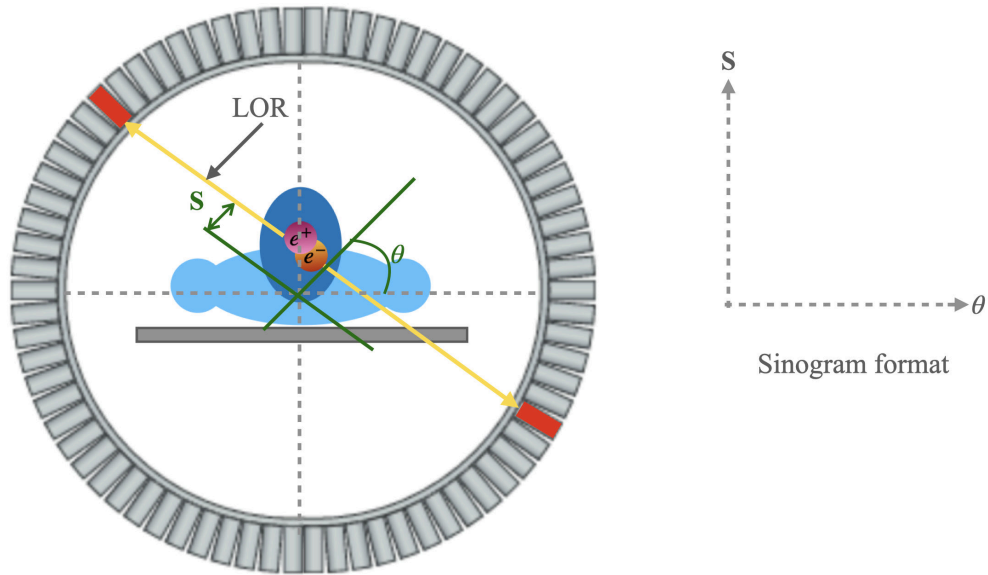
Rysunek 2.11: Illustration of the general Filter Back Projection algorithm.

of PET images [70].

2.6 PET Image Reconstruction Methods

Within the realm of PET, several methodologies exist for the reconstruction of PET images, only two prominent techniques as exemplars will be described, the Filtered Back Projection method (FBP) [73] and the Maximum Likelihood Expectation Maximization method (MLEM) [73, 74].

2.6.1 Filtered Back Projection (FBP)

The FBP is an analytic method of image reconstruction, which primary function is the reconstruction of high-resolution images from acquired projection data. The foundational principle of FBP centers on the mathematical transformation of collected projection data to construct either two-dimensional (2D) or three-dimensional (3D) images of the subject or object of interest. The FBP algorithm comprises two fundamental stages: filtering and back projection [73, 75].

Filtering: In the initial phase after stored data in a form of sinogram, the collec-
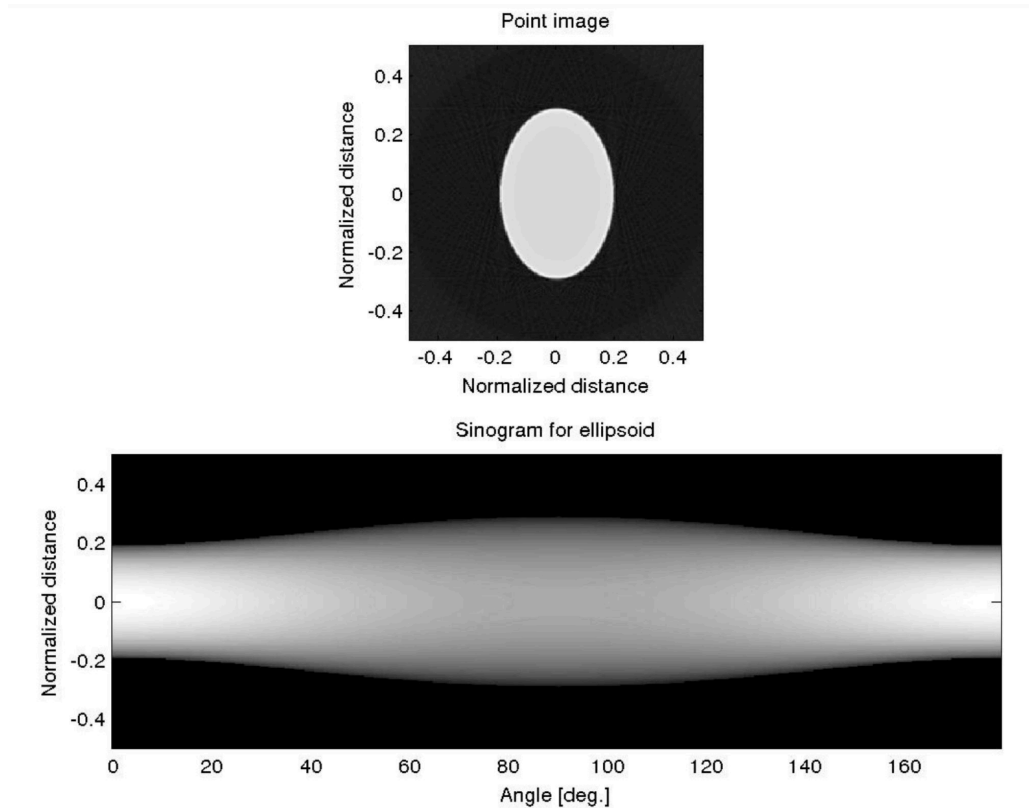
Rysunek 2.12: Example of sinogram for point in the center of scanner. Figure adapted from [72].

ted projection data undergoes filtering and the image is transformed using the Fast Fourier Transform (FFT) into frequencies domain. This process is integral in accentuating specific spatial frequencies within the data, thereby enhancing the visualization of fine structural details while concurrently mitigating the presence of undesirable artifacts.

Back Projection: Following the filtering stage, the filtered projection data is subject to back projection into the image space. During this step, each data point effectively contributes to pixel values across multiple locations within the image. Back projection process is executed iteratively for all angles of projection, thereby encompassing comprehensive spatial coverage as descripted in Figure 2.13. The comparison of back projection and filtered back projection method is illustrated in Figure 2.14. The ultimate outcome of the FBP algorithm is the reconstruction of an image that faithfully represents the distribution of relevant physical properties within the imaged object.
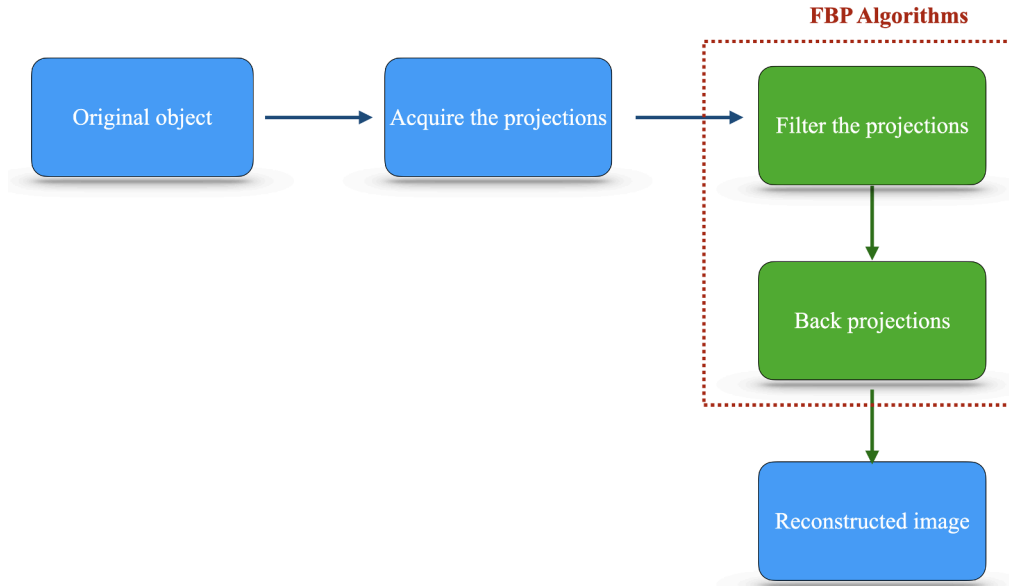
Rysunek 2.13: Schematic illustration of the sinogram determination.

In the context of CT, this translates to a depiction of X-ray attenuation coefficients, whereas in PET, the image conveys radiotracer concentration profiles.

2.6.2 Maximum Likelihood Expectation Maximization method (MLEM)

The MLEM method stands as a powerful iterative reconstruction algorithm employed extensively in various medical imaging modalities, including PET and SPECT. MLEM plays a pivotal role in the reconstruction of high-quality images from acquired projection data, addressing challenges such as noise, limited data, and inherent system imperfections. The core principle of MLEM hinges on an iterative statistical approach that iteratively refines an initial image estimate to converge towards the most likely image that would have produced the observed projection data. This method leverages the principles of maximum likelihood estimation (MLE) and the expectation-maximization (EM) algorithm, making it well-suited for situations where statistical modeling of the imaging process is advantageous [76].

The operational framework of MLEM unfolds as follows:

Initialization: MLEM commences with the provisioning of an initial image estimate, often denoted as $x^{(0)}$. This rudimentary image can manifest as a uniform field, a ru-
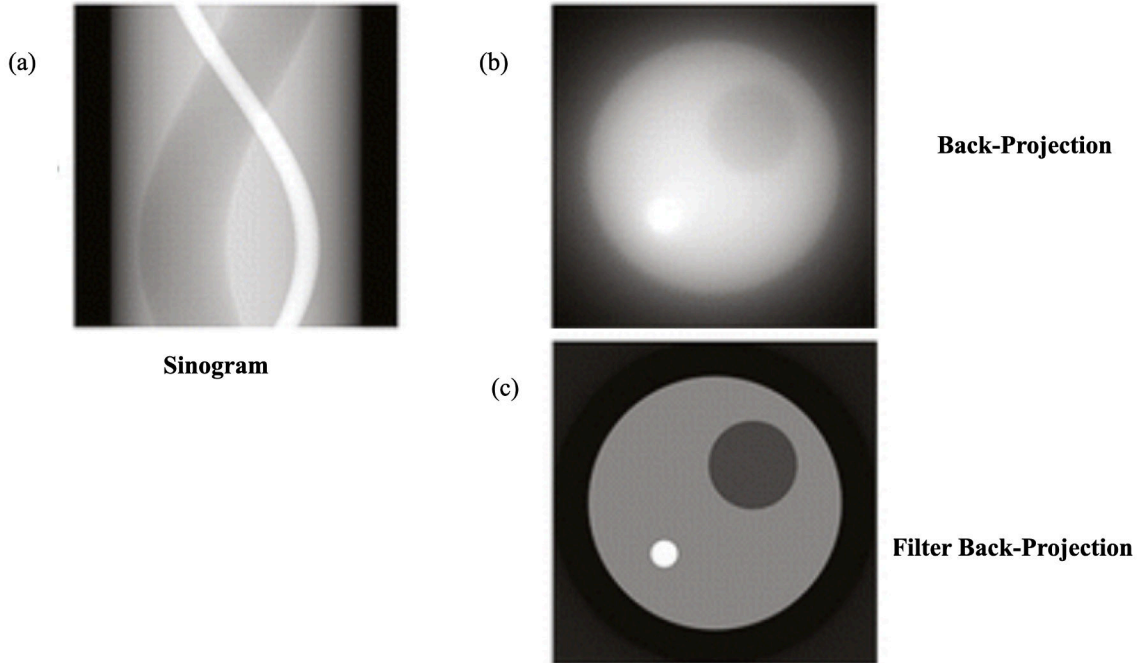
Rysunek 2.14: Comparison of the FBP method and BP method in PET image reconstruction. (a) Sinogram stored from data acquisition, (b) simple back projection algorithm method, (c) filtered back projection algorithm method. Figure adapted from [75].

dimentary reconstruction, or even an image derived from alternative reconstruction methodologies.

Forward Projection: The initial image estimate is subjected to a forward projection process, simulating the acquisition procedure and consequently generating synthetic projection data $p^{(0)}$.

$$p^{(0)} = Ax^{(0)} \tag{2.2}$$

where, $p^{(0)}$ stand the synthetic projection data, A is the system matrix representing the imaging system's response, and $x^{(0)}$ stand as the initial image estimate.

Update: A pivotal juncture in MLEM revolves around the juxtaposition of the synthetic projection data with the empirically acquired projection data $p_{measured}$. At each angular orientation, the quotient between measured and synthetic data confers correction factors.

$$C_i = \frac{P_{measured,i}}{p^{(0)}{}_i} \tag{2.3}$$

where, C_i is the correction factor at projection angle i, $P_{measured,i}$ is the measured projection data at angle i, and $p^{(0)i}$ is the synthetic projection data at angle i.

Correction: These correction factors undergo application to the initial image estimate, modulating it in accordance with the statistical likelihood of the observed data given the prevailing image estimate.

$$x^{(1)} = x^{(0)} \times \frac{P_{measured}}{p_0} = x^{(0)} \times C \tag{2.4}$$

where, $x^{(1)}$ is the updated image estimate, and C is a vector containing all the correction factors.

Iteration: The iterative nature of the MLEM algorithm is pivotal. This procedure involves repeated cycles, comprising Steps 2 to 4, continuously enhancing the accuracy of image estimations in each iteration. Consequently, the algorithm progressively refines the image estimates in pursuit of achieving the maximum likelihood estimation.

Convergence: The MLEM framework perseveres until the satisfaction of a predetermined convergence criterion is satisfied. Typically, this encompasses either reaching a predefined maximum number of iterations or achieving a stipulated change threshold in the image estimate between consecutive iterations. The schematic of the MLEM method display in Figure 2.15

The intrinsic iterative nature of MLEM empowers it to navigate and surmount numerous challenges germane to medical imaging.

Comparison result of FBP and MLEM method displays that FBP and MLEM are closely similar in result but MLEM is better than FBP in noisy images as shown in the Figure 2.16 [77].
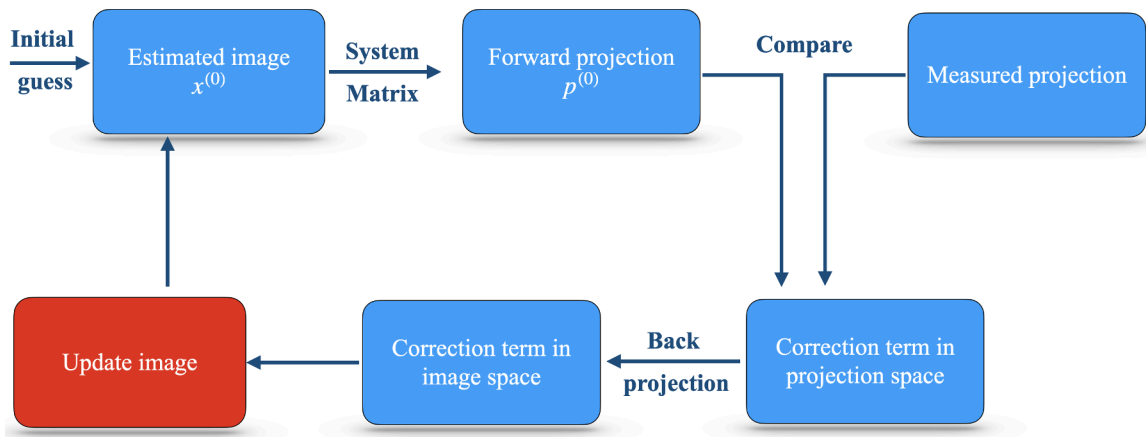
Rysunek 2.15: PET MLEM image reconstraction. The process starts with a initial guess called the system matrix. The iteration introduces the new feed of data from the detector and it continues until the system has reached convergence.
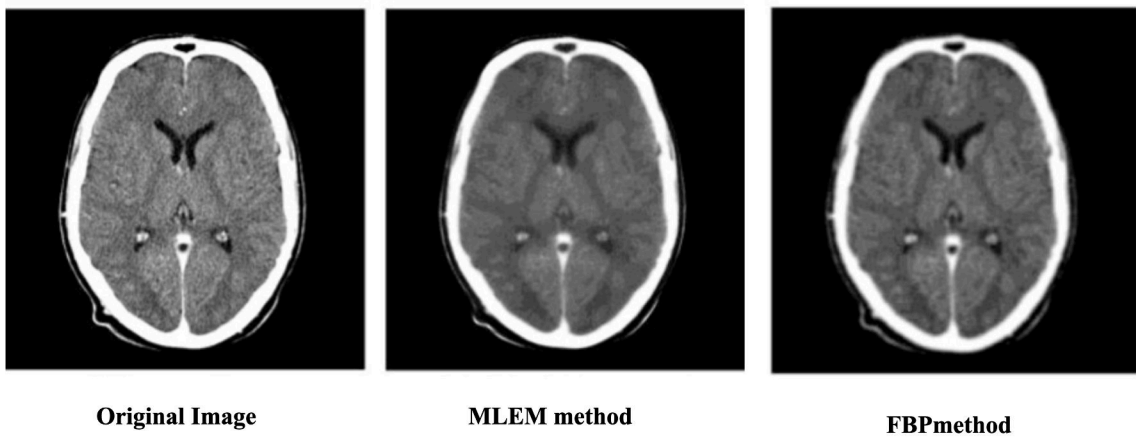
Rysunek 2.16: A Comparison of Filtered Back Projection and Maximum Likelihood Expected Maximization. Figure adapted from [77].

ROZDZIAŁ 3

THE J-PET DETECTOR

The Jagiellonian PET represents a pioneering advancement in Positron Emission To-mography technology, being the inaugural scanner constructed using plastic scintilla-tors. Known as J-PET, this multi-photon PET innovation has facilitated the creation of the inaugural images of positronium [36] and the first-ever multiphoton images [78]. Utilizing plastic scintillators as opposed to traditional inorganic materials, offers a more economical alternative; they are not only cost-effective but also offer flexibility in shaping, paving the way for more affordable total-body PET solutions [2, 21, 36, 64, 79, 80, 78].

3.1 Principle of operation of the J-PET scanner

The construction of the J-PET scanner is distinguished by its unique use of plastic scintillator strips, positioned in an axial arrangement. These scintillators are con-nected to two photomultipliers located at each end, acting as light guides for the transmission of optical photons. The interaction between the gamma quanta and the scintillator initiates the generation of optical photons, which travel to the ends of the strip. This dual functionality allows the scintillator strip to also serve as a light guide as discipted in Figure 3.1. A point of photon interaction with scintillator (ΔZ) can be calculated based on the arrival time of the signal to the up (or down) SiPM. At the next, the annihilation point of the electron and positron along LOR (Δl) is determined based on the difference between the arrival time of the gamma quanta to the up and down scintillator [2]. Because of the type of scintillators employed, the J-PET scanner utilizes primarily time information rather than energy deposition.

Within the photomultipliers, the optical photons are transformed into electric signals. These signals are subsequently processed through customized front-end elec-tronics boards and a triggerless data collection system. The gathered data is locally
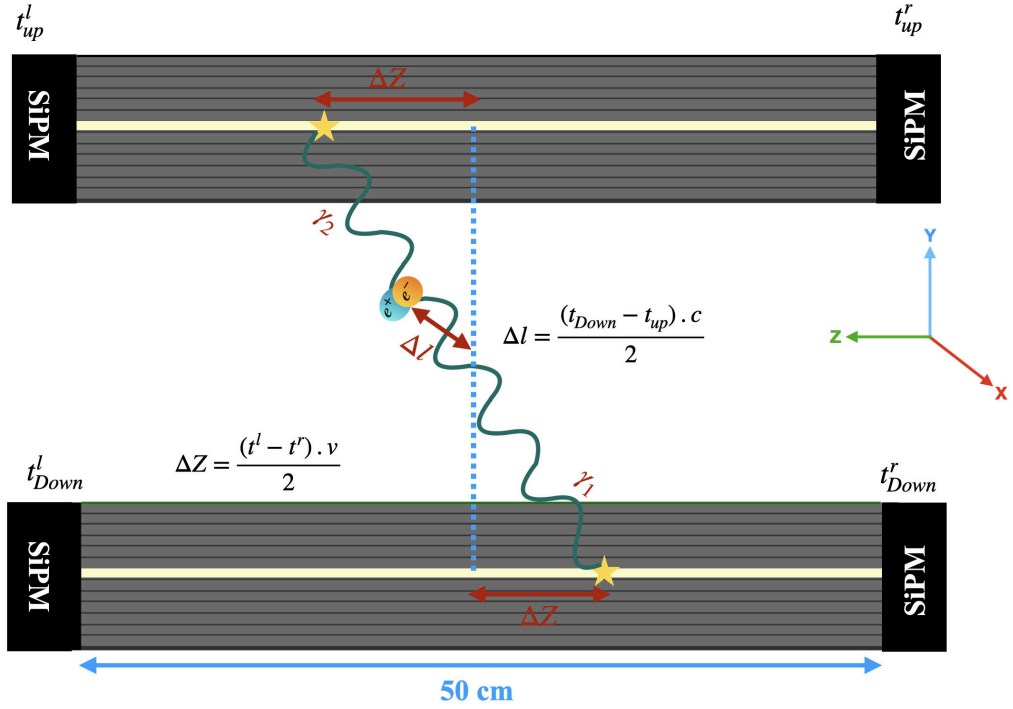
Rysunek 3.1: Two detection module setup with scintillators and SiPMs arrangements, principle of detection and reconstruction of annihilation positions in the J-PET plastic scintillator based technology where the axially arranged scintillator (gray) is readout by two photomultiplier of both ends (black).

stored and subject to analysis using the specialized J-PET Framework software (more explanation in section 3.3) [81].

3.2   Prototypes of the J-PET tomograph

The first human-scale prototype of the J-PET scanner was constructed from three layers of EJ230 plastic scintillator, having dimensions of $7 \times 19 \times 500 mm^3$, and coupled with Hamamatsu R9800 vacuum tube photomultipliers (PMT) at each end [34, 35, 36]. In the voltage domain, light signals converted by photomultipliers are examined at four distinct thresholds, maintaining a timing precision of 30 ps, and the data collection operates without the need for a trigger. With an inner diameter of 85 cm, it offers ample space to conduct any measurements achievable with traditional tomographs. This prototype has been instrumental in generating the first positronium image for Cardiac Myxoma and adipose tissue [36]. It has also been employed for

studies of discrete symmetries in the decays of positronium atoms and the multi-particle entanglement of photons resulting from positronium decay [34, 80, 78]. Figure 3.2 visually depicts this pioneering prototype of the J-PET scanner.

Rysunek 3.2: The first large scale prototype of the J-PET constructed in the tree layers arrangment of the plastic scintillator (back) coupled with PMT at each end (silver).

The most recent prototype developed by the J-PET Collaboration is a modular J-PET, incorporating SiPMs. This design is made up of 24 individual detection units, referred to as modules. Each module consists of 13 plastic scintillator strips, with the dimentions of $6 \times 24 \times 500$ mm^3. Within a module, every subsequent scintillator is oriented parallel to its predecessor, with the parallel sides possessing dimensions of 24×500 mm^2. SiPMs are affixed to both ends of all the scintillator strips, as depicted in Figure 3.3. These modules are assembled into a cylindrical configuration, forming the structure of the Modular J-PET [37].

Thanks to the distinctive design of the modular J-PET, this tomograph can be

Rysunek 3.3: Single module consist of 13 plastic scintillator (black) that coupled with SiPM from both ends.

disassembled and reassembled in a short amount of time, depending on the purpose of the study. Figure 3.4 provides a transverse illustration of the 24-Modular J-PET. The plastics scintillator chosen for the design of the Modular J-PET is BC-404. The primary selection criteria for BC404 plastics scintillator revolved around its time-related characteristics and light propagation properties, encompassing factors like light output, rise and decay time, and bulk light attenuation length. A overview of the properties of BC-404 plastic scintillators, produced by Saint-Gobain Crystals and Eljen Technology, is presented in Table 3.1 for reference. Each scintillator is wrapped with 3-M Vikuiti Enhanced Specular Reflector (ESR) and DuPont B Kapton foils. The 3-M Vikuiti ESR, known for its ultra-high reflectivity and non-metallic composition, while DuPont B Kapton foil is a black, light-tight foil. This combination provides robust protection against daylight exposure [82, 83, 84]

In light of the emission spectrum exhibited by BC-404 and the outcomes from scintillation light response evaluations conducted with various photomultipliers, the J-PET group concluded that the MPPC-1X4CH-ARRAY S13361-6674 Silicon pho-

tomultiplier, manufactured by Hamamatsu, emerged as the most suitable choice for advancing their research objectives. In the case of the Modular J-PET detector, each plastic scintillator is read out on both ends using SiPMs configured in a 1×4 matrix ($6 \times 6\ mm^2$) arrangement. Furthermore, each SiPM is equipped with two threshold set: 30 mV and 70 mV (refer to section 7.3.6).
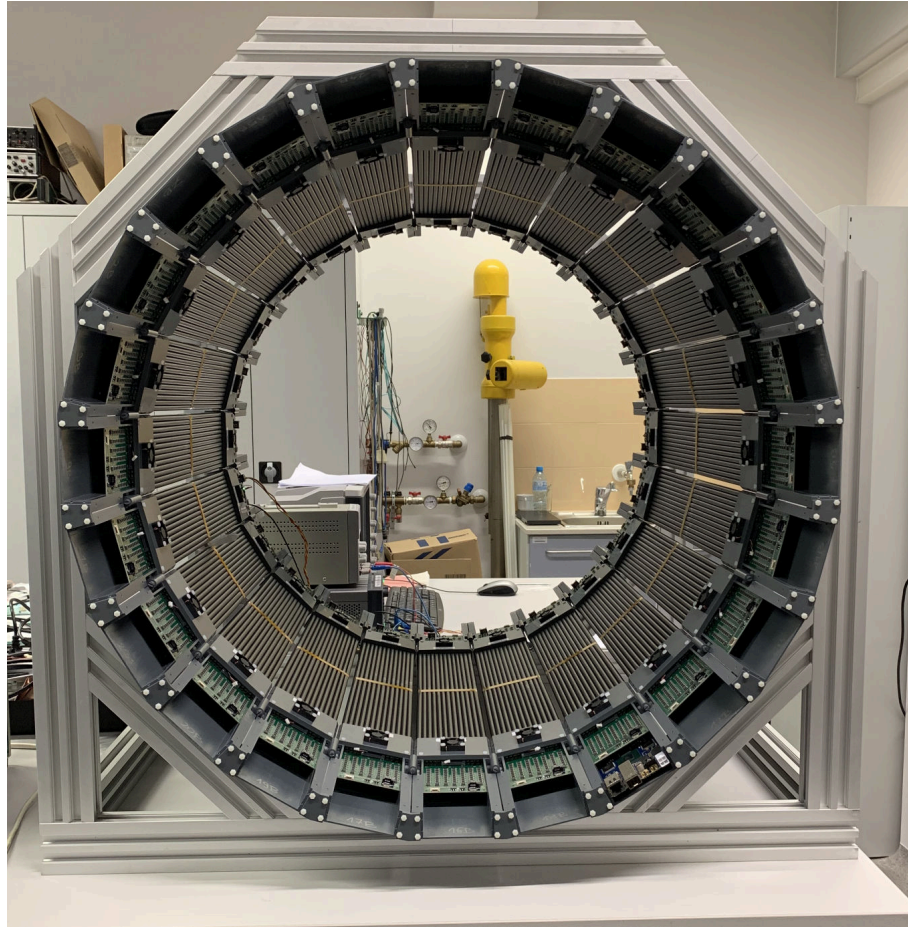
Rysunek 3.4: Illustration of the Modular J-PET.

The geometrical characteristics of the Modular J-PET have been explained in Table 3.2. In this thesis, the performance of the Modular J-PET is examined based on the NEMA NU2-2018 standards. Detailed discussions on this evaluation are provided in subsequent chapters.

Tabela 3.1: Properties of BC-404 plastic scintillators produced by Saint-Gobain Crystals and Eljen Technology. Data taken from [51, 52]

Light output (% Anthracene)	68	Wavelength of Max. Emission (nm)	408
Rise Time (ns)	0.7	Light Attenuation Length (cm)	140
Decay Time (ns)	1.8	Density (g/cm3)	1.032

Tabela 3.2: The geometrical characteristics of the 24 Modular J-PET

Scintillator type	BC-404
Light sensor	SiPM
Type of light sensor	Analog
Cross-section of scintillator	$24 \times 6 \ mm^2$
Axial length	50 mm
Diameter	739 mm
Time window	4 ns
Energy window	>200 keV

3.3 Triggerless Data Acquisition

The complete Data Acquisition System in the Modular J-PET prototype are probed in voltage domain based on Field-Programmable Gate Array (FPGA) electronics for efficient real-time processing of multiple data streams. Its hierarchical architecture centers around the Controller board, with Concentrator boards as hubs, and digitizing Endpoints on the detector modules [85, 4]. The data readout is performed in continuous mode, eliminating the necessity for a hardware trigger. The digitized responses from the detectors are stored in data buffers on the Endpoints and await the synchronization message. The messages, systematically are generated by the Controller board at a fixed frequency of 20 kHz, traverse through the Concentrator boards to reach the waiting Endpoints. In response, the Endpoints transfer the buffers' content back to the Concentrators. These Concentrators, acting as hubs, pool data from various Endpoints, encapsulate it into UDP packets, and efficiently dispatch it out of the system for storage via a high-speed 10 Gigabit Ethernet network. To summarize, the Modular J-PET scanner captures signals through voltage domain probing facili-

tated by the FPGA-based Multi-Voltage Threshold (MVT) system [86]. These signals are then acquired by the triggerless data acquisition system. The configuration of the detection system, as well as the placement of the Modular J-PET scanner and the DAQ server within the laboratory space, is illustrated in Figure 3.5 for reference and clarity.
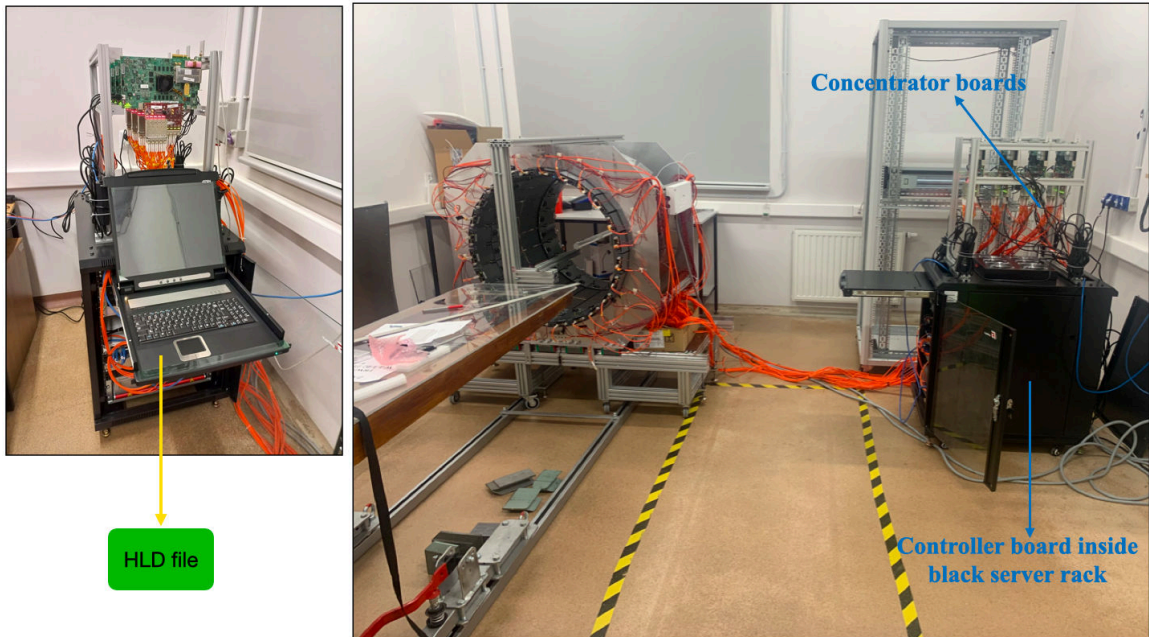
Rysunek 3.5: (Right): Display the placement of the Modular J-PET, patient bed, data acquisition system (DAQ) Modular J-PET. (Left): The DAQ is the integration of several components which consists of sensors, DAQ measurement hardware, the output/display module, and a computer with programmable software. It also contains the control module that store the digital data of the Modular J-PET detector [87].

3.4   J-PET framework

The data acquired from the Modular J-PET was subject to thorough analysis through the utilization of the J-PET Framework software [81]. This software suite is a versatile platform developed using the C++ programming language, enriched with ROOT libraries for its core functionalities [88, 89]. The J-PET Framework is structured into distinct functional blocks, each tasked with the conversion of raw data into higher-level data structures, as depicted in Figure 3.6. Users have the flexibility to

activate or deactivate specific modules as needed. The synchronisation of modules is efficiently managed by the JPetManager class, ensuring an adaptable framework that seamlessly accommodates the incorporation of novel tasks and functionalities. Throughout the analysis process, the output generated at each analytical stage is stored in dedicated ROOT files [81, 89]. In the initial steps of the analysis, each raw file from the Triggerless DAQ system is unpacked into a ROOT file. Subsequently, in the first analysis module, this file is transformed into the structure used by the J-PET Framework. In the following step, the photomultiplier signal is completed from times at specified thresholds, and its properties are calculated. Signals from opposite photomultipliers are then matched into hits, containing information about Arrival Time [ps], Energy, Position in the Scintillator (X,Y,Z), the two Signals that construct the hit, and the Time difference between the arrival times of two Physical Signals. The event definition is based on user choice and can contain one, two, or more hits within a specific time window, providing information about the Hits that construct this Event and its Type. Experimental setup properties, such as geometry, scintillator ID, dimensions, the time window used during signals matching, and the time window used during hits matching into events, are loaded from a dedicated JSON file. This comprehensive software architecture not only streamlines the data processing process but also offers users the flexibility to tailor their analytical configurations.

3.5   Time over Threshold

The initial data processing after the acquisition attempts to reconstruct Time Over Threshold (TOT) value of the photon energy depositions in the J-PET plastic scintillators. TOT-based methods traditionally rely solely on temporal data [90] specifically the times Δt_1 and Δt_2 as indicated in Figure 3.7 (b). The TOT value is computed as a weighted mean of the sum of signal widths at two distinct thresholds, with the weights determined by the difference between consecutive thresholds, as depicted in Figure 3.7(c). The formula for TOT values for each of the 4 SiPM-s in a matrix
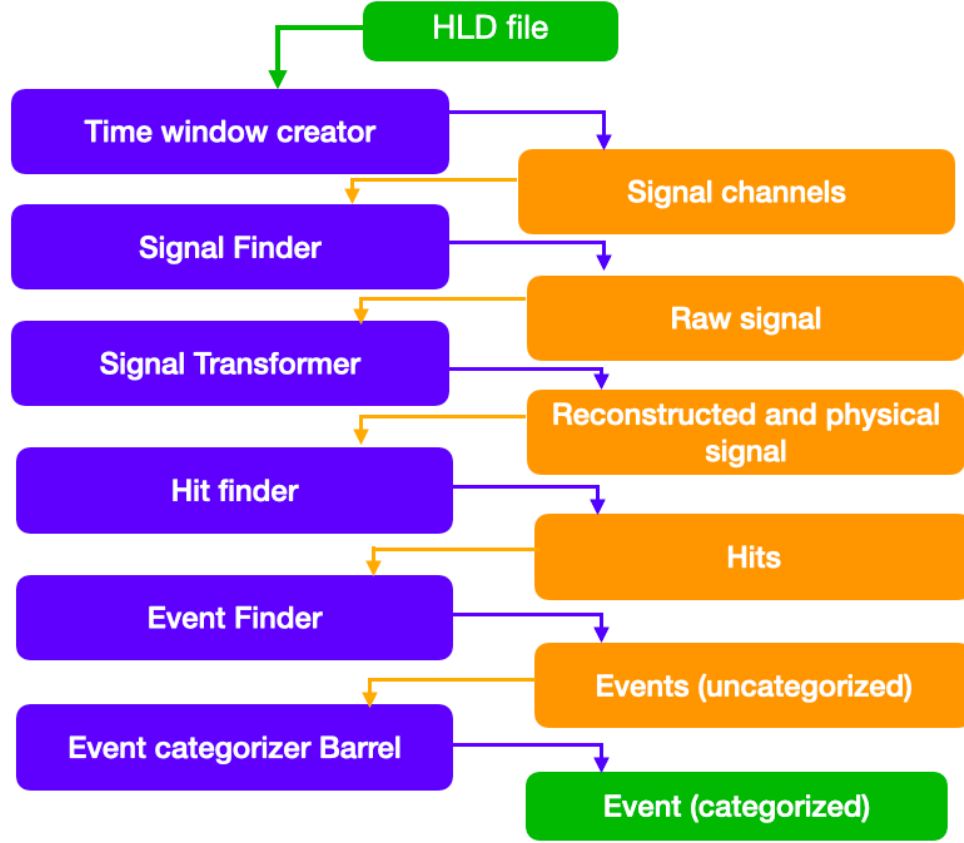
Rysunek 3.6: J-PET Framework structure. Figure adapted from [89].

separately for sides A and B of the scintillator strip is as follows:

$$TOT_{SiPM} = \Delta t_1.Th_1 + \Delta t_2.(Th_2 - Th_1) \tag{3.1}$$

In the analysis, the total TOT value associated with an interacting photon is estimated as the average of the TOT values recorded at both ends of the scintillator strips. This can be expressed as follows:

$$TOT = (TOT_{SiPM1} + TOT_{SiPM2})/2 \tag{3.2}$$
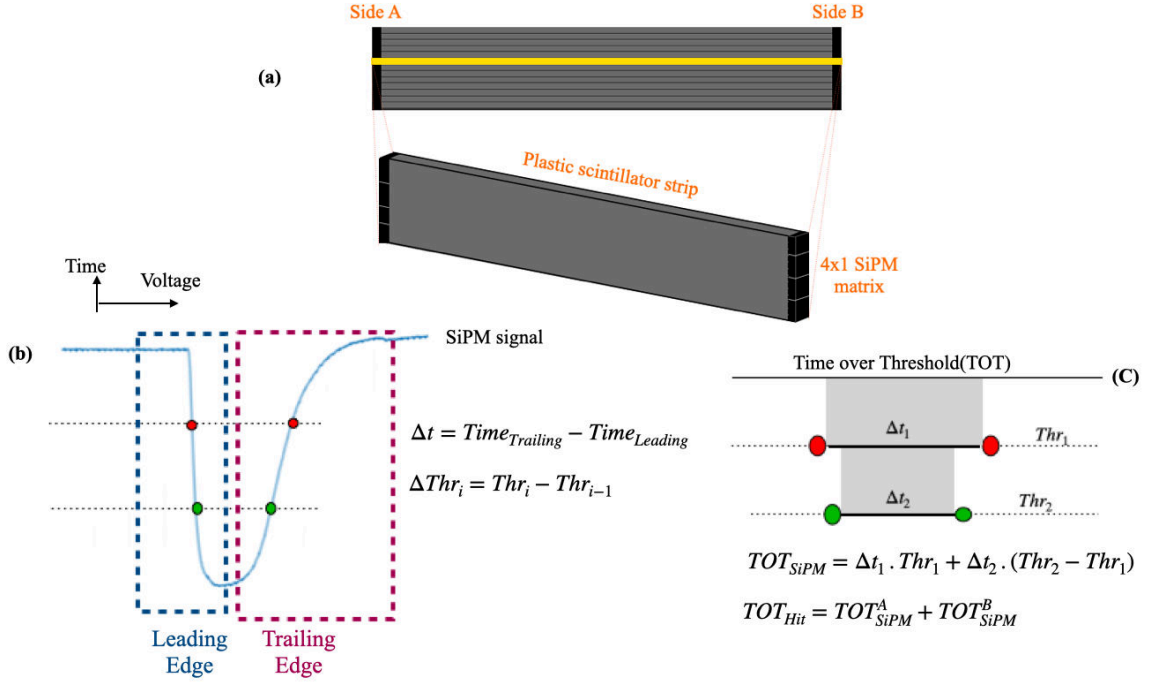
Rysunek 3.7: Reconstruction of SiPM signal in the Modular J-PET detector: (a) a single Module with a zoom on a single scintillator strip is represented, where scintillation light produced in a single scintillator strip is read out by a 4×1 matrix of SiPM-s on each side of the strip. (b) The collected light by the photomultiplier is converted into an electrical signal , which is characterized by a voltage dependence over time, denoted as V(t). The dots represent the crossing of signals with the voltage threshold with nominal values: -30 and -70 mV. Front-end electronics measure times of each signal crossing two predefined voltage thresholds at its leading and trailing edge. (c) The size of the SiPM signal, which is related to the amount of scintillation light, is estimated using a rectangular approximation based on threshold levels above the signal baseline and the times-over-threshold (TOT) t1 and t2, which are the differences between the trailing and leading edge times on each of the two voltage thresholds. Finally, the sum of the TOT values measured at both sides (side A and B) of the scintillator strip is used, as TOT characterizes the energy loss associated with the hit in the event.

ROZDZIAŁ 4

NEMA STANDARDS

The determination of PET scanner performance protocols was initially consolidated through the collaboration of the Society of Nuclear Medicine and later continued by the National Electrical Manufacturers Association (NEMA). Although NEMA acts as the dominant norm in the United States, in the field of PET it is used as an evaluator of PET scanner performance and a comparison between manufacturers in the world. The first standard was published as $NU2-1994$ in 1994 and updated every five years. NU $2-2018$ is the last published standard [6].

This standard outlines a comprehensive set of characteristics for PET scanners with a diameter greater than 26 cm, including spatial resolution, scatter fraction, noise equivalent count rate (NECR), sensitivity and image quality. These characteristics are essential for evaluating and comparing different PET tomographs, and are mandatory for any PET equipment intended for medical use worldwide. The performance characteristics of the PET scanner prototype can be evaluated through experimental measurement and with GATE Monte Carlo simulations. The recommended source for all characteristics is ^{18}F, However it is possible to do spatial resolution with ^{22}Na also. NEMA recommended special methods and phantoms for evaluation of scanner characteristics. In scenarios where manufacturers used different method or radioactivity for measurement, it becomes mandatory to establish traceability between the employed methods and the sanctioned official tests [6]. In the following subsections each of these characteristics and procedures are explained in details.

4.1   Sensitivity

The sensitivity of a PET scanner is a paramount measure of its capacity to detect and register gamma rays emitted during the annihilation events. This sensitivity directly impacts both the quality and the quantitative accuracy of the images produced. As

per the NEMA NU2-2018 standards, sensitivity is defined in terms of the counts per unit time that the detector can identify for each unit of activity present in a source. Essentially, it quantifies how well the scanner can pick up signals, which is crucial for distinguishing between healthy and pathological tissues, especially when the radiotracer uptake is minimal.

Conventionally, sensitivity value is denoted in the form of the true coincidence events rate, represented as cps/kBq. Higher sensitivity ensures that the scanner can produce clear images with lower doses of radioactive tracers, which is beneficial for patient safety and reduces exposure. The NEMA NU2-2018 standard set benchmarks for PET scanner sensitivity, ensuring that the devices in use provide reliable and accurate data for clinical and research applications.

The use of a sensitivity phantom is essential for evaluating this measurement. The sensitivity phantom consists of five aluminum tubes, each with a length of 700 mm, as depicted in Figure 4.1. Details regarding the inner and outer diameters of each sleeve are provided in Table 3.1.

Rysunek 4.1: Sensitivity Phantom with five sleeve tubes and one polyethylene tube (sixth layer) with length of 70 cm.

For measurement, the chosen radionuclide should be fluorine-18 (F-18), which should be uniformly mixed with water and introduced into the 70 cm polyethylene tube. Polyethylene will constitute the innermost tube, serving as the sixth layer of the sensitivity phantom.

Tabela 4.1: Sensitivity measurement phantom details

Tube number	Inside diameter (mm)	Outside diameter (mm)	Length (mm)
1	3.9	6.4	700
2	7.0	9.5	700
3	10.2	12.7	700
4	13.4	15.9	700
5	16.6	19.1	700

To ascertain the initial activity within the phantom, measurements should be conducted using a dose calibrator. This activity, denoted as $A_{cal,mass}$ and expressed in MBq, along with the duration of the assay, denoted as T_{cal}, should be meticulously recorded. Subsequently, the corrected initial activity, denoted as A_{cal}, shall be calculated as follows:

$$A_{cal} = A_{cal,mass}\frac{700mm}{L_{mass}}, \tag{4.1}$$

here, $A_{cal,mass}$ represents the measured activity, and L_{mass} signifies the measured source length in millimeters.

The activity of the radionuclide F must be maintained at a sufficiently low level to satisfy the condition that the rate of random coincidences is less than 5 %, or alternatively, that the percentage of dead time losses remains below 5 % [6]. The sensitivity phantom should be precisely positioned at two distinct locations: first, at the center of the axial FOV of the detector, and second, at a 10 cm radial offset from the transaxial FOV center. A total of 10,000 true events per slice should be meticulously collected for each measurement. However, it is worth noting that there exists no precise definition for the term 'slice.' The precise methodology for counting events per slice remains ambiguous in the standard, with only a mention of the need to rebin a single slice to allocate counts in oblique LORs to an appropriate image slice. To assign counts in oblique lines-of-response (LORs) to the image slice where the LOR intersects the scanner axis, the method of single slice rebinning should be employed. The commencement of the measurement is marked by the starting time,

denoted as T_j, which is duly recorded alongside the measurement duration, $T_{j,acq}$, and the total number of collected counts. The rate, represented as $R_{j,i}$, pertaining to the $j-th$ sleeve should be determined by dividing the counts for the $i-th$ slice by the duration, resulting in counts per second. The measurement protocol initiates with the smallest aluminum tube containing the source within the polyethylene tube. Subsequently, each of the four sleeves is sequentially added to the phantom, and the measurement is repeated. Values for T_j, and $R_{j,i}$ are meticulously recorded for each measurement.

The total count rate (R_j), adjusted for the effects of radioactive decay, can be calculated using the following formula:

$$R_{CORR,j} = \frac{(T_{j,acq}ln2)exp(ln2\frac{T_j - T_{cal}}{T_{1/2}})}{T_{1/2}(1 - exp(ln2\frac{-T_{j,acq}}{T_{1/2}})))}R_j, \tag{4.2}$$

where T_{cal} stand for calibration radioactivity measurement time and $T_{1/2}$ stand for radionuclide half time. To acquire the count rate devoid of attenuation effects (denoted as $R_{CORR,0}$), it is imperative to perform data fitting employing the subsequent equation:

$$R_{CORR,j} = R_{CORR,0}.exp(-\mu_m.2X_j), \tag{4.3}$$

here, X_j represents the cumulative thickness of the tube wall, with μ_m denoting the linear attenuation coefficient. Ultimately, the system sensitivity (expressed in counts/sec/kBq) is derived from the following formula:

$$S_{tot} = \frac{R_{CORR,0}}{A_{cal}}. \tag{4.4}$$

The axial sensitivity profile can be ascertained by plotting the sensitivity for each slice based on measurements taken with the smallest tube (R_1) positioned at the central location as following formula:

$$S_i = \frac{S_{1,i}}{R_1} . S_{tot}. \tag{4.5}$$

4.2 Scatter fraction

The scatter fraction of a PET scanner quantifies the fraction of events used for image reconstruction in which one or both of the annihilation photons scatter within the patient. The first purpose of this procedure is to measure the relative system sensitivity to scattered radiation. The second purpose of this procedure is to measure the effect of system dead time and generation of random event at several levels of source activity. It is typically measured at relatively low source activities to minimize the contribution of accidental coincidences. The scatter fraction is expressed as a dimensionless ratio between the number of scattered coincidences and the sum of the scattered and true coincidences events [6]. A lower scatter fraction indicates better image quality [91].

To evaluate scatter fraction a scatter phantom is needed. The scatter phantom is a solid cylinder composed of polyethylene with a specific gravity of $(0.96 \pm 0.01)\ g/cm^3$. The cylinder has an outside diameter of $(20.3 \pm\ 0.3)\ cm$ and a length of $70\ cm$. At a radial distance of $4.5\ cm$ from the cylinder's axis, a hole with a diameter of $(0.64\ \pm\ 0.2)\ cm$ was drilled parallel to the cylinder's axis as shown in Fig 4.2. A test phantom line source insert with a polyethylene coated plastic tube having an outside diameter of $(0.48\ \pm\ 0.3)\ cm$, an inside diameter of $(0.32\ \pm\ 0.2)\ cm$, and at least $80\ cm$ in length was placed inside the hole of the phantom. The centeral $(70\ \pm\ 0.2)\ cm$ part of this test phantom line source should be filled with a water well mixed with precisely measured amount of radioactive and sealed at both ends. The experimental procedure commences with a relatively high activity source into the field of view of the PET scanner. Subsequent measurements are conducted as the radioactivity within the phantom undergoes decay over multiple half-lives. As the radioactive activity diminishes, there is a corresponding decrease in the observed event rate. The corrected initial activity (A_{cal}) that is used in future analysis, shall be computed as:

$$A_{cal}\ =\ A_{cal,meas}\ \frac{700\ mm}{L_{meas}}, \tag{4.6}$$

where, $A_{cal,means}$ the initial activity in the phantom which is determined from the ac-

tivity injected into the phantom as measured in a calibrated dose calibrator, L_{means}, stand the measured source length.
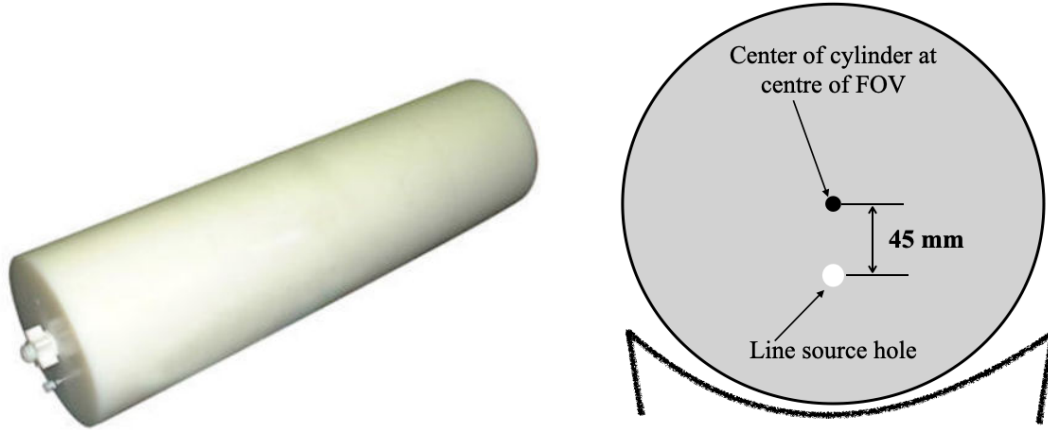
Rysunek 4.2: (Left): Scatter phantom consist of three segments which assembled together during measurements, (right) : Positioning of scatter phantom on the bed.

The scatter phantom is positioned parallel to the scanner's axis, and it was precisely centered in both the transverse and axial FOV with an accuracy of within 5 mm. In order to ensure precise results, it is essential to position the test scatter phantom at the exact center of the FOV of the detector, and the table shall be positioned such that the trough of the table is positioned 15 ± 1 cm below the center of the transverse FOV.

There exist two distinct data recording methods: one involving randoms estimation and the other without it. The report is obligated to explicitly indicate whether a randoms estimate was employed during the data acquisition process. If a randoms estimate was indeed utilized, the report must additionally delineate the specific method employed for randoms estimation. Regardless of the chosen method, it is imperative that each acquisition comprises a minimum of 500,000 prompt counts to ensure data integrity and statistical robustness. Data acquisition shall be performed at intervals more frequent than half of the radionuclide half-life, denoted as $T_{1/2}$, until the occurrence of true event losses falls below the threshold of 1.0%. Should the data be subjected to processing using the alternate method, which does not involve randoms

measurement, the acquisition process shall be conducted to ensure that both true event losses remain below 1.0% and that the randoms-to-true ratio remains below 1.0% throughout the final three frames of the acquisition sequence. The durations of the individual acquisitions, denoted as T_{acqj}, must adhere to the constraint of being shorter than one-fourth of the radionuclide half-life, $T_{1/2}$.

In the case of tomographs featuring an axial FOV measuring 65 cm or less, it is mandatory to record the number of random counts $(C_{j,i})$, and generate both prompt and random sinograms for each acquisition denoted as j of slice i. However, it's important to note that in instances where no randoms estimate is accessible, only prompt sinograms shall be generated. The subsequent processing steps apply to each prompt sinogram i within every acquisition j' and they are as follows:

A) Pixels that are situated beyond a radial distance of 12 cm from the center of the scanner's transaxial Field of View (FOV) must be assigned a value of zero. The radial position of a pixel is determined by the radial displacement from the mean physical line-of-response measured by that particular pixel.

B) In the case of each projection angle Φ featured within the sinogram, it is imperative to ascertain the precise location of the center of the line source response.

C) Each projection should be shifted so that the pixel at the center of the line source response is aligned with the central pixel of the sinogram.

D) Subsequent to the alignment process, a summation projection shall be generated by summing the aligned sinogram over the range of projection angles:

$$C(r)_{i,j} = \sum_{\phi} C(r - r_{center}(\Phi), \Phi)_{i,j}, \tag{4.7}$$

where, r corresponds to the pixel number in a projection, with r = 0 designates the radial center of the sinogram. Φ represents the projection number in the sinogram, and $r_{center}(\phi)$ refers to the center of the line source response in projection Φ.

E) The counts per pixel, denoted as $C_{L,i,j}$ and $C_{R,i,j}$, which correspond to the left and right edges, respectively, of the 40 mm wide strip situated at the center of the sinogram, are to be calculated by utilizing linear interpolation as depicted in

Figure 4.3. The interpolation points should align with physical distances of $+20$ mm from the center of an un-shifted sinogram. To perform this interpolation, a line is drawn between the center points of the two nearest pixels to $C_{L,i,j}(C_{R,i,j})$, and their measured values (counts per pixel) at these points are employed in the calculation.

F) To calculate the random plus scatter counts $(C_{r+s,i,j})$, the average of the interpolated pixel intensities $C_{L,i,j}$ and $C_{R,i,j}$ should be multiplied by the number of pixels between the edges of the 40 mm wide strip (including fractional values) and added this result to the counts in the pixels outside the strip, including partial pixels.

G) Also, for the total event counts $(C_{TOT,i,j})$ in slice "i" of acquisition "j," simply sum of all pixels in the summation projection. Furthermore, The average activity $(A_{ave,j})$ for each acquisition should be calculated. The next phase of the analysis
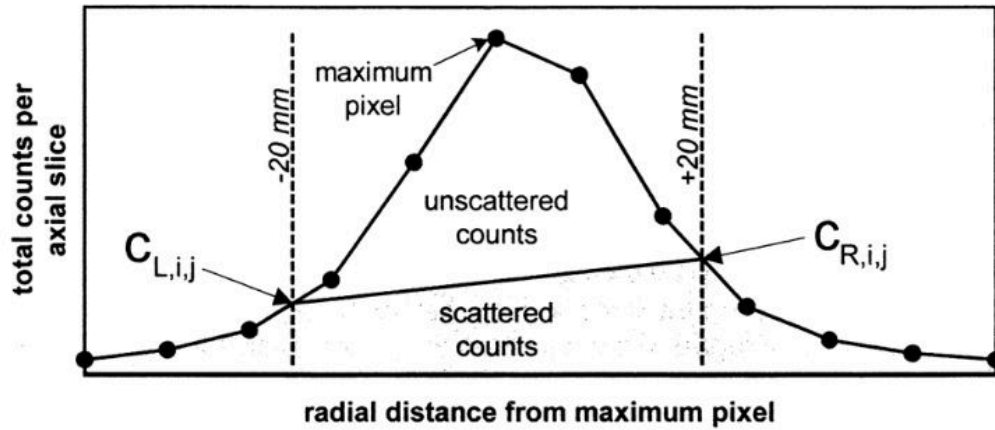
Rysunek 4.3: Integration of background counts inside and outside of 40 mm strip. Figure adapted from [6]

is divided into two parts: one method involving random estimation and the other method conducted without it.

1. Method with random estimation

   The system scatter fraction for acquisition "j," sum the counts over slices is computed by the following formula:

$$SF_j = \frac{\sum_i C_{r+s,i,j} - \sum_i C_{r,i,j}}{\sum_i C_{TOT,i,j} - \sum_i C_{r,i,j}}. \tag{4.8}$$

45

Additionally, for each acquisition "j," with acquisition time ,$T_{acq,j}$, compute the system event rates as follows:

- The total event rate:

$$R_{TOT,j} = \frac{1}{T_{acq,j}} \sum_i C_{TOT,i,j}. \tag{4.9}$$

- The true event rate:

$$R_{t,j} = \frac{1}{T_{acq,j}} \sum_i (C_{TOT,i,j} - C_{r+s,i,j}). \tag{4.10}$$

- The random event rate:

$$R_{r,j} = \frac{1}{T_{acq,j}} \sum_i C_{r,i,j}. \tag{4.11}$$

- The scatter event rate:

$$R_{s,j} = \frac{1}{T_{acq,j}} \sum_i (C_{r+s,i,j} - C_{r,i,j}). \tag{4.12}$$

Based on the this parameter, the Noise Equivalent Count Rate (NECR) for the system is computed differently:

- For systems that utilize an unprocessed delayed channel for randoms estimation:

$$R_{NEC,j} = \frac{R_{t,j}^2}{R_{TOT,j} + R_{r,j}}. \tag{4.13}$$

- For all other systems, including those using a processed delayed channel or a singles-event-based randoms estimation:

$$R_{NEC,j} = \frac{R_{t,j}^2}{R_{TOT,j}}. \tag{4.14}$$

2. Method without random estimation

The system scatter fraction (SF) is computed for the final three acquisitions

denoted as j within the sequence, where the count loss rates and random rates are both below 1.0% of the true rate. In this scenario, it is assumed that $C_{r+s,i,j'}$ contains a negligible number of random counts and primarily consists of scatter counts. Similarly, C_{TOT} for these acquisitions primarily comprises true and scatter counts. The calculation for the system scatter fraction (SF) is as follows:

$$SF = \frac{\sum_i \sum_{j'} C_{r+s,i,j'}}{\sum_i \sum_{j'} C_{TOT,i,j'}}. \tag{4.15}$$

Additionally, for each acquisition j with acquisition time , $T_{acq,j}$, compute the system event rates as follows:

- The total event rate:

$$R_{TOT,j} = \frac{1}{T_{acq,j}} \sum_i .C_{TOT,i,j}. \tag{4.16}$$

- The true event rate:

$$R_{t,j} = \frac{1}{T_{acq,j}} \sum_i .(C_{TOT,i,j} - C_{r+s,i,j}). \tag{4.17}$$

- The random event rate:

$$R_{r,j} = R_{TOT,j} - (\frac{R_{t,j}}{1 - SF}). \tag{4.18}$$

- The scatter event rate:

$$R_{s,j} = (\frac{SF}{1 - SF})R_{t,j}. \tag{4.19}$$

Furthermore, it is worth noting that the NEC equation retains an identical form, as demonstrated in equations 4.14 and 4.15.

For the system report, create a plot depicting the five specified quantities ($R_{TOT,j}$, $R_{t,j}$, $R_{r,j}$, $R_{s,j}$, $R_{NEC,j}$) as functions of the average effective radioactivity concentration ($a_{ave,j}$). Additionally, report the derived value from the plot as indicated:

- Peak true count rate ($R_{t,peak}$).

- Peak NEC count rate ($R_{NEC,peak}$).

- The activity concentration at which ($R_{t,peak}$) is reached.

- The activity concentration at which ($R_{NEC,peak}$) is reached.

The average effective radioactivity concentration can be computed from the following formula:

$$a_{ave} = \frac{A_{ave}}{V} \tag{4.20}$$

where V stand for the PET scatter phantom total volume and A_{ave} can be computed from the following formula:

$$A_{ave} = A_{cal}\frac{T_{1/2}}{T_{acq}ln2}exp(\frac{T_{cal}-T}{T_{1/2}}ln2)(1 - exp(\frac{-T_{acq}}{T_{1/2}}ln2)) \tag{4.21}$$

where, A_{cal} stand for corrected initial activity, T_{cal} stand for time of the measurement, T_{acq} stand for duration of acquisision, and $T_{1/2}$ is the radioisotopic half- life time.

4.3   Spatial resolution

Spatial resolution in a system pertains to its capacity to distinguish between two distinct emission spots following image reconstruction. This assessment involves the imaging of point sources in air, followed by image reconstruction devoid of any smoothing or apodization [6]. The purpose of this measurement is to characterize the widths of the reconstructed image point spread functions (PSF) of compact radioactive sources. The width of the point spread function is measured by its full width at half-maximum amplitude (FWHM) and full width at tenth-maximum amplitude (FWTM). This measurement method characterizes the intrinsic spatial resolution of the data produced by the scanner. It does not characterize the reconstruction process or spatial resolution of a clinical image [6].

For all systems, the assessment of spatial resolution must be conducted in the transverse slice along two directions, typically radial and tangential. Additionally, an

axial resolution measurement is also mandatory. The dimensions of the pixel size within the transverse slice are determined by the transverse field of view and the image matrix size. To ensure the accurate measurement of the point spread function's width, it is imperative that the FWHM extends across a span of at least three pixels. Furthermore, during the reconstruction process, the pixel size must not exceed one-third of the expected FWHM in all three dimensions. The radionuclide selected for this measurement should be either ^{18}F or ^{22}Na, with an activity level maintained at a sufficiently low level to meet one of the following criteria:

a. Ensure that the percent dead time losses remain below five percent, or

b. Ensure that the random coincidence rate remains below five percent of the total event rate.

Each of the point sources utilized in this context should be composed of a minute quantity of concentrated activity, with dimensions not exceeding 1 mm in each direction. It is permissible to employ a capillary tube or a similar object to encase and confine the radioactive material. The placement of sources should adhere to the following criteria:

- In the axial direction, sources must be positioned along planes located at the center of the axial Field of View (FOV) and also at a distance of three-eighths of the axial FOV from the center of the FOV.

- In the transverse direction, sources should be situated at distances of 1 cm, 10 cm, and 20 cm from the center of the plane.

These sources should be aligned either horizontally or vertically with respect to the line intersecting the system axis, ensuring that the radial and tangential directions align with the image grid. It's essential to achieve precise positioning:

- In the transaxial plane, the positioning accuracy should be within ±2 mm for the source at a 1 cm offset. For sources positioned at offsets of 10 cm and 20 cm in the transaxial plane, the positioning accuracy should be within ±5 mm.

- In the axial direction, the positioning accuracy should be maintained within ±2 mm for all sources.

To ensure the reliability of the spatial resolution data, it is required that a minimum of 100,000 counts be acquired at all six positions. For the reconstruction of this data, the filtered back projection (FBP) method (as explained in section 2.6.1), with no smoothing or apodization, should be employed.

The spatial resolution, represented by the FWHM and FWTM, of the point source response function must be ascertained by constructing one-dimensional response functions. These functions are generated along profiles that traverse the image volume in three orthogonal directions, passing through the peak of the distribution. To determine the width of the response functions in the two directions perpendicular to the measurement direction, the width should be approximately twice the FWHM. Each FWHM (and FWTM) is calculated through linear interpolation between adjacent pixels that correspond to half (or one-tenth) of the maximum value of the response function (refer to Figure 4.4 for illustration). The maximum value of the response function is established by fitting a parabolic curve using the peak point and its two nearest neighboring points. Subsequently, the values are converted to distances in millimeters by multiplying them by the pixel size.
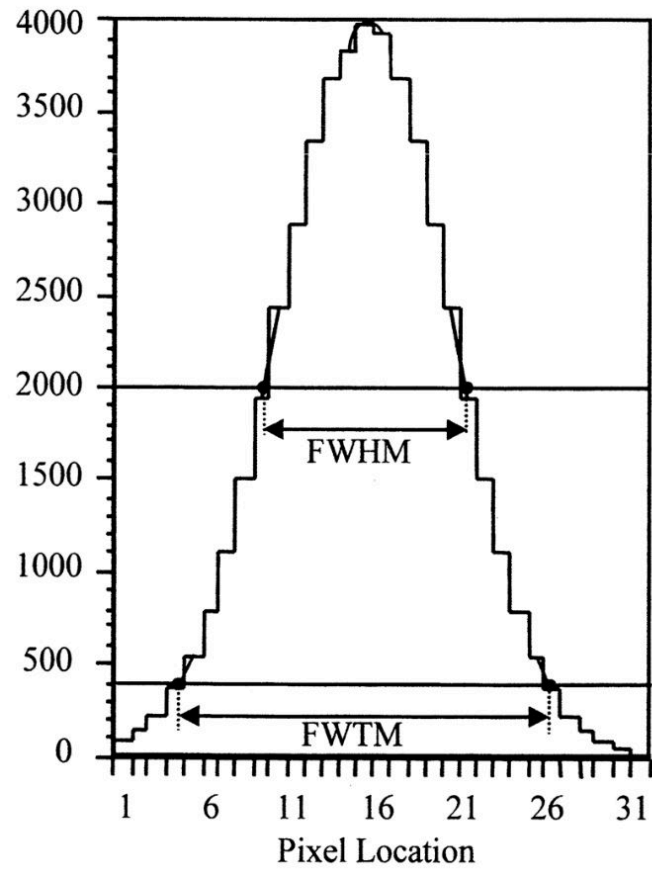
Rysunek 4.4: Illustrates the response function, with its FWHM and FWTM, is typically determined through graphical interpolation.

ROZDZIAŁ 5

SIMULATION OF THE J-PET DETECTOR WITH THE GATE SOFTWARE

Simulation serves as an indispensable avenue for unraveling the intricacies of system performance. In this realm, the Geant4 Application for Tomographic Emission (GATE) simulation software [92, 93, 94] rigorously validated toolkit within the nuclear medicine and molecular imaging. GATE's status as a trusted simulation platform based on Monte Carlo method, empowers researchers to emulate intricate processes, providing a virtual arena for in-depth analysis. The conducted simulations within this thesis have exclusively been executed through the utilization of the GATE simulation software version 9.0.

5.1 Simulated geometry

The initial and crucial step in conducting simulations involves the meticulous construction of a geometry that faithfully replicates the precise dimensions of the scanner. This entails modeling the physical arrangement of the detector rings, the configuration of scintillation materials, and the positions of PMTs.

In the case of the Modular J-PET tomograph, it comprised 24 modules, and the rectangular plastic scintillator strips were organized within cuboidal modules. The Modular J-PET scanner was simulated with a fixed inner diameter of 739.72 mm and 500 mm lengths of the strips, employing a single-layer setup [37]. Each module comprised 13 BC-404 plastic scintillator strips measuring 24 $mm \times 6$ $mm \times 500$ mm, arranged adjacent to one another with a 1 mm gap between them. Each plastic scintillator was read out at both ends by SiPMs. Only the material properties of the BC-404 scintillator ($1.021 g.cm^{-3}$) were included in the simulations. These simulations were conducted with the assumption that the detection chamber, phantom, and source were placed in air. The final architectural representation, is depicted in Figure 5.1. It is visualized through the capabilities of the GATE software. For improved visualization,

the BC-404 plastic scintillator is represented in gray, and the SiPMs are depicted in black in all figures.
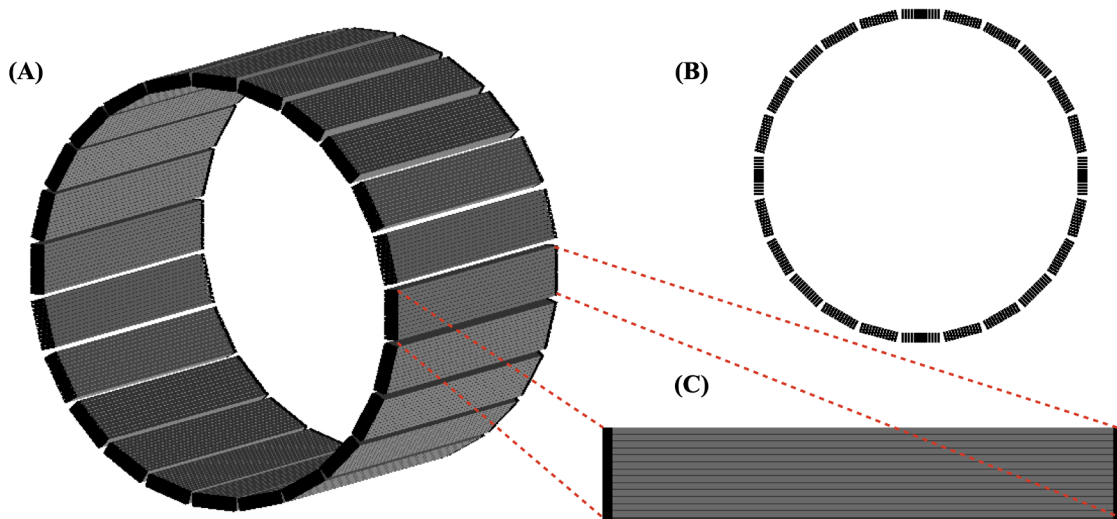
Rysunek 5.1: (A): Geometries of the Modular J-PET prototype simulated in the GATE software, (B): Cross section of 24-Module J-PET,(C): GATE visualization of one module of Modular J-PET. The plastic scintillator strips are depicted in gray, while the SiPMs on both sides of the module are displayed in black.

5.2 Material

GATE effectively harnesses the potential of an extensive material database encompassing a catalog of default materials and elements. This resource proves indispensable, serving as a cornerstone for materials employed in simulations. Each material is defined by its constituent elements and corresponding density, a fundamental attribute that empowers GATE to simulate the intricate interactions of radiation with these elements [95]. Illustrated in Fig 5.2, an exemplar material from the GATE database is presented. In cases where the utilized material diverges from those initially cataloged in the database, manual integration becomes feasible. Fig 5.3 presents the GATE material database with included of the plastic scintillator, a vital component within the 24 Modular J-PET configuration.

```
[Elements]
Hydrogen:     S= H  ; Z=  1. ; A=   1.01  g/mole
Helium:       S= He ; Z=  2. ; A=   4.003 g/mole
Lithium:      S= Li ; Z=  3. ; A=   6.941 g/mole
Beryllium:    S= Be ; Z=  4. ; A=   9.012 g/mole
Boron:        S= B  ; Z=  5. ; A=  10.811 g/mole
Carbon:       S= C  ; Z=  6. ; A=  12.01  g/mole
Nitrogen:     S= N  ; Z=  7. ; A=  14.01  g/mole
Oxygen:       S= O  ; Z=  8. ; A=  16.00  g/mole
Fluorine:     S= F  ; Z=  9. ; A=  18.998 g/mole
Neon:         S= Ne ; Z= 10. ; A=  20.180 g/mole
Sodium:       S= Na ; Z= 11. ; A=  22.99  g/mole
Magnesium:    S= Mg ; Z= 12. ; A=  24.305 g/mole
Aluminium:    S= Al ; Z= 13. ; A=  26.98  g/mole
Silicon:      S= Si ; Z= 14. ; A=  28.09  g/mole
Phosphor:     S= P  ; Z= 15. ; A=  30.97  g/mole
Sulfur:       S= S  ; Z= 16. ; A=  32.066 g/mole
Chlorine:     S= Cl ; Z= 17. ; A=  35.45  g/mole
```

```
[Materials]
Vacuum: d=0.000001 mg/cm3 ; n=1
        +el: name=Hydrogen ; n=1

Aluminium: d=2.7 g/cm3 ; n=1 ; state=solid
        +el: name=auto ; n=1

AluminiumEGS: d=2.702 g/cm3 ; n=1 ; state=solid
        +el: name=Aluminium ; n=1

Uranium: d=18.90 g/cm3 ; n=1 ; state=solid
        +el: name=auto ; n=1

Silicon: d=2.33 g/cm3 ; n=1 ; state=solid
        +el: name=auto ; n=1

Germanium: d=5.32 g/cm3 ; n=1 ; state=solid
        +el: name=auto ; n=1

Yttrium: d=4.47 g/cm3 ; n=1
        +el: name=auto ; n=1
```

Rysunek 5.2: An exemplary illustration of the GATE material database.

Tabela 5.1: Information about the simulated radioactive source.

Source isotope	type of source	shape	Length (mm)	diameter (mm)	lifetime (s)	Activity (MBq)
^{22}Na	point like source	Circle	-	4.8	82049760	9.2
^{18}F	Line source	Cylinder	700	3.2	6586.2	7.5
^{68}Ge	Line source	Cylinder	700	2.6	23410080	2.6

5.3 Source

The source plays a pivotal role within the simulation framework and requires precise user specification. Initiating source simulation involves defining user parameters, encompassing source's geometrical configuration and dimensions, emission type and lifetime. In this thesis, a range of sources has been employed, with the selection contingent upon the specific study type. These sources include ^{22}Na, ^{18}F, and ^{68}Ge, each chosen strategically to align with the nature of the investigation. ^{22}Na point sources are utilized to discern spatial resolution, while ^{68}Ge line sources serve as tools for sensitivity evaluation. Additionally, a set of ^{18}F line sources contributes to the assessment of Noise Equivalent Count Rate (NECR) and scatter fraction. Table 5.1 presents the usful information of distinct source types which were used for evaulation of the performance charactristics of the Modular J-PET detector.

```
Plastic:  d=1.18 g/cm3 ; n=3; state=solid
          +el: name=Carbon ; n=5
          +el: name=Hydrogen ; n=8
          +el: name=Oxygen ; n=2

BC-404: d=1.021 g/cm3 ; n=2; state=solid
          +el: name=Carbon ; n=10
          +el: name=Hydrogen ; n=11

HDPE: d=0.954 g/cm3 ; n=2; state=solid
          +el: name=Carbon ; n=2
          +el: name=Hydrogen ; n=4

          Polyethylene:  d=0.96 g/cm3 ; n=2
          +el: name=Hydrogen ; n=2
          +el: name=Carbon    ; n=1

Biomimic:  d=1.05 g/cm3 ; n=3; state=solid
          +el: name=Carbon    ; n=5
          +el: name=Hydrogen ; n=8
          +el: name=Oxygen ; n=2

CZT:  d=5.68 g/cm3 ; n=3; state=solid
          +el: name=Cadmium    ; n=9
          +el: name=Zinc         ; n=1
          +el: name=Tellurium ; n=10
```

Rysunek 5.3: An exemplary illustration of the GATE material database with added BC-404 information [96].

5.4   Phantoms

PPhantoms hold a fundamental role in this work, serving as indispensable components. In the GATE simulations, two distinct types of phantoms are employed: voxel-based and analytical phantoms, the latter being characterized by analytically defined geometries. For the performance studies presented in the subsequent chapters, analytical phantoms were exclusively utilized. These include the NECR/scatter fraction phantom and the NEMA sensitivity phantom [38], which will be explained in the sections that follow.

5.4.1   Sensitivity phantom

The NEMA sensitivity phantoms are comprised of five distinct aluminum sleeves, each characterized by precise dimensions as elucidated in Table 4.1. A visual representation of the sensitivity phantom, visualized through the GATE software, is depicted in Figure 6.1.
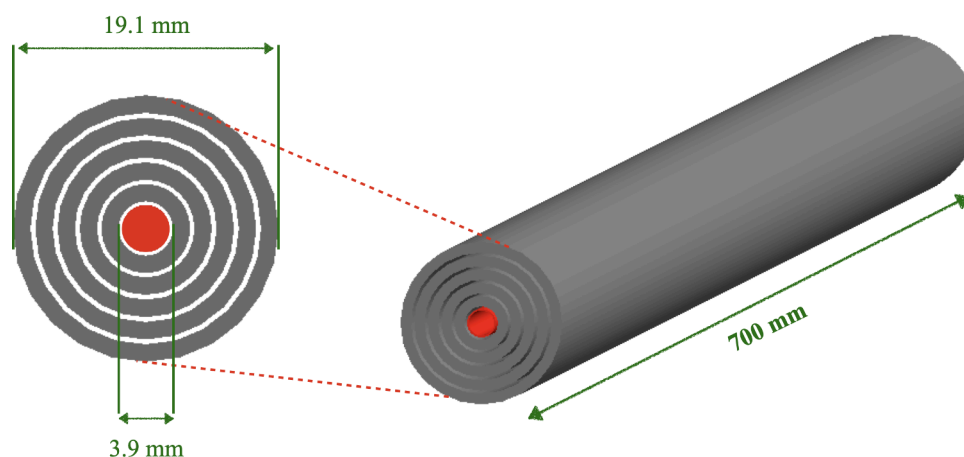
Rysunek 5.4: (Right): GATE visualization of sensitivity Phantom with five sleeve tubes displayed with gray and one polyethylene tube with length of 70 cm displayed with red. (Left) illustration of sensitivity phantom cross section, red point represented the line source inside the phantom. The figure isn't to scale.

5.4.2 Scatter fraction and NECR phantom

The determination of scatter fraction necessitates the use of a unique phantom characterized by its cylindrical geometry and composition, which is crafted from polyethylene material. To accurately measure the simulated performance of the Modular J-PET scanner, employed the NEMA scatter phantom, defined by the NEMA NU 2-2018 protocol (complete explanation in section 4.2). As illustrated in Figure 5.5, this simulated phantom takes the form of a 70 cm long solid cylinder with diameter of 203 mm, and a specific gravity of 0.96 g/cm^3. It's important to note that this phantom is meticulously centered and aligned parallel to the axial axes of the scanner. Significantly, this particular phantom serves a dual purpose, not only in scatter fraction estimation but also in NECR assessments. The sole distinction between the two applications lies in the NECR determination, where various activity concentrations within the source are employed as a distinguishing factor.
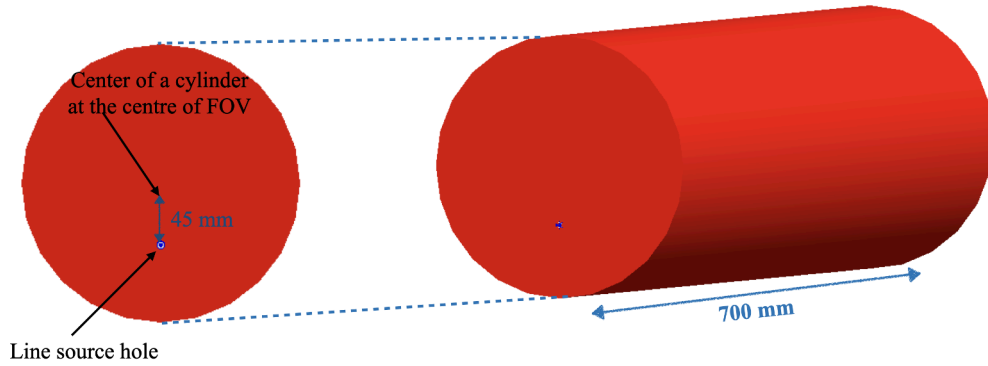
Rysunek 5.5: (Right): GATE visualization of scatter fraction Phantom with red and line source hole with blue. phantom placed in the center of the scanner. (Left) illustration of scatter fraction phantom cross section, display the place of source. The The figure isnot scale.

5.5 Physical processes

In our simulations, we utilized a set of physical processes known as "emlivermore polar," which employs the low-energy Livermore model for accurate electromagnetic interactions [97, 98]. This model is specifically designed for precise tracking of electrons, hadrons, and ions in scenarios without magnetic fields. The processes it covers include photo-electric effects, Compton scattering, Rayleigh scattering, gamma conversion, bremsstrahlung, ionization, as well as fluorescence and gamma photon polarization. These processes rely on cross-section data obtained from shell cross-section data [97], in contrast to high-energy processes that often use parameterized data.

5.6 GATE Output

The GATE simulation framework offers users a range of choices for output data file formats during the pre-acquisition phase. Noteworthy among these formats are RO-OT, ASCII, Interfile, Sinogram, and others. For the specific objectives of this thesis, all simulations were performed and saved exclusively in the ROOT format to ensure optimal compatibility and streamline subsequent analyses. The ROOT file format, designated as the primary repository for GATE simulation results, encapsulates a comprehensive array of information associated with detected events. This encompas-

sing data set includes crucial details such as annihilation position, detection time, coordinate data, energy deposition, and more. It is essential to highlight that this information is stored in list mode, enabling its flexible utilization for future analyses or event selection criteria.

5.6.1   Event selection

In the realm of PET imaging, the process of detecting and classifying coincidence events plays a pivotal role in the formation of accurate images. A single positron-electron annihilation event, as well as any subsequent interactions involving secondary particles, results in a sequence of photon interactions. These interactions collectively constitute what we refer to as a single event. Any two scatterings within an event may form a coincidence event. Coincidence events detected during PET imaging can be categorized into three main types: true coincidence events, scatter coincidence events, and accidental (or random) coincidence events, as explained in greater detail in Section 2.4. The schematic definitions of these different types of coincidences are depicted in Figure 2.10. Scatter and random coincidence events contribute to background noise and can compromise the image quality.

To mitigate the contribution of events involving photons scattered within the detector and the patient's body, a filtering process is applied to the simulated events. This filtering relies on specific criteria based on the correlations between two key factors: the time of interaction of gamma quanta with the scintillator (referred to as "hit time") and the amount of energy transferred by gamma quanta to electrons within the material (referred to as "energy deposition") [91]. In plastic scintillators, energy deposition primarily occurs due to Compton interactions, resulting in a range of energy values typically between 0 and 341 keV for 511 keV photons. By applying a fixed energy threshold of 200 keV, the majority of coincidence events involving multiple Compton scatterings within the detector are filtered out [2]. This action aims to reduce the scatter fraction, thereby enhancing image quality [99]. Therefore, to extract true coincidences from the entire set of coincidences, specific criteria are established. True coincidence events are defined as those events in which only two

interactions are recorded, and both interactions involve an energy loss exceeding the fixed energy threshold of 200 keV. Additionally, it is required that the Time of Flight (TOF) between these interactions is less than 4 ns.

In all of the simulations, were applied an energy resolution of 23 % for energy of 340 keV [100] and a time resolution of 628 ps. Time resolution values have been obtained through experimental measurements conducted on the Modular J-PET system.

Prior to analysis, simulated data were smeared taking into account experimental position resolutions. In the radial and tangential directions the hit position was shifted to the center of the scintillator, while in the axial direction, it was smeared with the sigma of 1.5 cm.

ROZDZIAŁ 6

EVALUATION OF NEMA CHARACTERISTIC OF MODULAR J-PET THROUGH SIMULATION

The evaluation of the PET scanner prototype's performance characteristics is accomplished through a combination of experimental measurements and GATE Monte Carlo simulations, following the guidelines outlined in the NEMA NU2-2018 standard [1]. GATE software was utilized the to simulate Modular J-PET tomograph geometries, replicating the conditions of experimental measurements. The NEMA characteristics encompass parameters such as spatial resolution, scatter fraction, NECR, and sensitivity.

All simulations accounted for both primary and secondary scatterings of annihilation photons within the detector material. Simulated interactions were convolved with experimentally determined resolutions to provide accurate times and positions of interactions. To minimize the occurrence of events involving gamma photons scattered in the phantom or detector, we implemented selection criteria based on correlations among coincidence time window, and energy deposition of annihilation photons within the detector during signal processing (further details are available in Chapter 5).

6.1 Sensitivity

In order to calculate the sensitivity of the scanner, a 70 cm linear 2.6 MBq source of ^{68}Ge was simulated inside the sensitivity phantom (see section 5.4.1 for more details on the phantom). This simulation was repeated for decreasing amount of aluminum tubes from 5 to 1. In each simulation, the source and phantom were placed in two different positions: the center of the AFOV and 10 cm offset from the tomograph center as shown in fig 6.1. To extract true coincidences, the selection criteria for true coincidences were applied, which were described in the chapter 5. In order to meet the
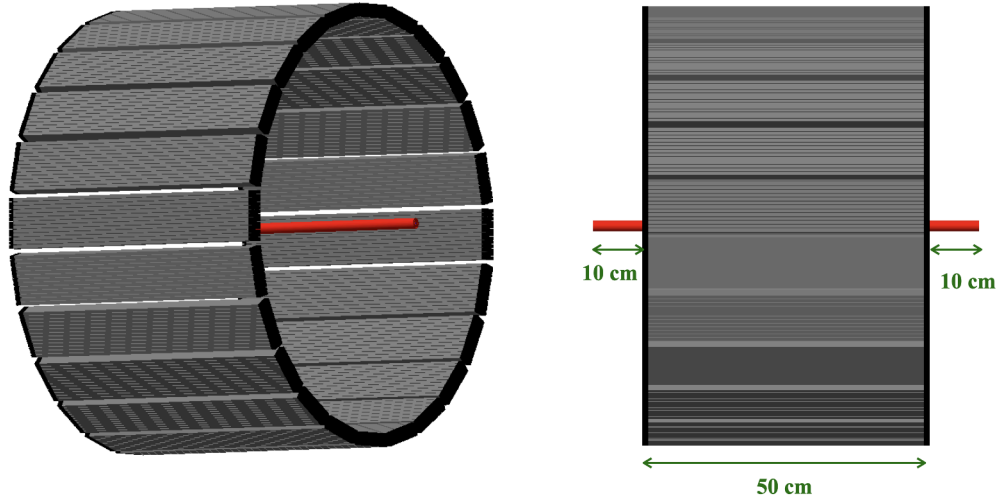
Rysunek 6.1: (Left): GATE visualization of the Modular J-PET with sensitivity phantom located in the center of the FOV. (Right) illustration of side view of the simulated sensitivity measurement, presenting place of source and phantom. The figure isn't to scale.

NEMA standard, the number of true coincidences for each slice of the PET scanner should be at least 10,000, simulation done for 200 s. According to NEMA standards, the activity must be such that the number of accidental coincidences is less than 5% of all prompt coincidences. In this case, the activity of 2.6 MBq and 200 seconds of simulation met this requirement, less than the 3% of the registered events were accidental coincidences for all simulation. In the simulation, a total of 692k prompt coincidences were registered, with the number of each type of coincidence summarized in Table 6.1. However, it is crucial to emphasize that the Modular J-PET encompasses a 50 cm AFOV. Consequently, the activity of the source contained within the detector requires normalization. Determination of the activity of the source utilized during the measurement period proceeds as follows:

$$A_{normalized} = A_{cal} \frac{50 \ cm}{70 \ cm}. \tag{6.1}$$

$$A_{normalized} = 2.6 \ MBq \frac{50 \ cm}{70 \ cm} = 1.85 \ MBq. \tag{6.2}$$

Tabela 6.1: The number of each type of coincidence for the sensitivity simulation.

Type of simulation	True coincidence	Phantom-scattered coincidence	Detector-scattered coincidence	Random coincidence
1 sleeve in center of detector	452943 ± 673	19472 ± 139	188481 ± 434	15022 ± 122
2 sleeves in center of detector	425430 ± 674	31851 ± 178	175190 ± 418	13870 ± 117
3 sleeves in center of detector	397381 ± 630	44770 ± 211	167050 ± 480	14811 ± 121
4 sleeves in center of detector	378420 ± 615	53911 ± 232	155090 ± 393	13220 ± 114
5 sleeves in center of detector	357010 ± 597	62681 ± 250	145861 ± 381	12932 ± 113
1 sleeve in 10 cm radial offset	456671 ± 675	20272 ± 142	197222 ± 444	15911 ± 126
2 sleeve in 10 cm radial offset	430664 ± 656	34421 ± 185	180412 ± 424	15151 ± 123
3 sleeves in 10 cm radial offset	405855 ± 637	47440 ± 217	171300 ± 413	14580 ± 120
4 sleeves in 10 cm radial offset	381411 ± 617	58400 ± 241	162642 ± 403	14060 ± 118
5 sleeves in 10 cm radial offset	360282 ± 600	67641 ± 260	151371 ± 389	13611 ± 116

Although sensitivity provides an overall value for the entire detector, there exists a sensitivity profile that varies along the scanner axis. To derive this profile, the detection chamber is divided into slices, typically cylindrical segments between individual rings of crystals, defining the AFOV for PET tomography.

To plot the axial sensitivity profile as per Equation 4.5, the count rate for each simulation was initially graphed against the accumulated thickness of the sleeve walls. This dataset then underwent a fitting process utilizing Equation 4.3, with the resulting graphical representation depicted in Figure 6.2. Subsequently, the system sensitivity was computed based on Equation 4.4. Below, you can find the results for the system sensitivity obtained from measurements conducted with the PET Sensitivity Phantom in both positions:

$$S_0 = \frac{2450 \pm 59.5 \ cps}{1850 \ kBq} = 1.32 \pm 0.03 \ \frac{cps}{kBq}. \tag{6.3}$$
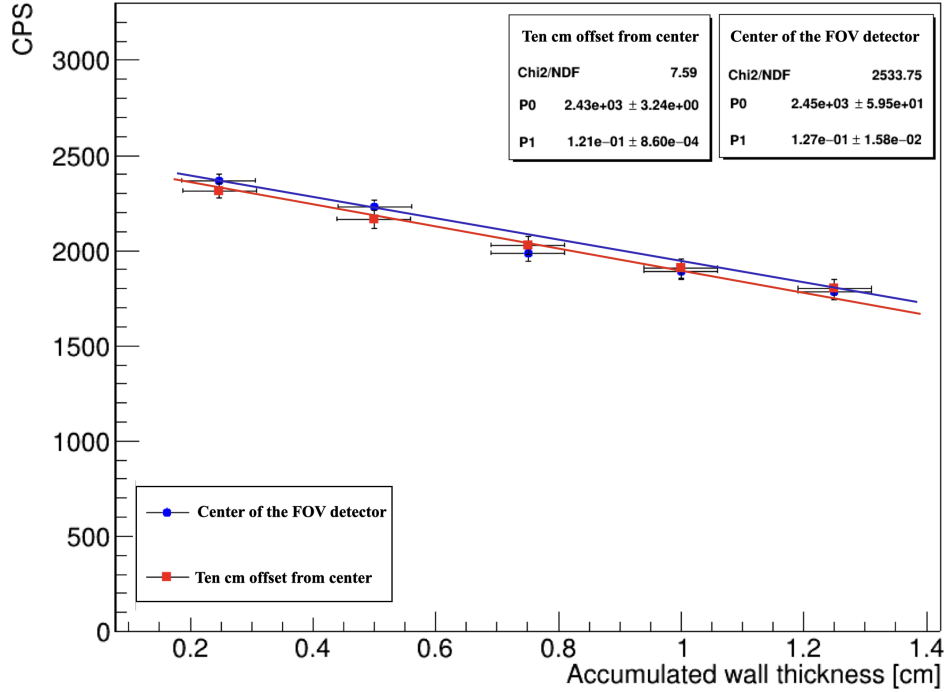
Rysunek 6.2: Illustrates how R_j (cps) varies with the accumulated sleeve wall thickness. As depicted, there is a noticeable decrease in count rate as the wall thickness increases. These measurements were obtained at the center of the detector and at the ten cm offset from the center of the detector, and the data is fitted to the equation specified in Eq. 4.3.

$$S_{10} = \frac{2430 \pm 3.24 \; cps}{1850 \; kBq} = 1.31 \pm 0.001 \; \frac{cps}{kBq}. \tag{6.4}$$

The axial sensitivity profiles for the smallest tube presented in Fig 6.3 correspond to the center of the scanner FOV and 10 cm offset from the tomograph center. As shown in Fig. 6.3, the peak sensitivity value is equal to 2.8 cps/kBq and 2.75 cps/kBq in the center of the scanner FOV and 10 cm offset from the tomograph center, respectively.

6.2 Scatter fraction, Count losses, and Randoms measerment

6.2.1 Scatter fraction

To assess the count-rate performance and scatter fraction, a simulated scatter phantom (as detailed in Section 5.4.2), was employed. The simulation mirrored the di-
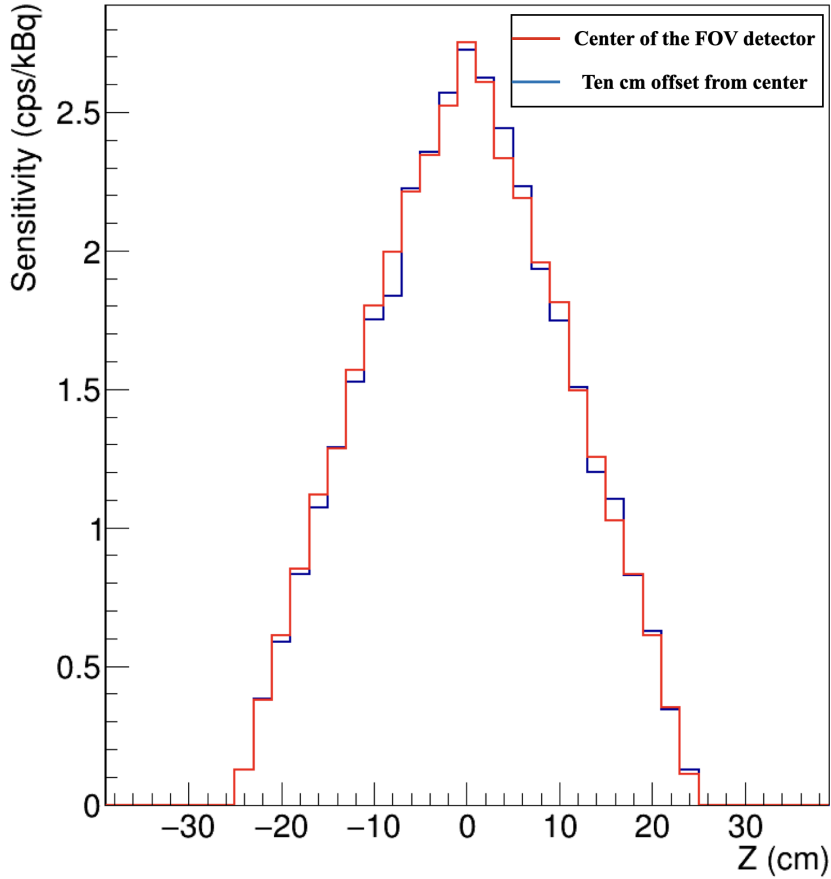
Rysunek 6.3: Axial sensitivity profile for the smallest sleeve in both positions. The peak sensitivity value is equal to 2.8 cps/kBq in the center of the scanner FOV and 2.75 cps/kBq in 10 cm offset from the tomograph center.

mensions and source positioning recommended in the NEMA-NU2 2018 guidelines, using a 700 mm long and 6.4 mm diameter ^{18}F line source with activity 7.5 MBq positioned 45 mm below the center within a polyethylene scatter cylindrical phantom measuring 700 mm in length and 203 mm in diameter, as depicted in Fig. 6.4 . Given the lower activity, a simulation time of 500 seconds was considered for estimating the scatter fraction. In accordance with the NEMA NU 2-2018 protocol, the value of the activity for obtaining the scatter fraction is limited by the condition that the ratio between the random and true coincidences should be smaller than 1%. For the scatter fraction simulation with 1 MBq activity, a random to true coincidence ratio of 0.000016% was achieved. Results of random event rate show up that there was no detected random event in this simulation. The NEMA NU 2-2018 also requires that a
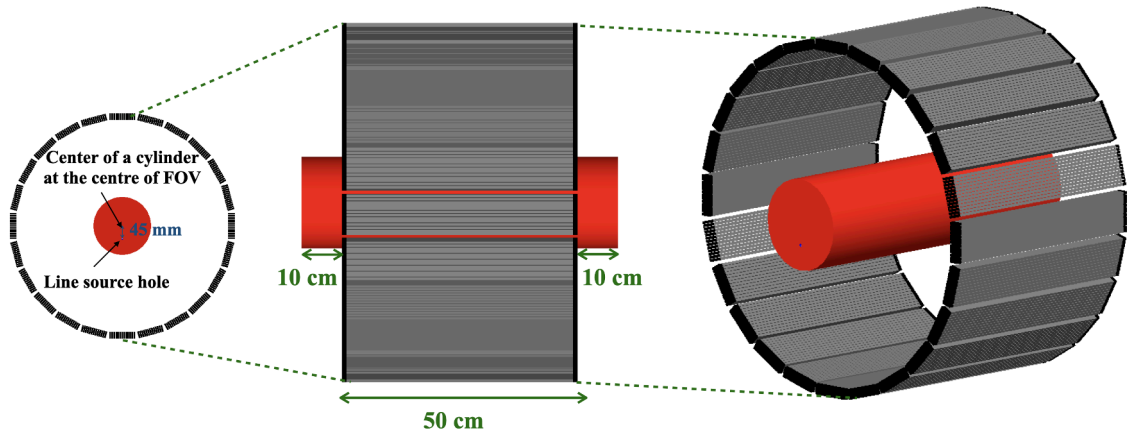
Rysunek 6.4: (Left): Cross section of 24-Module J-PET, display the place of source and phantom inside the detector, (middle): GATE visualization of side of 24-Module J-PET with NEMA scatter phantom (red color) in the center of the detector. (Right): GATE visualization of 24-Module J-PET with NEMA scatter phantom.

Tabela 6.2: The number and percentage of each type of coincidence for the scatter fraction simulation.

Activity	True coincidence	Phantom-scattered coincidence	Detector-scattered coincidence	Random coincidence
1MBq	334139 ± 578 (59.11 ± 0.10)	219472 ± 463 (38.82 ± 0.06)	11554 ± 107 (2.06 ± 0.01)	56 ± 7 (0.000099 ± 0.009)

minimum of 500k prompt counts must be acquired, and in our studies, 565k prompt coincidences were detected. Table 6.2 displays the number and percentage of different types of coincidences in the scatter fraction simulation.

In accordance with NEMA standard, the scatter fraction was determined through the application of the SSRB algorithm, as elaborated in Section 4.2. This methodology involved segmenting the detection chamber into 2 cm slices and generating a dedicated sinogram for each of these slices [101]. Rebinned sinograms are subsequently summed into a single sinogram, as illustrated in the Fig 6.5. Utilizing this cumulative sinogram, all projections are shifted along the "Displacement" axis, with the maximum value being set to zero, before being aggregated to obtain a 1-dimensional profile, as demonstrated in the Fig 6.6.
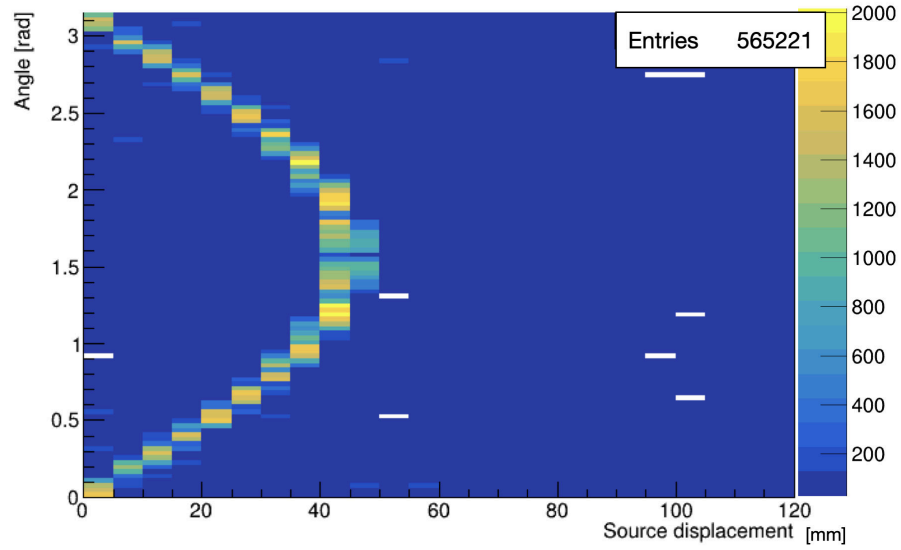
Rysunek 6.5: Illustrates sinogram was obtained as a sum of all aligned sinograms for whole scanner.
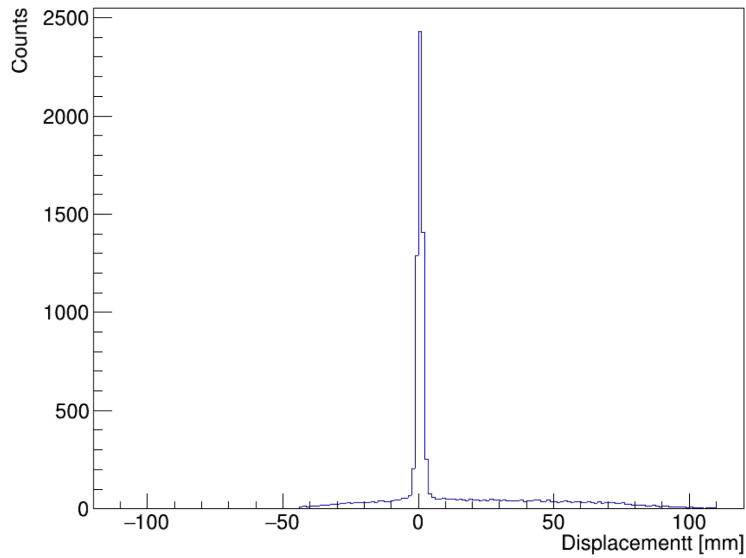
Rysunek 6.6: A one-dimensional profile involves a calculation aligned to zero utilizing the maximum value and summing the projections of the sinogram.

After summation, the counts per pixel values at distances of ±2 cm from the sinogram center are computed. The count per pixel values from the left and right sides of the projection profile at ±2 cm from the sinogram center are determined based on linear interpolation between the two nearest pixels, as illustrated in the Fig. 6.7. The area encompassed by the profile spanning the line connecting these two
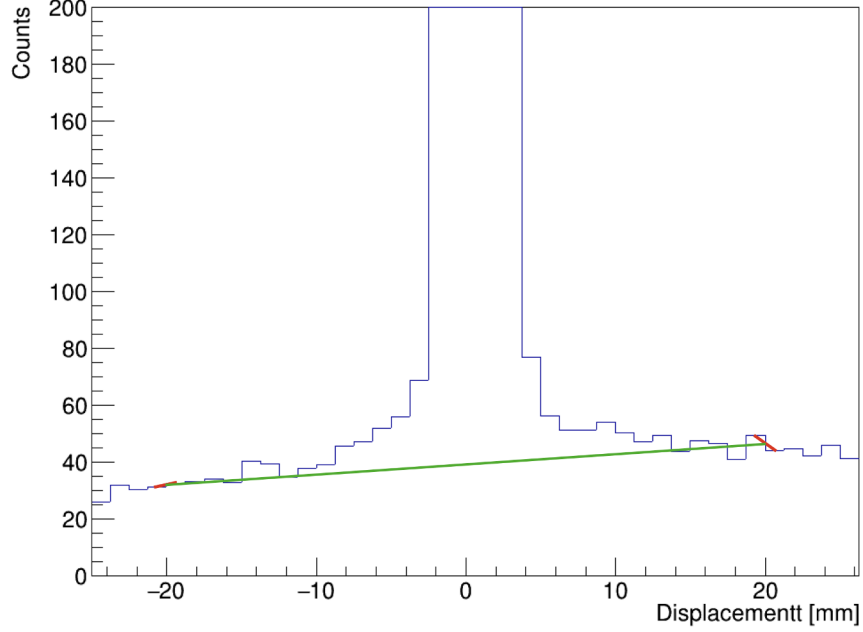
Rysunek 6.7: One-dimensional profile calculated as aligned to zero using maximum value and summed projections of sinogram, used to differentiate the true and the false (scattered and accidental) coincidences. Coincidences over the green line are treated as true coincidences, while those below as scattered and accidental ones.

points at ±2 cm signifies true coincidences, whereas the area located below this line corresponds to scattered (and accidental) coincidences (C_{r+s}), as denoted in Fig 6.7. Per the NEMA standard, when computing the random plus scatter counts (C_{r+s}), the procedure involves multiplying the average of interpolated pixel intensities C_{Left} and C_{Right} by the number of pixels between the edges of the 40 mm region. This outcome is then added to the counts in pixels outside the 40 mm region. The counts within the 40 mm region ($C_{central}$) and those outside this range (C_{side}) are determined as follows:

$$C_{central} = 2585 \pm 51 \; counts. \tag{6.5}$$

$$C_{side} = 5043 \pm 71 \; counts. \tag{6.6}$$

$$C_{r+s} = C_{central} + C_{side} = 7627 \pm 87.3 \; counts. \tag{6.7}$$

The uncertainty associated with the count numbers in all case was determined by computing the square root of the respective counts. The total event counts (C_{TOT})

were derived by aggregating the counts from all pixels within the summation projection. The total event count is calculated as follows:

$$C_{TOT} \; = \; 18950 \; \pm \; 138 \; counts. \tag{6.8}$$

According to NEMA norm, two methods were employed to calculate the scatter fraction: one involving random estimation, and the other without. For the Modular J-PET, the second approach was utilized. The outcome of this analysis reveals that the scatter fraction for the Modular J-PET, using Equation 4.15, is equal:

$$SF \; = \; 40.3 \; \pm \; 2.3 \; [\%]. \tag{6.9}$$

The uncertainty of the scatter fraction was determined using the principles of error propagation.

6.2.2 NECR

Noise Equivalent Count Rate(NECR), is a measure of the scanner's performance that takes into account the effects of scattered and random coincidences as a function of the source activity. It is a measure of the effective sensitivity of the scanner and is defined as follows:

$$NECR = \frac{(T)^2}{T + S + R}, \tag{6.10}$$

where, T represents the number of true coincidences, S represents the number of scattered coincidences, and R represents the number of random coincidences. The goal of maximizing NECR is to obtain a balance between the number of true coincidences, which contributes to image quality, and the number of scattered and random coincidences, which contribute to noise in the image. Typically, the NECR curve shows a peak at a certain activity concentration, beyond which it gradually decreases. This peak represents the optimal source activity for a fixed scanner geometry, with smaller values indicating that lower activity can be used to achieve better results. Additionally, the NECR is directly proportional to the square of the Signal to Noise Ratio

(SNR^2), a key parameter used to evaluate the quality of reconstructed PET images.

To assess the count-rate and NECR performance, the scatter fraction simulation was conducted using varying activity levels. The method employed to derive the NECR aligns with the approach used for measuring and computing the scatter fraction. Considering a substantial range of activity concentrations and higher levels of activity, a simulation duration of 1 second was adopted for each simulation. The corrected activity, as per Equation 4.6 and utilized for NECR simulation, spans from 2.4 MBq to 88 MBq, a range selected based on the activity levels outlined in the experimental findings (refer to section 8.2). The activity concentration can also be computed using Equation 4.20, falling within the range of 0.11 kBq/cc to 4 kBq/cc. For each simulation the total count rate was computed as:

$$R_{TOT} = \frac{1}{T_{acq}} C_{TOT}, \tag{6.11}$$

where, T_{acq} stand for the acquisition time and C_{TOT} stand for total event count. and true count rate $(R_{t,j})$, scatter count rate $(R_{s,j})$, and random count rate $(R_{r,j})$ are defined by the following formulas:

$$R_{t,j} = \frac{1}{T_{acq,j}} \sum_i (C_{TOT,i,j} - C_{r+s,i,j}). \tag{6.12}$$

$$R_{s,j} = (\frac{SF}{1 - SF}) R_{t,j}. \tag{6.13}$$

$$R_{r,j} = R_{TOT,j} - (\frac{R_{t,j}}{1 - SF}). \tag{6.14}$$

The results of count rates are presented in Fig 6.8. Uncertainty in the count rates was computed according to the error propagation law. The NECR count rate for the system is computed as:

$$R_{NEC,j} = \frac{R_{t,j}^2}{R_{TOT,j}}. \tag{6.15}$$

Figure 6.8 displays also the count rates as a function of the activity concentration. Peaks were observed at an activity concentration of 4 kBq/cc, wherein the NECR peak reached 132 ± 11 cps. Notably, at this same activity concentration, the total

count rate, true count rate, and scatter count rate were recorded at582 $\pm$ 11 cps, 344.95 $\pm$ 33 cps, and 237 $\pm$ 21 cps, respectively.
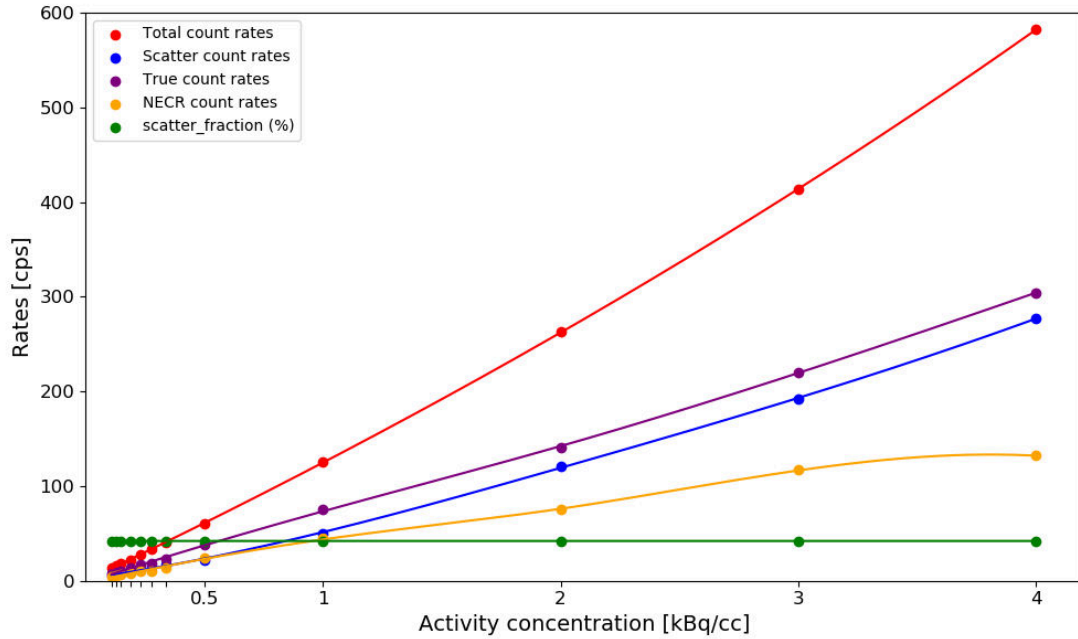
Rysunek 6.8: Count rates of different types of coincidences and NECR as a function of activity concentration (in kBq/cc).

6.3   Spatial resolution

The spatial resolution of a PET scanner denotes its capability to discern distinct points following image reconstruction [6]. The evaluation of spatial resolution is contingent upon the localization within the AFOV of the scanner. According to standard procedures, the determination of the Point Spread Function (PSF) mandates assessments at six distinct positions. Along the axial direction, the prescribed positions include placing the source both at the central point of the AFOV and at a distance three-eighths away from the scanner's central axis. In the transverse direction, the specified positions involve distances of 1 cm, 10 cm, and 20 cm from the scanner's axis. Figure 6.9 illustrates a schematic representation of the spatial arrangement of a point-like source within the detector. For the assessment of spatial resolution, a ^{22}Na point-like source, measuring 0.5 cm in diameter and containing 9.2 MBq of activity,
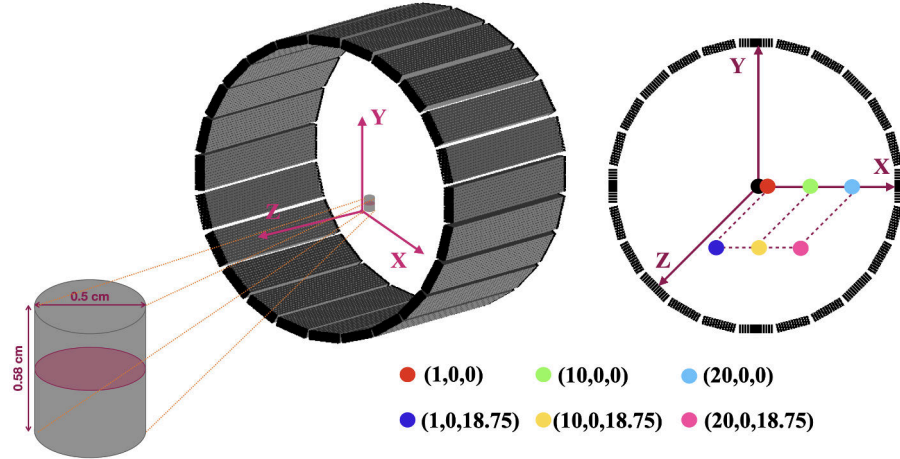
Rysunek 6.9: (Left) Representation of axis orientation in the Modular J-PET detector and exemplary of the ^{22}Na source inside the phantom in position (1, 0,0). ^{22}Na is in the center of aluminum phantom and active area is such as circle plane in the half of the phantom length. (Right) Schematic illustration of source positions within the Modular J-PET, black point shows the center of the detector. Please note that the figure is not drawn to scale. The unit of position measurement is in cm.

was simulated. This source was encased in an aluminum cylinder with a length of 0.58 cm and a diameter of 0.5 cm. Simulations were conducted at six different positions, each for a duration of 10 seconds. The activity of the simulated source corresponds precisely to the activity of the ^{22}Na source utilized in our experimental measurements. NEMA standard required to the number of the random coincidences should be less than 5% of all collected events. Table 6.3 presents the count and percentage of each type of coincidental event for the six varied positions. Notably, in the modular case, the ratio of random to total events is consistently lower than 5%. According to the NEMA norm, for each position of the source, the number of collected prompt coincidences should be at least 100,000.The acquisition duration of 10 seconds, alongside the 9.1 MBq activity of the source, satisfactorily meets this requirement.

Following the implementation of data smearing and the subsequent event selection process, reconstruction of the data was carried out. Although the NEMA standard recommends employing the FBP algorithm for reconstructed image, we pursued higher-resolution imaging using MLEM iterative reconstruction and present the outcomes achieved through MLEM iterative reconstruction with optimized parameters

Tabela 6.3: The number and percentage of each type of coincidence for the spatial resolution simulation in six different positions.

Position [cm]	Total event counts	True coincidence	Scatter coincidence	Random coincidence
(1,0,0)	321398	218160 ± 467 $(66.5 \pm 0.14)\%$	91088 ± 301 $(27.7 \pm 0.09)\%$	12151 ± 110 $(3.7 \pm 0.03)\%$
(10,0,0)	311280	210291 ± 485 $(68.4 \pm 0.04)\%$	88205 ± 296 $(28.3 \pm 0.09)\%$	12784 ± 113 $(4.1 \pm 0.03)\%$
(20,0,0)	330461	219702 ± 468 $(66.43 \pm 0.14)\%$	96094 ± 309 $(29.07 \pm 0.09)\%$	14666 ± 121 $(4.43 \pm 0.03)\%$
(1,0,18.75)	100409	65697 ± 271 $(65.42 \pm 0.002)\%$	31121 ± 176 $(30.991 \pm 0.07\%$	3591 ± 60 $(3.57 \pm 0.05)\%$
(10,0,18.75)	104554	69843 ± 271 $(66.8 \pm 0.002)\%$	31120 ± 176 $(29.7 \pm 0.14)\%$	3591 ± 60 $(3.43 \pm 0.05)\%$
(20,0,18.75)	136097	92962 ± 311 $(68.3 \pm 0.22)\%$	41804 ± 191 $(30.71 \pm 0.14)\%$	2781 ± 52 $(2.04 \pm 0.03)\%$

for high-resolution imaging (utilizing 10 iterations) [102, 103].

The image reconstruction process utilized the Quantitative Emission Tomography Iterative Reconstruction (QETIR) software, developed by the MEDISIP group at Ghent University in Belgium [104]. This software operates with both Time-of-Flight (TOF) and non-TOF List-Mode (LM) data, which can be converted into TOF or non-TOF sinograms as required. A prominent feature of the QETIR reconstruction software is its capability to independently generate a sensitivity map. To create a sensitivity map using QETIR, the user is required to initiate a sensitivity map configuration. This involves specifying parameters such as sensitivity map size $(200, mm \times 200, mm \times 200, mm)$, voxel dimensions $(2.5, mm \times 2.5, mm \times 2.5, mm)$, and the number of back-to-back photons per voxel (20000), among other relevant details. Figures 6.10 and 6.11 exemplify sensitivity maps of the Modular J-PET generated by the QETIR image reconstruction software. After image reconstruction and generation image for each position, each image underwent a bin-by-bin reading process. Subsequently, a line profile was extracted through the distribution peak for all three directions in compliance with the NEMA standards [6]. The FWHM of the resulting distributions was identified as the point spread function (PSF), serving as a pivotal metric for spatial resolution [102, 105]. In the subsequent step, the FWHM for each
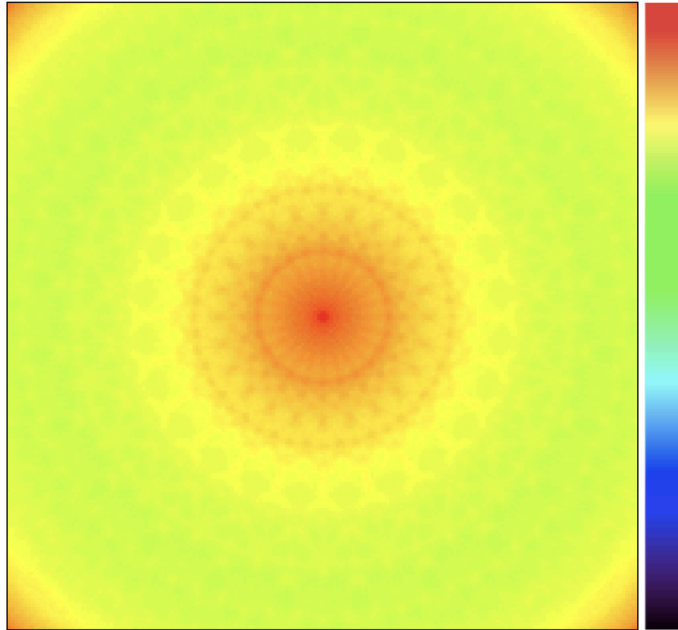
Rysunek 6.10: Transverse plane (-25 cm , 25 cm) representation extracted from the sensitivity map of the Modular J-PET, generated using QETIR software.
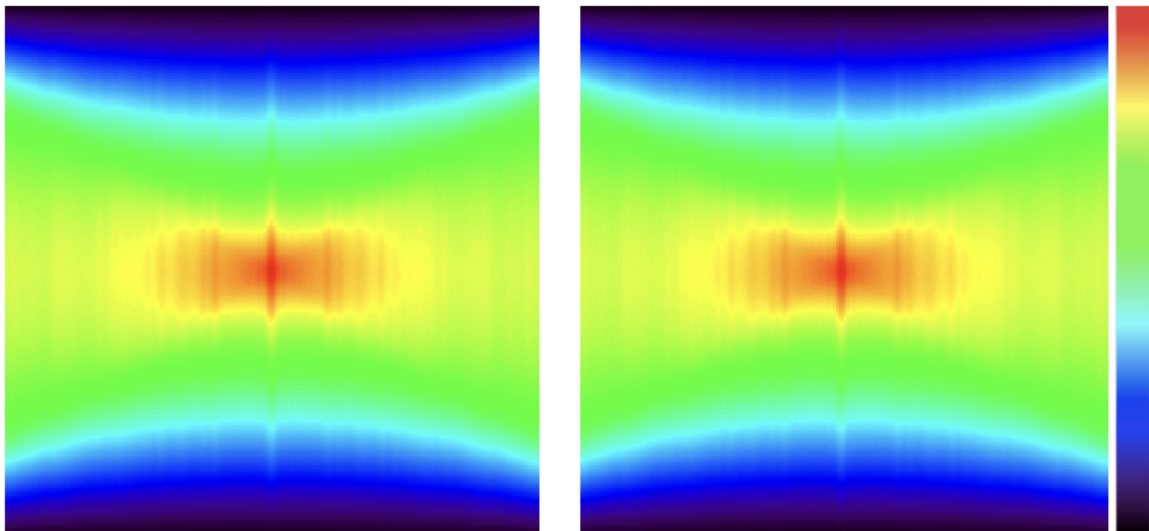
Rysunek 6.11: (Left) Coronal plane (-25 cm , 25 cm) and (Right) Sagittal plane (-25 cm , 25 cm) visualizations extracted from the sensitivity map of the Modular J-PET.

measured point in three directions was calculated. Determining the maximum value of each line profile was done by employing a parabolic fit of the peak point and its two nearest-neighbor points. Subsequently, the FWHM was calculated using linear

interpolation between neighboring bins at half of this maximum value, as illustrated in Fig 4.4.

In this method, a linear interpolation between two consecutive bins was conducted using calculations based on the midpoint of the bins on both the left and right sides of the distribution. The determination of parameters for the linear fit, specifically focused on the right-sided distribution , involved an analytical process based on two distinct equations:

$$y_1 = a_{right}x_1 + b_{right} \tag{6.16}$$

$$y_2 = a_{right}x_2 + b_{right} \tag{6.17}$$

By performing a subtraction operation between these two equations, one can derive the parameters a_{right} and b_{right} characterizing the linear fit between two adjacent bins on the right side, along with their respective uncertainties:

$$a_{right} = \frac{y_1 - y_2}{x_1 - x_2} \tag{6.18}$$

$$b_{right} = y_1 - a_{right}x_1 \tag{6.19}$$

uncertainty of a_{right} and b_{right} were calculated as:

$$\delta a_{right} = \sqrt{(\frac{\delta a_{right}}{\delta x_1})^2 \Delta x_1^2 + (\frac{\delta a_{right}}{\delta x_2})^2 \Delta x_2^2} \tag{6.20}$$

$$\delta b_{right} = \sqrt{(\frac{\delta b_{right}}{\delta a_{right}})^2 \Delta a_{right}^2 + (\frac{\delta a_{right}}{\delta x_1})^2 \Delta x_1^2} \tag{6.21}$$

The determinations were based on $\Delta x = \Delta x_1 = \Delta x_2 = \frac{binwidth}{\sqrt{3}}$, where binwidth represents the width of the bin equal to 2.5 mm. The identical procedure was executed to determine the linear fit for the left side of the distribution. Subsequently, the calculation for the Full Width at Half Maximum (FWHM) was as follows:

$$FWHM = x_{right} - x_{left} \tag{6.22}$$

The uncertainty in estimating FWHM can be computed through the error propagation law:

$$\Delta FWHM = \sqrt{x_{right}^2 - x_{left}^2} \qquad (6.23)$$

where, x_{right} and x_{left} represent the points of intersection between FWHM interpolation and the linear fit from the right and left sides, respectively, which was calculated from the formula:

$$H_{1/2} = a_{right}x_{right} + b_{right} \qquad (6.24)$$

The equation involving $H_{1/2}$ denotes one half of the maximum value obtained from the parabolic fit applied to the distribution's peak. FWHM and its corresponding uncertainty estimation for the distribution along three directions were conducted for all positions after applying the hit position uncertainty along the Z-axis equal to 15.0 mm. Figures 6.12, and 6.13 present the image of QETIR software for position (1,0,0) which is very close to the center of the detector in three direction for TOF and Non TOF reconstructed image, respectively. Used time resolution (FWHM) for this reconstruction was equal 628 ps.
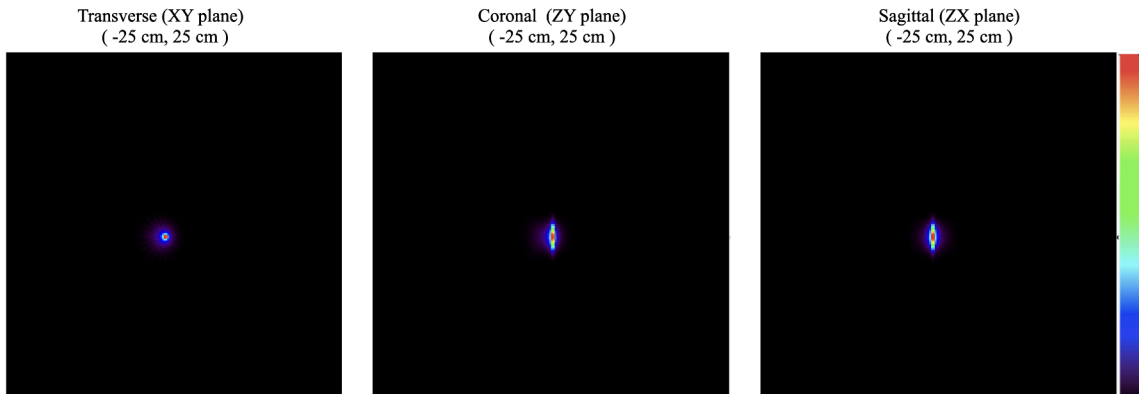
Rysunek 6.12: The outcomes of image reconstruction were generated using TOF List Mode data for the source positioned at (1,0,0). The displayed images were obtained from the first iteration and showcase the reconstructed image in three directions.

The presented images were obtained from the first iteration of each reconstruction. In the next step, a line profile was extracted from each image in three directions. Figures 6.14, 6.15, and 6.16 display the FWHM results for the position (1,0,0) in both
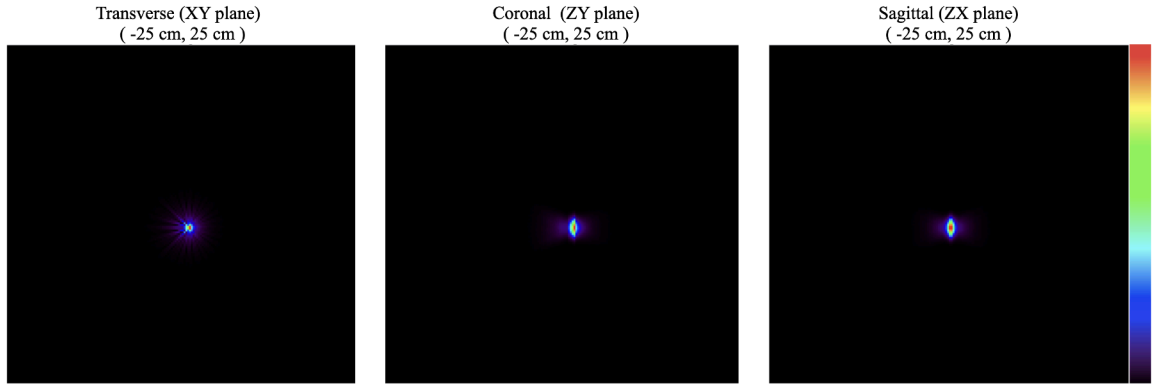
Rysunek 6.13: The outcomes of image reconstruction were generated using Non-TOF List Mode data for the source positioned at (1,0,0). The displayed images were obtained from the first iteration and showcase the reconstructed image in three directions.

TOF and Non-TOF reconstructions along the x-axis, y-axis, and z-axis, respectively.
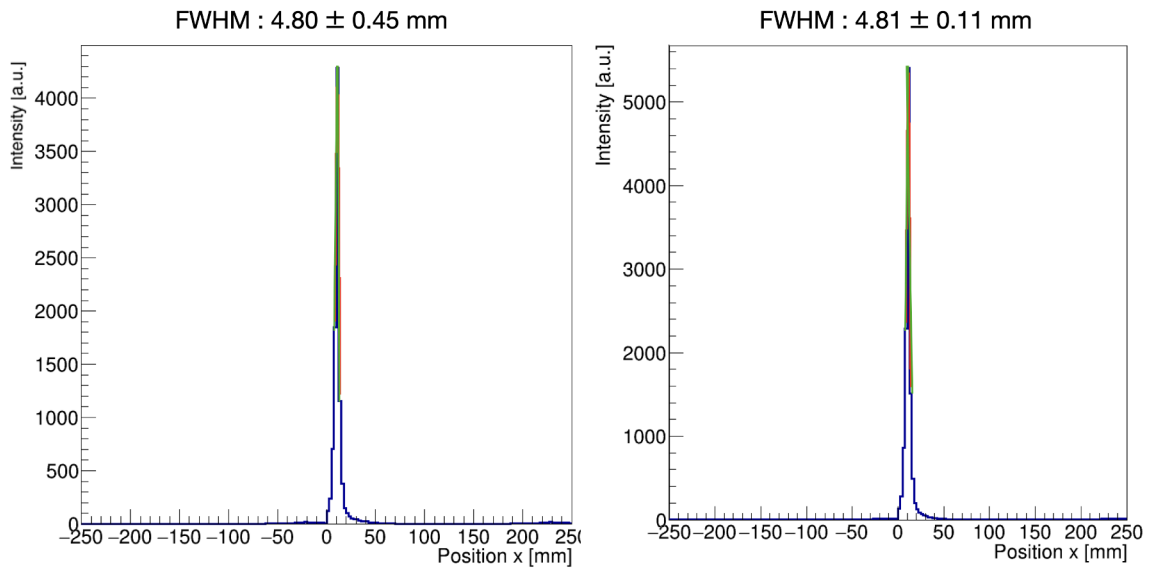
Rysunek 6.14: FWHM and its uncertainty estimation for distribution along x -axis performed at position (1,0,0), (left) for TOF reconstructed image, and (right) Non-TOF reconstructed image.

Subsequently, the FWHM and their corresponding uncertainty was computed for all positions and tabulated in Table 6.4. Using the TOF image reconstruction methods are demonstrated improvement in axial direction. In order to have high spatial

FWHM : 7.27 ± 0.25 mm

FWHM : 7.27 ± 0.54 mm
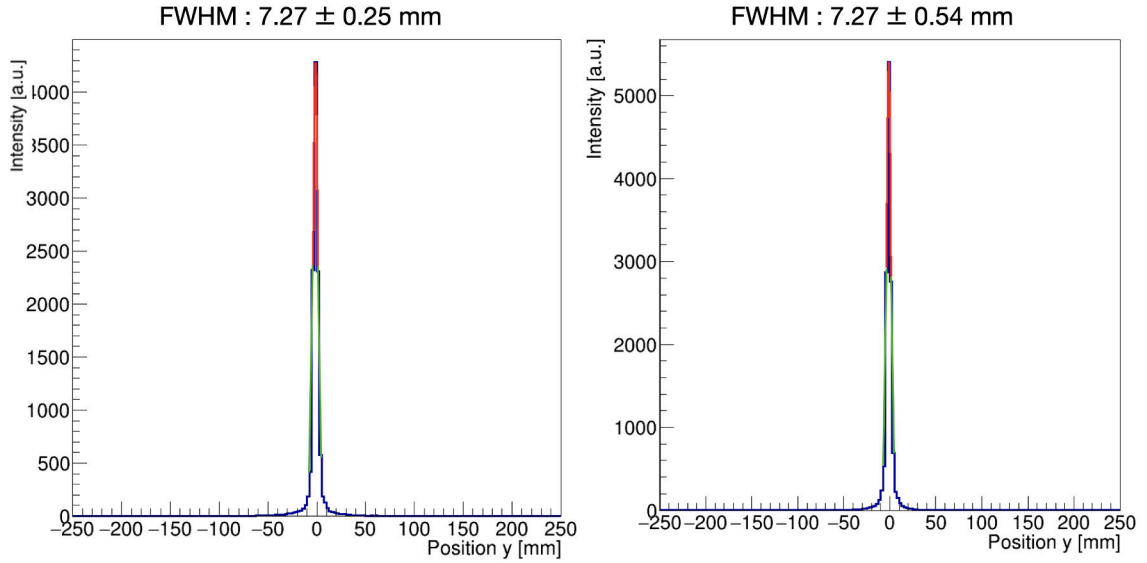
Rysunek 6.15: FWHM and its uncertainty estimation for distribution along y -axis performed at position (1,0,0), (left) for TOF reconstructed image, and (right) Non-TOF reconstructed image.

FWHM : 29.05 ± 0.54mm

FWHM : 34.75 ± 0.36 mm
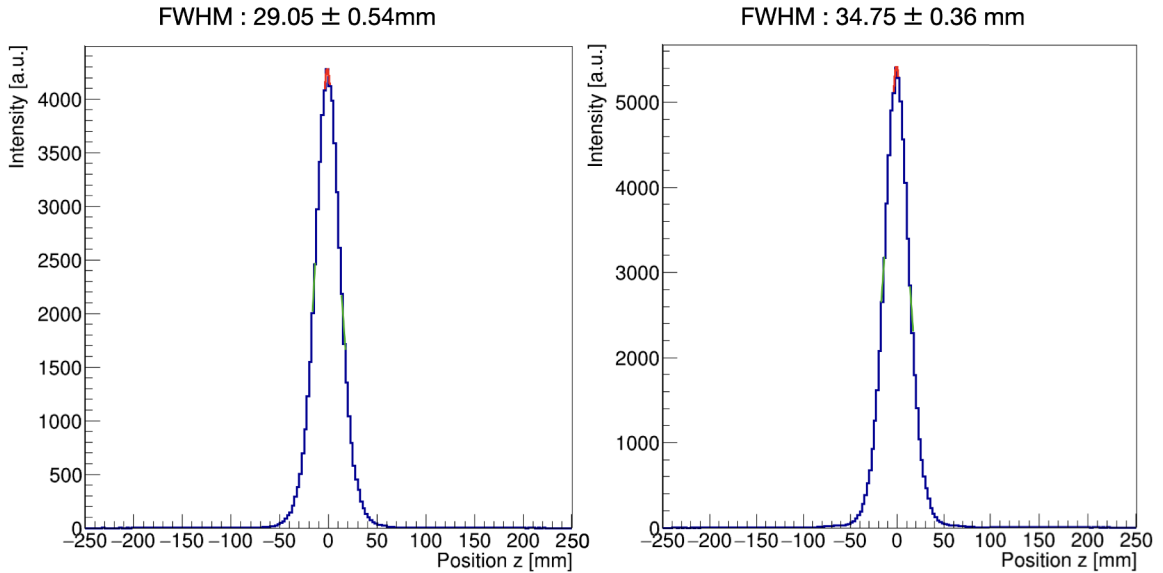
Rysunek 6.16: FWHM and its uncertainty estimation for distribution along z -axis performed at position (1,0,0), (left) for TOF reconstructed image, and (right) Non-TOF reconstructed image.

resolution, iterative process was performed for 10 iteration with 1 subset. The results of FWHM in three direction as function of iteration number are presented in Fig 6.17.

Source position (cm)		Radial FWHM (mm)	Tangential FWHM (mm)	AXial FWHM (mm)
(1,0,0)		4.80 ± 0.45	7.27 ± 0.25	29.05 ± 0.54
(10,0,0)		4.80 ± 0.54	7.27 ± 0.66	27.00 ± 0.89
(20,0,0)	TOF	6.08 ± 0.74	12.37 ± 0.82	29.50 ± 0.94
(1,0,18.75)		4.80 ± 0.12	7.27 ± 0.41	30.89 ± 0.44
(10,0,18.75)		9.73 ± 0.56	7.27 ± 0.39	34.06 ± 0.58
(20,0,18.75)		7.27 ± 0.11	17.83 ± 0.14	34.06 ± 0.13
(1,0,0)		4.81 ± 0.11	7.27 ± 0.54	34.75 ± 0.36
(10,0,0)		4.81 ± 0.14	7.27 ± 0.207	31.62 ± 0.611
(20,0,0)	Non-TOF	6.70 ± 0.09	12.75 ± 0.90	34.50 ± 0.94
(1,0,18.75)		4.81 ± 0.21	7.27 ± 0.94	35.00 ± 0.65
(10,0,18.75)		9.73 ± 0.19	7.27 ± 0.50	34.96 ± 0.218
(20,0,18.75)		7.38 ± 0.11	15.83 ± 0.16	34.75 ± 0.26

Tabela 6.4: FWHM values (in mm) for various positions: A comparison between TOF and Non-TOF image reconstruction methods for different positions. The radial FWHM represents values along the X-axis, the tangential FWHM represents values along the Y-axis, and the axial FWHM represents values along the Z-axis.

The spatial resolution in radial direction was calculated $4 \pm 0.1mm$, in tangential direction was calculated about $4.5 \pm 0.12mm$, and in the axial direction was calculated around $18.5 \pm 0.16mm$ for TOF reconstructed image.
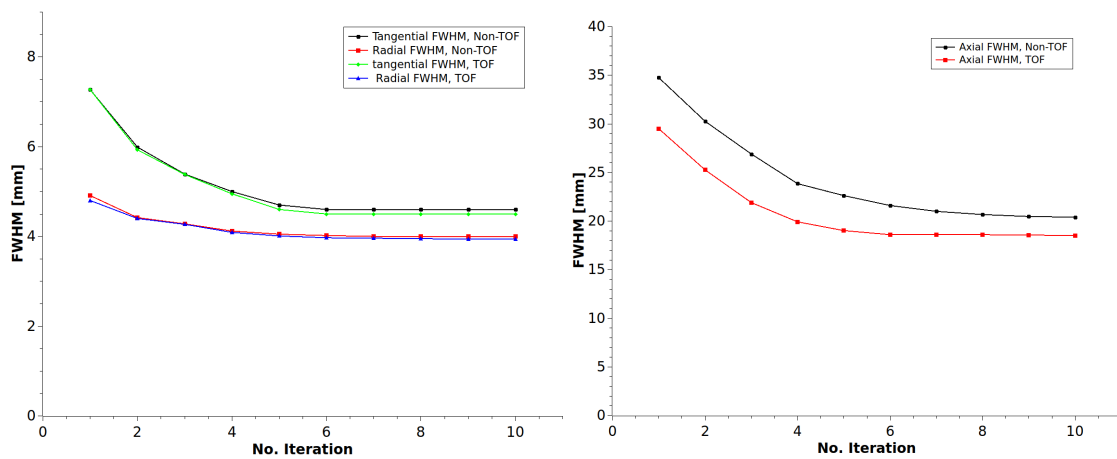
Rysunek 6.17: FWHM values as function of the iteration number for positions (1,0,0) in three directions. (left): radial and tangential FWHM with TOF and Non-TOF image reconstruction methods, (right): Axial FWHM with TOF and Non-TOF image reconstruction methods.

ROZDZIAŁ 7
MEASUREMENTS PERFORMED WITH MODULAR J-PET SCANNER AND DATA PRESELECTION

Measurements conducted in April 2023 followed the guidelines set forth by the NEMA standards. These measurements were executed using the Modular J-PET scanner, a detailed description of which can be found in Section 3.2. The temperature within the laboratory setting was consistently monitored through the utilization of a dedicated control station, illustrated in Figure 7.1. This control station enabled us to maintain a stable and controlled temperature environment, a crucial aspect of ensuring the consistency and validity of our results. It is important to note that for each measurement conducted during this assessment, a specific source was employed. Detailed information regarding the selection and characteristics of these sources is provided in the subsequent section.

Rysunek 7.1: Temperature control station in laboratory

7.1 Sources

Three different type of radioactive source were used in this study: sodium point like source (^{22}Na), Germanium line source (^{68}Ge) and Fluorine line source (^{18}F).

7.1.1 Point like source

The point source utilized for spatial resolution measurements was a Sodium-22 (^{22}Na) isotope [6, 106]. This ^{22}Na isotope was encapsulated within a stainless steel cylinder, characterized by an outer diameter of 4.76 mm and a height of 5.72 mm, as illustrated in Figure 7.2. Within the capsule, the active diameter was to be 3.18 mm.

On the calibration day, on September 15, 2020, the measured activity of the ^{22}Na source was documented as 18.5 MBq. Subsequently, during the course of measurements, the source's activity was 9.2860 MBq.

One of the primary advantages of using ^{22}Na is its relatively long half-life of 2.602 years. This extended half-life ensures a stable and long-lasting source of positron emissions, which is beneficial for conducting experiments and calibration over an extended period without needing frequent replacements [107]. ^{22}Na decays by positron emission. The energy spectrum of positrons emitted by ^{22}Na is very similar to that of Fluorine-18 (^{18}F), a commonly used radiotracer in clinical PET imaging. This similarity allows to study the performance of PET scanners and test new imaging techniques using ^{22}Na as a surrogate for ^{18}F [102].

7.1.2 Line source

Germanium 68

The line source was employed for sensitivity measurements was a Germanium-68 (^{68}Ge) source. This source was securely enclosed within a polyethylene tube, possessing a length of 700 mm and an outer diameter of 2.6 mm, as depicted in Figure 7.3. Both ends of the tube were hermetically sealed, ensuring the source's integrity and safety. The selection of the tube's diameter was based on compatibility with the inner diameter of apertures in the sensitivity phantom, while the tube's length adhered
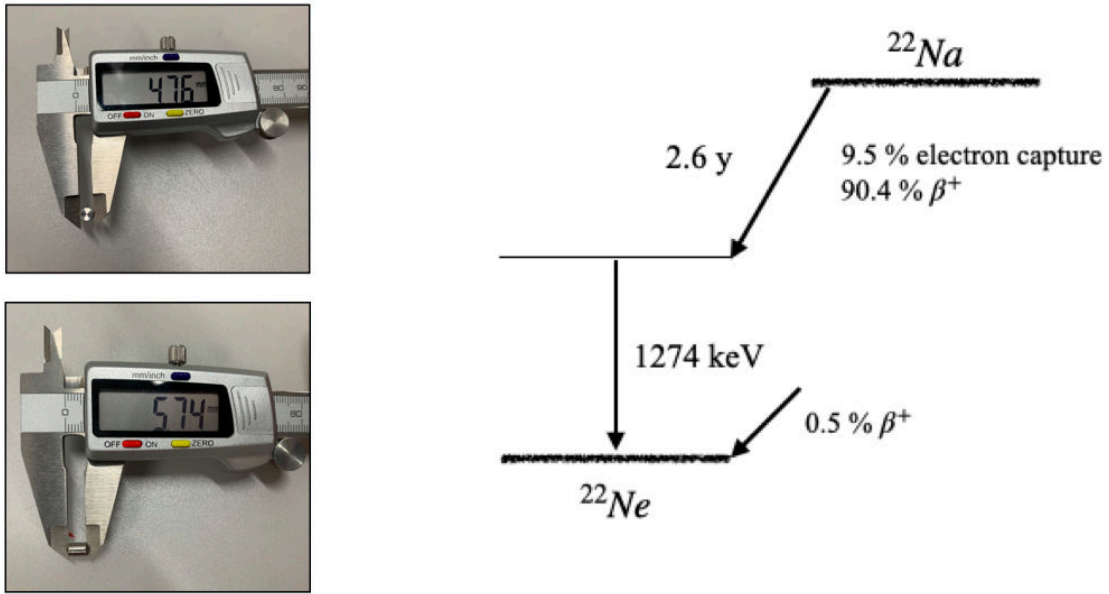
Rysunek 7.2: (Left): ^{22}Na Point source inside the stainless steel cylinder with outside diameter of 4.76 mm and 5.74 mm length, (Right) : Schematic of ^{22}Na decays. Figure adapted from [107].

to recommendations outlined in the NEMA standard. The radiopurity of this source exceeded 99.0 %.

The measured activity of the ^{68}Ge source on the calibration day, which was on September 28, 2022, was recorded as 4.436 MBq. Subsequently, during the course of measurements, the source's activity were exhibited variations within the range of 2.6106 MBq to 2.5803 MBq, as detailed in Table 7.1.

This ^{68}Ge source also played a pivotal role in system calibration. Its substantial half-life, extending over a period of 270.95 days, established it as a highly suitable choice for serving as a calibration source for routine quality control within the PET scanner, a key aspect highlighted in reference [108]. It is worth noting that ^{68}Ge undergoes radioactive decay, leading to the production of ^{68}Ga, which acts as its daughter isotope. ^{68}Ga, characterized by its significantly shorter half-life of 67.71 minutes, predominantly undergoes β^+ decay, forming the stable isotope Zinc-68 [108]. This radioactive decay process is visually depicted in Figure 7.4, underscoring the fundamental principles underlying the source's behavior and transformation within

the PET system calibration context.

However, it is essential to acknowledge that when compared to ^{18}F, this source presents certain limitations, such as a lower positron yield and a longer positron range within the tissue, owing to its higher mean energy [109, 110]. In contrast, ^{18}F boasts advantages, including its favorable half-life and efficient transportation between medical facilities and radiopharmaceutical production centers, rendering it the preferred choice for clinical routine applications [109, 110].
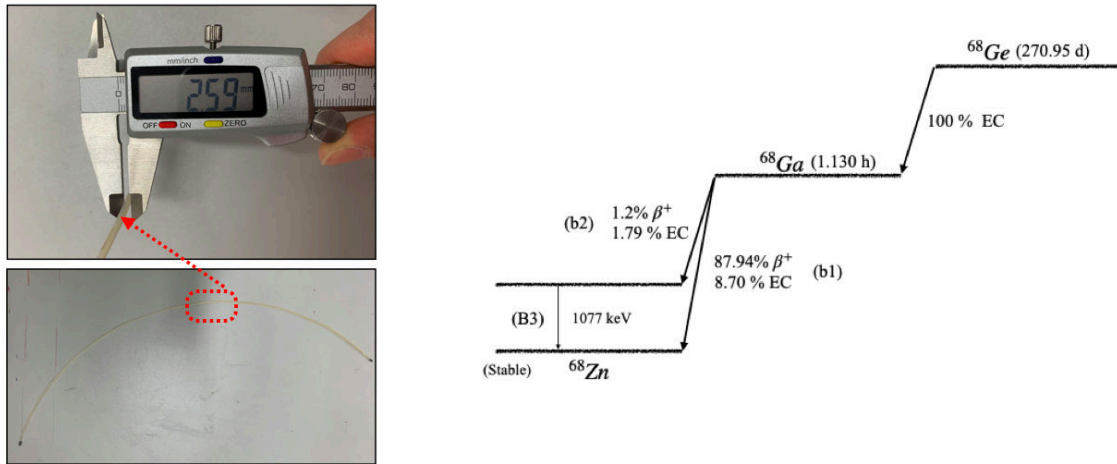
Rysunek 7.3: (Left): ^{68}Ge line source inside the polyethylene tube, 2.59 mm of the outside diameter of tube, (Right) schematic of ^{68}Ge decays. Figure adapted from [108].

Fluorine 18

In my research, I have harnessed the unique properties of Fluorine-18 (^{18}F) for scatter and NECR measurements[6, 111]. To prepare my solution, I mixed 6 ml of ^{18}F with 3 ml of water. 4.5 ml of this prepared solution was injected into a polyethylene tube measuring 700 mm in length and having an outer diameter of 4.2 mm while pushing the plunger in gently to avoid air bubbles. After sealing both ends of the tube, we agitated it to ensure a uniform distribution of the mixture, as depicted in Figure 7.4. The initial activity of ^{18}F was recorded as 350 MBq at 8:44 am on April 13, 2023, only a part of 350 MBq was finally used in line source. The initial activity after injected solution to line source was recorded 49.13 MBq at 11:44 am and at the start of our

measurements, it stood at 7.871 MBq

^{18}F (109.72 *min*)

ϵ (1.655 *MeV*)
3.14 %

β^+ (0.633 *MeV*)
96.86 %

^{18}O
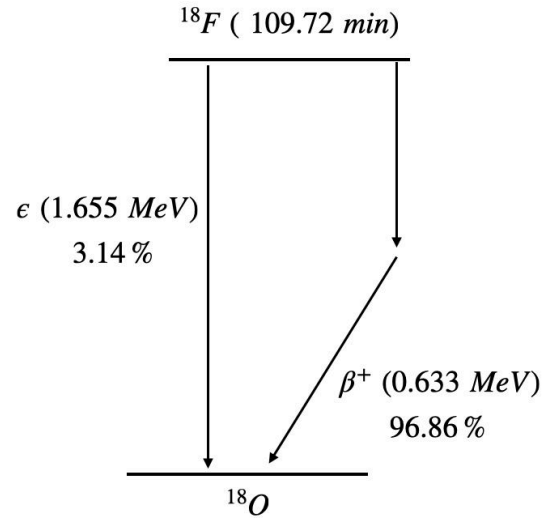
Rysunek 7.4: (Right): Display the 70 cm tube that uniformly filled with a water solution containing ^{18}F isotope with a well defined activity. (Left): Schematic decay of the ^{18}F. Figure adapted from [112].

7.2 Measurements performed with Modular J-PET

7.2.1 Spatial resolution measurement with Point like source

A point-like source containing 9.2 MBq of ^{22}Na was used to investigate the spatial resolution of the Modular J-PET scanner. The characteristics of this ^{22}Na point-like source have been extensively discussed in Section 7.1.1. This ^{22}Na point-like source, was meticulously positioned at the precise center of a plexi rod, which was constructed from Plexiglas material.The plexi rod itself had specific dimensions, measuring 62.23 *cm* in length and 30.20 *mm* in outer diameter, as visually represented in Figure 7.5. To facilitate the visual identification of the source's exact position within the rod, a prominent line was incorporated into its design. The secure placement of the Plexi rod within the scanner necessitated the use of aluminum supports. These supports were crafted with lengths of 25.5 cm, 46 cm, and 87 cm, and they were
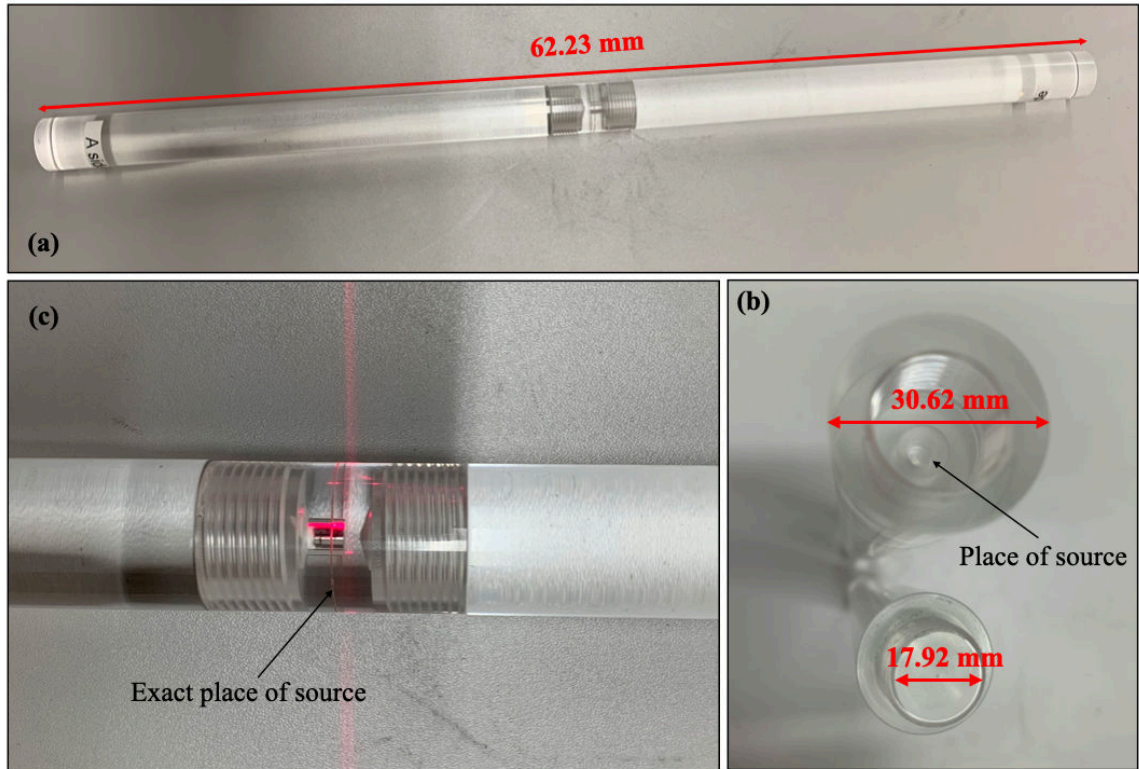
Rysunek 7.5: (a): The 62.23 mm length plexi rod for point source measurements in Modular J-PET detector spatial resolution experiment. (b) Cross- section of the middle of plexi rod with an outside diameter of 30.62 mm. Source is placed in the center of the plexi rod. (c): Place of the point like source in the plexi rod, the line in the plexi rod represented the exact place of source inside plexi rod.

positioned on both sides of the detector, as explicitly illustrated in Figure 7.6. Given the length of the Plexi rod, these aluminum supports were deliberately situated on the exterior of the detector's AFOV. This positioning was crucial to minimize the potential introduction of additional scattering artifacts during our data analysis. In strict accordance with NEMA standards, precise markings denoting specific positions were applied to the aluminum supports. Of particular significance was the designation of position (0,0,0). To validate the accuracy of both source and plexi rod positioning, an initial 5-minute test measurement was conducted at the position (0,0,0). Following this validation step, a series of 5-minute short test measurements were executed for each designated position. Subsequent to a thorough examination of the control histograms, a 1-hour measurement was conducted for each source position. Figure 7.7
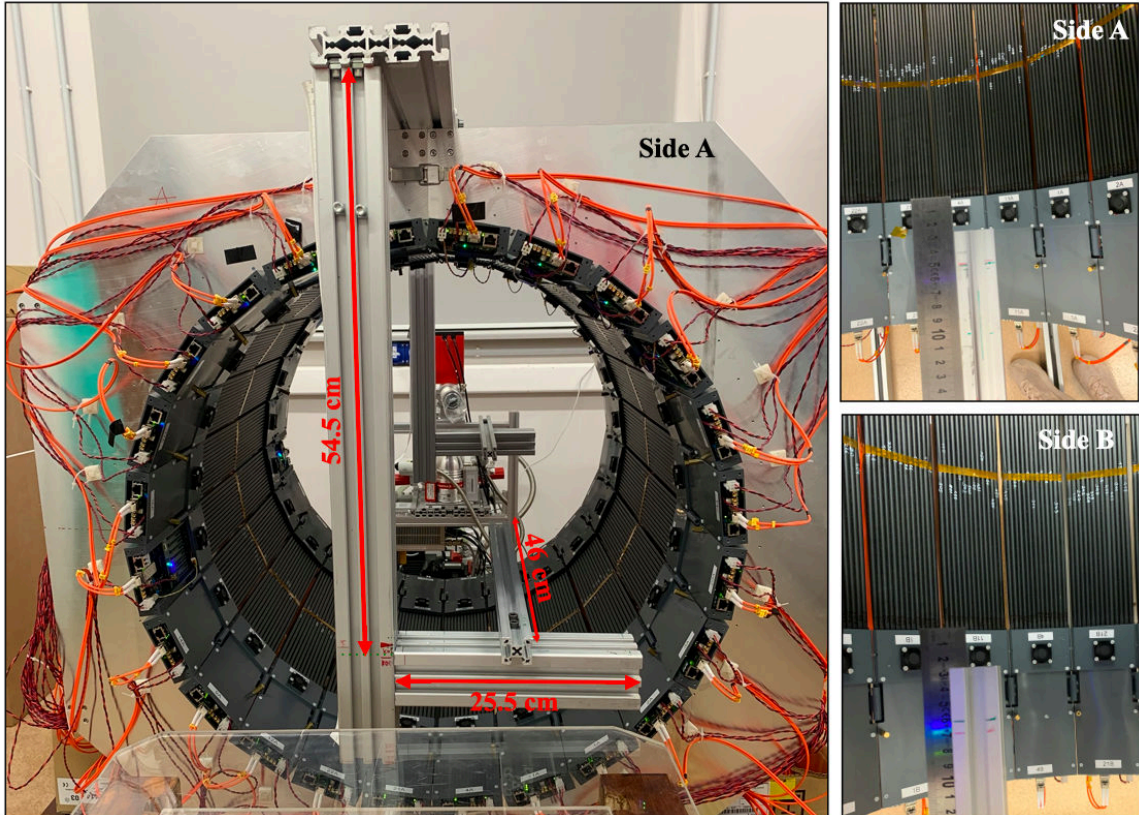
Rysunek 7.6: (left): Aluminum supports used to locate the plexi rod and sensitivity phantom inside the Modular J-PET scanner. (Right) Top view of the aluminum supports in both sides, showing that the aluminum supports are located outside of AFOV scanner at both sides.

represents the point like source inside plexi rod in the different position inside the Modular J-PET.

7.2.2 Sensitivity measurement with sensitivity phantom

To investigate the sensitivity of the Modular J-PET scanner, a 700 mm ^{68}Ge line source in conjunction with a PET sensitivity phantom was employed. The use of aluminum supports was instrumental in securing the phantom within the detector. These aluminum supports were strategically positioned on the exterior of the detector's AFOV to prevent any additional artifacts from affecting our analysis. The PET sensitivity phantom was positioned with a 10 cm offset from each side of the AFOV detector along the z-axis. It's important to note that the active part of the source was
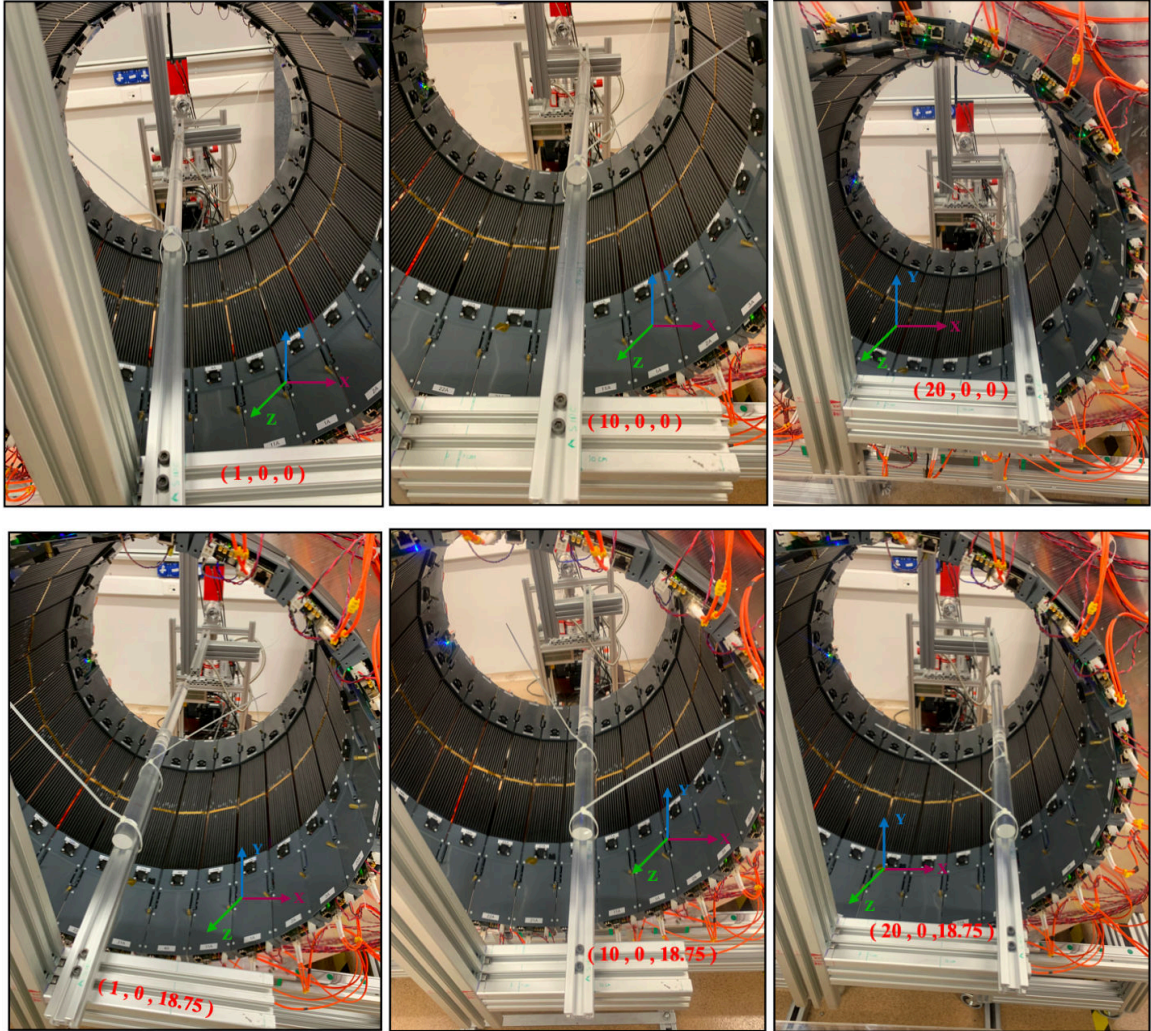
Rysunek 7.7: Six different positions inside the Modular J-PET scanner of sodium point like source placed in the plexi rod.

aligned to cover the active portion of the scintillators, specifically scattering effects as illustrated in Figure 7.8. Sensitivity measurements was adhered to the NEMA standard, which specifies that the measurement should start from the smallest tube and increase the thickness with each subsequent tube. This process was repeated until all sleeves had been utilized. Furthermore, in accordance with the NEMA norm, sensitivity measurements were conducted both at the center of the detector's AfOV and at a 10 cm offset from the center of the detector's AfOV. To facilitate this, specific positions were marked on the aluminum supports. These positions were designated
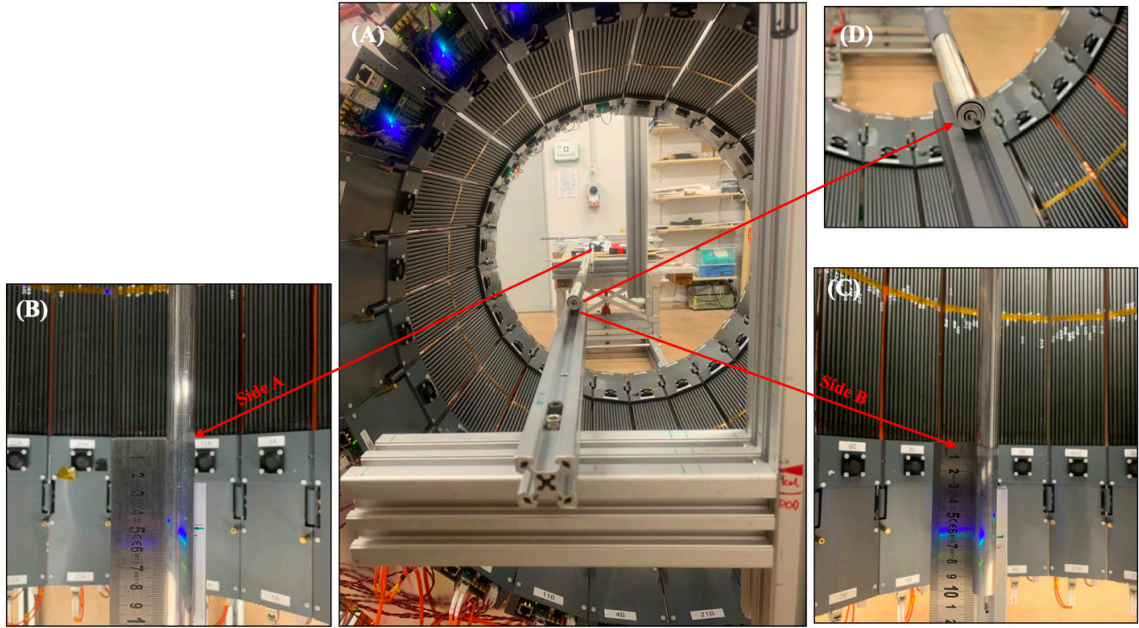
Rysunek 7.8: (A): Depicts the arrangement of the 5 sleeves of the sensitivity phantom inside the Modular J-PET, positioned at the center of the detector. (B) and (C) respectively illustrate Side A and Side B of the detector, showcasing the 10 cm extension of the sensitivity phantom beyond the AFOV. These images also highlight the strategic placement of aluminum supports on the exterior of the detector's axial field of view. (D): Provides a zoomed-in view of the sensitivity phantom, offering a detailed depiction of all the sleeves.

with coordinates (0,0) and (10,0) in the x and y dimensions, respectively, measured in centimeters, as demonstrated in Figure 7.9.

For quality assurance and precise positioning confirmation, I was conducting a 10-minute test measurement for each position and each tube of the sensitivity phantom. Following position confirmation, I was proceeding with the main sensitivity measurements, which spanned 6 hours for each tube and each position, totaling 10 comprehensive measurements.

7.2.3 Scatter fraction measurement with scatter phantom

To investigate the scatter fraction of the Modular J-PET scanner, I employed an ^{18}F source in conjunction with a PET scatter phantom and a dedicated bed with a width of 51.4 cm, as illustrated in Fig. 7.10. Prior to commencing the measurements,
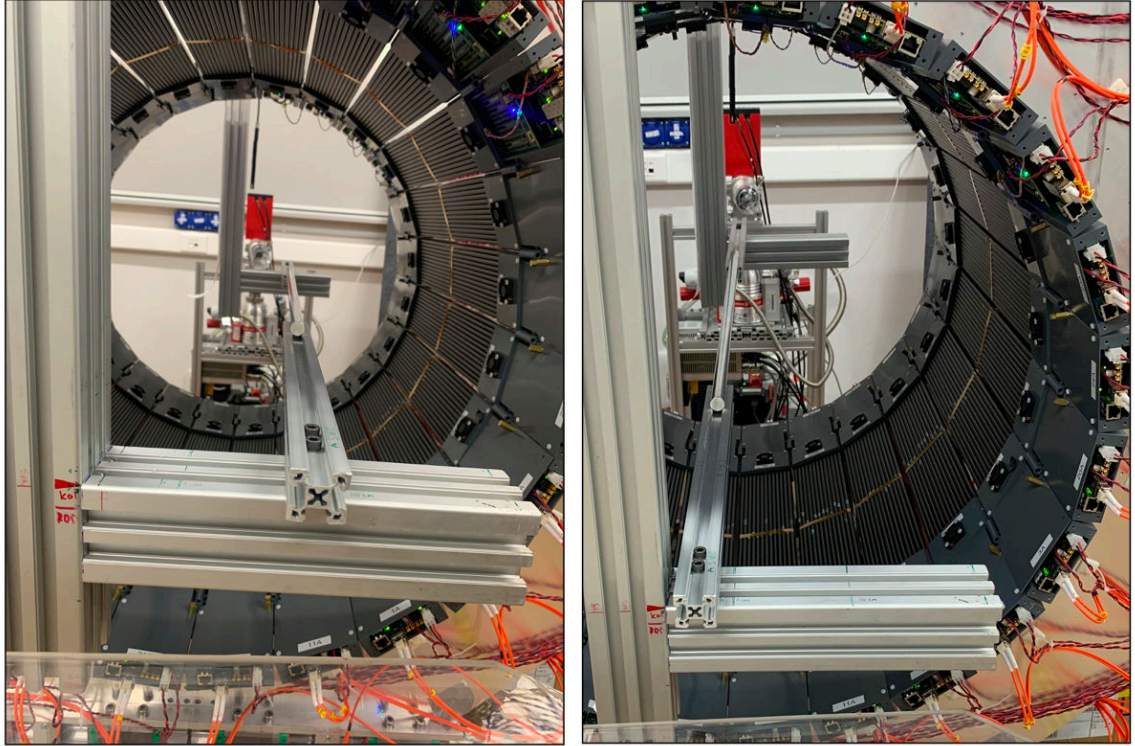
Rysunek 7.9: (Left): Depicts the arrangement of the 5 sleeves of the sensitivity phantom inside the Modular J-PET, positioned at the center of the detector. (Right): Displays the arrangement of the 5 sleeves of the sensitivity phantom inside the Modular J-PET, positioned at a 10 cm offset from the center.

three sections of the phantom were attached to each other. Subsequently, the scatter phantom was positioned at the center of the detector using guide lines drawn on the phantom. A specially constructed thread was affixed precisely along the y-axis, originating from one side of the detector and extending to both the top and bottom centers of the detector. The phantom was then carefully positioned on a dedicated bed, aligning its long axis with the z-axis of the J-PET scanner. To prevent any unintended movement of the scatter phantom on the bed, additional supports were employed, as depicted in Fig. 7.10.

After preparing the ^{18}F solution, as described in Section 7.1.2, we inserted the uniform 80 cm ^{18}F line source into the designated location. Given that the length of the PET Scatter Phantom is 70 cm, the ^{18}F uniform line source was positioned within the phantom in such a way that it covered the active region of the detector. Notably,
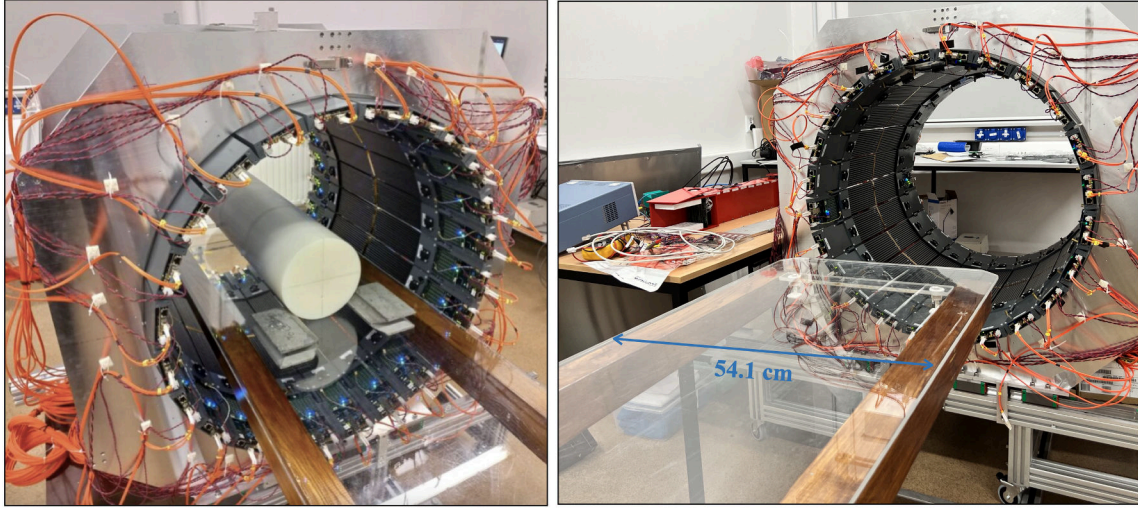
Rysunek 7.10: (Right): Depicts the experimental setup for scatter fraction measurement. the bed including the plexi and wooden. (left): Displays the PET scatter phantom placed on the dedicated bed.

the length of the line source exceeded that of the phantom, resulting in a portion of the line source extending beyond the AFOV of the scanner (See Figure 7.11). Upon the source activity decreasing to 7.871 MBq, I was initiated the measurement
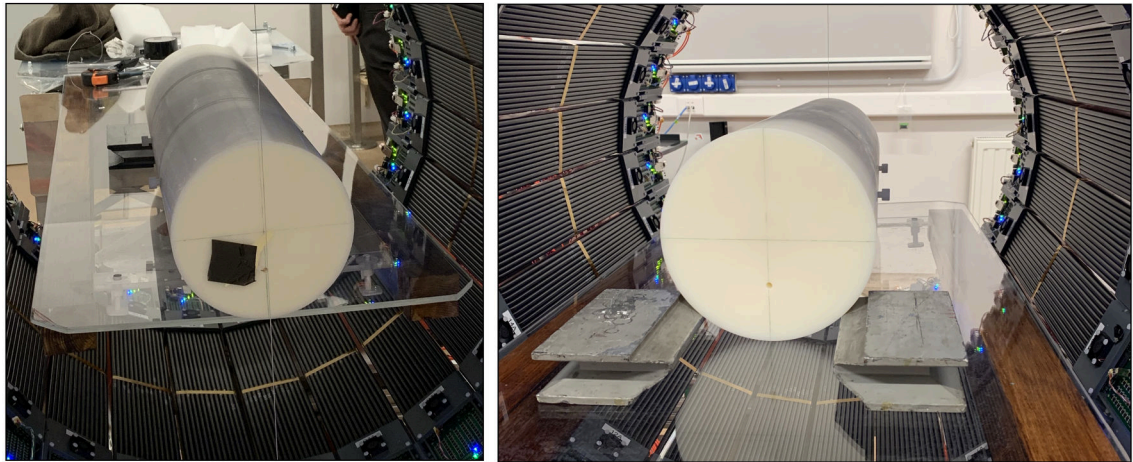
Rysunek 7.11: (Left): Visible in this image is a taut thread running along the y-axis. The line on the phantom's edge conceals the positions of these threads. Additionally, the remainder of the line source is depicted as extending beyond the phantom's boundaries. (Right): This image showcases the phantom supported on both sides.

process. Subsequently, following the generation and verification of control histograms, including position profiles along the x and y-axes, as well as along the y and z-axes, I continued the measurements for a duration 3 hours.

7.3   Data selection criteria

The J-PET Framework software serves as a comprehensive toolset for developing reconstruction and calibration procedures essential for J-PET tomography [89]. It enables the recovery of complete events from the trigger-less data acquisition system. Consequently, one of the fundamental challenges faced by the analysis software lies in the accurate selection of data. In response to this challenge, a set of criteria has been devised to facilitate the judicious selection of data, taking into account temporal, geometrical, and energy deposition attributes of the recorded photons. This data selection process is primarily based on measurements obtained from point-like sources.

Point-like source measurements were conducted over a duration of 3 hours in the center of the detector. These measurements are elaborated upon in detail in Section 7.2. This data selection procedure, driven by specific criteria, is instrumental in reconstructions within the context of J-PET tomography. Main advantage of choosing a point like source measurements is used a ^{22}Na radionuclide as a positron source.

7.3.1   The criteria based on coincidence time window

The initial stage of the data selection process is based on a coincidence time window that aimed at eliminating scattered events from the analysis. The determination of this coincidence time window primarily depends on the dimensions of the detectors and should include all possible situations. In the worst situation, two gammas within the same coincidence event are registered in the opposite detection modules inside the Modular J-PET detector, resulting in the maximum length difference along the LOR. The distance separating these two gamma-ray interactions, as calculated using the Pythagorean theorem, is approximately 89.28 cm.

As a consequence, the time difference between the detection of these two gamma-

ray interactions represents the longest possible time and is defined as follows:

$$\Delta x = c \ \times \ \Delta t \tag{7.1}$$

Where Δx stand for a distance from the reconstructed positions of hits, c stand for the speed of light in vacuum ($c = 29.98 \ cm/ns$), and Δt stand for a time difference between two hits. For the Modular J-PET detector, characterized by a 50 cm AFOV and a 73.97 cm diameter, the calculated time difference stands at approximately 2.97 ns. To account for a comprehensive range of coincidence event, a conservative approach is employed, wherein a 4 ns coincidence time window is adopted. This 4 ns window, although exceeding the theoretically derived value, serves as an overestimation to encompass all potential situations. Figure 7.12 provides a schematic representation illustrating the detection of two hits by opposite detection modules within the detector, further underscoring the rationale behind the choice of the 4 ns coincidence time window.
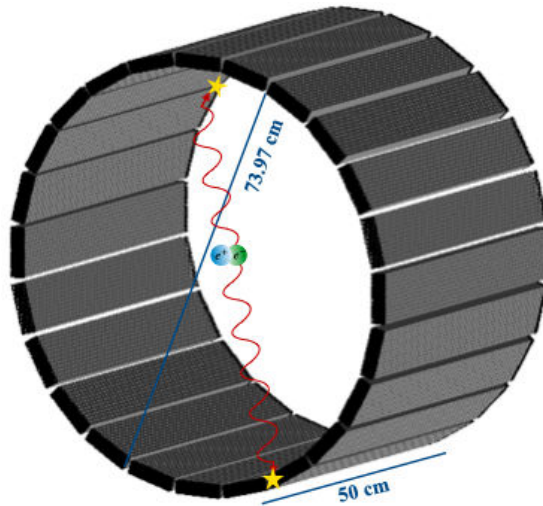
Rysunek 7.12: Schematic representation of two hits detected by two scintillator in the opposite detection modules. Point of interactions are denoted as yellow stars.

7.3.2 The criteria based on number of hits

The second stage of the selection process aims to further refine the dataset by filtering out potential scatterings that may have met the previous conditions. Specifically, it involves the exclusion of events with one, three, or more hits, while retaining events that exhibit precisely two hits within the defined coincidence time window. The impact of this selection criterion on the dataset is visually depicted in Figures 7.13 and 7.14. Under this criterion, events characterized by two hits constitute only a fraction of the total number of hits within the 4 ns coincidence time window, approximately amounting to 9.65%. This number was achieved from the ^{22}Na source measurements were conducted over a duration of 3 hours in the center of the detector.
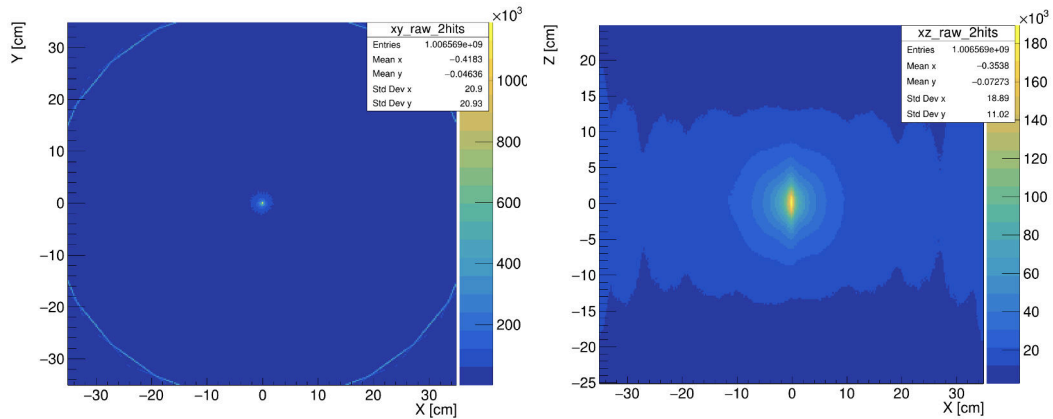
Rysunek 7.13: Control histogram of annihilation point after two hits selection criterion in 4 ns coincidence time window: (Left) XY position of annihilation point and, (Right) XZ position of annihilation point. It is important to note that this is from the a point like ^{22}Na source measerment, which is elongated along Z due to worse resolution of hit coordinate determination at this axis.
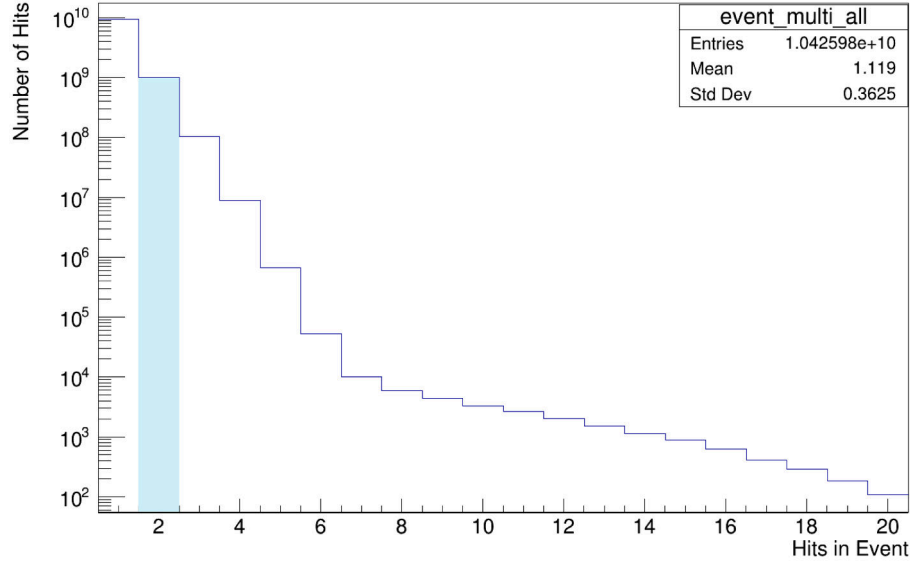
Rysunek 7.14: The distribution of the multiplicity of the hits in event in 4 ns coincidence time window in logarithmic scale. In this case, only the events with two hits were taken into account.

7.3.3 The criteria based on number of SiPM signals.

The subsequent stage of data selection focuses on the number of SiPMs connected to both ends of each detector module. For this reasons, a multiplicity criterion is introduced, which entails monitoring the number of SiPM signals. In the ideal case 8 SiPM signals is expected. So, for the majority of scintillators, this multiplicity cut is set at 8. However, for scintillator ID 284, a multiplicity of 5 is applied, while for scintillator IDs 208, 213, 225, 280, 342, 353, 365, and 458, a multiplicity cut of 7 is employed. The impact of this multiplicity criterion on the data-set is elucidated in Figure 7.15.

7.3.4 The criteria based on the geometry

To enhance the data sample purity concerning annihilation events, an approach involving the implementation of additional selection criteria based on the geometry of the recorded hits was employed. To optimize the Modular J-PET detector's performance in detecting annihilation events, it became imperative to establish specific selection

94
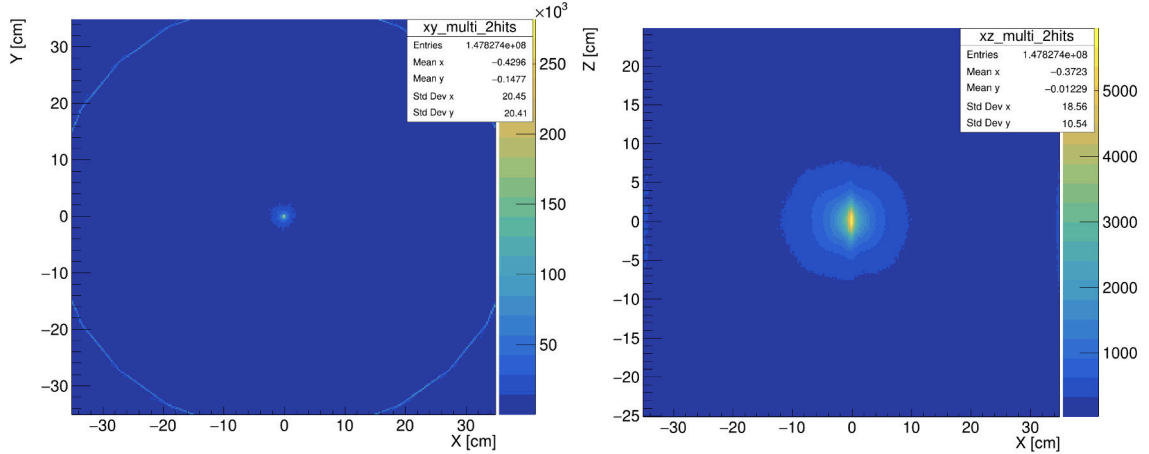
Rysunek 7.15: Control histogram of annihilation point after two hits and multiplicity selection criterion in 4 ns coincidence time window: (Left) XY position of annihilation point and, (Right) XZ position of annihilation point. It is important to note that this is from the a point like ^{22}Na source measerment, which is elongated along Z due to worse resolution of hit coordinate determination at this axis.

criteria focusing on the interaction's position within the scintillator strip.

In particular, it was determined that the z-coordinate of the annihilation position should be confined within a range of ±25 cm. This range aligns with the scintillators' active region. Any annihilation point with a z-coordinate exceeding 25 cm was subsequently excluded from the analysis. This schematic representation of the selection criterion is depicted in Figure 7.16, illustrating the region of interest within which annihilation events are considered for further analysis. In the context of the Modular J-PET detector, imaging analysis is limited to the x and y planes, delineated by a circular region with a 60 cm diameter, as depicted in Figure 7.17. To achieve precise annihilation point reconstruction in J-PET imaging, a stringent criterion is employed. It involves the inclusion of events in which the distance between the Line-of-Response (LOR) connecting hits and the geometric center of the detector is less than 30 cm.

This criterion effectively screens out annihilation points that are excessively distant from the center of the detector, as illustrated in Figure 6.18. As a consequence of implementing this selection process, the number of events that meet the criteria decreases from $1.00 \times 10^9 counts$ to $4.41 \times 10^7 counts$ of the total number of two-hit events. However, this reduction in the number of events is accompanied by a sub-
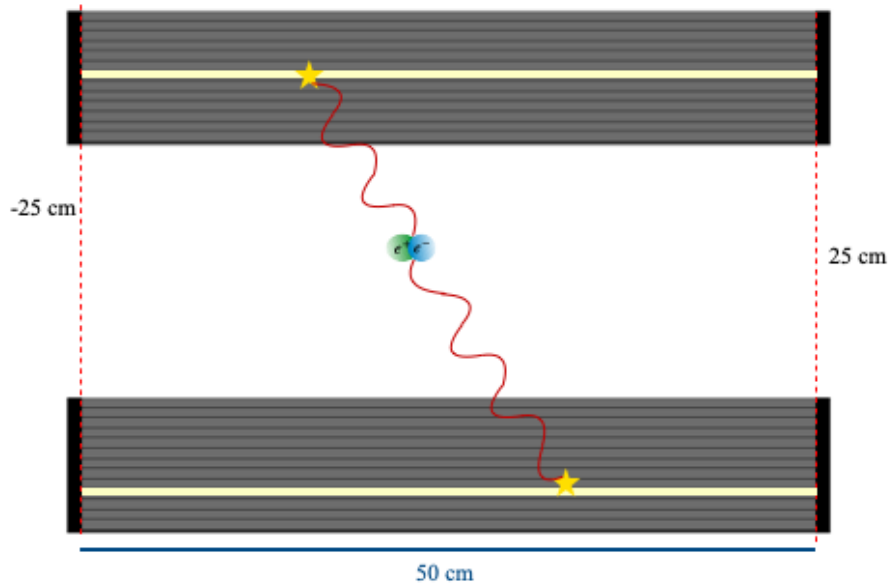
Rysunek 7.16: Schematic representation of two opposing modules within the Modular J-PET detector, registering gamma quanta originating from an annihilation point. Only annihilation points falling within the range of (-25, 25) cm along the z-axis are considered and accepted for further analysis.

stantial decrease in background noise, a pivotal consideration in the context of any imaging technique.
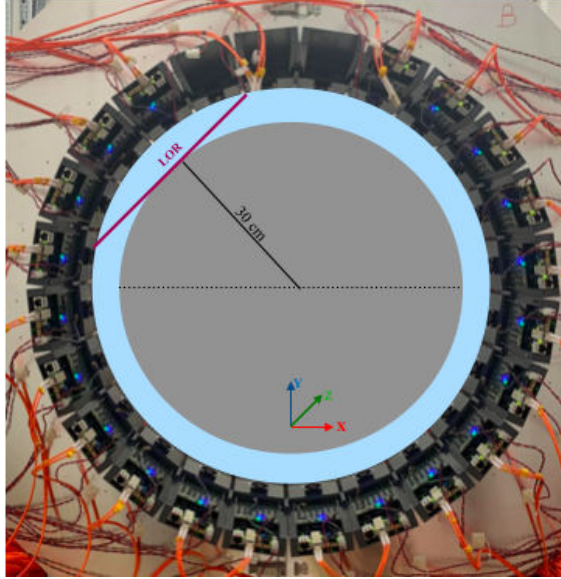
Rysunek 7.17: Example of the reconstructed event. The transverse filed of view (blue circle) is limited by 60 cm diameter circle (gray circle). The reconstructed events are represented by the purple line (LOR).
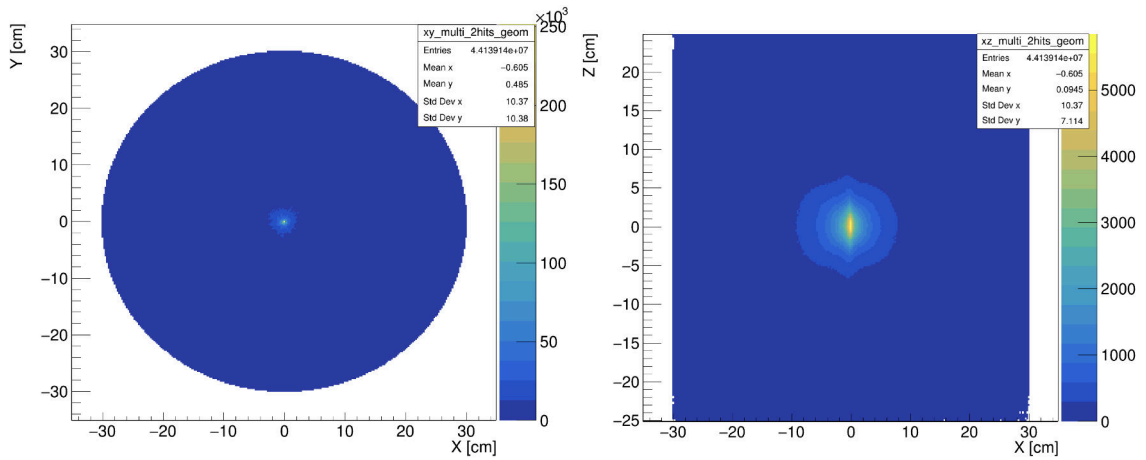
Rysunek 7.18: Control histogram of annihilation point after applying geometry cuts to pre-selection criteria in 4 ns coincidence time window: (Left) XY position of annihilation point. (Right) XZ position of annihilation point. It is important to note that this is from the a point like ^{22}Na source measerment, which is elongated along Z due to worse resolution of hit coordinate determination at this axis.

7.3.5 The criteria based on the scatter test

Additional scattering events that managed to persist through the preceding stages of the analysis are regarded as candidates for annihilation events. To further refine the data set and exclude these additional scattering events, a scatter test (ST) is employed. The scatter test quantifies the probability of a secondary photon traveling in a direct path between interactions i and j, as computed the following figure:

$$\delta_{i,j} = d_{i,j} - c \times \Delta t_{i,j}, \qquad (7.2)$$

where $d_{i,j}$ represents the spatial separation between recorded interactions, while the constant c signifies the speed of light. Additionally, $\Delta t_{i,j}$ denotes the difference in the recorded times of these interactions. Specifically, within the Modular J-PET framework, the term $\Delta t_{i,j}$ corresponds to the calculation of the time of flight (TOF) of a photon. The probability that the two recorded hits originate from the same photon increases as the ST function approaches zero.
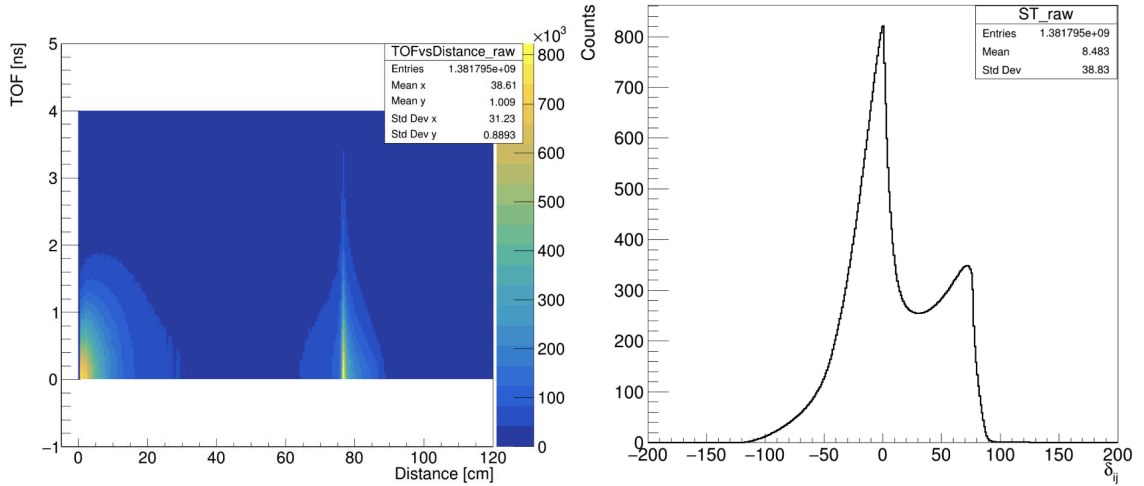
Rysunek 7.19: (Left): Two-dimensional histogram depicting the spatial separation as a function of Time of Flight (TOF) for all events, (Right): Illustrates $\delta_{i,j} = d_{i,j} - c \times \Delta t_{i,j}$. Secondary scattering interactions are identifiable by small $\delta_{i,j}$ values and are subsequently excluded from consideration. Interactions with $\delta_{i,j}$ more than 40 cm are designated as primary photon candidates.

Hence, it is essential that the spatial separation between interactions closely aligns with the expected TOF of a photon. As shown in Figure 7.19(a), spatial separation is depicted as a function of TOF, while Figure 7.19(b) displays the distribution of $\delta_{i,j}$ across all events and all combinations of two interactions within each event. Here, it is noteworthy that the structure at large $\delta_{i,j}$ values originates from pairs of primary annihilation photons (recorded with spatial separation but close in time), whereas the peak at $\delta_{i,j} \approx 0$ results from recorded secondary scattered photons.

In case of recorded interaction pairs with $\delta_{i,j}$ less than the 40 cm in Fig 7.19 (b), the later of two interactions is identified as a secondary scattering and removed from the event. Consequently, only event candidates featuring exactly two retained interactions, as per the aforementioned selection, are utilized for constructing Line-of-Response (LOR) information for subsequent image reconstruction. Figure 7.20(a) provides insight into the spatial separation as a function of TOF after applying the $\delta_{i,j} > 40\ cm$ criterion, and Figure 7.20(b) illustrates the distribution of $\delta_{i,j}$ across all events after applying the $\delta_{i,j} > 40\ cm$ criterion.
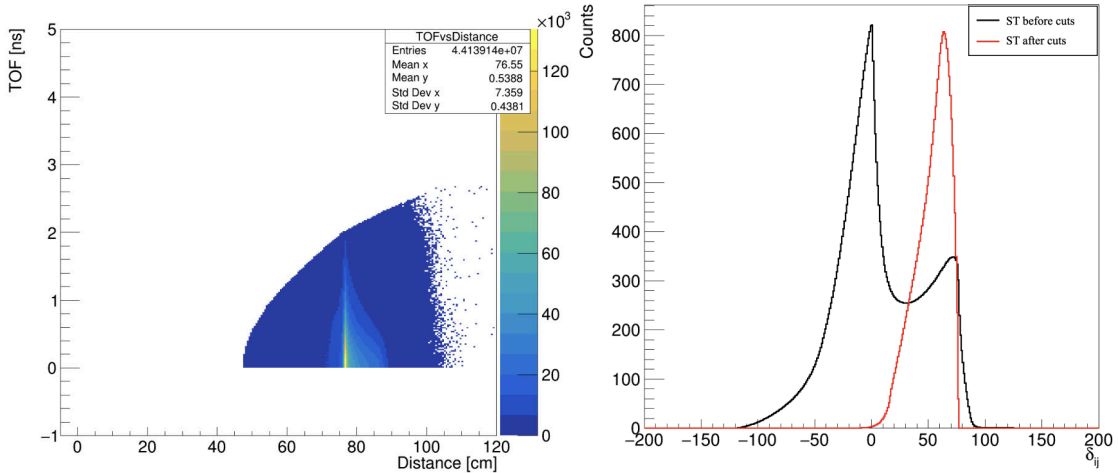
Rysunek 7.20: (Left): Two-dimensional histogram depicting the spatial separation as a function of Time of Flight (TOF) after adding $\delta_{i,j} > 40cm$, (Right): Illustrates comparison of the $\delta_{i,j} = d_{i,j} - c.\Delta t_{i,j}$ for all events and after adding $\delta_{i,j} > 40cm$. Only events with two primary photon interactions remaining after the selection are used to construct LOR-s for image reconstruction.

The impact of these criteria on the annihilation point is depicted in Figure 7.21. The ST function remains pivotal in differentiating genuine annihilation events from

additional scattering occurrences, thereby enhancing the quality of the reconstructed images.
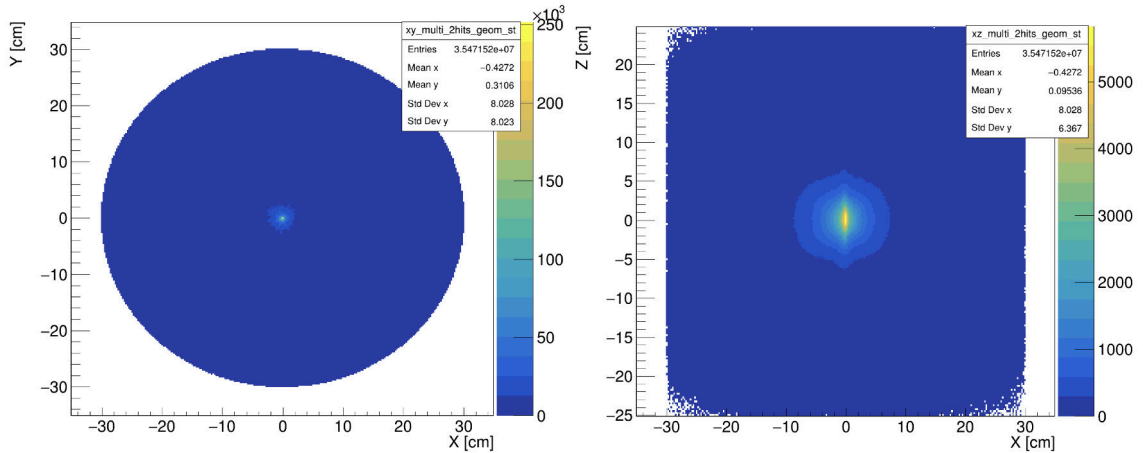
Rysunek 7.21: Control histogram of annihilation point after appliyng scatter test cuts to pre-selection criteria in 4 ns coincidence time window: (Left) XY position of annihilation point and, (Right) XZ position of annihilation point. It is important to note that this is from the a point like ^{22}Na source measerment, which is elongated along Z due to worse resolution of hit coordinate determination at this axis.

7.3.6 The criteria based on the times over threshold

After the initial selection criteria, the final stage of data refinement involves an assessment of the origin of the hit distribution. Within the framework of the J-PET detector, this assessment is conducted through an analysis of Time Over Threshold (TOT) information [113] (refer to section 3.5).

To perform TOT-based selection the data from measurement with the PET Sensitivity Phantom with 5 sleeves in position (0,0) cm was chosen. The main advantage of this type of measurement is the fact that all the scintillators along their entire length are sensitive to incoming photons at the same time. Histogram of TOT depends on scintillator ID and summary histogram of all the TOT values for all scintillators are presented in Figure 7.22. Histogram of TOT for an exemplary scintillator after selection criterion for two hits in event can be found in Figure. 7.23, bin width on TOT histogram is equal to $40\ ns \times mV$. Histogram of TOT were analyzed for all scintillator of the Modular J-PET detector. The histogram plotting TOT against scintillator

100
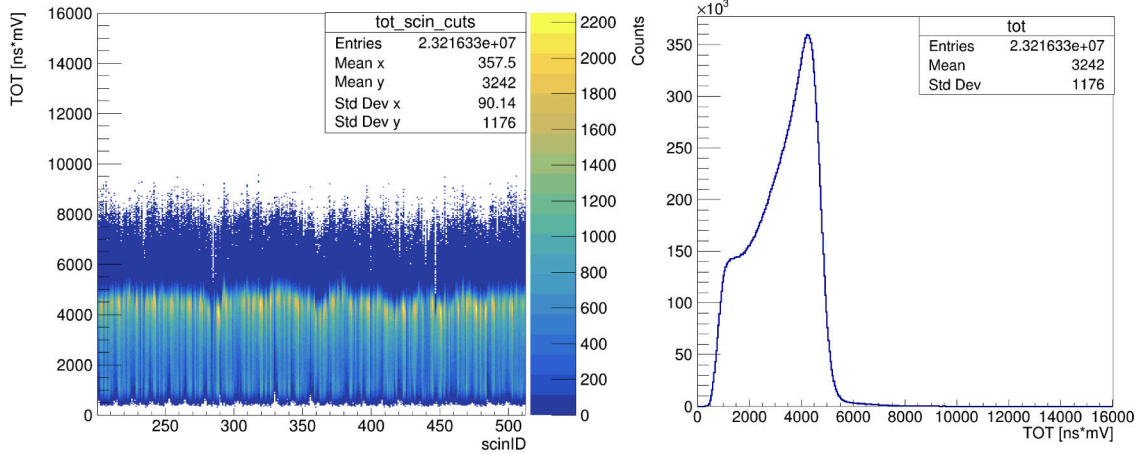
Rysunek 7.22: (Left): The TOT spectra depict individual results for each scintillator strip, identified by their respective scintillator IDs, starting from 200. These spectra are displayed prior to normalization. (Right): The sum histogram of TOT values is derived from the y-projection of the left plot, encompassing all scintillators.
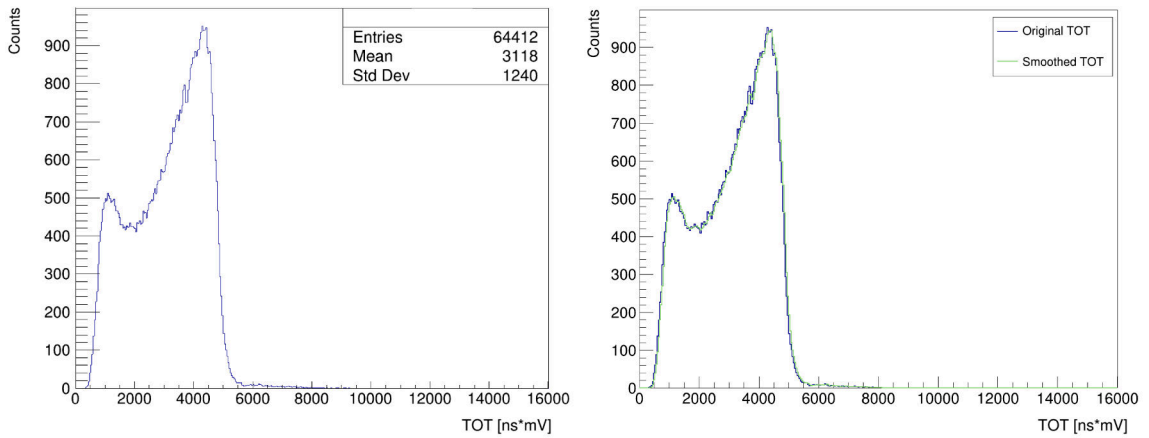
Rysunek 7.23: (Left) : The histogram of TOT values for the scintillator ID =208. (Right): The histogram of TOT values for the scintillator ID =208 before and after smoothed with the Moving Average method. Bin width in each histogram is equal to $40 \ ns \times mV$.

ID presents an initial TOT plot, requiring subsequent TOT calibration. The TOT calibration process is primarily focused on normalizing the TOT measurements for each SiPM. Therefore the Compton edge position estimation was performed. In the context of TOT calibration, each histogram underwent a reevaluation, and the data were smoothed using a Moving Average (MA) technique. The utilization of MA

holds significance in enhancing data quality and facilitating a more visually coherent representation of the histograms. To implement MA, we calculated the average count value for each bin within the histogram using the following formula:

$$counts_i = \frac{1}{3} \times \sum_{j=i-1}^{i+1} counts_j \qquad (7.3)$$

where, $counts_i$ denotes the average count value for the i-th bin. It is derived by summing the counts ($counts_j$) of the current bin along with those of the two adjacent bins, namely the previous and the next bins. This sum is then divided by 3. This iterative approach was systematically applied, bin by bin, commencing from the third bin onwards. The uncertainty associated with the moving average was determined using the principles of error propagation.

In the subsequent step, the first derivative of the TOT distribution was computed for each of the smoothed histograms. The outcomes, exemplified by an exemplary histogram, are illustrated in Figure 7.24. The minimum point on the first derivative curve corresponds to the inflection point of the histogram. Within a range encompassing 10% around this minimum, a parabolic fit was applied. This fitting process facilitated the estimation of the Compton edge position value. The Compton edge positions for all scintillators are graphically presented in Figure 7.25.

To normalize the data, the midpoint of the Compton edge position values, which is equal to $4801 ns \cdot mV$, was determined as the reference. Consequently, the Compton edge position values computed from the first derivative were divided by this reference value of $4801 ns \cdot mV$. These results were adopted as the correction coefficients for all histograms. In the next step, these correction coefficients were applied to the data and effect of the results is presented in Fig 7.26. The Compton edge positions for all scintillators are visually presented in Fig 7.27.

In the subsequent stage of data analysis, an investigation was conducted to determine if there existed any discernible dependence between the TOT and the position of interaction of gamma quanta along the scintillators. To explore this possibility, each scintillator was divided into 25 segments within the range of -25 cm to +25 cm,

χ² / ndf	0.1408 / 8
Prob	1
p0	1.336e+04 ± 3.820e+03
p1	−5.634 ± 1.599
p2	0.0005907 ± 0.0001672
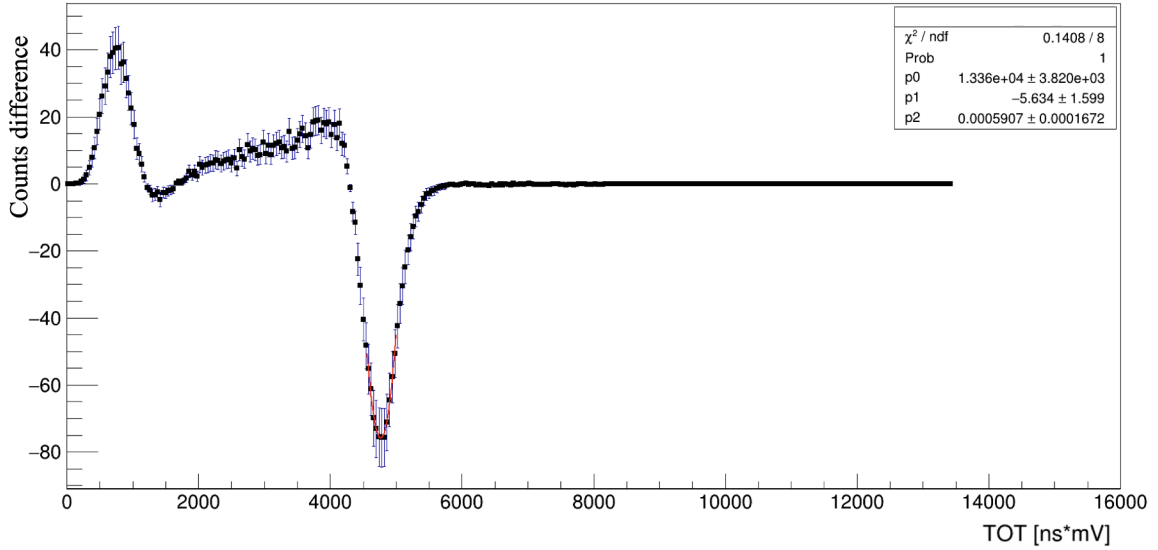
Rysunek 7.24: The first derivative of the smoothed histogram was obtained, and the associated error bars were calculated by summing the uncertainties of two consecutive points derived from the smoothed histogram.
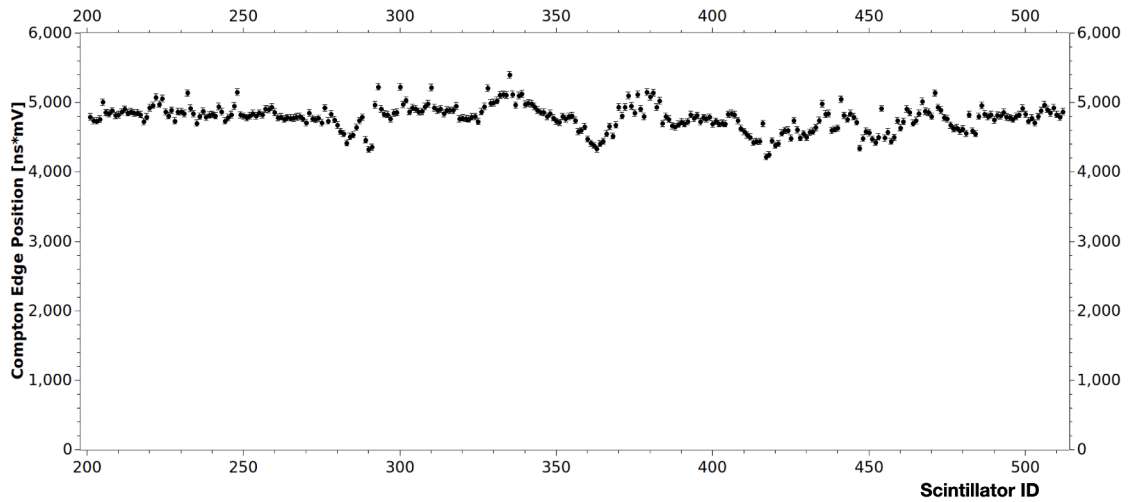
Rysunek 7.25: The Compton edge position values for all scintillators within the Modular J-PET detector.

with intervals of 2 cm between each point, as illustrated in Figure 7.28. histogram of TOT as function of the position of interaction of gamma quanta along the scintillators displayed in the Fig 7.29. Then, a dedicated histogram was generated for each interaction point from the dataset. Figure 7.30 showcases an exemplary histogram of
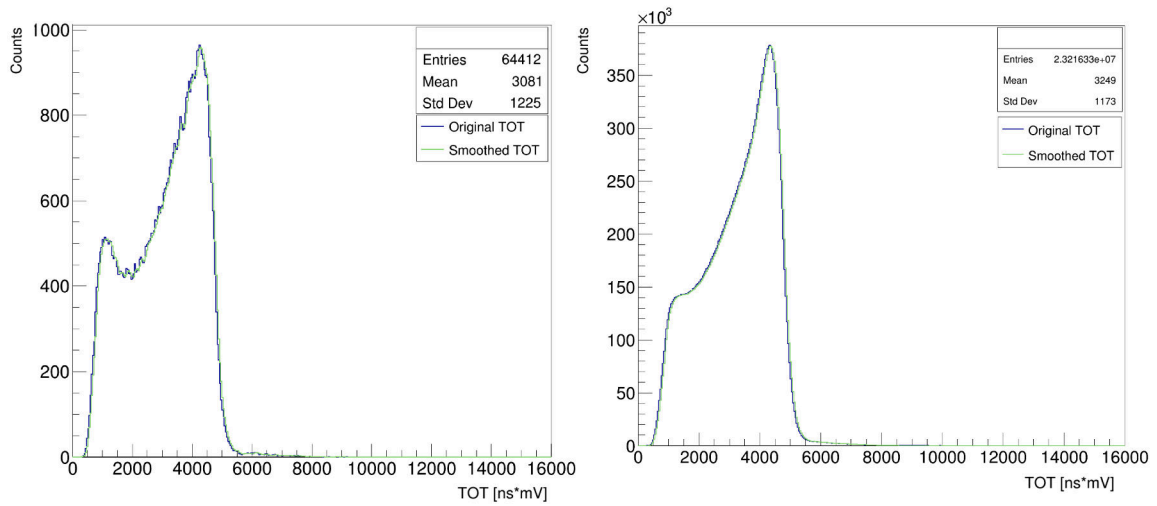
Rysunek 7.26: (Left): The histogram of TOT values for the scintillator ID =208 after correction. (Right): The sum histogram of TOT values is derived from the y-projection of the left plot, encompassing all scintillators after correction.
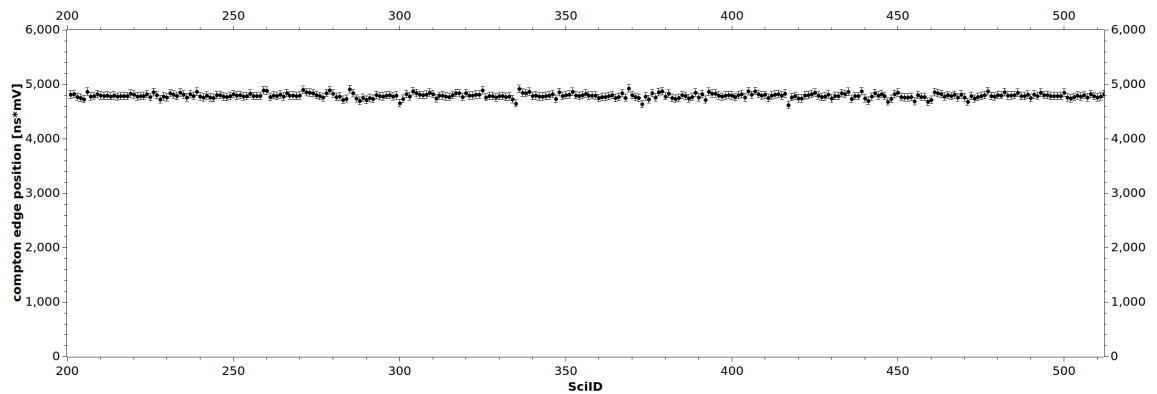
Rysunek 7.27: The Compton edge position values for all scintillators within the Modular J-PET detector after correction.

TOT for one particular position of interaction (center of the scintillator with ID=13), along with the derivative of the smoothed histogram obtained through the moving average technique.

Figure 7.31 illustrating the Compton edge position for all interaction points along the scintillators. Notably, there is no discernible dependence of the TOT on the position of interaction of gamma quanta along the z-axis of a scintillator. The fitted line remains essentially flat. Consequently, there is no need to incorporate a dependence
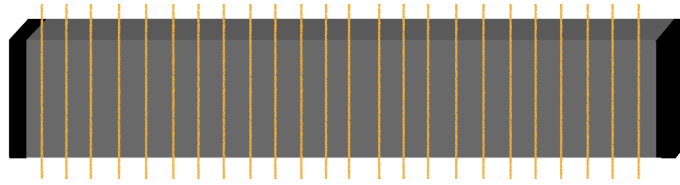
Rysunek 7.28: The scintillator was divided into 25 segments, with each segment spanning 2 cm. Please note that the figure provided is not to scale.
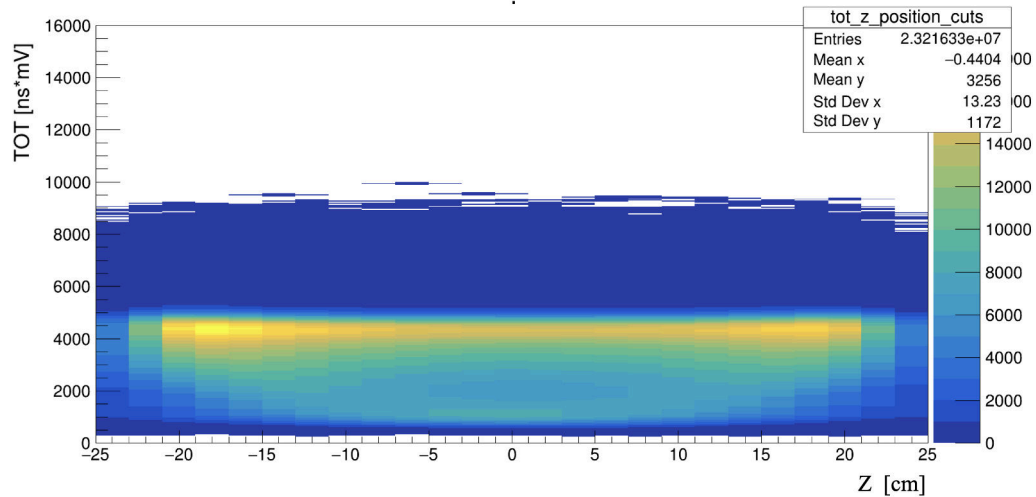
Rysunek 7.29: The TOT spectra depict individual results for each interaction points of gamma quanta along scintillators.
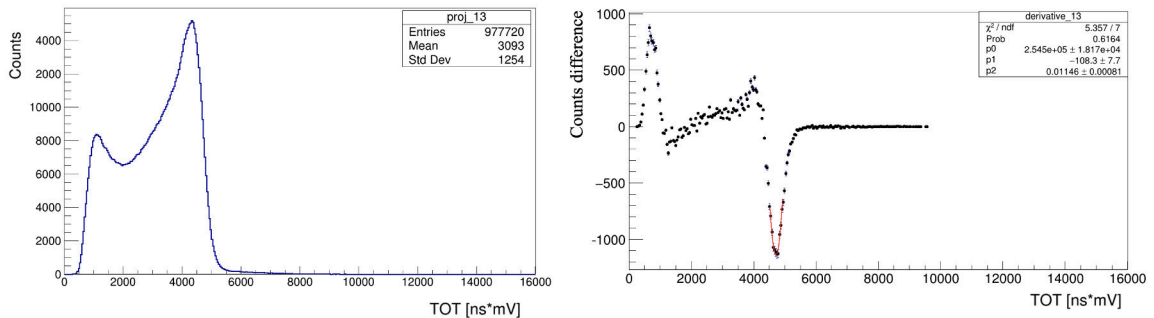
Rysunek 7.30: (Left): A histogram depicting all TOT values for positions at 0 cm (center of the scintillator). (Right): The first derivative of the aforementioned histogram. The minimum of this first derivative can be accurately characterized by a parabolic fit, enabling precise determination of the minimum point.

between TOT and interaction point into the data analysis. Consequently, a TOT range spanning from $2824ns \cdot mV$ to $4801ns \cdot mV$ will be applied for future analyses. The implementation of a lower limit of $2824ns \cdot mV$ for TOT values serves to diminish the
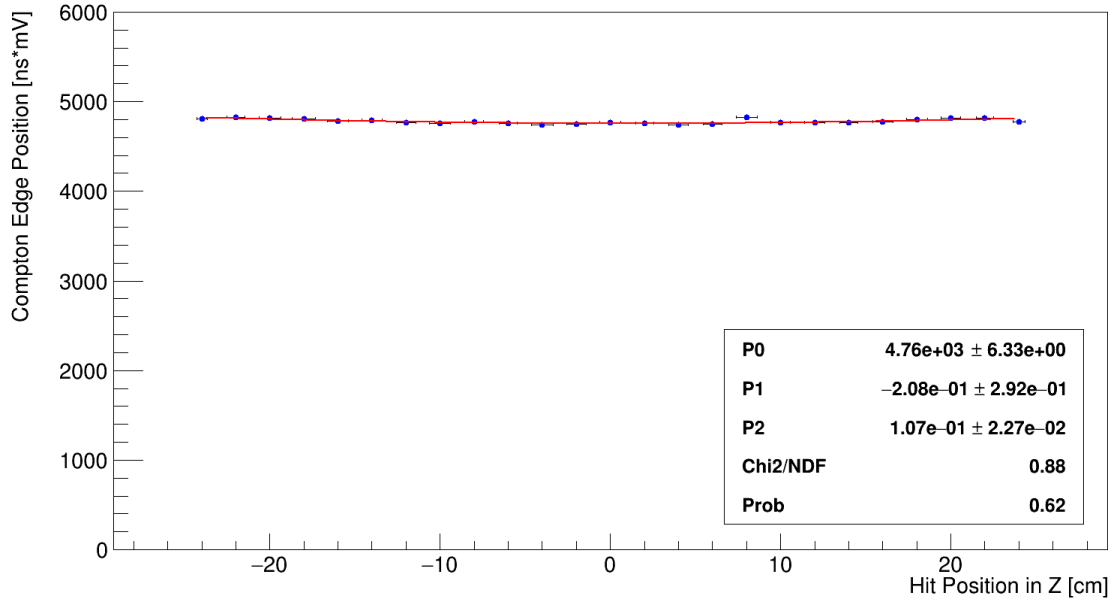
Rysunek 7.31: The values of Compton edges position have been determined for all the scintillators at 25 points of interaction along the z-axis. A quadratic function has been fitted.

influence of hits originating from secondary photon scatterings within the strips of the Modular J-PET detector. Conversely, the imposition of an upper limit of $4801 ns \cdot mV$ for TOT values mitigates the impact of deexcitation photons on the TOT spectrum. The impact of applying this TOT range is visually illustrated in Figure 7.32, which showcases the removal of all improperly categorized events from the background of the image.

The TOT normalization method, as previously described, serves as the initial data selection criterion at the hit level. Its primary purpose is to eliminate background noise and reduce the data size. The subsequent data selection criteria are applied at the event level. Following this preliminary preselection process, the dataset earmarked for further analysis is significantly reduced, constituting approximately 0.42% of the original volume of the raw data. List of all event selection criteria are listed in table 7.1 with the number of counts after each selection.
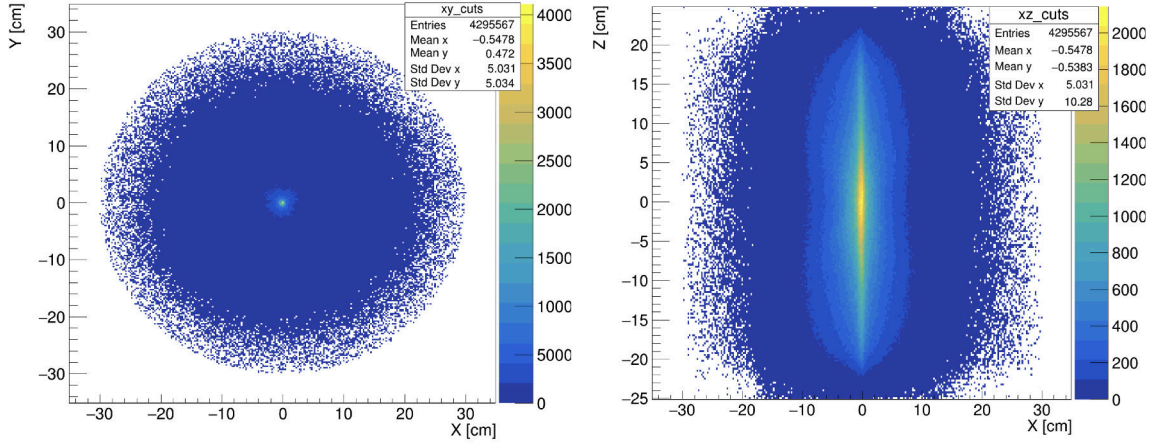
Rysunek 7.32: Control histogram of annihilation point after appliyng TOT rang to pre-selection criteria in 4 ns coincidence time window: (Left) XY position of annihilation point and, (Right) XZ position of annihilation point.

Tabela 7.1: List of all event selection criteria and percentage of the total counts after each selection from the raw data survived. The results are counted from the ^{22}Na source measurement in the center of detector's AFOV.

Type of selection	Number of counts	Percentage of the total number of raw data survived
2hits in 4 ns time window	1006569000	100%
Multiplicity + 2hits in 4 ns	147827400	14.68%
Multiplicity + 2hits in 4 ns + Geometry	44139140	4.38%
Multiplicity + 2hits in 4 ns +Scatter test + Geometry	35471520	3.52%
Multiplicity + 2hits in 4 ns + TOT + Scatter test + Geometry	4295567	0.42%

ROZDZIAŁ 8

EVALUATING PERFORMANCE CHARACTERISTICS OF THE MODULAR

J-PET BASED ON EXPERIMENTAL MEASUREMENTS

The results of the measurements described in Section 7.2 are presented herein. Each step of the analysis is founded upon the principles outlined in Chapter 4 and is elaborated upon comprehensively. Prior to commencing the analysis of each segment, preselection conditions, as stipulated in Section 7.3, were meticulously applied to the dataset.

8.1 Sensitivity

In accordance with Chapter 4, the sensitivity estimation procedure exclusively seeks true coincidence events. The application of preselection methods was instrumental in minimizing superfluous background interference. Subsequently, the assessment proceeded to ascertain compliance with the NEMA standard conditions for sensitivity measurement.

While the recommended radionuclide for sensitivity measurement is typically ^{18}F, In the case of the Modular J-PET is employed a ^{68}Ge source. The NEMA standard mandates that during sensitivity measurement, at least one of the two following conditions must be satisfied:

- The percentage of dead time losses is less than 5 %.

- The random coincidence rate is less than 5 % of the total event rate.

Both conditions stipulated by the NEMA standard for sensitivity measurement were examined for Modular J-PET. The following subsection provides a comprehensive explanation of these assessments.

8.1.1 Dead time losses

Dead time is defined as the minimum time interval between two consecutive counts, which must occur for them to be recorded as distinct events within a detector. When the dead time of the detector is known, it becomes possible to deduce the true counting rate based on the measured value [114] . In the context of a paralyzable dead time, the relationship between the actual counting rates and the measured counting rates is as follows:

$$M = Ne^{-NT}, \tag{8.1}$$

where, N represents the real counting rate, M stands for the measured counting rate and T denotes the dead time within the detector. This formula has been derived with consideration for an initially Poissonian process in the context of radioactive decay. To calculate the percentage of dead time losses using this formula, the initial step involves determining the number of counts per module (N_{module}). To achieve this, we need to ascertain the number of counts per scintillator in each module (N_{sci}^K), as illustrated in Figure 8.1. [115].

$$N_{module} = \sum_{k=1}^{13} N_{sci}^k. \tag{8.2}$$

Given that the distance between the source and each scintillator within the module varies, we must first calculate N_{sci}^K for each scintillator using the following formula:

$$N_{sci}^K = \frac{\Omega}{4\Pi} \times n \times P, \tag{8.3}$$

where, Ω represents the solid angle, n denotes the number of emitted particles and P represents the probability of interaction in plastics scintillator for 511keV, which has been empirically ascertained to be 0.2 [100]. The determination of the solid angle Ω can be readily computed using the following equation:

$$\Omega = 4arctan\frac{\alpha\beta}{2d\sqrt{4d^2 + \alpha^2 + \beta^2}}, \tag{8.4}$$
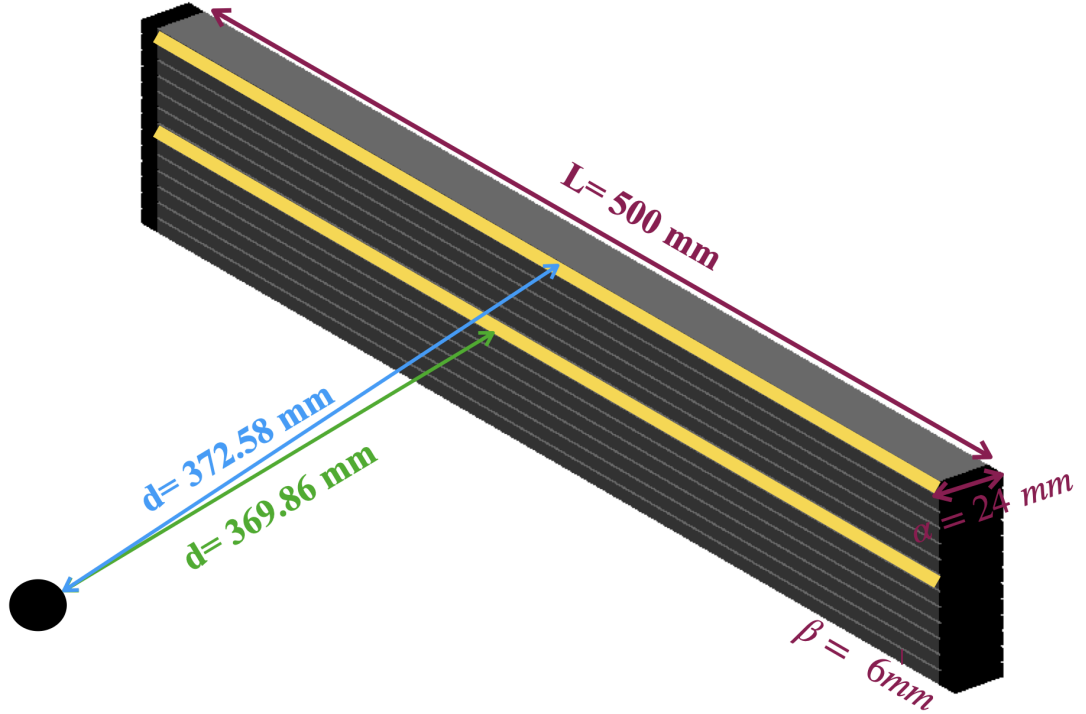
Rysunek 8.1: Schematic depiction of the relative spatial Configuration of scintillators within the module, and the radioactive source employed in the sensitivity measurements. The assumption is made that the activity is localized within a point source positioned at the center of the detector. The figure is not drawn to scale.

where, α represents the dimension of the scintillator, with a value of $\alpha = 24$ mm, β signifies another dimension of the scintillator, measuring $\beta = 6$ mm, and d represents the distance between the source and the scintillator surface, as illustrated in Figure 8.1, with a range value of $d = 369.86$mm to $d = 372.58$mm.

For an activity of 2.6 MBq utilized in the sensitivity measurement, the resultant values for Ω, N_{sci}^K, and N_{module} are 0.0181, 751/s, and 9763/s, respectively. It is noteworthy that the dead time of the readout, combined with the rapid signals emanating from the scintillators within the Modular J-PET system, is on the order of 20 ns [116]. Consequently, the count losses per module attributable to the dead time of the Module J-PET system remain around 1%, thus satisfying the first condition as stipulated.

8.1.2 Random coincidence rate

To determine the number of random coincidences, it assumed that we have two rectangular pulses, each with durations τ_1 and τ_2, which are statistically distributed according to Poisson statistics with average frequencies n_1 and n_2 [117]. In this context, the parameter n represents the average number of real coincidences occurring per unit of time. Therefore, the quantities $(n_1 - n)$ and $(n_2 - n)$ represent the number of pulses in the respective channels, after subtracting the number of real coincidences. The time interval during which random coincidences may occur is then given by $(n_1 - n)\tau_1$ and $(n_2 - n)\tau_2$ for the first and second channels, respectively. The calculation of the random coincidences rate involves multiplying these time intervals by the number of pulses in the second channel:

$$n_{random} = (n_1 - n)\tau_1(n_2 - n) + (n_2 - n)\tau_2(n_1 - n) = (n_2 - n)(n_1 - n)(\tau_1 + \tau_2). \quad (8.5)$$

Considering that the count rates in both channels significantly exceed the coincidence rates (i.e., $n_1 \gg n$ and $n_2 \gg n$). Additionally, if the pulse duration are identical in both channels ($\tau_1 = \tau_2 = \tau$), the random coincidences rate can be expressed as:

$$n_{random} = n_2 \, n_1 \, (\tau_1 + \tau_2) = 2 \, n_2 \, n_1 \, \tau. \quad (8.6)$$

In the case of sensitivity measurements with a time window size of 4 ns (equal to τ) and where $n_1 = n_2 = N_{module} = 9763/s$, the obtained rate of random coincidences is equal:

$$n_{random} = 0.7625293/s. \quad (8.7)$$

This indicates that the rate of random coincidences is less than 1% of the total event rate in the case of the sensitivity measurement.

8.1.3 Estimation of Modular J-PET sensitivity

A ^{68}Ge radioactive isotope in the form of a line source was employed for measurements with the PET sensitivity phantom, replacing the conventional ^{18}F radionuclide [118].

The active length of this source measures 70 cm. The source's activity was determined based on the known half-life of ^{68}Ge and the initial activity value measured by the manufacturer on September 28, 2022. Measurements utilizing the PET sensitivity phantom were conducted between April 20, 2023, and April 25, 2023. During this time frame, the initial activity of the utilized source experienced a change, decreasing from 2610.6 kBq to 2580.3 kBq. For sensitivity measurement purposes, the corrected initial activity for the actual source length (which should be calculated using Eq. 3.2) remains equal to the initial activity. Each measurement was conducted over a duration of 6 hours, with a slight variation of a few minutes. The change in activity during each measurement amounted to 0.0017 MBq, which can be considered negligible. As such, it can be assumed that the average activity at the start and end times of each measurement is denoted as A_{cal}.

However, it's important to note that the source's activity within the detector needs to be normalized because of the different length of AFOV detector and line source length. The activity of the used source during the measurement period is thus determined as follows:

$$A_{normalized} = A_{cal} \frac{50 \ cm}{70 \ cm}.$$ (8.8)

Table 8.1 represented value of corrected initial activity and normalized activity in positions (0,0,0) and (10,0,0) [cm] for all 5 sleeves separately. As evident from the table, the normalized activity of ^{68}Ge exhibits a reduction by a factor of 0.71.

The activity employed for subsequent analysis is derived from the normalized activity.

The subsequent criterion outlined in the NEMA standard stipulates the necessity of collecting a minimum of 10,000 true coincidences per imaging slice. Nonetheless, the unique geometry of the Modular J-PET detector enables the clear determination of annihilation positions and gamma quanta interactions with scintillators, rendering the practice of single-slice rebinning unnecessary. For subsequent analysis, this categorization into slices is carried out based on the annihilation position, aligning with the approach employed in [117, 1] and a 'slice' is defined as a region with a uniform

Tabela 8.1: Corrected initial activity and normalized activity for various positions(cm) within the detector with different sleeve number, and measurement duration.

Measerment	Corrected Iinitial activity (kBq)	Normalized activity (kBq)	Measurement duration (s)
5 sleeves in position (0,0,0)	2610.6	1864.71	21664
4 sleeves in position (0,0,0)	2606.9	1862.07	21208
3 sleeves in position (0,0,0)	2604.6	1860.42	21418
2 sleeves in position (0,0,0)	2599.7	1856.92	21270
1 sleeve in position (0,0,0)	2597.3	1855.21	20225
1 sleeve in position (10,0,0)	2590.5	1850.35	21015
2 sleeves in position (10,0,0)	2588.8	1849.14	21120
3 sleeves in position (10,0,0)	2586.5	1847.49	21021
4 sleeves in position (10,0,0)	2580.3	1843.07	21404
5 sleeves in position (10,0,0)	2584.4	1845.99	20037

size of 2 cm. It is worth noting that gamma quanta can interact with the entire active length of a scintillator, as depicted in Figure 8.2. In this classification (3D mode),
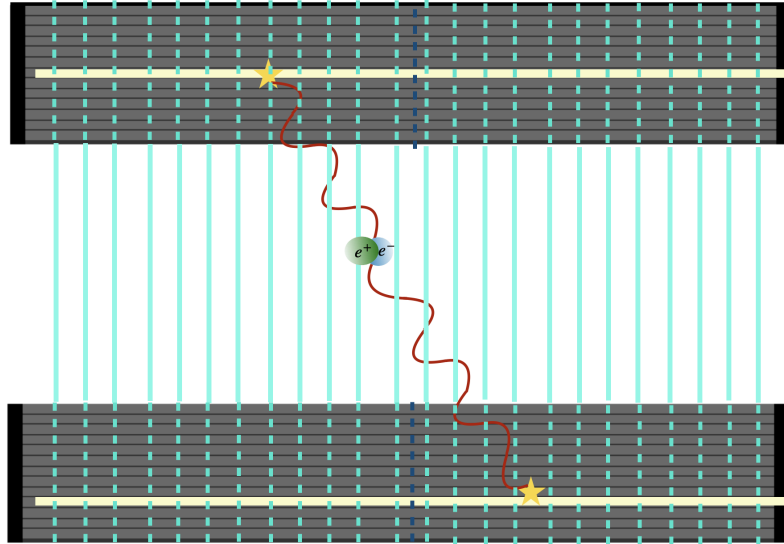
Rysunek 8.2: Illustration depicting two deployment modules oriented in opposite directions, with the space between them divided into slices of 2 cm width. The central slice is demarcated by the scintillator's center (indicated by the dark blue dotted line) positioned precisely in the middle. Please note that the figure is not drawn to scale.

profiles were generated for each sleeve measurement, both at the central position of the detector and at a 10 cm offset from the center. Exemplary histograms for 1 and 5 sleeves in both positions are visually presented in Figure 8.3 and Figure 8.4.
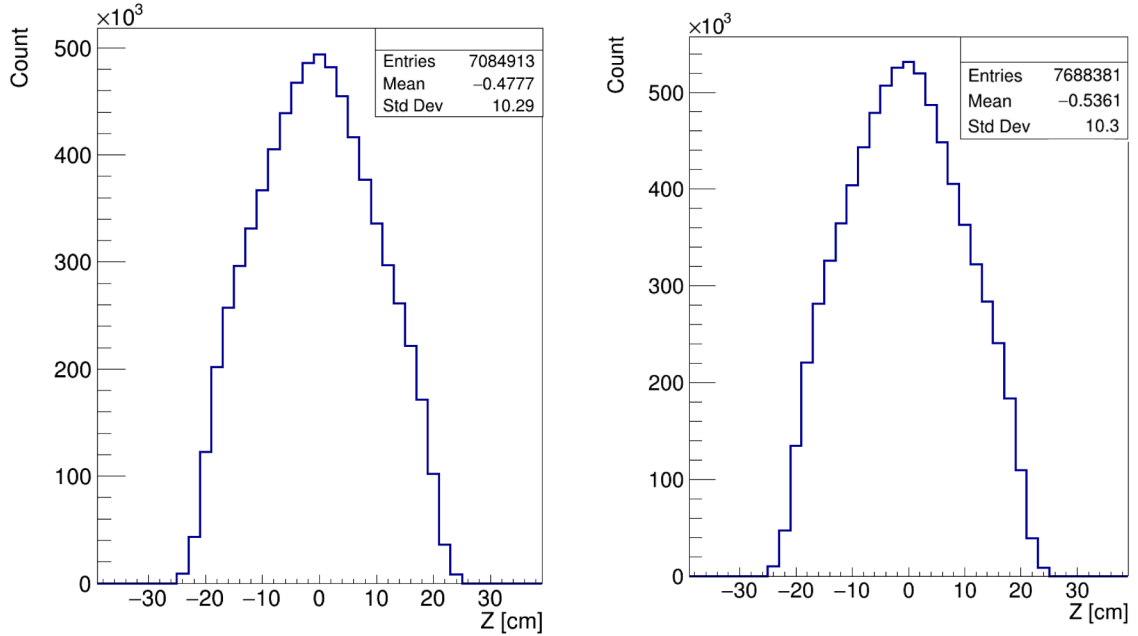
Rysunek 8.3: The Z projection has been generated using information regarding the annihilation position for a source positioned at the center of the detector's AFOV. On the left, the projection represents data for a single sleeve, while on the right, it illustrates the information gathered from five sleeves.

In the subsequent step, the corrected total count rate for each sleeve is computed using Equation 4.2:

$$R_{CORR,j} = \frac{(T_{j,acq}ln2)exp(ln2\frac{T_j-T_{cal}}{T_{1/2}})}{T_{1/2}(1 - exp(ln2\frac{-T_{j,acq}}{T_{1/2}})))}R_j, \tag{8.9}$$

where $T_{j,acq}$ represents the acquisition duration of the j-th measurement, T_{cal} denotes the calibration radioactivity measurement time, T_j indicates the measurement starting time and $T_{1/2}$ stands for the radionuclide half-life. To obtain the count rate free from attenuation effects with the Ge source, we selected a measurement reference with 5 sleeves positioned at (0,0,0). Assuming that the source activity was determined at noon and In this context, since $T_j - T_{cal} = 0$ for the Ge source, the measurement duration was specified as 6 hours and 8 minuets (22103 s), and the half-life of Ge is 270.95 days (23410080 s). We can derive the value of $R_{CORR,j}$ with the following
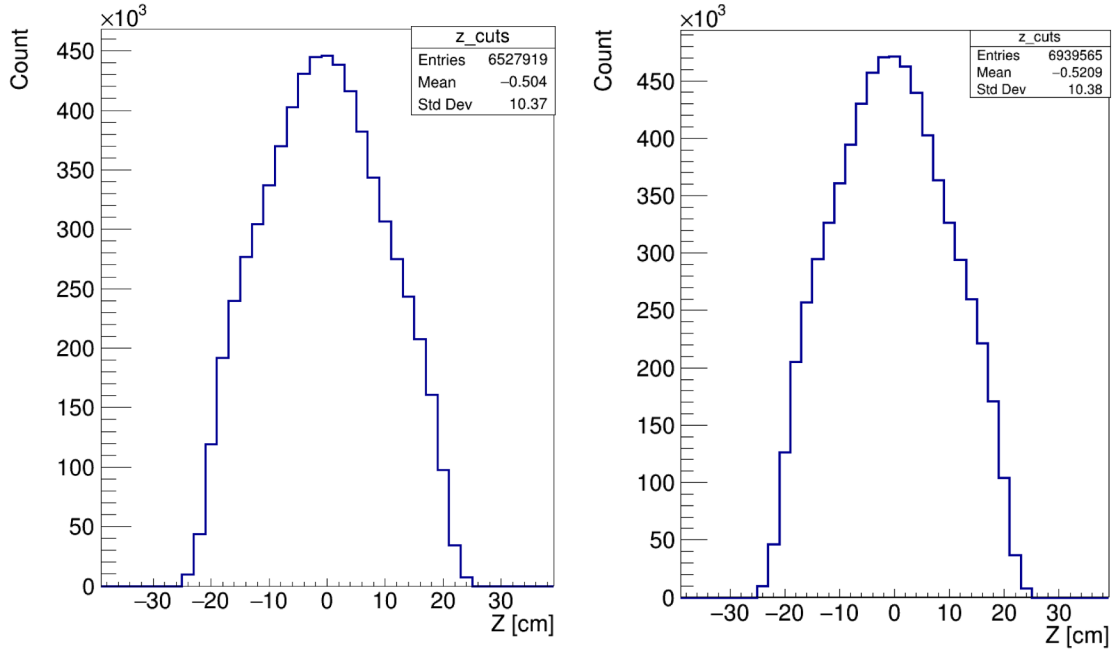
Rysunek 8.4: The Z projection has been generated using information regarding the annihilation position for a source positioned at the ten cm offset from the center of the detector's AFOV. On the left, the projection represents data for a single sleeve, while on the right, it illustrates the information gathered from five sleeves.

considerations:

$$R_{CORR,j} = 1.00031 R_j. \tag{8.10}$$

As is evident, the discrepancy between $R_{CORR,j}$ and R_j is negligible, rendering further calculations of $R_{CORR,j}$ for each measurement unnecessary. Consequently, for subsequent analyses, R_j was considered equivalent to $R_{CORR,j}$.

In the subsequent stage, the number of counts for each measurement was adjusted by normalizing it to its duration, thereby deriving the total count rate(R_j). The precise measurement time was determined by considering the number of time windows. These time windows were counted at the initial analysis level (as outlined in Section 3.3) [118]. This approach ensures the accurate calculation of the actual measurement duration (T_{meas}) and can be obtained using the following formula:

$$T_{meas} = \frac{\sum_{i=1}^{n} tw_i}{f}, \tag{8.11}$$

In this context, the symbol tw_i represents the number of time windows from the i-th file, with f representing the clock frequency, set at 20 kHz for Modular J-PET. It's worth noting that this method yields an accurate measurement duration. Table 81. refers details of such calculation for each measurement.

In the next step, the R_j was graphically represented as a function of the accumulated thickness of the sleeve walls (i.e., the combined thickness of the metal sleeve walls). This dataset was then subjected to a fitting process using Equation 4.3, with the resulting plot illustrated in Figure 8.5. The first data points, corresponding to
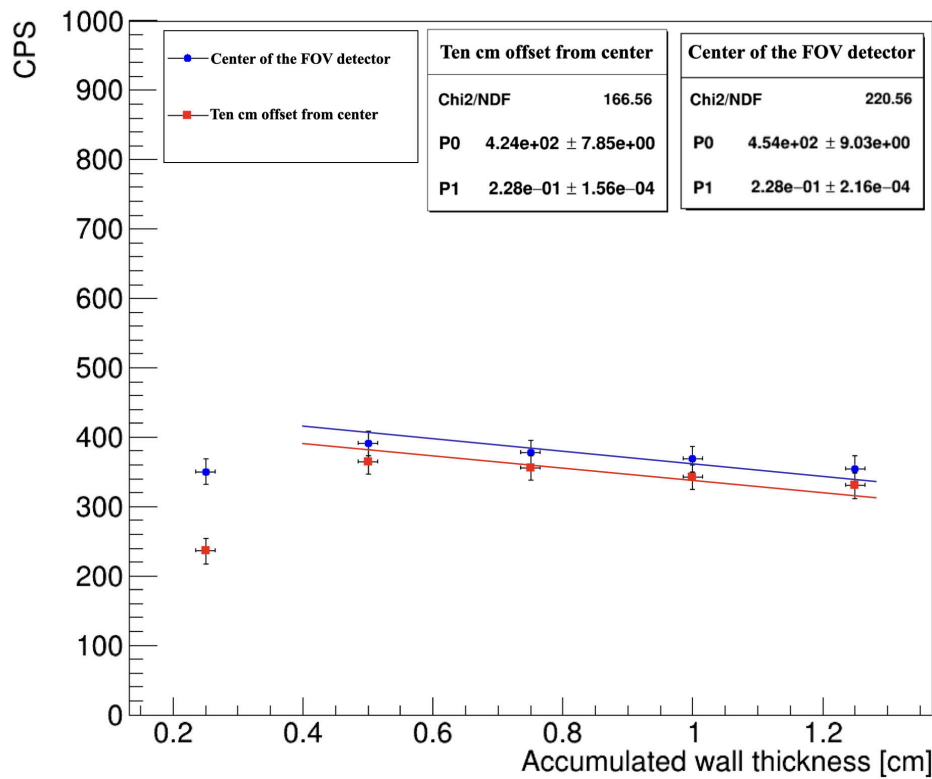
Rysunek 8.5: Illustrates how R_j (Counts Per Second) varies with the accumulated sleeve wall thickness. As depicted, there is a noticeable decrease in count rate as the wall thickness increases. These measurements were obtained at the center of the detector and at the ten cm offset from the center of the detector. The data is fitted with equation specified in Eq. 4.3.

measurements with a single sleeve (accumulated wall thickness equal to 0.25 cm) for both positions, were intentionally excluded from the data fitting process. This omission was deemed necessary due to the fact that these initial data points did not

conform to the general trend observed within the remaining dataset, as mentioned in reference [118]. This deviation can be primarily attributed to a smaller number of positrons undergoing annihilation within the first sleeve, leading to a reduced count rate. The value of the parameter P_0 in the fitting corresponds to $R_{CORR,0}$, which is measured at 454 ± 9 cps for the central position of the detector's AFOV and 424 ± 8 cps for the position with a 10 cm offset from the center of the detector, respectively.

Therefore, the system's sensitivity can be computed employing Equation 4.4, wherein we utilize the normalized activity in lieu of A_{cal}. It is pertinent to note that the variation in activity during the measurement remained below 100 kBq, which is almost negligible. Consequently, the average activity during the measurement at a specific phantom position be employed for the determination of the system's sensitivity. To assess its uncertainty, we will apply the error propagation law:

$$\delta(S) \; = \; \frac{\delta R_{CORR,0}}{A_{cal}}.$$ (8.12)

Below, you can find the results for the system sensitivity obtained from measurements conducted with the PET sensitivity phantom in both positions:

$$S_0 \; = \; \frac{454 \; \pm \; 9.03 \; cps}{1859.86 \; kBq} \; = \; 0.244 \; \pm \; 0.011 \; , \frac{cps}{kBq}.$$ (8.13)

$$S_{10} \; = \; \frac{424 \; \pm \; 7.8 \; cps}{1847.2 \; kBq} \; = \; 0.230 \; \pm \; 0.004 \; . \frac{cps}{kBq}.$$ (8.14)

The axial sensitivity profile for the smallest tube in the central position can be computed and visualized following the calculation of the system sensitivity, as described in Eq 4.5. The axial sensitivity profile is presented in Fig 8.6 for the center of the detector and for a 10 cm offset from the center of the detector. The sensitivity peak values obtained for the Modular J-PET system, both at the center of the scanner's Field of View (FOV) and at a 10 cm offset from the tomograph center, are 0.68 cps/kBq and 0.62 cps/kBq, respectively. These values indicate that the peak sensitivity at the center of the scanner's FOV is greater than that at the 10 cm offset from the tomograph center.
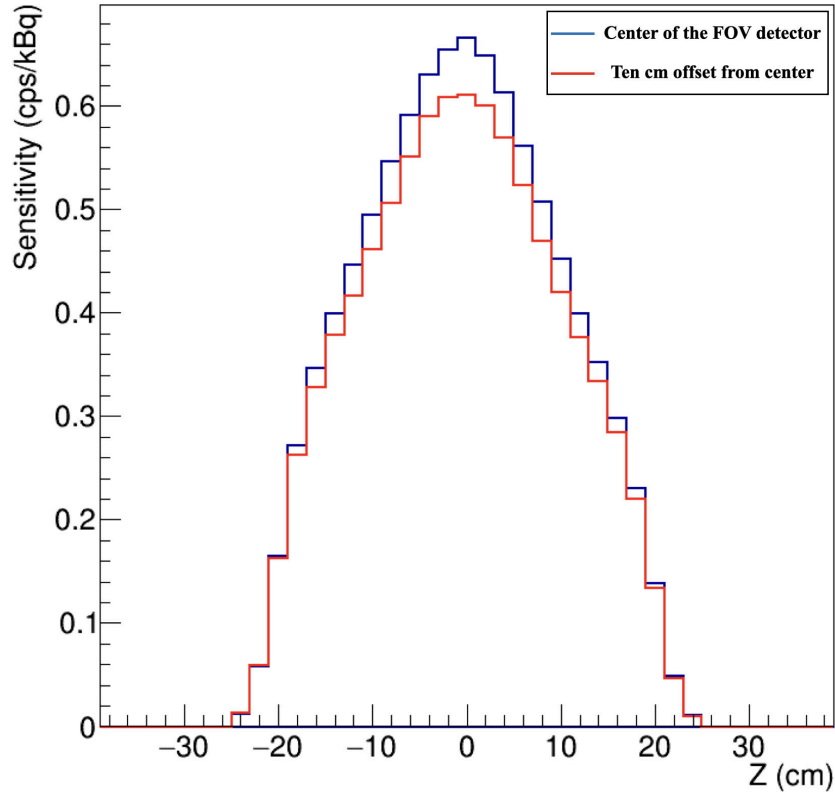
Rysunek 8.6: Axial sensitivity profile for the smallest sleeve in both positions.

It is essential to note that the sensitivity of the detector varies depending on the applied data conditions. In the context of PET scanner, sensitivity is defined as the number of detected counts per unit of time for each unit of activity present in the radiation source. The sensitivity is strongly dependent on the count rate after the application of all data selection criteria. In the presented results, a multiplicity criterion of 8 SiPMs connected to both ends of each detector module is applied for the majority of scintillators. However, scintillator ID 284 is subject to a multiplicity criterion of 5, while scintillator IDs 208, 213, 225, 280, 342, 353, 365, and 458 have a multiplicity cut of 7 applied (see section 7.3.3). It is worth noting that changing the multiplicity criterion has a direct impact on the axial sensitivity profile and overall system sensitivity. Additionally, we assessed the sensitivity of the Modular J-PET system under three different scenarios:

- Scintillator ID 284 with a multiplicity of 5, and for all other scintillators, a multiplicity greater than or equal to 7.

118

- Scintillator ID 284 with a multiplicity of 5, and for all other scintillators, a multiplicity greater than or equal to 6.

- All scintillators with a multiplicity greater than or equal to 5.
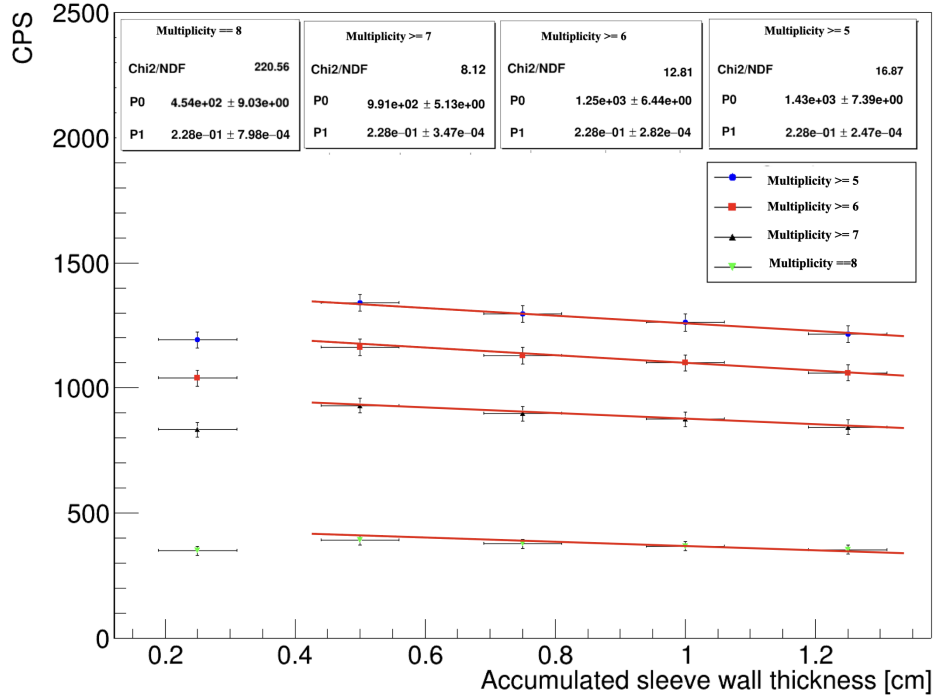
Rysunek 8.7: Illustrates R_j (Counts Per Second) as function of the accumulated sleeve wall thickness. These measurements were obtained at the center of the detector for different multiplicity cuts, and the data is fitted to the equation specified in Eq. 4.3.

Figure 8.7 illustrates the count rate (Rj in cps) as a function of the accumulated sleeve wall thickness for various multiplicity cuts at the center of the FOV detector. The results for the system sensitivity for center of the detector's FOV in different multiplicity cuts can be found below:

$$S_{0,multiplicity>=7} = \frac{991 \pm 5.13 \; cps}{1859.86 \; kBq} = 0.5328 \pm 0.0027 \; \frac{cps}{kBq}. \tag{8.15}$$

$$S_{0,multiplicity>=6} = \frac{1250 \pm 6.41 \; cps}{1859.86 \; kBq} = 0.6720 \pm 0.0034 \; \frac{cps}{kBq}. \tag{8.16}$$

$$S_{0,multiplicity>=5} = \frac{1430 \pm 7.39 \; cps}{1859.86 \; kBq} = 0.7688 \pm 0.0039 \; \frac{cps}{kBq}. \tag{8.17}$$

119

The results demonstrate that the system sensitivity is notably higher when a multiplicity criterion of greater than or equal to 5 is applied to all scintillators. The axial sensitivity profiles for all cases are presented in Figure 8.8, revealing a peak sensitivity of $2.4, cps/kBq$ when a multiplicity criterion of greater than or equal to 5 is employed.
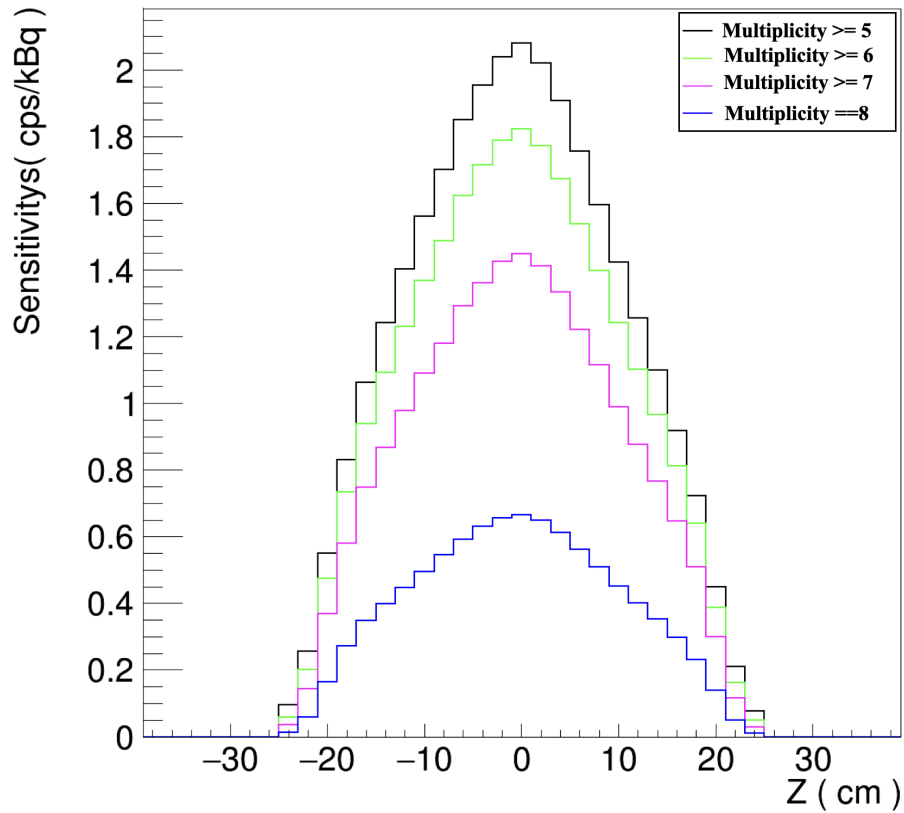
Rysunek 8.8: Axial sensitivity profile for the smallest sleeve in the center of the FOV detector for different multiplicity cuts.

8.2 Scatter fraction

To guarantee the precision and quality of PET images, it is imperative to assess and rectify the impact of scattered radiation. Data has been processed as delineated in chapter 7 to mitigate part of scattered events. As mentioned in Chapter 4, there exist two distinct methodologies for computing the Scatter Fraction value, namely, with and without random estimation. In the context of the J-PET scanner, the method

devoid of random estimation was employed [118].

The comprehensive procedure for scatter fraction and NECR measurement is explicated in Section 7.2.3. For this measurement, a ^{18}F line source with an initial activity of 7.511 MBq at the start time of measurement was utilized. The corrected initial activity (A_{cal}) was computed using Equation 4.6:

$$A_{cal} = 7871.98 \ kBq \ \frac{700 \ mm}{700 \ mm} = 7871.98 \ kBq. \tag{8.18}$$

For this measurement, it is imperative to stipulates the expression of activity concentration in units of kBq/cc, as detailed in Formula 4.20. In this context, V represents the total volume of the PET scatter phantom, which is equivalent to 22,000 ml, and A_{ave} denotes the average activity, which is derived in accordance with Equation 4.21. During this measurement, the corrected line source activity was determined to be 7.871 MBq at time T_{cal}. Since $T_{cal} - T$ equals 0 in this measurement, the calculation of A_{ave} can be performed using the following formula:

$$A_{ave} = A_{cal} \frac{T_{1/2}}{T_{acq}ln2}(1 - exp(\frac{-T_{acq}}{T_{1/2}}ln2)), \tag{8.19}$$

where $T_{1/2}$ represents the half-life of ^{18}F, which is equal to 109.771 minutes, and T_{acq} stands for the acquisition duration. With an acquisition duration of 185 min, the average activity can be calculated as follows:

$$A_{ave} = 4.64242 \ MBq. \tag{8.20}$$

In accordance with the data processing instructions outlined in the NEMA standard, for tomography with AFOV less than 65 cm, a single sinogram should be generated for each slice using oblique sinograms with the Single Slice Rebinning (SSRB) technique. To create the sinogram, following the data preselection step, the coordinates of the interaction point of gamma quanta with the scintillator material along the x-, y-, and z-axes were recorded. Subsequently, these two positions of interaction with the scintillator, denoted as (x_1, y_1) and (x_2, y_2), are used to define the line-of-response

(LOR) for a given event, as illustrated in Fig 8.9. In its general form, the LOR
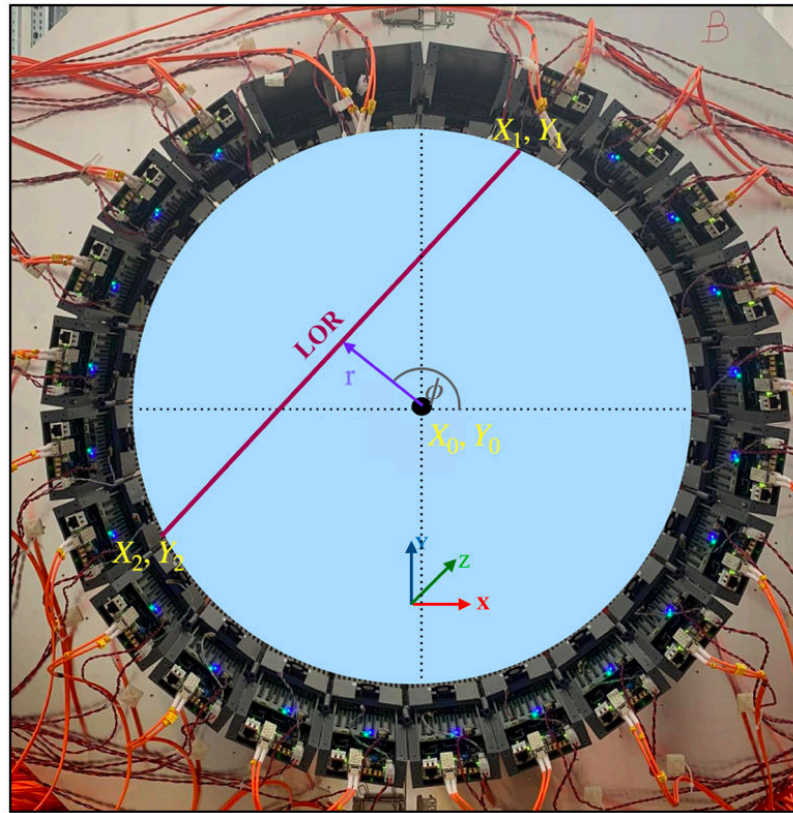
Rysunek 8.9: Illustrates the LOR represented as a line connecting two interaction points, and the subsequent conversion of the LOR into sinogram format.

equation can be expressed as follows:

$$Ax + By + C = 0, \tag{8.21}$$

where B=1 and A and C are calculated as:

$$A = -\frac{y_1 - y_2}{x_1 - x_2}. \tag{8.22}$$

$$C = ax_1 - y_1. \tag{8.23}$$

In order to generate a sinogram, it is imperative to determine both the radial offset

(r) and the angle (ϕ). The angle ϕ can be computed using the following formula:

$$\phi = atan2(y_r, x_r). \tag{8.24}$$

The radial offset represents the minimal distance between the center of the detector denoted as (x_0, y_0) and the line-of-response (LOR) defined by (x_r, y_r). It is calculated as:

$$r = \sqrt{x_r^2 + y_r^2}, \tag{8.25}$$

where

$$x_r = \frac{B(Bx_0 - Ay_0) - AC}{A^2 + B^2} = \frac{-b}{a + \frac{1}{a}}. \tag{8.26}$$

$$y_r = \frac{A(-Bx_0 - Ay_0) - BC}{A^2 + B^2} = \frac{-1}{x} \times x_r. \tag{8.27}$$

Every LOR was converted into a sinogram format following the calculations described earlier and was allocated to a specific slice utilizing the Single Slice Rebinning (SSRB) technique. Each scintillator, measuring 50 cm in length, was divided into 25 segments along its length, with each individual slice measuring precisely 2 cm. In this approach, oblique sinograms are transformed into rebinned sinograms using the SSRB algorithm. The rebinning algorithm essentially rearranges the three-dimensional data into a stack of conventional two-dimensional data sets, where each transaxial slice is organized as a sinogram [119, 120]. In each sinogram, all pixels located beyond 120 mm from the center of the scanner's transaxial FOV are assigned a value of zero. Following this step, the rebinned sinograms are consolidated into a single sinogram, as depicted in Figure 8.10. A summation projection is generated from this final sinogram, illustrated in Figure 8.11.

Utilizing this summed sinogram, all projections are aligned such that the maximum value corresponds to zero, and they are summed to produce a one-dimensional profile, as shown in Figure 8.12. Following the summation, counts per pixel are computed from both the left and right sides of the projection profile, specifically at ±20 mm from the center of the sinogram. This computation involves employing linear in-
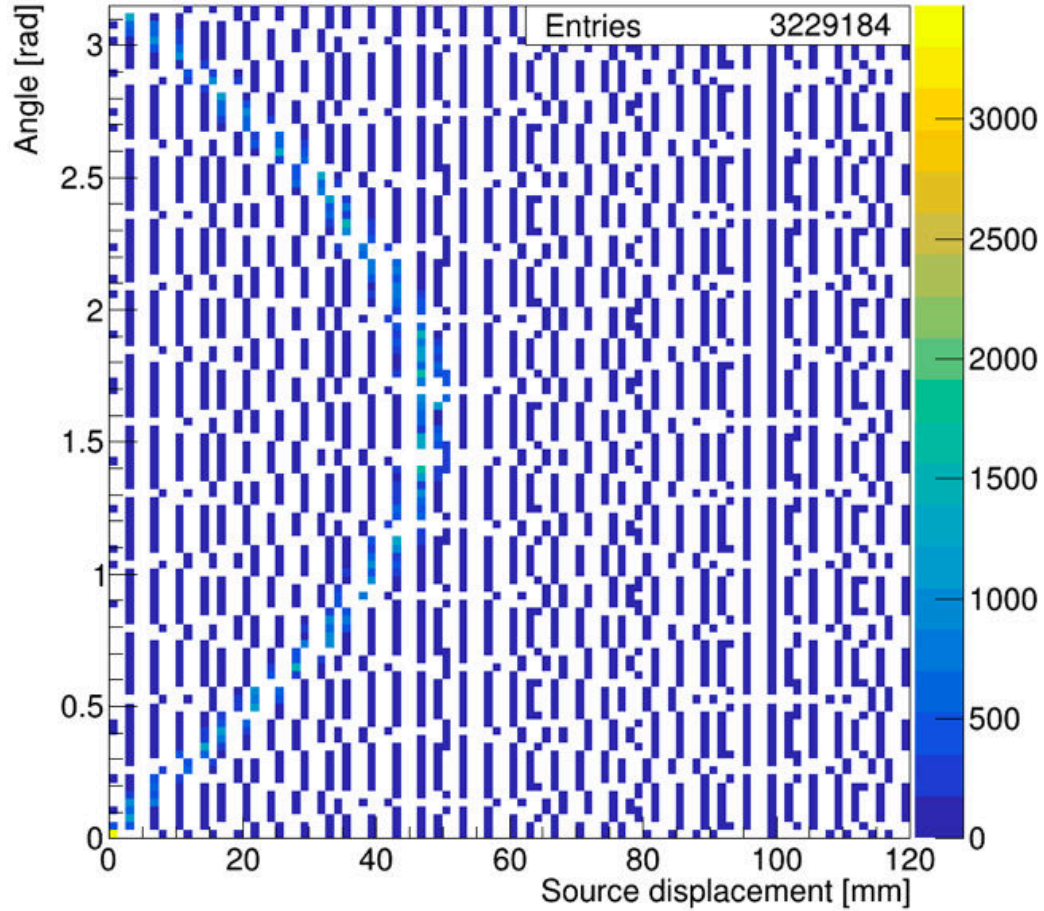
Rysunek 8.10: Illustrates final sinogram was obtained as a sum of all aligned sinograms.

terpolation between the nearest pair of pixels, a technique illustrated in Figure 8.13. The linear interpolation is determined by the calculations of the bin center points situated on the distribution's left and right sides. The parameters for the linear fit on the left side of the distribution were determined based on the following two equations:

$$y_1 = a_{left}x_1 + b_{left}. \tag{8.28}$$

$$y_2 = a_{left}x_2 + b_{left}. \tag{8.29}$$

By subtracting one of these equations from the other, one can derive the parameters a_{left} and b_{left}, which describe the linear fit between two bins on the left side, along
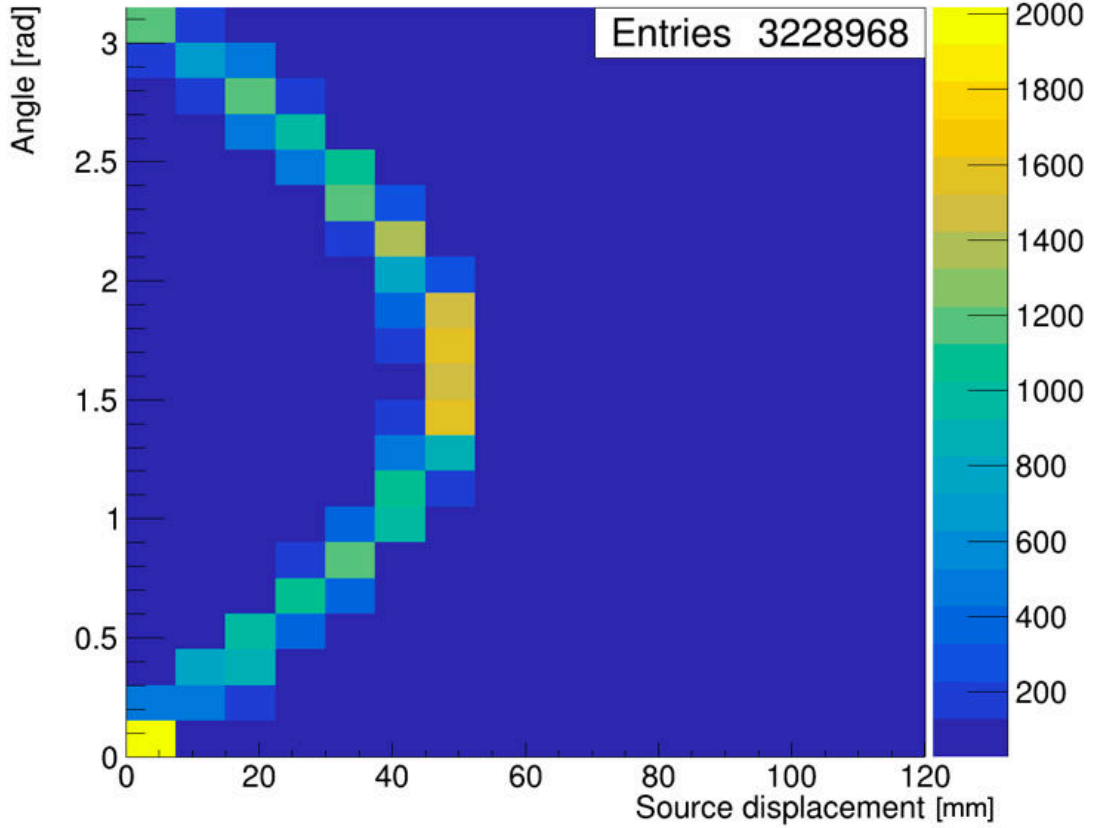
Rysunek 8.11: Depicts the final sinogram, which was reprocessed within the ROOT environment for visual clarity. Notably, this particular sinogram was excluded from subsequent analyses.

with their associated uncertainty:

$$a_{left} = \frac{y_1 - y_2}{x_1 - x_2}. \tag{8.30}$$

$$b_{left} = y_1 - a_{left}x_1. \tag{8.31}$$

uncertainty of a_{left} and b_{left} were calculated as:

$$\delta a_{left} = \sqrt{(\frac{\delta a_{left}}{\delta x_1})^2 \Delta X_1^2 + (\frac{\delta a_{left}}{\delta x_2})^2 \Delta X_2^2}. \tag{8.32}$$

$$\delta b_{left} = \sqrt{(\frac{\delta b_{left}}{\delta a_{left}})^2 \Delta a_{left}^2 + (\frac{\delta a_{left}}{\delta x_1})^2 \Delta X_1^2}. \tag{8.33}$$

In the determination of the uncertainties for a_{left} and b_{left}, it's important to note
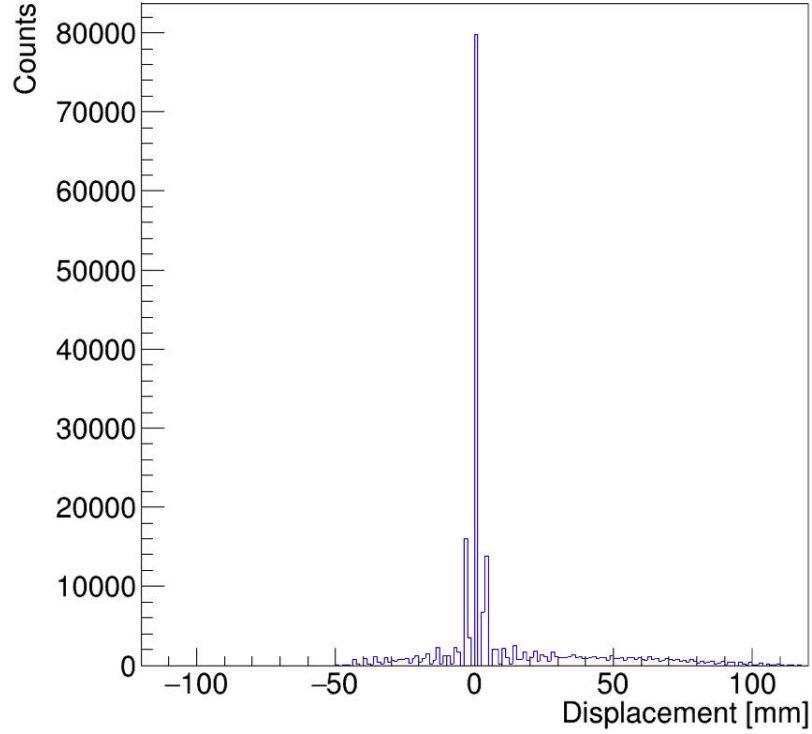
Rysunek 8.12: Illustrates the one-dimensional profile, calculated by aligning to zero using the maximum value and summing the projections of the sinogram.

that the uncertainty of y was not considered, and $\Delta X = \Delta X_1 = \Delta X_2 = \frac{binwidth}{\sqrt{3}}$. A similar procedure was executed to establish a linear fit for the right side of the distribution. Applying the above formula and replacing x_{left} and x_{right} with ± 20 mm, respectively, allows for the calculation of the counts per pixel:

$$C_{left} = a_{left} * (-20) + b_{left} = 785.667 \ counts. \tag{8.34}$$

$$C_{right} = a_{right} * (+20) + b_{right} = 841.374 \ counts. \tag{8.35}$$

According to the NEMA standard, in the calculation of the random plus scatter counts ($C_{r+s,i,j}$), one should multiply the average of interpolated pixel intensities $C_{L,i,j}$ and $C_{R,i,j}$ by the number of pixels between the edges of the 40 mm region and then add this result to the counts in the pixels outside the 40 mm region. The counts within the 40 mm region ($C_{central}$) and those outside the 40 mm region (C_{side}) are determined

126
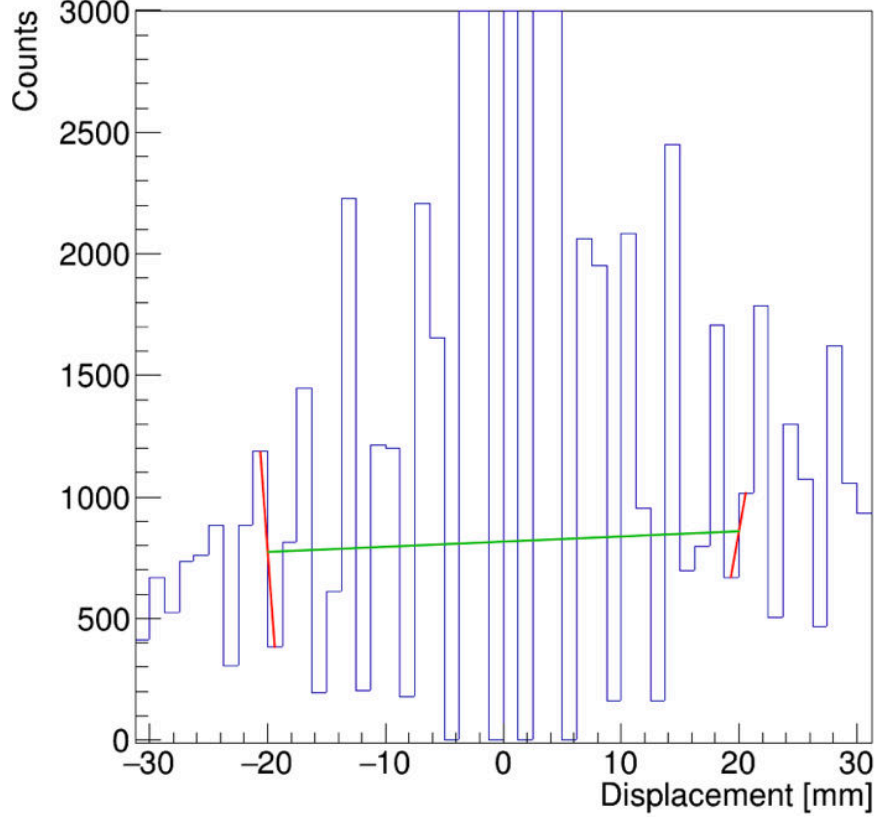
Rysunek 8.13: Graphical explanation of determination of linear interpolation between middle point of two nearest bins at $\pm$ 20 mm, which a_{left}, b_{left}, a_{right}, and b_{right} is equal to -643.08, -12076.5, 278.667, and -4731.96, respectively.

as follows:

$$C_{central} = 26025 \pm 161 \ counts. \tag{8.36}$$

$$C_{side} = 59625 \pm 325 \ counts. \tag{8.37}$$

In all cases, the uncertainty in the count numbers was computed as the square root of the counts. The total event counts (C_{TOT}) were determined by summing the counts of all pixels in the summation projection. Total event counts is equal to:

$$C_{TOT} = 205471 \pm 453 \ counts. \tag{8.38}$$

The scatter fraction was computed using Equation 4.15, resulting in the following value:

$$SF = 41.68 \pm 0.19 \ [\%]. \tag{8.39}$$

127

For an acquisition time (T_{acq}) of 148 min, the following count rates were estimated: total count rate ($R_{TOT,j}$), true count rate ($R_{t,j}$), scatter count rate ($R_{s,j}$), random count rate ($R_{r,j}$), and NECR count rate ($R_{NEC,j}$):

$$R_{TOT,j} = \frac{1}{T_{acq,j}} \sum_i C_{TOT,i,j} = 23.20 \pm 0.05 \ (cps). \qquad (8.40)$$

$$R_{t,j} = \frac{1}{T_{acq,j}} \sum_i (C_{TOT,i,j} - C_{r+s,i,j}) = 13.53 \pm 0.10 \ (cps). \qquad (8.41)$$

$$R_{s,j} = (\frac{SF}{1-SF}) R_{t,j} = 9.67 \pm 0.10 \ (cps). \qquad (8.42)$$

$$R_{r,j} = R_{TOT,j} - (\frac{R_{t,j}}{1-SF}) = 7.522E - 07 \pm 0.23 \ (cps). \qquad (8.43)$$

$$R_{NEC,j} = \frac{R_{t,j}^2}{R_{TOT,j}} = 7.88 \pm 0.11 \ (cps). \qquad (8.44)$$

The results of the random event rate indicate that there were minimal random events detected during this measurement.

The subsequent step involves plotting various count rates, namely the total count rate ($R_{TOT,j}$), true count rate ($R_{t,j}$), scatter count rate ($R_{s,j}$), and the NECR count rate ($R_{NEC,j}$), as functions of activity concentration. In accordance with the NEMA standard, the duration of individual acquisitions (T_{acq}) should be less than one-fourth of the radionuclide half-life ($T_{\frac{1}{2}}$). To create the count rate plots, files corresponding to 30 minutes intervals were selected. In all cases, the acquisition time remained below 6 minutes. The average activity concentration was calculated using Equation 4.20 (as shown in Table 8.2). The count rate plots for total, true, and scatter count rates are presented in Figure8.14 as functions of average activity concentration (kBq/cc). Measurement with higher activity levels was not feasible due to DAQ buffer limitations. For small average activity concentrations within the range of 0.113 kBq/cc to 0.342 kBq/cc, the peak total, true, and scatter count rates were recorded as $31.19 \pm 0.52 \ (cps)$, $18.18 \pm 0.99 \ (cps)$, and $13.00 \pm 1.08 \ (cps)$, respectively, for an average activity concentration of 0.342 kBq/cc. Similarly, the NECR count rates are depicted in Figure 8.14 as functions of average activity concentration (kBq/cc).

Tabela 8.2: Scatter fraction for 7 different activity for Modular J-PET scanner using the NEMA standard method.

No. measurement	obtained time (s)	Counts	Average activity (kBq)	Average activity concentration (kBq/cc)	scatter fraction (%)
1	113.747	56596	7534.116	0.342	41.69
2	135.683	61795	6236.4308	0.283	41.31
3	159.822	65977	5151.540	0.234	41.09
4	187.634	70207	3503.187	0.193	41.70
5	219.286	72486	4255.364	0.152	41.33
6	255.302	73615	2893.433	0.131	41.10
7	392.310	71489	2486.752	0.113	41.30

The peak NECR count rate was measured at 10.60 ± 1.17 (*cps*) for an activity concentration of 0.342 kBq/cc.
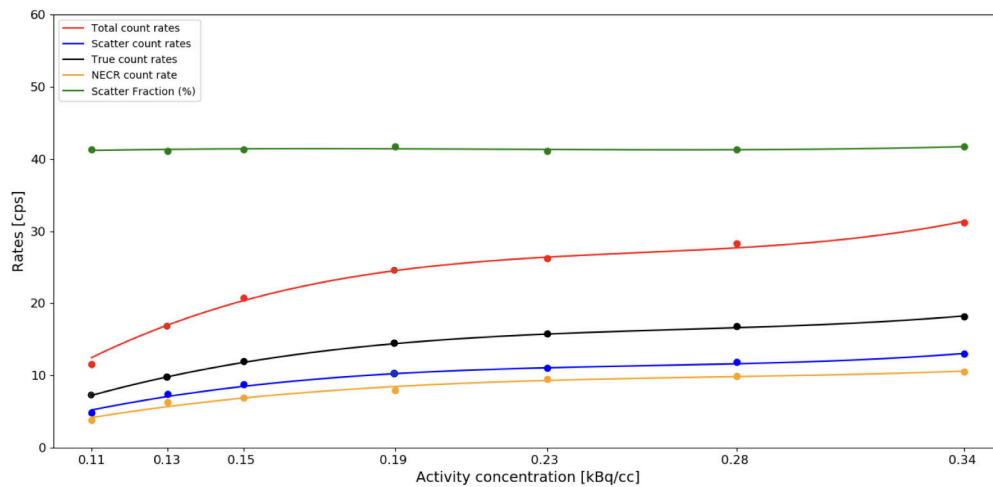
Rysunek 8.14: The count rates of various coincidence types, NECR, and scatter fraction (%) are typically plotted as functions of the average activity concentration (kBq/cc) for the Modular J-PET.

8.3   Spatial resolution

According to Chapter 4, spatial resolution is defined as the ability to differentiate between two separate points after image reconstruction. To attain high-quality reconstructed images, it is essential to eliminate background elements, such as scattering and random coincidence events, from the dataset.

For spatial resolution measurement, the NEMA standard recommends using a radionuclide such as ^{22}Na. Alongside the prescribed source for these measurements, the NEMA norm specifies that the activity of the source should be sufficiently low to meet one of the following conditions:

- The percentage of dead time losses is less than 5 %.

- The random coincidence rate is less than 5 % of the total event rate.

Already described in Sections 8.1.1 and 8.1.2, here results for higher source activity are presented.

8.3.1 Dead time losses

This calculation was performed using formulas 8.2 and 8.3 for a ^{22}Na source with an activity of 9.2860 MBq on the day of measurement. The numberof counts per scintillator in each module was calculated as:

$$N_{sci}^{K} = \frac{\Omega}{4\Pi} \times n \times P \; = \; 2674/s, \qquad (8.45)$$

where, Ω represents the solid angle, n denotes the number of emitted particles and P represents the probability of interaction in plastics scintillator for 511keV. The number of counts per module was calculated as:

$$N_{module} = \sum_{k=1}^{13} N_{sci}^{K} \; = \; 34762/s. \qquad (8.46)$$

Consequently, the count losses per module attributable to the dead time of the Module J-PET system is:

$$\frac{M}{N_{module}} \; = \; e^{-N_{module}T} = 0.99930 \qquad (8.47)$$

count losses per module attributable to the dead time of the Module J-PET remain less than 1%, thus satisfying the first condition as stipulated.

8.3.2 Random coincidences rate

To calculate the frequency of random coincidences, we make the assumption that two rectangular pulses, each with durations denoted as τ_1 and τ_2, follow a statistical distribution in line with Poisson statistics. These pulses exhibit average frequencies of n_1 and n_2, as expressed in formula 8.7. For the activity level of 9.2 MBq, the average occurrence of genuine coincidences per unit of time for each module, equating to 34762 /s. Given a 4 ns coincidence time window and an activity level of 9.2 MBq, the calculation of the rate of random coincidences is as follows:

$$n_{random} = n_2 \; n_1 \; (\tau_1 + \tau_2) = 2 \; n_2 \; n_1 \; \tau \; = \; 9.66717/s \tag{8.48}$$

When employing a ^{22}Na source positioned at (20,0,18.75), the observed total count rate is recorded as 350 cps (as detailed in Figure 8.16. 1261040 count per 1 hour measurement). Notably, this count rate reveals a random coincidence rate that is determined to be around 2.7% of the total count rate.

8.3.3 Estimation of spatial resolution

For this measurement, a 9.2 MBq ^{22}Na source was utilized, placed within a plexi rod, and positioned at various locations. Data acquisition time for each measurement was 1 hour. The specifics of the spatial resolution measurement methodology are detailed in section 7.2.1, while the comprehensive process for image analysis and reconstruction is outlined in section 6.3.

The positioning of the source within the detector plays a crucial role in the spatial resolution measurement, aligning with the NEMA standard positions in centimeters: (1,0,0), (10,0,0), (20,0,0), (1,0,18.75), (10,0,18.75), and (20,0,18.75) for the Modular J-PET (as depicted in Figure 6.9). The XY position and XZ position of annihilation point after pre-selected data for two specific position (1,0,0) and (20,0,18.75) are displayed in Figure 8.15 and Figure 8.16, respectively. These particular positions were selected due to their significance: (1,0,0) is in close proximity to the center of the Modular J-PET, while (20,0,18.75) represents a location close to the edge of the

Modular J-PET.
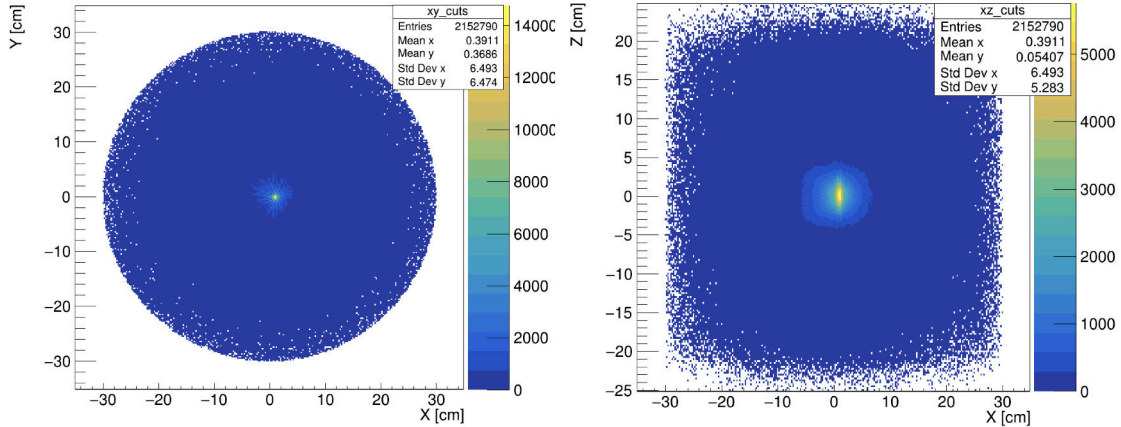
Rysunek 8.15: Histogram of annihilation points for position (1,0,0): (Left) XY projection of annihilation point and, (Right) XZ projection of annihilation points.
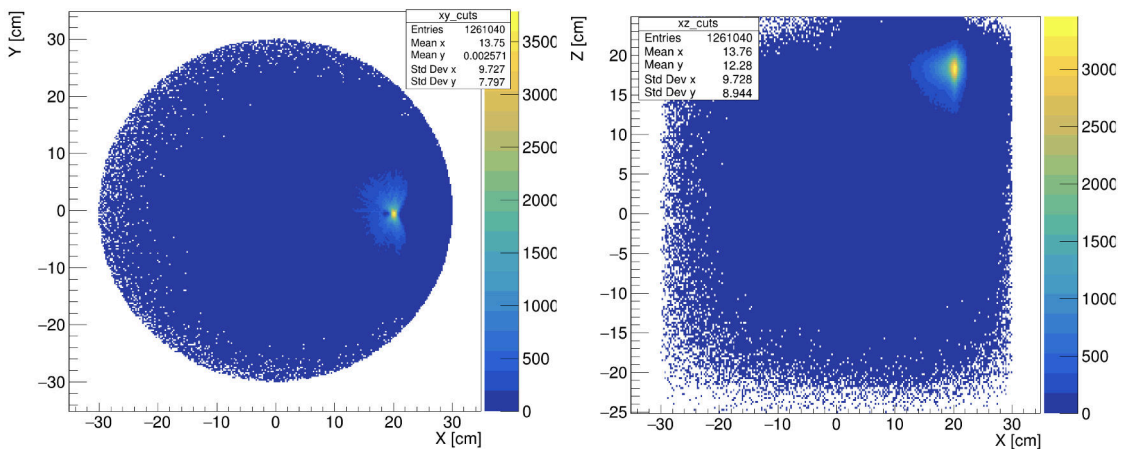
Rysunek 8.16: Histogram of annihilation points for position (20,0,18.75): (Left) XY projection of annihilation point and, (Right) XZ projection of annihilation points.

The QETIR software functions effectively with both TOF and Non-TOF List-Mode data, providing the flexibility to convert the data into either TOF or Non-TOF sinograms as necessary. Two distinct types of List Mode data were generated subsequent to preselecting data for image reconstruction: one for TOF and another for Non-TOF reconstruction. The first List Mode entails the interaction points in the x-axis, y-axis, and z-axis for two hits in each event, specifically utilized for Non-TOF image reconstruction. Conversely, the second List Mode incorporates the interaction

points in the x-axis, y-axis, z-axis, and the time of interaction with the scintillator for two hits in each event, serving as the foundation for the TOF-reconstructed image.

The integration of TOF information in PET reconstruction significantly enhances image quality. TOF data aids in estimating the emission points along each LOR during PET reconstruction. This information is used to update image voxels only along each segment of the response line, defined by the TOF resolution, rather than the entire LOR. This targeted approach reduces interdependence among image voxels, leading to diminished noise propagation. As a result, it enables faster and more consistent convergence, thereby improving the detectability of lesions [121].
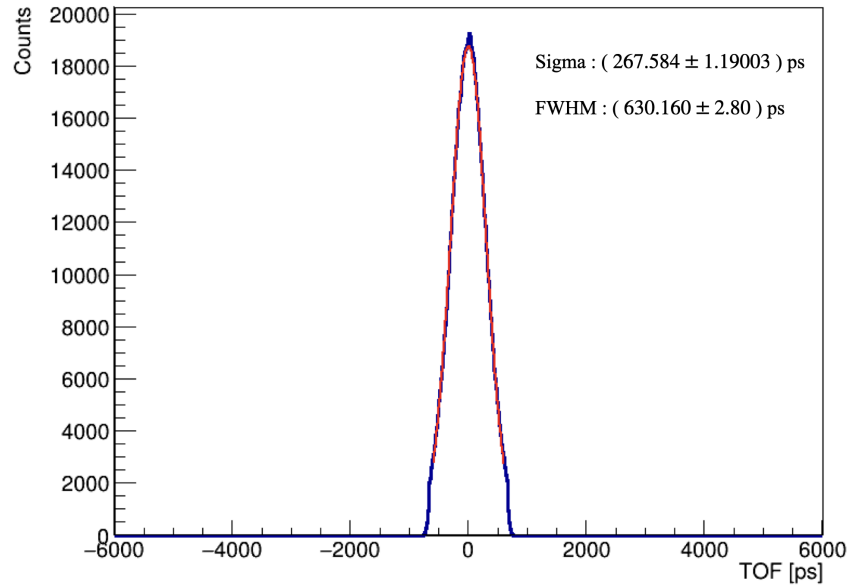
Rysunek 8.17: TOF spectrum for preselected data for Modular J-PET scanner from the 6 hours measurement with the ^{65e}Ge Line source inside the 5 sleeve sensitivity phantom in the center of the FOV Modular J-PET.

For the Modular J-PET, TOF estimation was conducted by Keyvan Tayefi, a member of the J-PET group, based on experimental data. Figure 8.17 displays the TOF spectrum for preselected data. The TOF resolution (σ) is calculated to be (267.6 ± 1.2) ps. This precise TOF information is instrumental in achieving improved image reconstruction and subsequently enhancing the overall diagnostic capabilities of the Modular J-PET system.

Following image reconstruction, the AMIDE software was employed to visualize the image and ascertain the precise source position. Figures 8.18 and 8.19 showcase the results of the reconstructed images in three directions using the QETIR software for TOF and Non-TOF List Mode data, positioned at (1,0,0), respectively. Likewise, Figures 8.20 and 8.21 exhibit the reconstructed images in three directions, utilizing TOF and Non-TOF List Mode data, this time positioned at (20,0,18.75).

The presented images were obtained from the first iteration of each reconstruction. In the next step, a line profile was extracted from each image in three directions.
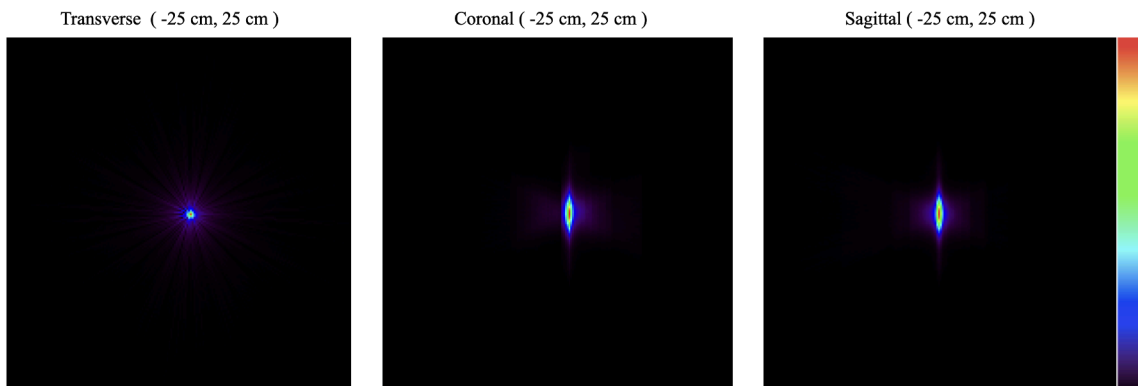
Rysunek 8.18: The results of image reconstruction generated using TOF List Mode data for the source positioned at (1,0,0). Displayed images were obtained from the first iteration and showcase the reconstructed image in three directions.
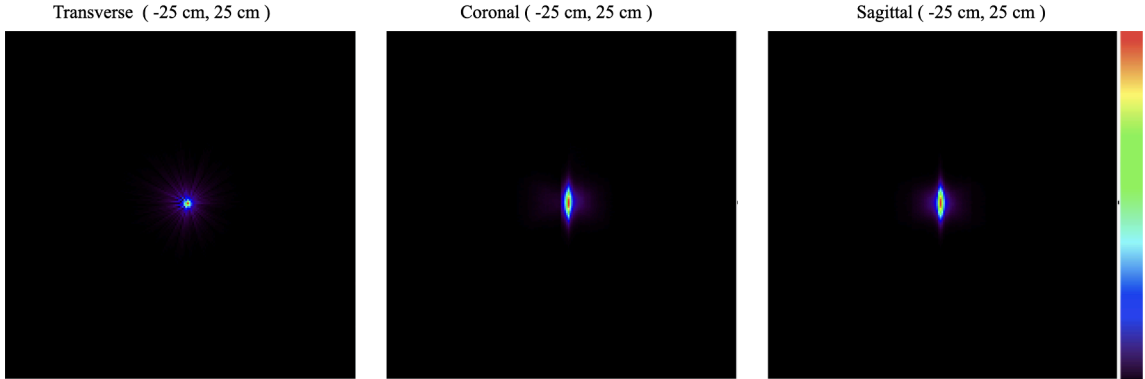
Rysunek 8.19: The results of image reconstruction generated using Non-TOF List Mode data for the source positioned at (1,0,0). Displayed images were obtained from the first iteration and showcase the reconstructed image in three directions.
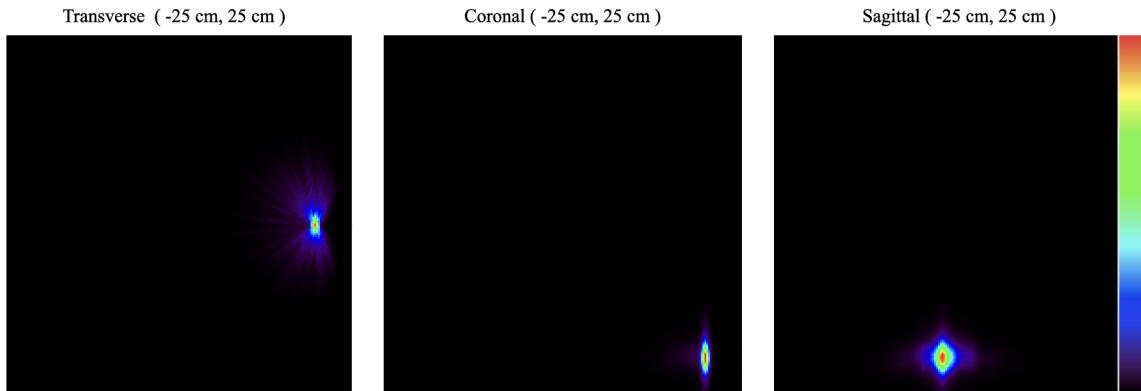
Rysunek 8.20: The results of image reconstruction generated using TOF List Mode data for the source positioned at (20,0,18.75). Displayed images were obtained from the first iteration and showcase the reconstructed image in three directions.

Subsequently, the FWHM and their corresponding uncertainty was computed using NEMA norm methods detailed in section 6.3 for all positions. Figures 8.22, 8.23, and 8.24 display the FWHM results for the position (1,0,0) in both TOF and Non-TOF reconstructions along the x-axis, y-axis, and z-axis, respectively.
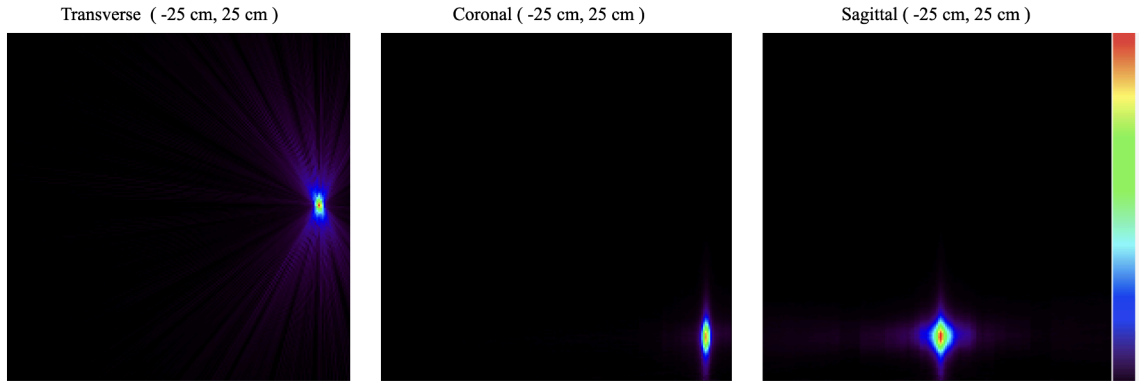
Rysunek 8.21: The results of image reconstruction were generated using Non-TOF List Mode data for the source positioned at (20,0,18.75). Displayed images were obtained from the first iteration and showcase the reconstructed image in three directions.

Figures 8.25, 8.26, and 8.27 display the FWHM results for the position (20,0,18.75) in both TOF and Non-TOF reconstructions along the x-axis, y-axis, and z-axis, respectively. in all position the results of using TOF MLEM List Mode is visable in the z-axis. Moreover, the FWHM values and their associated uncertainties derived for all positions are tabulated in Table 8.2, delineating the results for TOF and Non-TOF reconstructed images.

Notably, the FWHM value for the distribution along the y-axis surpasses the FWHM value for the distribution along the x-axis. This difference is primarily attributed to the dimensions of the cross-section of the plastic scintillators, measuring $6\ mm \times 24\ mm$, resulting in increased uncertainty in the depth of the plastic scintillators. The FWHM experiences its greatest challenge along the z-axis, primarily due to the distinctive geometry of the Modular J-PET detector, as highlighted earlier. The unique design and structure of the detector play a crucial role in determining the spatial resolution, indicating the challenges in achieving optimal resolution across all axes.

QETIR software was used for image reconstruction, which is iterative algorithms, all of the above results is for 1st iteration which will be more comparable with FBP results [103, 122]. For spatial resolution measurement, reconstruction done for 10
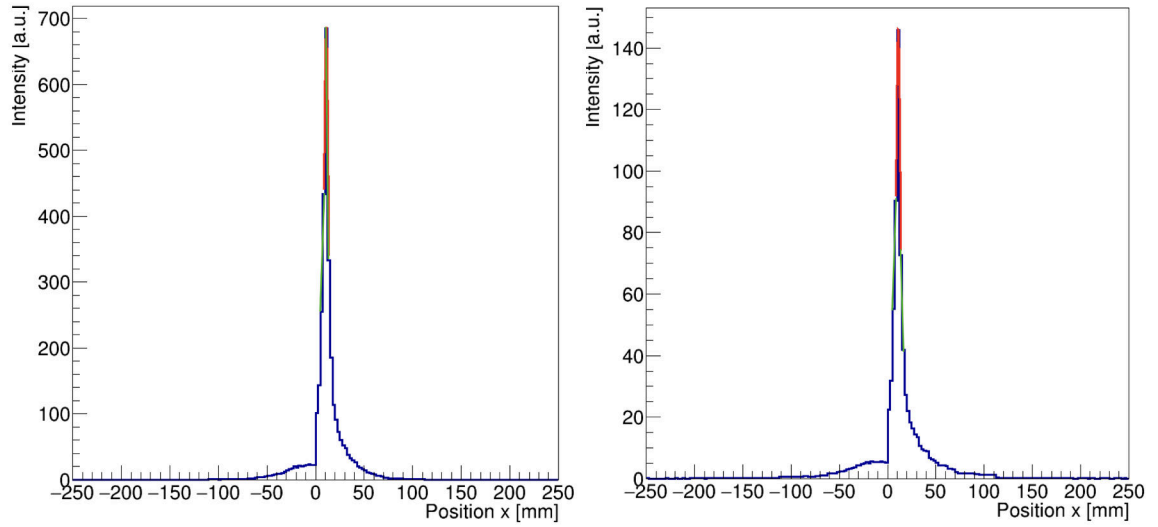
Rysunek 8.22: FWHM and its uncertainty estimation for distribution along x -axis performed at position (1,0,0), (left) for TOF reconstructed image, it is equal to 4.92 ± 0.55 mm, and (right) Non-TOF reconstructed image, it is equal to 4.92 , 0.12 mm.

iteration with 1 subsets. The results of FWHM for three direction for position (1, 0, 0) with TOF and Non-TOF image reconstruction methods is presented in Fig 8.28.
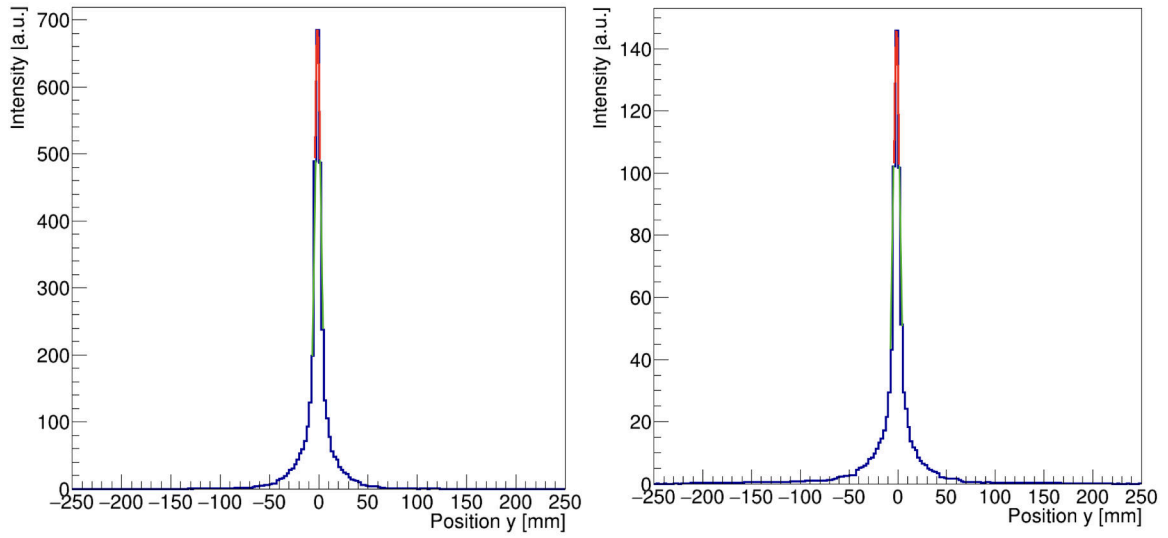
Rysunek 8.23: FWHM and its uncertainty estimation for distribution along y -axis performed at position (1,0,0), (left) for TOF reconstructed image, it is equal to 7.38 ± 0.54 *mm*, and (right) Non-TOF reconstructed image, it is equal to 7.38 ± 0.11*mm*.
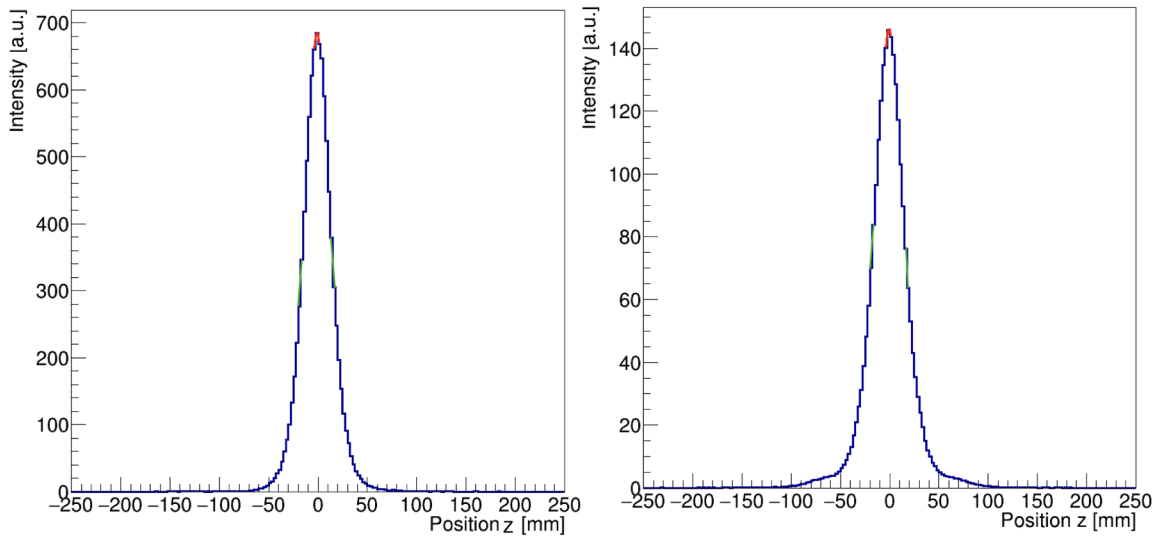
Rysunek 8.24: FWHM and its uncertainty estimation for distribution along z -axis performed at position (1,0,0), (left) for TOF reconstructed image, it is equal to 29.51 ± 0.52 *mm*, and (right) Non-TOF reconstructed image, it is equal to 34.43 ± 0.10*mm*.
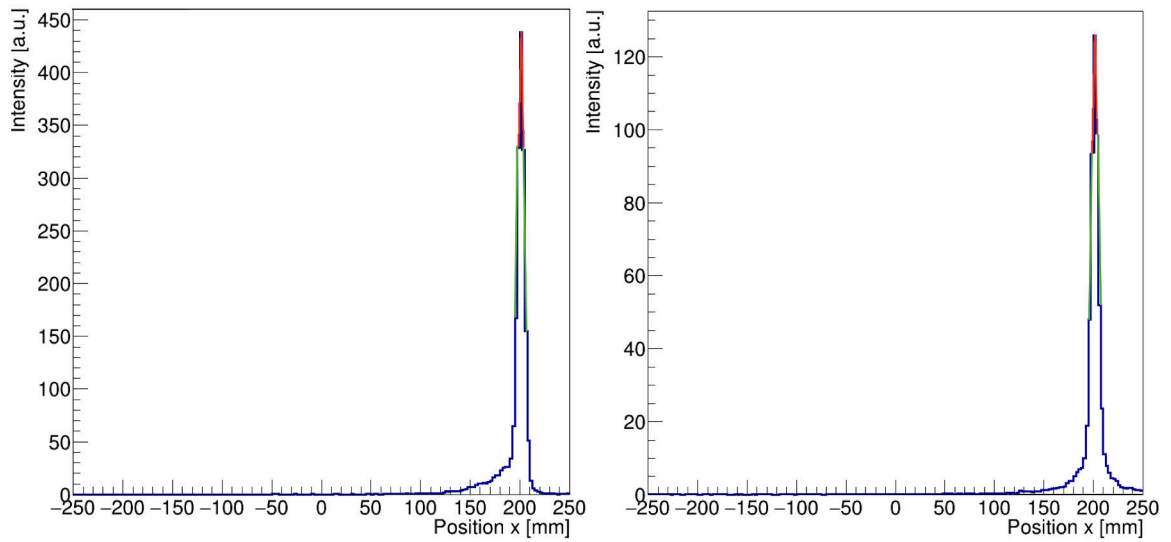
Rysunek 8.25: FWHM and its uncertainty estimation for distribution along x -axis performed at position (20,0,18.75), (left) for TOF reconstructed image, it is equal to 7.38 ± 0.37 mm, and (right) Non-TOF reconstructed image, it is equal to 7.53 ± 0.10 mm.
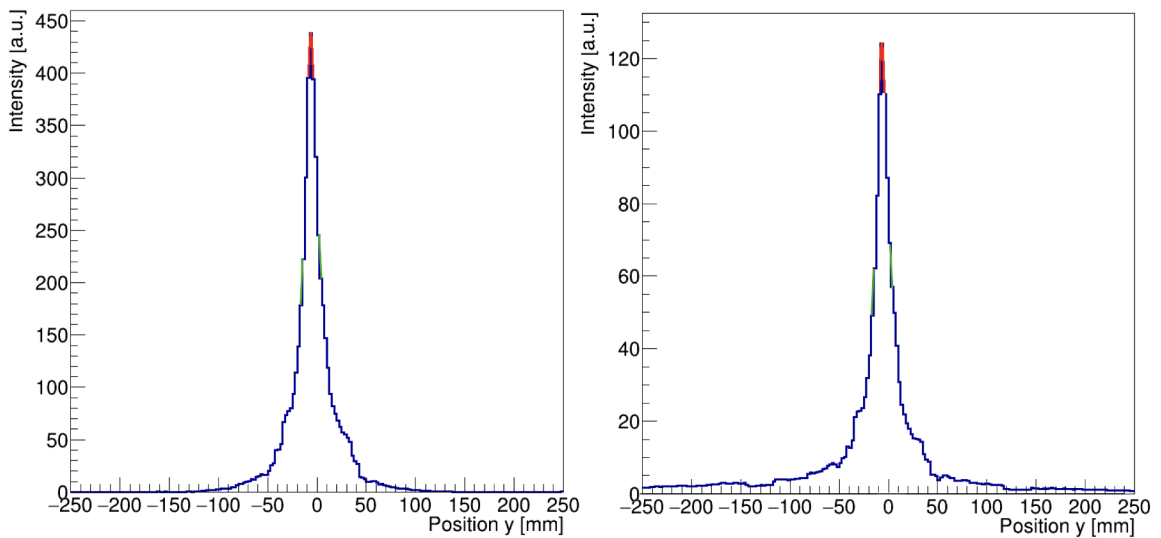
Rysunek 8.26: FWHM and its uncertainty estimation for distribution along y -axis performed at position (20,0,18.75), (left) for TOF reconstructed image, it is equal to 17.21 ± 0.32 mm, and (right) Non-TOF reconstructed image, it is equal to 14.42 ± 0.10 mm.
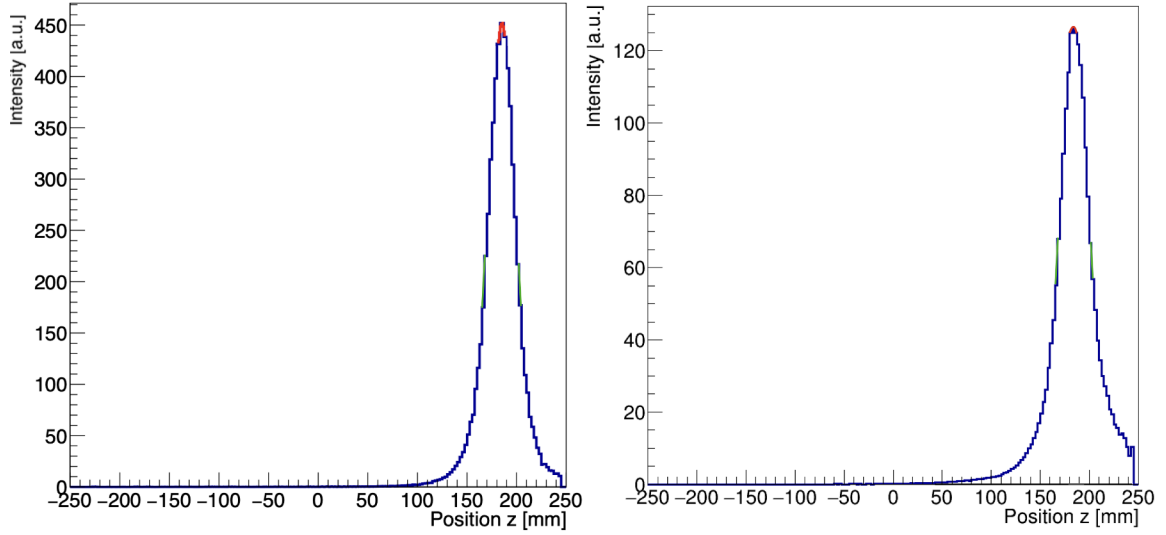
Rysunek 8.27: FWHM and its uncertainty estimation for distribution along z -axis performed at position (20,0,18.75), (left) for TOF reconstructed image, it is equal to 34.43 $\pm$ 0.28 mm, and (right) Non-TOF reconstructed image, it is equal to 35.00 $\pm$ 0.09 mm.

Tabela 8.3: FWHM values and uncertainties (in mm) for various positions: Comparison between TOF and Non-TOF image reconstruction methods. The radial FWHM represents values along the X-axis, the tangential FWHM represents values along the Y-axis, and the axial FWHM represents values along the Z-axis. All reported results were derived for the first iteration.

Source position (cm)		Radial FWHM (mm)	Tangential FWHM (mm)	Axial FWHM (mm)
(1,0,0)		4.92 $\pm$ 0.55	7.38 $\pm$ 0.54	29.50 $\pm$ 0.52
(10,0,0)		4.92 $\pm$ 0.13	7.38 $\pm$ 0.10	27.04 $\pm$ 0.51
(20,0,0)	TOF	6.50 $\pm$ 0.40	12.13 $\pm$ 0.30	29.50 $\pm$ 0.30
(1,018.75)		4.92 $\pm$ 0.57	7.38 $\pm$ 0.49	31.96 $\pm$ 0.52
(10,018.75)		9.83 $\pm$ 0.69	7.37 $\pm$ 0.10	34.42 $\pm$ 0.75
(20,018.75)		7.38 $\pm$ 0.37	17.21 $\pm$ 0.32	34.43 $\pm$ 0.28
(1,0,0)		4.92 $\pm$ 0.12	7.38 $\pm$ 0.11	34.42 $\pm$ 0.10
(10,0,0)		4.92 $\pm$ 0.30	7.38 $\pm$ 0.228	31.83 $\pm$ 0.56
(20,0,0)	Non-TOF	6.50 $\pm$ 0.09	12.50 $\pm$ 0.07	35.00 $\pm$ 0.09
(1,018.75)		4.92 $\pm$ 0.00	7.38 $\pm$ 0.12	34.42 $\pm$ 0.13
(10,018.75)		9.83 $\pm$ 0.17	7.21 $\pm$ 0.10	35.42 $\pm$ 0.20
(20,018.75)		7.53 $\pm$ 0.10	14.42 $\pm$ 0.10	35.00 $\pm$ 0.09
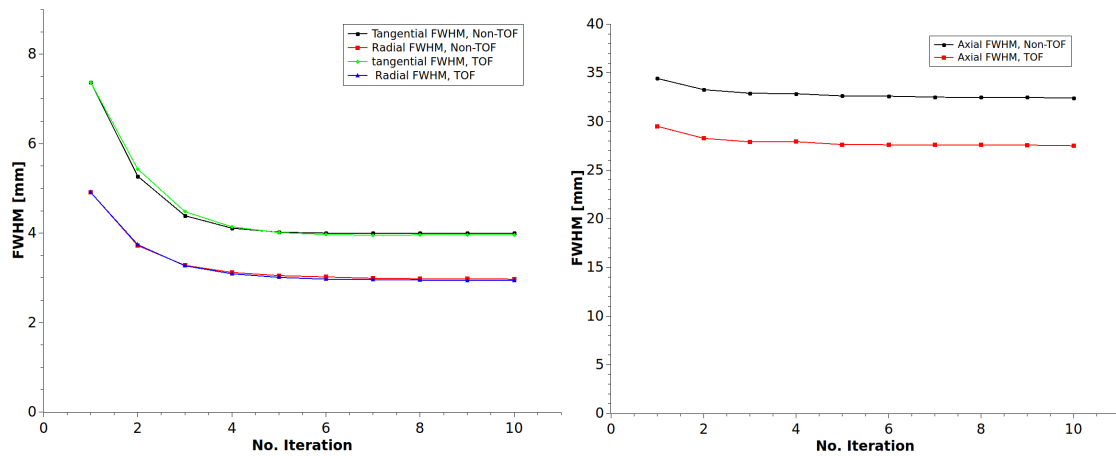
Rysunek 8.28: FWHM values as function of the iteration number for positions (1,0,0) in three direction. (left): Radial and tangential FWHM with TOF and Non-TOF image reconstruction methods, (right): Axial FWHM with TOF and Non-TOF image reconstruction methods. TOF image reconstruction methods is only improving axial PSF.

COMPARISON OF MODULAR J-PET WITH STATE OF THE ART PET SCANNERS

9.1 Commercial PET tomographs

The PET scanner market, valued at close to 1 billion US dollars, is predominantly governed by key industry players like: General Electric Healthcare (GE) [123], Siemens Healthcare [124], and Philips Healthcare [125], collectively claiming a market share of about 90%. Additionally, smaller PET scanner producers offer more than a dozen distinct scanner models, vying to introduce devices with advanced features. Research teams actively focus on enhancing scanner characteristics and developing cost-effective whole-body scanners.

The advent of Total-Body (TB) PET scanners has widened the scope of molecular imaging, enabling applications in various fields like cardiovascular disease, multi-organ imaging, physiological studies, treatment monitoring, and whole-body dynamic imaging [126, 127, 128]. These functionalities were previously unattainable due to the limited AFOV of conventional tomographs. Prototype scanners with expanded AFOV, such as the Total Body Biograph Vision Quadra tomograph, Total Body PENPET-Explorer tomograph, Total Body uExplorer tomograph, and the J-PET scanner—based on plastic scintillator strips discussed in this thesis—are examples of advancements in this area. The subsequent section outlines a detailed characterization of these devices.

9.1.1 Total Body uExplorer tomograph

The uExplorer system consists of 8 PET units aligned in an axial direction, each measuring 24.02 cm in axial length and 78.6 cm in diameter (detectors face-to-face), totaling a length of 194.0 cm. Each unit houses 24 detector modules, with 70 block-detectors arranged in a 5 × 14 matrix (transaxial × axial). These detectors are made

of LYSO crystals, each 2.76 × 2.76 × 18.1 mm, utilizing four 6 × 6 mm silicon photomultipliers for signal readout. In the transaxial direction, detectors share energy information for Compton-scatter recovery, while axial blocks do not communicate for this purpose. The uExplorer system encompasses 13440 detector blocks with 564480 LYSO crystals and 53760 silicon photomultiplier channels. This system is coupled with a 160-slice CT scanner, enabling helical acquisition with high precision and a minimum slice thickness of 0.5 mm. The patient bed is designed to ensure accurate alignment ($<$ 2 mm fusion accuracy) between PET and CT scans for precise imaging alignment [129].

Rysunek 9.1: Photograph of the uEuExplorer total-body PET/CT scanner installed at the EXPLORER Molecular Imaging Center in Sacramento, CA. Figure was adapted from [129].

The capability of each PET unit to generate coincidence events extends to unit differences within ±4, maintaining a maximum acceptance angle of 57.0°, as predetermined by the manufacturer. This configuration was consistently employed in all tests conducted in this study, with the exception of the NEMA NU 2-2018 spatial resolution

Location	position	Tangential FWHM (mm)	Radial FWHM (mm)	Axial FWHM (mm)
Center AFOV	1 cm	3.0	3.0	2.8
Center AFOV	10 cm	3.1	3.4	3.2
Center AFOV	20 cm	4.0	4.7	3.2
1/8th AFOV	1 cm	2.9	3.0	2.9
1/8th AFOV	10 cm	3.2	3.6	3.1
1/8th AFOV	20 cm	4.4	4.6	3.3

Tabela 9.1: Spatial resolution of ^{18}F point sources measured with Fourier-rebinned filtered back projection reconstruction. Table was adapted from [129].

test [129]. The installation of the uExplorer scanner took place at the EXPLORER Molecular Imaging Center, situated within UC Davis Health, in May 2019 (as depicted in Fig 9.1). Subsequent to its installation, the scanner's inaugural human imaging studies commenced in June 2019.

The system sensitivity, evaluated using a 70-cm line source containing a low activity of ^{18}F (approximately 4 MBq) and placed within a set of 5 concentric aluminum sleeves, measured 174 kcps/MBq at the center of the field of view and 177 kcps/MBq at a 10-cm radial offset.

For count-rate evaluation, a 70-cm-long scatter phantom was employed to assess the uExplorer's performance. Results detailing trues, scatters, random coincidences, and NECR were obtained from prompt- and delayed-coincidence SSRB sinograms displayed in Fig 9.2. The system achieved a peak NECR of 1,524 kcps with the 70-cm-long scatter phantom at a concentration of 17.3 kBq/mL, displaying an average scatter fraction of 36.3 Spatial resolution assessment involved imaging ^{18}F (about 300 kBq) capillary sources with an inner diameter of 0.5 mm and less than a 1-mm axial extent. Spatial resolution, as per NEMA NU 2-2018 standards using an ^{18}F point source and Fourier-rebinned filtered backprojection reconstruction, is summarized in Table 1.

9.1.2 Total Body PennPET-Explorer tomograph

The PennPET Explorer utilizes 64 lutetium-yttrium oxyorthosilicate scintillation crystals in an 8 × 8 array, each measuring 3.86 × 3.86 × 19 mm³. These crystals pair with
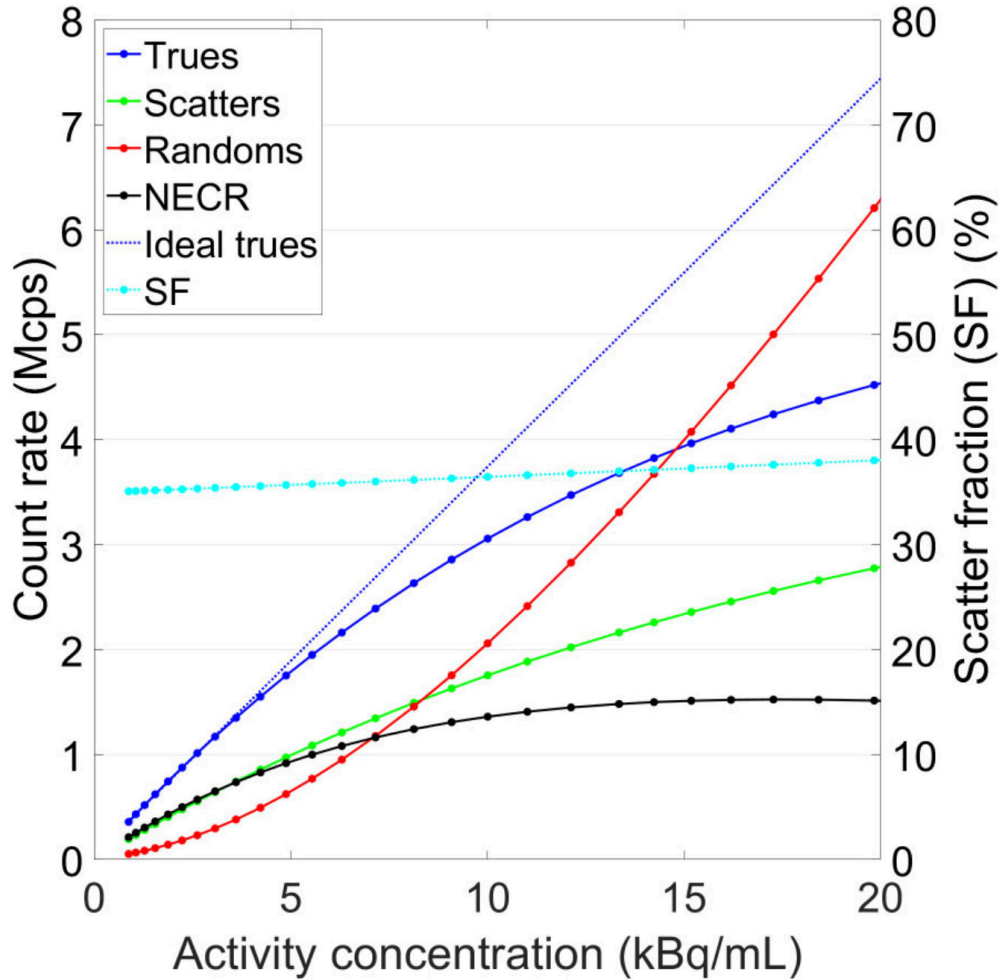
Rysunek 9.2: Measured count-rates with 70-cm-long scatter phantom. Count-rate measures are plotted vs. left vertical axes; scatter fractions are plotted vs. right vertical axes. Figure was adapted from [129].

a digital SiPM by Philips Digital Photon Counting, providing ideal crystal identification, high count-rate capability, and excellent timing resolution. Operating at 5°C with close ring spacing, the system maintains a cool, dry environment independently of ambient conditions. Each ring segment, 76.4 cm in diameter and 22.9 cm axially, houses 18 modules of 28 detector tiles in a 4 × 7 array, with the prototype comprising 3 ring segments (see Fig. 9.3) [103]. The prototype 3-ring-segment system underwent performance measurements to enhance hardware, software, and exhibit the Penn-PET Explorer's capabilities. Due to gaps between ring segments, system sensitivity halved, reducing the Axial Field of View (AFOV) from 70 to 64 cm. All evaluations
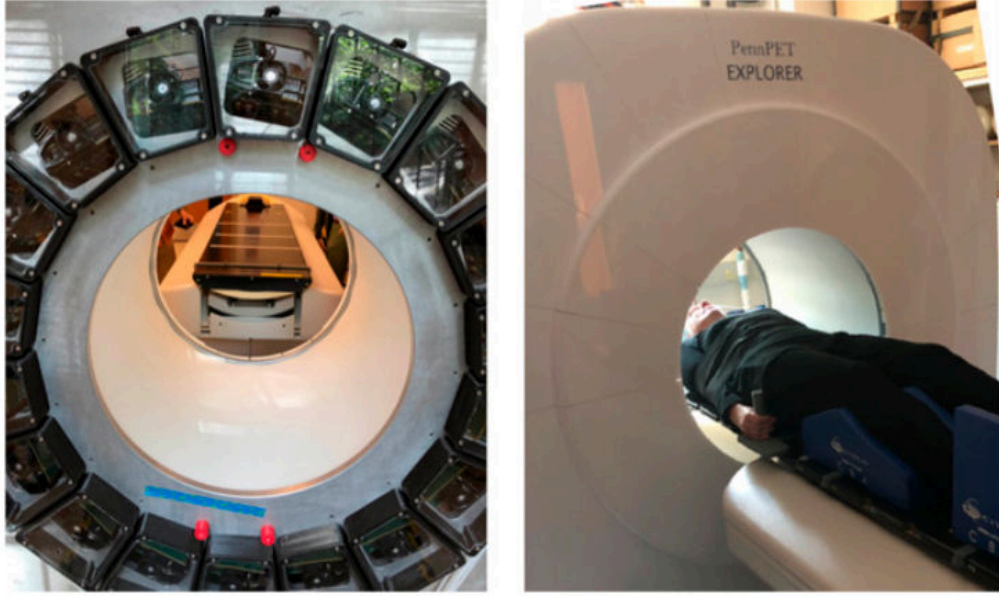
Rysunek 9.3: Prototype configuration of the PennPET Explorer, featuring three ring segments enclosed in a dry, cool environment. The rear view of the gantry exhibits modular detector and electronic bays, along with the couch featuring a flat pallet installed for human studies. Figure was adapted from [103].

were conducted using a fixed 440–660 keV energy window and a 4 ns coincidence window.

Sensitivity measurements were taken at two positions (at 0 cm and 10 cm offset from the center of the FOV detector) using a 70-cm-long ^{18}F line source encased in aluminum tubes. The sensitivity recorded was 54 kcps/MBq at 0 cm radius and 57 kcps/MBq at 10 cm offset from the center of the FOV detector.

Count-rate measurements were carried out using a 70-cm long ^{18}F line source positioned within a scatter phantom, initially set at an activity concentration of about 40 kBq/mL. Figure 9.4 illustrates the count-rate performance. The calculated scatter fraction remains constant at 32% within this activity range. Additionally, the NECR gradually increases beyond the point where trues equal randoms (at 15 kBq/mL), reaching 1,050 kcps at 38 kBq/mL.

Spatial resolution was determined by imaging a 0.5-mm-diameter ^{22}Na point source encapsulated within a $1cm^3$ plastic cube at various radial (1, 5, 10, 15, and 20 cm) and axial (0, 4, 12, 20, 24, and 28 cm) positions concerning the AFOV center.
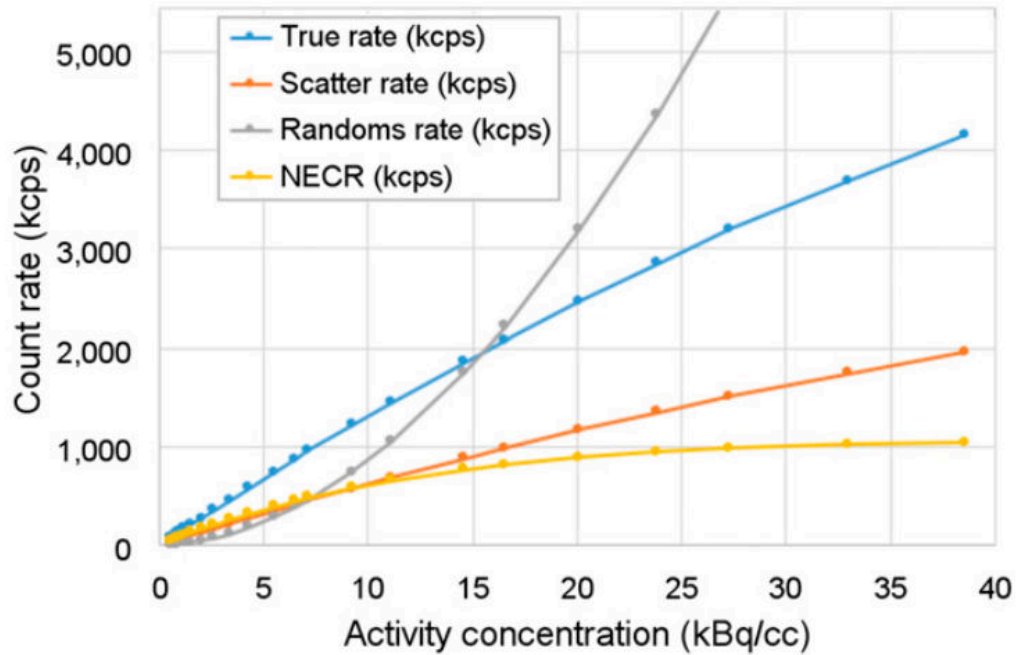
Rysunek 9.4: The The results of the NEMA NU-2 count-rate performance, using a 70-cm line source placed within a 20-cm-diameter polyethylene scatter cylinder for the PennPET detector. Figure was adapted from [103].

The results were obtained for LM-OSEM iterative reconstruction using parameters optimized for high-resolution imaging ($1cm^3$ voxels, 4 iterations). Tables 9.2 present a summary of the spatial resolution outcomes for LM-OSEM, utilizing data from both 1-ring-segment and 3-ring-segment (axial acceptance angle from 8° to 40°).

9.1.3 Total Body Biograph vision Quadra tomograph

The Biograph Vision Quadra is built upon the technology initially developed for the Biograph Vision 600 PET/CT system [111]. It incorporates lutetium-oxoorthosilicate crystals measuring $3.2, mm \times 3.2, mm \times 20, mm$, directly coupled to a SiPM array featuring 16 output channels. Each detector block comprises eight mini-blocks, where adjacent detector blocks share a common electronic unit. With a total axial span of 320 crystals and a 78 cm transaxial FOV, the Biograph Vision Quadra achieves an AFOV spanning 106 cm. The system captures all possible LORs utilizing a maximum full ring difference (MRD) of 85 crystal rings, offering an acceptance angle of 52°. For

Rings	Radius	Tangential FWHM (mm)	Radial FWHM (mm)	Axial FWHM (mm)
1	1 cm	3.9 ± 0.3	3.8 ± 0.3	3.6 ± 0.3
1	10 cm	-	-	-
1	20 cm	-	-	-
3	1 cm	3.9 ± 0.2	3.9 ± 0.3	3.9 ± 0.3
3	10 cm	4.2 ± 0.2	3.9 ± 0.2	3.9 ± 0.3
3	20 cm	5.6 ± 0.2	3.9 ± 0.4	3.7 ± 0.3

Tabela 9.2: Transverse Spatial Resolution of PennPET Explorer Whole-Body Imager. Table was adapted from [103],

Axial position (cm)	Axial position (cm)	Tangential FWHM (mm)	Radial FWHM (mm)	Axial FWHM (mm)
13.3	3.19	3.58	3.78	
13.3	10	4.38	3.47	3.84
13.3	20	5.82	3.12	4.21
53.0	1	3.35	3.31	3.77
53.0	10	4.38	3.53	3.90
53.0	20	5.84	3.33	4.27

Tabela 9.3: Spatial resolution in MRD 85 mode. Table was adapted from [111].

all performance measurements, a coincidence time window of 4.7 ns was utilized.

The performance evaluation of the Biograph Vision Quadra PET/CT system, installed at the nuclear medicine department of Inselspital Bern, was benchmarked according to the NEMA NU 2-2018 standard. Spatial resolution was assessed at six different positions using a point source with a 0.25 mm diameter containing 393 kBq of ^{22}Na. Table 9.3 details the spatial resolution results in MRD 85 mode.

For the count rate measurements, a 3 mm wide and 70 cm long polyethylene capillary was filled with 894 MBq of ^{18}F and placed inside a scatter phantom. Prompt and random sinograms were generated for each acquisition and each slice. Due to the extended AFOV of the Quadra, only slices within the central 65 cm of the AFOV were employed for histogram generation. Figure 9.5 depicts count rate plots for trues, randoms, scatter, and NECR measured at MRD 85. Observations revealed that all events were recorded irrespective of the MRD setting, with a peak NECR of 1613 kcps observed at 27.49 kBq/mL.
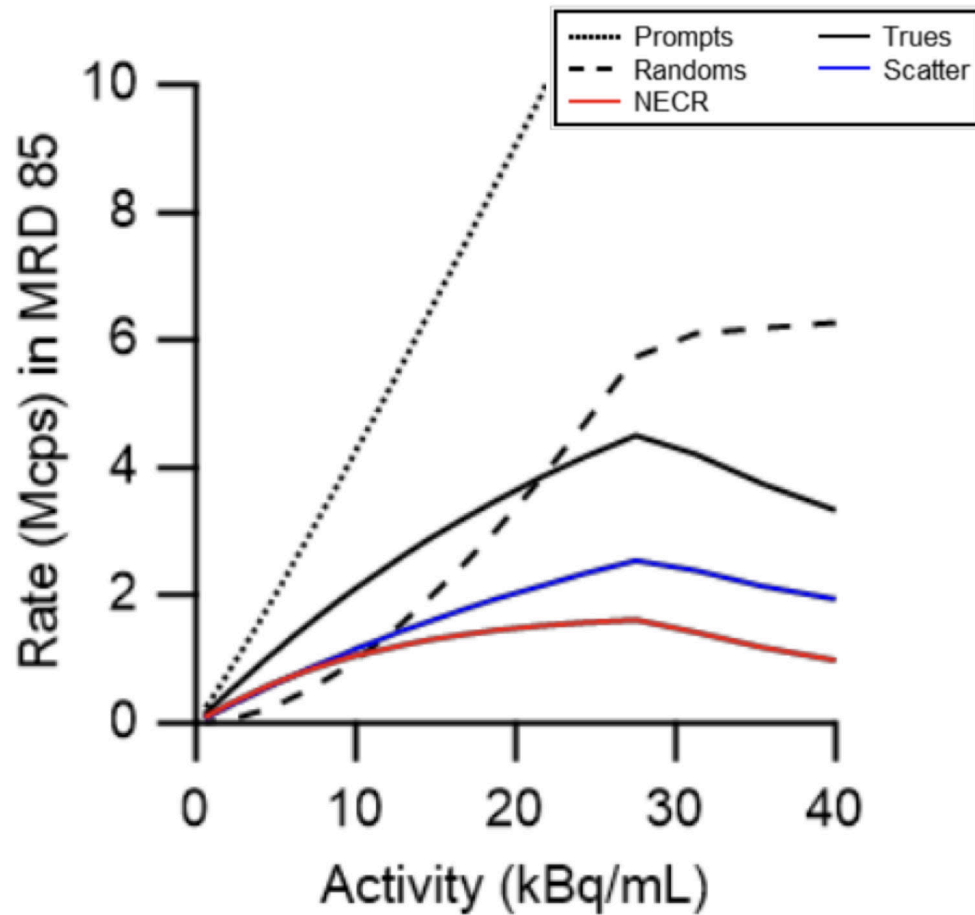
Rysunek 9.5: Graphs representing prompt, random, true, scatter, and NEC rates for MRD 85. Figure was adapted from [111].

The sensitivity measurements utilized the same 70 cm long polyethylene capillary, filled over a total length of 68 cm with an aqueous solution of 4.56 MBq of ^{18}F. Surrounding the line source were five concentric aluminum sleeves of matching length, each with known radiation attenuation. The system's sensitivities for MRD 85 at the center of the detector measured 82.6 cps/kBq and at a 10 cm offset from the center, registered 84.1 cps/kBq. Thus, the average system sensitivities amount to 83.4 cps/kBq for MRD 85.

9.2 Comparison performance characteristics of commercial PET tomograph

The production and deployment expenses associated with PET devices using crystal scintillators currently restrict their broad application in diagnostic, therapeutic, and research facilities. Presently, many PET developers recognize the substantial construction costs of these systems as a major impediment and are actively seeking cost-effective alternatives. The incorporation of budget-friendly components in the construction of the J-PET, such as plastic detectors and a minimized quantity of photomultipliers, significantly reduces the overall production costs of the total-body PET system. While the total-body EXPLORER, employing inorganic scintillators, is estimated to cost around 10 million euros, the total-body Modular J-PET scanner, featuring a 200 cm AFOV, is estimated to cost approximately 2 million euros. Leveraging the substantial reduction in scintillator cost and a decreased SiPM quantity in contrast to the uEXPLORER, it can be asserted that the J-PET technology showcases promising performance in both imaging attributes [1] and cost efficiency perspectives.

In Tab. 9.4, we outline the performance characteristics of plastic detectors in the Modular J-PET scanner and various commercial PET tomographs. The scatter fraction of $(41.68 \pm 6.27)\%$ in the Modular J-PET falls within the expected range seen in other systems. As a metric for comparing cost-effective Total-Body PET scanners, scanner sensitivity has been paramount. The system sensitivity of the J-PET is lower than that of the total-body scanner, yet it is comparable to the sensitivities of current commercial tomographs.

Augmenting the sensitivity of the Modular J-PET is feasible by introducing a second detection layer or extending the AFOV. This enhancement, through the enlargement of the AFOV, predominantly boosts the scanner's sensitivity with the increase in axial length. The J-PET scanner, constructed with plastic scintillator strips equipped with two photodetectors at their ends, offers an advantageous solution in expanding the AFOV. Unlike other solutions in the market, where the addition of crystals, photomultipliers, channels, computing power, or power supply significantly

150

escalates costs, the process of enlarging the AFOV in the Modular J-PET necessitates solely the replacement of strips (without altering the read-out elements). Although the using the large length of plastic scintillators results in larger spatial resolution in the axial direction, but enhancing the axial spatial resolution in plastic scintillators can be achieved by employing a Wavelength Shifter (WLC) between the layers.

Moreover, the Modular J-PET scanner offers flexibility in adjusting the diameter of the detection chamber by adding or removing modules, thereby tailoring the scanner to imaging needs and patient size (refer to Fig 9.6). Modular J-PET scanner assembly functions at room temperature with regular humidity and requires no dedicated air-conditioning system. The system's power requirements remain low due to the minimal number of photomultipliers and signal processing units. In summary, the J-PET technology presents a total-body PET scanner with numerous advantages, delivering performance characteristics comparable to both existing commercial and presently developed PET devices.
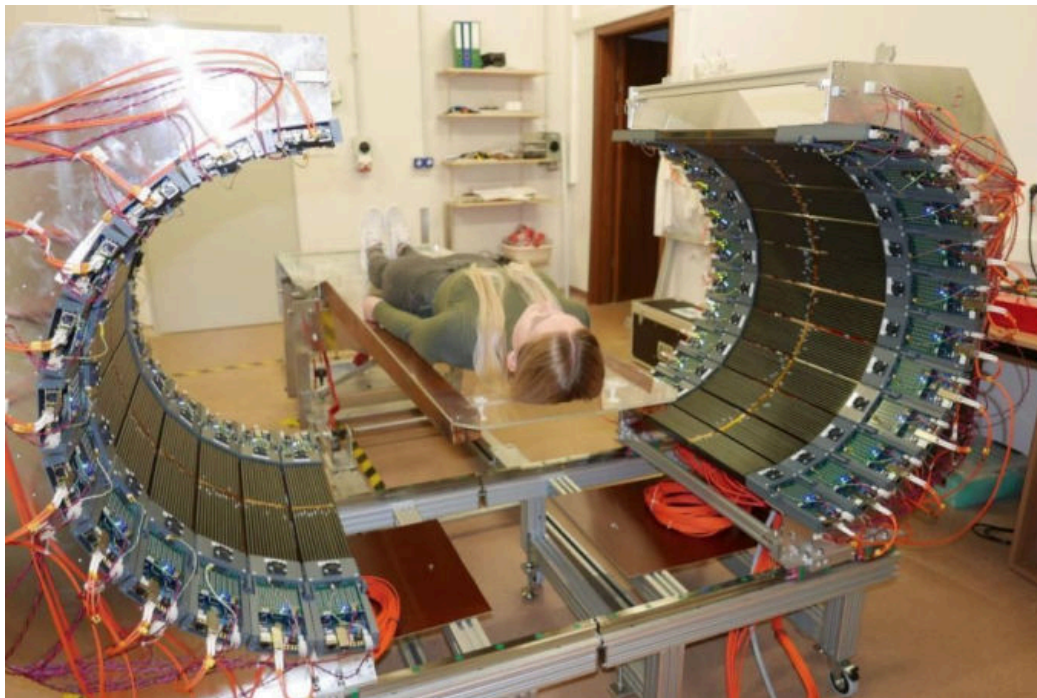
Rysunek 9.6: The Modular J-PET prototype, installed in the laboratory in the Jagellonian University, while it is being closed the system around a student already lying on the table.

	Modular J-PET	Total Body uExplorer	PENPET Explorer	Biograph Vision Quadra
Company/facility	Jagellonan University, J-PET group	UC Davis and United Imaging Healthcare	UPenn, KAGE Medical and Philips	Siemens Healthineers, Turku PET
Scintillator type	BC-404	LSO (18.1 mm)	LYSO (19mm)	LSO (20 mm)
Light sensor	MPPC-1X4CH-ARRAY S13361-6674	SensL J-series	Philips Digital Photon Counting	MRD 85
Type of light sensor	Analog	Analog	Digital	Analog
Scintillator cross section (mm^2)	24 × 6	2.76 × 2.76	3.86 × 3.86	3.2 × 3.2
Axial length (cm)	50	194	64	106
Diameter (cm)	73.9	74	76.4	82
No. of modules	24	-	18	38
No. rings	1	-	3	32
Time window (ns)	4	4.5-6.9	4	4.7
Energy window (keV)	> 200	430–645	440-600	435 - 585
Sensititvity in center (cps/kBq)	2.1	174	54	82.6
Sensitivity in 10 cm offset from center(cps/kBq)	1.8	177	57	84.1
Scatter fraction (%)	41.68 ± 0.19	36.3	32	37
Radial FWHM (mm)	4.9 ± 0.2	3.0	3.9 ± 0.4	3.19
Tangential FWHm (mm)	6.1 ± 0.2	3.0	3.9 ± 0.4	3.58
Axial FWHM (mm)	30.10 ± 0.01	2.8	4.1 ± 0.2	3.78

Tabela 9.4: A comparison between the Modular J-PET plastic detector and the various commercial PET tomographs.

ROZDZIAŁ 10

SUMMARY AND PROSPECT FOR TOTAL BODY J-PET TOMOGRAPH

The thesis encompasses a comprehensive examination, investigating the performance characteristics of the Modular J-PET. A thorough analysis and assessment of the NEMA standards were conducted for the J-PET device, focusing on evaluating spatial resolution, scatter fraction, NECR, and sensitivity based on the NEMA NU2-2018 standard. Additionally, it involves validating the experimental data obtained from the Modular J-PET scanner using Monte Carlo modeling with GATE simulations.

10.0.1 Sensitivity

Sensitivity measurements were conducted using a sensitivity phantom consisting of 5 aluminum sleeves, positioned at the center of the detector's FOV and also at a 10 cm offset from the center of the detector's FOV. A 70 cm ^{68}Ge source with an activity of 2.6 MBq was employed for the sensitivity measurement. The normalized activity was determined based on the length of the plastic scintillator to calculate the system's sensitivity.

The sensitivity profiles were estimated for the Modular J-PET scanner using varying multiplicity cuts, demonstrating that the sensitivity increases as the multiplicity number decreases, reaching comparable results with the simulations for a multiplicity greater than or equal to 5. This similarity is attributed to the absence of optical photon simulations in the simulation phase. Figure 10.1 presents the axial sensitivity profile for experimental data with different multiplicity cuts and simulation results for a 1 sleeve phantom at the center of the detector. The peak sensitivity profile for experimental data with multiplicity cuts greater than or equal to 5 is 2.4 cps/kBq, while for simulation results, it is 2.9 cps/kBq in the center of the detector. Furthermore, the results of the sensitivity simulation demonstrate that the system sensitivity for the J-PET system at the center of the detector's FOV and at a 10 cm offset from

the center of the detector's FOV are 1.324 $\pm$ 0.032 cps/kBq and 1.313 $\pm$ 0.0017 cps/kBq, respectively.

The sensitivity of the Modular J-PET is expected to increase by extending the length of the plastic scintillator strips and employing a multi-layer PET scan, as previously discussed in Chapter 9.
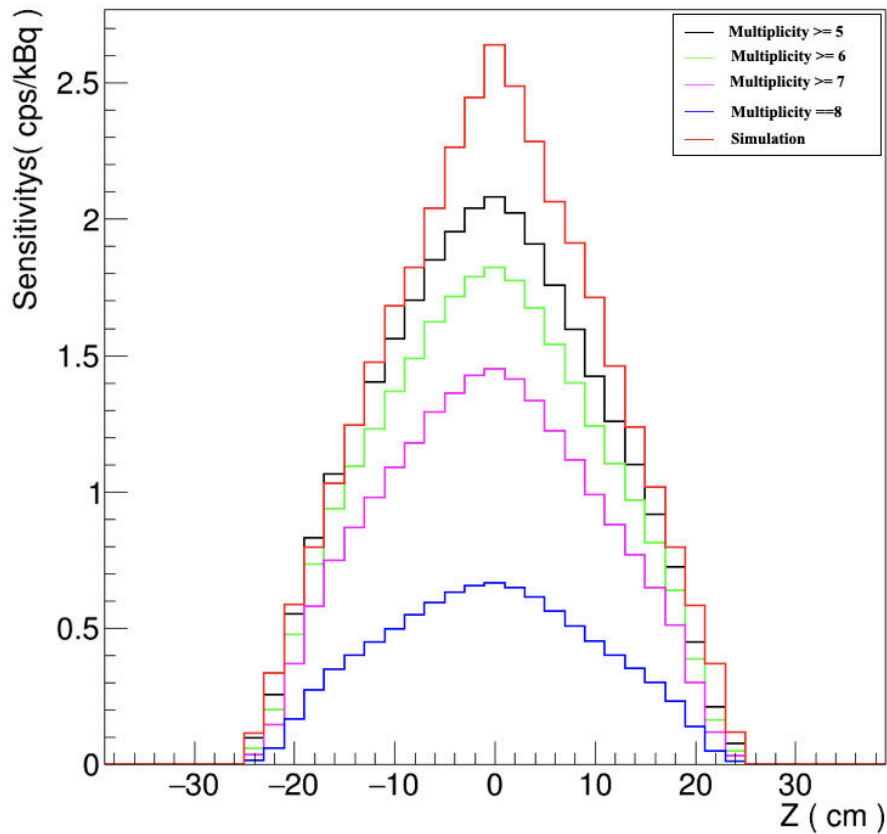
Rysunek 10.1: Axial sensitivity profile for the smallest sleeve in the center of the FOV detector for different multiplicity cuts. Red line presents the axial sensitivity profile for the center of the detector from simulation part.

10.0.2 Scatter fraction, count rate

Scatter fraction measurements were conducted using the PET Scatter Phantom positioned on the dedicated bed and aligned at the detector's FOV. The insert, housing an ^{18}F source, was placed with a 4.5 cm offset in the bed direction and centered along the detector's axial FOV. Data was collected over a duration of 3 hours with varying activity, ranging from 7.5 MBq to 2.4 MBq, adhering to preselection criteria

outlined in Chapter 7. Utilizing SSRB algorithms, the calculated scatter fraction for the Modular J-PET was determined to be 41.68 $\pm$ 0.19 %. The count rates and NECR were computed for average activity concentrations ranging from 0.11 kBq/cc to 0.34 kBq/cc. Notably, at an average activity concentration of 0.342 kBq/cc, the recorded peak total, true, scatter count rates, and NECR were 31.19 $\pm$ 0.52 (*cps*), 18.18 $\pm$ 0.99 (*cps*), 13.00 $\pm$ 1.08 (*cps*), and 10.60 $\pm$ 1.17 (*cps*), respectively.

To assess the count-rate performance with GATE software, a simulation of a scatter phantom with a length of 70 cm and a 70 cm ^{18}F line source at varying activities was conducted for the Modular J-PET scanner. Utilizing the SSRB algorithms, the scatter fraction calculated from the simulation results for the Modular J-PET was $(40.3 \pm 2.3)\%$.

Figures 10.2 and 10.3 illustrate the comparison between the measured and simulated true, scatter, and total coincidence count rates, NECR, and scatter fraction as functions of activity concentration in the 70 cm phantoms of the Modular J-PET scanner. The simulations identified a peak NECR of 12.75 cps at an activity concentration of 0.34 kBq/cc. A good agreement between the simulated and experimentally measured plots of true, scatter, and total count rates is depicted in Figures 10.2. However, the relative difference between the simulated and measured peak NECR was found to be 9.86%. Additionally, the relative difference between the simulated and experimental results of scatter fraction was 3.43%. The observations regarding the random event rate suggest a minimal occurrence of random events detected in both the measurement and simulation.
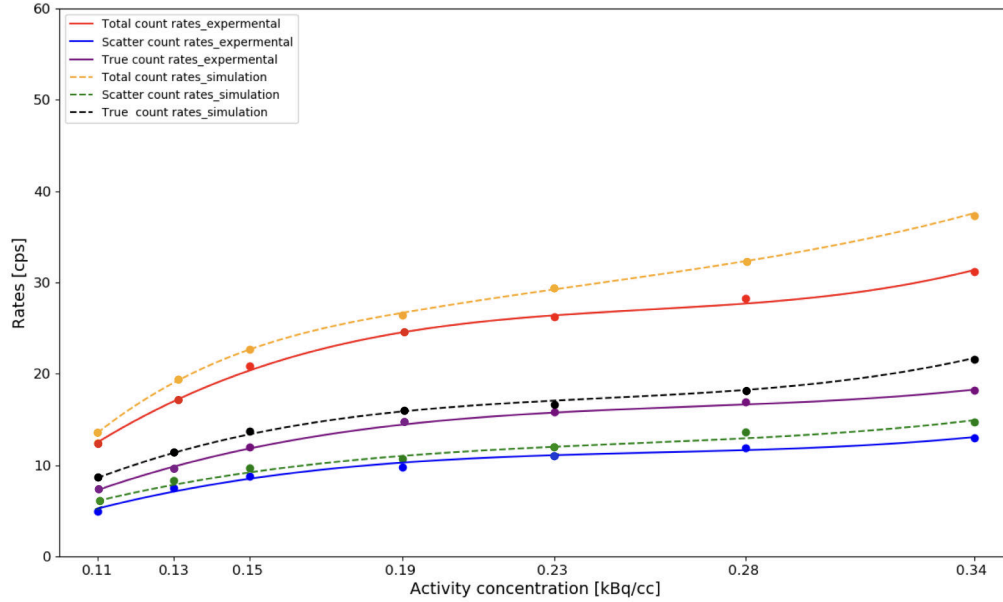
Rysunek 10.2: Comparison Plots: Simulated and Experimentally Measured Total, True, and Scatter Coincidence Count Rates as function of average activity concentration (kBq/cc) for the 700 mm Long Phantom in the Modular J-PET Scanner.
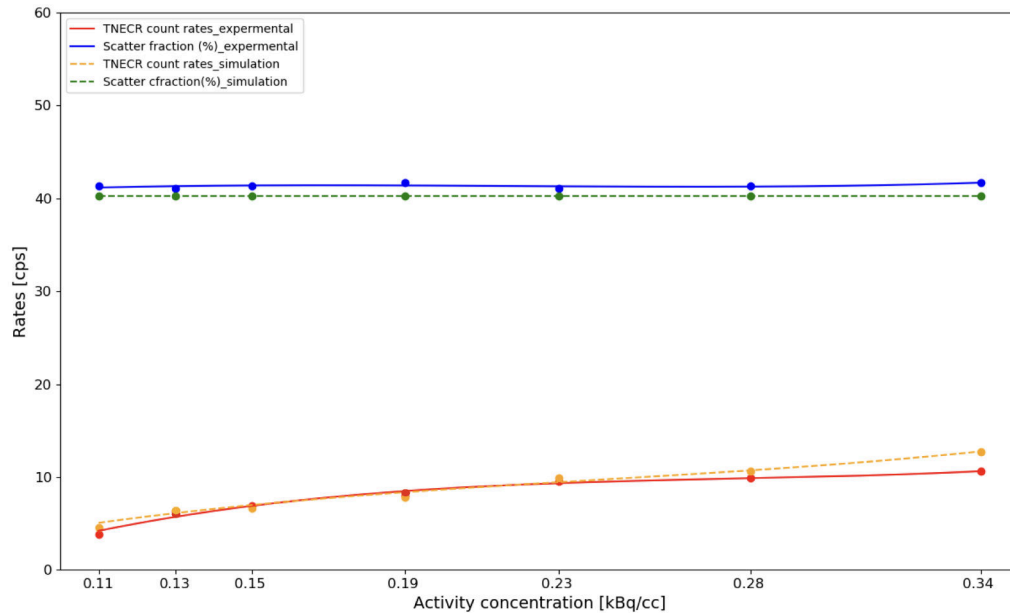
Rysunek 10.3: Comparison Plots: Simulated and Experimentally Measured NECR Count Rates and scatter fraction as function of average activity concentration (kBq/cc) for the 700 mm Long Phantom in the Modular J-PET Scanner.

10.0.3 Spatial resolution

For the measurement of spatial resolution, a ^{22}Na point source with an activity of 9.2 MBq was placed inside a Plexiglas rod. These point sources were positioned at axial distances of zero and three-eighths of the AFOV and radial distances of 1, 10, and 20 cm, following the NEMA standard. Data were collected separately for each source position and reconstructed using the Maximum Likelihood Expectation-Maximization (MLEM) iterative algorithm by QETIR software for both TOF and Non-TOF List Mode data.

The FWHM and its uncertainty for all positions are presented in Table 10.1 for TOF List Mode data. The average radial FWHM was calculated to be 4.91 ± 0.56 mm, 7.37 ± 0.41 mm, and 6.93 ± 0.39 mm at positions 1 cm, 10 cm, and 20 cm from the detector's center, respectively. The average tangential spatial resolution was determined as 7.37 ± 0.52 mm, 7.37 ± 0.10 mm, and 14.67 ± 0.30 mm at the same positions, while the average axial FWHM was calculated as 30.73 ± 0.52 mm, 30.73 ± 0.63 mm, and 31.96 ± 0.29 mm.

In the simulation part, a ^{22}Na point-like source with a diameter of 0.5 mm and an activity of 9.2 MBq was simulated in the same six positions as the experimental measurement. The results of the spatial resolution simulation were reconstructed using the MLEM iterative algorithm. The FWHM and its uncertainty for all positions are presented in Table 10.1 for both the experimental and simulated spatial resolution in the tangential, radial, and axial directions. The average radial spatial resolution for simulation was found to be 4.80 ± 0.59 mm, 7.26 ± 0.55 mm, and 6.67 ± 0.42 mm at positions 1 cm, 10 cm, and 20 cm from the detector center, respectively. The average tangential spatial resolution was determined as 7.27 ± 0.47 mm, 7.27 ± 0.59 mm, and 15.1 ± 0.4 mm at the same positions, while the average axial spatial resolution was calculated as 29.97 ± 0.49 mm, 30.53 ± 0.74 mm, and 31.78 ± 0.11 mm. The differences between simulation and experimental data are also presented in Table 10.1.

Tabela 10.1: FWHM for simulation and expemental part

Location	Position (cm)	Radial FWHM [mm]		Tangential FWHM [mm]		Axial FWHM [mm]	
		Experimental	Simulation	Experimental	Simulation	Experimental	Simulation
Center of AFOV	1	4.92 ± 0.55	4.80 ± 0.45	7.38 ± 0.54	7.27 ± 0.25	29.50 ± 0.52	29.05 ± 0.54
	10	4.92 ± 0.13	4.80 ± 0.54	7.38 ± 0.10	7.27 ± 0.66	27.04 ± 0.51	27.00 ± 0.89
	20	6.50 ± 0.40	6.08 ± 0.74	12.13 ± 0.30	12.37 ± 0.89	29.50 ± 0.30	29.50 ± 0.94
3/8 of AFOV	1	4.92 ± 0.57	4.80 ± 0.12	7.38 ± 0.49	7.27 ± 0.41	31.96 ± 0.52	30.89 ± 0.43
	10	9.83 ± 0.69	9.73 ± 0.56	7.37 ± 0.10	7.27 ± 0.399	34.42 ± 0.75	34.06 ± 0.58
	20	7.38 ± 0.37	7.27 ± 0.11	17.21 ± 0.32	17.83 ± 0.14	34.43 ± 0.28	34.06 ± 0.13

10.1 Prospect for Total Body J-PET tomograph

Th conventional PET scanners with AFOV 15-30 cm have limitations in terms of image quality and dynamic imaging. Increase of the AFOV to cover the total-body offer better diagnostic capabilities but are costly. There is a need for affordable alternatives to make Total Body PET more accessible for clinical use, facilitating research in areas like drug delivery and treatment planning [130].

J-PET tomography is an innovative technology made of plastic scintillators. Unlike traditional PET scanners with radial detectors, J-PET uses an axial arrangement of detection panels. This unique design allows for a cost-effective Total Body PET scanner with a long axial field of view (AFOV) of up to 2.5 meters [130, 4].

The Total Body J-PET scanner is composed of 24 detection panels arranged axially in a cylindrical configuration, with a length of 200 cm. Each panel is comprised of 2 modules, with an array of wavelength-shifting (WLS) strips positioned between them. The module, serving as the detection unit, consists of 16 plastic scintillation strips, each with dimensions of 6 mm $\times$ 30 mm $\times$ 200 cm. These strips are coupled with silicon photomultipliers at both ends, as illustrated in Figure 10.4 [104]. Modularity in PET construction allows for adjustable imaging chambers, benefiting patients with varying sizes or conditions such as obesity or claustrophobia.

The future of cost-effective Total Body PET diagnostics lies in plastic scintillators and the implementation of the J-PET concept. The cost of plastic Total body PET components is approximately five times lower than that of crystal-based systems [4]. Crystal scintillators constitute a significant portion of the total costs in crystal-based Total body PET scanners. Plastic scintillators are over ten times less expensive than LYSO crystals. In addition, major part of the Total Body PET comes from electronics and SiPMs, which is reduced in plastic Total Body PET with axially arranged scintillator strips, as the readout is mainly located at the ends of the cylindrical detector rather than covering the full cylinder surface as in crystal-based PET detectors. Overall, the cost of electronics in plastic Total Body J-PET is proportional to the trans-axial cross-section of the detector, while in crystal-based Total Body PET, it

is proportional to the area of the detection cylinder. As a result, plastic Total Body J-PET may be more than five times less expensive than crystal-based Total Body PET, making it a practical and cost-effective solution for a wide range of clinical applications [4].
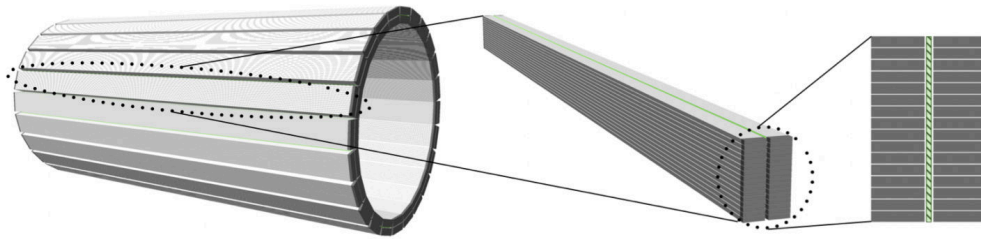
Rysunek 10.4: (Left) Visualization of the Total Body J-PET scanner with GATE software. (Middle) illustration of the panel composed of two modules. (Right) Transvers illustration of the detection panels and WLS (hashline pattern) in between. Figure is adapted from [104].

SPIS TABEL

165

166

168

171

REFERENCES

[1] P. Moskal, P. Kowalski, R. Shopa, and et al., "Phys. med. biol.," vol. 66, no. 17, ac16bd, 2021.

[2] P. Moskal, S. Niedzwiecki, T. Bednarski, and et al., "Nucl. instrum. meth. a," vol. 764, 317–321, 2014.

[3] P. Moskal, S. Niedźwiecki, and et al., "Acta phys. pol. b," vol. 48, no. 1757, 2017.

[4] P. Moskal and E. Stępień, "Pet clin," vol. 15, no. 4, 439–452, 2020.

[5] P. Moskal, O. Rundel, D. Alfs, and T. Bednarski, "Phys. med. biol.," vol. 61, no. 5, 2025–2047, 2016.

[6] National Electrical Manufacturers Association (NEMA). Rosslyn, VA, 2018, Standards Publication NU 2-2018.

[7] World Health Organization. https://www.who.int/news-room/fact-sheets/ detail/cancer. (2022).

[8] D. N. Louis and et al., "Neuro oncol," vol. 23, 2021.

[9] C. Catana, A. R. Guimaraes, and B. R. Rosen, "J nucl med," vol. 54, no. 5, pp. 815–824, 2013.

[10] L. K. Griffeth, "Proc (bayl univ med cent)," vol. 18, no. 4, pp. 321–330, 2015.

[11] R. J. Gillies and T. Beyer, "Cancer res," vol. 76, no. 21, pp. 6163–6166, 2016.

[12] J. B. S. Joshua L Ryan Vasantha D Aaron, "Seminars in ultrasound, ct and mri," vol. 40, no. 5, pp. 376–390, 2019.

[13] Cleveland Clinic. "PET Scan." https://my.clevelandclinic.org/ health/ diagnostics/ 10123-pet-scan. (2023).

[14] A. Alavi, T. J. Werner, E. Stępień, and P. Moskal, "Bio-algorithms and med-systems," vol. 17, no. 4, pp. 203–212, 2021.

[15] M. E. Mayerhoefer, H. Prosch, L. Beer, and et al., "Eur j nucl med mol imaging," vol. 47, no. 1, pp. 51–60, 2020.

[16] S. D. Voss, "Pediatr radiol," vol. 53, no. 7, pp. 1443–1453, 2023.

[17] O. Martin and e. a. Schaarschmidt, "Journal of nuclear medicine," vol. 61, no. 8, pp. 1131–1136, 2020.

[18] S. Vandenberghe, P. Moskal, and J. S. Karp, "Ejnmmi physics," vol. 7, no. 1, p. 35, 2020.

[19] M. Kapoor and A. Kasi, Updated 2022 Oct 3. Available from: https:// www.ncbi. nlm.nih.gov/ books/ NBK559089/, 2022.

[20] S. Vandenberghe et al., "Ejnmmi physics," vol. 3, p. 3, 2016.

[21] P. Moskal and E. Stępień, "Bio-algorithms and med-systems," vol. 17, no. 4, 199–202, 2021.

[22] T. Hui, Y. Gu, and et al., "Americantitle of roentgenology," vol. 215, no. 2, pp. 1–13, 2020.

[23] S. Surti, M. E. Werner, and J. S. Karp, "Physics in medicine & biology," vol. 58, pp. 3995–4012, 2013.

[24] S. Surti and J. S. Karp, "Physics in medicine & biology," vol. 60, pp. 5343–5358, 2015.

[25] A. R. Pantel and et al., "Journal of nuclear medicine," vol. 63, no. 5, pp. 646–648, 2022.

[26] New Choice Health , 2022, https://www.newchoicehealth.com/procedures/whole-body-pet-scan. ().

[27] S. R. Cherry, Jones, and et al., "Journal of nuclear medicine," vol. 59, no. 1, pp. 3–12, 2018.

[28] P. Kowalski, W. Wiślicki, and et al., "Acta physica polonica b," vol. 47, p. 549, 2016.

[29] W. Krzemień and Świerk. NCBJ, "Acta physica polonica b," vol. 47, p. 561, 2016.

[30] N. G. Sharma, M. Silarski, and et al., "Jchps," vol. Special Issue 4, pp. 27–30, 2016.

[31] L. Raczyński, W. Wiślicki, and et al., "Physica medica," vol. 80, pp. 230–242, 2020.

[32] P. Moskal, T. Bednarski, and et al., "Nuclear med. rev.," vol. 15C, pp. 68–69, 2012.

[33] P. Moskal, Salabura, and et al., "Bio-algorithms and med-systems," vol. 7, pp. 73–78, 2011.

[34] D. Kamińska, A. Gajos, and et al., "Eur. phys. j. c," vol. 76, p. 445, 2016.

[35] P. Moskal, N. Zoń, and et al., "Nucl. instrum. meth. a," vol. 775, pp. 54–62, 2015.

[36] P. Moskal, K. Dulski, and et al., "Science advances," vol. 7, eabh4394, 2021.

[37] M. Dadgar and P. Kowalski, "Acta physica polonica b," vol. 51, 309–311, 2020.

[38] P. Kowalski, W. Wiślicki, and et al., "Phys. med. biol," vol. 63, p. 165 008, 2018.

[39] M. M. Khalil. 2017, Basic Science of PET Imaging.

[40] P. G.-R. Spectrometry. 2008, Interactions of Gamma Radiation with Matter, 25-38.

[41] G. B. Saha. 2010, Basics of PET Imaging: Physics, Chemistry, and Regulations . Springer.

[42] R. K. Parajuli, M. Sakai, and et al., "Sensors (basel)," vol. 22, no. 19, p. 7374, 2022.

[43] C. L. John, E. T. George, and W. K. David. 2017, Encyclopedia of Spectroscopy and Spectrometry.

[44] X. Yu, X. Zhang, and et al., "Crystals," vol. 12, no. 9, p. 1302, 2022.

[45] A. Wibowo and et al., "Communications materials," vol. 4, p. 21, 2023.

[46] P. Lecoq, "Nuclear instruments and method in physics," vol. 809, pp. 130–139, 2016.

[47] R. Mao, L. Zhang, and R.-Y. Zhu, "Ieee transactions on nuclear science," vol. 55, no. 4, pp. 2083–2089, 2008.

[48] National Institute of Standards and Technology, 2020, https://nist.gov/pml. (2023).

[49] Crystal , https://www.crystals.saint-gobain.com. (2023).

[50] Vilardi and et al., "Nuclear instruments and methods," vol. 564, pp. 506–514, 2006.

[51] Eljen Technology. https://eljentechnology.com. (2023).

[52] "Saint-gobain crystals." https://www.crystals.saint-gobain.com. (2023).

[53] M. Koshimizu, "Applied physics," vol. 62, no. 1, p. 010 503, 2023.

[54] A. Migdall, S. V. Polyakov, J. Fan, and J. C. Bienfang, "Single-photon generation and detection physics and applications," vol. 45, 2013.

[55] "Photomultiplier tubes." https://www.matsusada.com/ application/ps/ photomultiplier_tubes. (2019).

[56] R. Klanner, "Nuclear instruments and methods," vol. 926, pp. 36–56, 2018.

[57] R. Klanner, "Nuclear instruments and methods," vol. 926, pp. 36–56, 2019.

[58] McLaughlin, J. Biagio, and G. Gallina, "Sensors," vol. 21, no. 17, p. 5947, 2021.

[59] "Hamamatsu." Photomultiplier tubes and related products. Product Catalogue, https://www. hamamatsu. com/ jp/ en.html. (2022).

[60] F. T. Ardebili and M. Ghafouri, "Acta physica polonica b," vol. 51, p. 421, 2020.

[61] S. Gundacker, R. M. Turtos, E. Auffray, M. Paganoni, and P. Lecoq, "Phys. med. biol," vol. 64, p. 055 012, 2019.

[62] C. H. X. U, "Study of the silicon photomultipliers and their applications in positron emission tomography," 2014.

[63] P. Moskal and et al., "Physics in medicine and biology," vol. 64, 2019.

[64] P. Moskal and et al., "Nature reviews physics," vol. 1, no. 9, 527–529, 2019.

[65] J. Rong, Haider, and et al., "Nature communications," vol. 14, p. 3257, 2023.

[66] P. Moskal and E. Stępień, "Frontiers in physics," vol. 10, p. 969 806, 2022.

[67] E. Miele, G. Spinelli, and F. T. et al., "Journal of experimental clinical cancer research," vol. 27, p. 52, 2008.

[68] D. .Rosik, "On the design of affibody molecules for radiolabeling and in vivo molecular imaging," 2013, pp. xi, 55.

[69] X. Huang. 2010, Table of radionucluide, https://www.bipm.org/ documents/20126/53814638

[70] R. E. Schmitz, A. M. Alessio, and P. E. Kinahan, The Physics of PET/CT scanners. 2010, Imaging Research Laboratory, Department of Radiology, University of Washington.

[71] A. K Jha and et al., "Indiantitle of radiology and imaging," vol. 24, no. 2, pp. 103–106, 2014.

[72] J. A. Jensen, Radon Transform and Filtered Backprojection. 2016, http://bme.elektro.dtu.dk

[73] A. Gelman and et al., "Technical report, department of statistics, university of california," vol. 349, 1992.

[74] R. Shopa, J. Baran, and et al., "Ieee transactions on radiation and plasma medical sciences," vol. 7, no. 5, p. 509, 2023.

[75] J. Seibert, "Pediatric radiology," vol. 44, no. Suppl 3, pp. 431–439, 2014.

[76] G. L. Zeng, "Journal of nuclear medicine technology," vol. 46, no. 2, pp. 129–132, 2018.

[77] N. Sengee and et al., "Proceedings of the 2017 international conference on computational biology and bioinformatics," 2017.

[78] P. Moskal, A. Gajos, M. Mohammad, and et al., "Nature communications," vol. 5658, 2021.

[79] P. Moskal, P. Rzaca, and E. Stepien, "Bio-algorithms and med-systems," vol. 17, no. 4, 301–399, 2021.

[80] S. Sharma, J. Chhokar, C. Curceanuand, and et al., EJNMMI Phys, vol. 7, 2020.

[81] W. Krzemień, A. Gajos, K. Kacprzak, and et al., "Softwarex," vol. 11, p. 100 487, 2020.

[82] 3M. https://www.3m.com, (accessed March 24, 2021). ().

[83] Dupont. https://www.dupont.com, (accessed March 24, 2021). ().

[84] L. Kaplon, "Ieee transactions on nuclear science," vol. 67, no. 10, pp. 2286–2289, 2020.

[85] G. Korcyl and et al., "Ieee transactions on medical imaging," vol. 37, 22526–2535, 2018.

[86] M. Pałka and et al, "Jinst," vol. 12, p. 08 001, 2017.

[87] G. Korcyl et al., "Ieee transactions on medical imaging," vol. 37, no. 11, p. 2526, 2018.

[88] R. Brun and F. Rademakers, "Nuclear instruments and methods," vol. 389, pp. 81–86, 1997.

[89] W. Krzemień and A. G. andet al., "Arxiv preprint arxiv:1503.00465," 2015.

[90] I. Kipnis, Collins, and et al., "Nuclear science, ieee transactions on," vol. 44, pp. 289 –297, 1997.

[91] P. Kowalski, P. Moskal, and et al., "Acta phys. pol. a," vol. 127, 1505–12, 2015.

[92] S. Jan and et al., "Physics in medicine and biology," vol. 49, 4543–4561, 2004.

[93] S. Jan and et al., "Physics in medicine and biology," vol. 56, 881–901, 2011.

[94] D. Sarrut and et al., "Medical physics," vol. 41, no. 6 Part 1, 2014.

[95] Gate Collaboration. "Opengate." https://github.com/OpenGATE/Gate/blob/ develop/ GateMaterials.db. (2022).

[96] Gate database. "physics." https://www.physics.purdue.edu/ jones105/ phys56400$_F$all2017/s_ bc400 − 404 − 408 − 412 − 416 − data − sheet.pdf. ().

[97] G. Collaboration. "Geant4 - physics reference manual." http://geant4.web.cern.ch / geant4/ UserDocumentation/ UsersGuides/ PhysicsReferenceManual/fo/ PhysicsReferenceManual.pdf. (2016).

[98] V. Ivanchenko and S. Incerti, "Epj web of conferences," vol. 142, p. 01 016, 2017.

[99] P. Kowalski, W. Wiślicki, and et al., "Acta physica polonica b," vol. 47, p. 549, 2016.

[100]   S. Niedźwiecki, "Master's thesis, jagiellonian university," 2011.

[101]   D. Witherspoon et al., "Journal of nuclear medicine," vol. 28, no. 11, pp. 1717–1724, 1987.

[102]   T. Murata, K. Miwa, N. Miyaji, et al., "Ejnmmi physics," vol. 3, p. 26, 2016.

[103]   J. S. Karp and et al., "Nucl med," vol. 61, no. 1, pp. 136–143, 2020.

[104]   M. Dadgar, "Feasibility study of lesion detection by means of total-body jagiellonian positron emission tomography scanner," Ph.D. dissertation, Jagiellonian University, Kraków, 2022.

[105]   T. Murata, K. Miwa, and N. e. a. Miyaji, "Ejnmmi physics," vol. 3, no. 26, 2016.

[106]   A. González-Montoro and et al., "Nuclear instruments and methods in physics research, a," vol. 920, pp. 58–67, 2019.

[107]   I. Bartošová, V. Slugen, and et al., "Journal of physics: Conference series," vol. 516, p. 012 023, 2014.

[108]   B. E. Zimmerman, J. Cessna, and R. Fitzgerald, "Journal of research of the national institute of standards and technology," vol. 113, no. 5, pp. 265–280, 2008.

[109]   Sanchez-Crespo and Alejandro, "Applied radiation and isotopes," vol. 76, pp. 55–62, 2013.

[110]   C. L. Loirec and C. Champion, "Nuclear instruments and methods," vol. 582, no. 2, pp. 644–653, 2007.

[111]   A. P. George and et al., "Journal of nuclear medicine," 2021.

[112]   J. Ermert and B. Neumaier, The Radiopharmaceutical Chemistry of Fluorine-18: Nucleophil 2019, chapter5-4057.

[113]   F. Gonnella and et al., "Nuclear instruments and methods," vol. 789, pp. 52–57, 2015.

[114]   V. Becares and J. Blazquez, "Science and technology of nuclear installations," vol. 2012,

[115]   G. F. Knoll, Radiation Detection and Measurement, 3rd. John Wiley & Sons, 1999.

[116] G. Korcyl, S. Niedźwiecki, and S. Sharma, "Private correspondence," 2023.

[117] E. Czaicka, master's thesis, Zakład Fizyki Jądro, 2008.

[118] M. Pawlik-Nied¹wiecka, "Phd's thesis, jagiellonian university," 2023.

[119] R. Key, "Pet image reconstruction: Methodology and quantitative accuracy,"

[120] C. Labbe. "Determination of a set of existing algorithms for comparative evaluation." https://stir.sourceforge.net/ links/parapet/ $Task1_3.AlgorithmSurvey.pdf, Accessed1$ (2004).

[121] A. Mehranian and et al., "Journal of medical imaging," vol. 49, pp. 3740–3749, 2022.

[122] A. Suljic, P. Tomse, L. Jensterle, and D. Skrk, "Radiol oncol," vol. 49, no. 3, pp. 227–233, 2015.

[123] GE Healthcare, https://www.gehealthcare.com/shop, accessed on November 4, 2023.

[124] Siemens Healthineers, https://www.siemens-healthineers.com/en-us/medical-imaging , note = "[Accessed on November 4, 2023]",

[125] Philips Healthcare, https://www.usa.philips.com/healthcare/e/image-guided-therapy , Accessed on November 4, 2023.

[126] S. Vandenberghe, P. Moskal, and J. S. Karp, "Ejnmmi physics," vol. 7, p. 35, 2020.

[127] S. Surti, P. Pantel, and J. Karp, "Ieee transactions on radiation and plasma medical sciences," vol. 4, no. 3, pp. 283–292, 2020.

[128] A. Alavi, B. Sabouryn, and L. Nardo, "Clinical nuclear medicine," vol. 47, no. 1, pp. 43–55, 2022.

[129] B. A. Spencer and et al., "Journal of nuclear medicine," vol. 62, no. 6, pp. 861–870, 2021.

[130] M. Dadgar and et al., "Ejnmmi physics," vol. 10, p. 62, 2023.